On Growth and Stifling of Localized Corrosion Attacks in CO2 and Acetic Acid Environments : Application to the Top-of-Line Corrosion of Wet Gas Pipelines Operated in Stratified Flow Regime

J. Amri

HAL Id: tel-00521868

https://theses.hal.science/tel-00521868

Submitted on 28 Sep 2010

INSTITUT POLYTECHNIQUE DE GRENOBLE

T H E S E

pour obtenir le grade de

DOCTEUR DE l'Institut Polytechnique de Grenoble

Spécialité : *« Matériaux, Mécanique, Génie Civil, Electrochimie »*

préparée à :

Institute for Energy Technology (IFE) - Norway
Laboratoire de Science et Ingénierie des Matériaux et des Procédés (SIMAP) - France
Laboratoire d'Electrochimie et de Physicochimie des Matériaux et des Interfaces (LEPMI) - France

dans le cadre de **l'Ecole Doctorale**

« Ingénierie - Matériaux, Mécanique, Environnement, Energétique, Procédés, Production »

présentée et soutenue publiquement

par

Jamel AMRI

le 10 Novembre 2009

On Growth and Stifling of Localized Corrosion Attacks in CO_2 and Acetic Acid Environments : Application to the Top-of-Line Corrosion of Wet Gas Pipelines Operated in Stratified Flow Regime

--- DIRECTEURS DE THÈSE ---

Ricardo P. NOGUEIRA
Egil GULBRANDSEN

--- JURY ---

Tor HEMMINGSEN	University of Stavanger - Norway	Président
Bernard NORMAND	Institut National des Sciences Appliquées de Lyon - France	Rapporteur
Roy JOHNSEN	Norwegian University of Science and Technology - Norway	Rapporteur
Ricardo P. NOGUEIRA	Institut Polytechnique de Grenoble - France	Directeur de thèse
Egil GULBRANDSEN	REC Solar - Norway	Codirecteur de thèse
Michel BONIS	Total - France	Examinateur
Mohsen ACHOUR	ConocoPhillips - USA	Examinateur
Rolf NYBORG	Institute for Energy Technology - Norway	Examinateur

Preface

This doctoral thesis is published as a partial fulfilment of the requirements for the Ph.D. degree at Institut Polytechnique de Grenoble (France). Most of the experimental work was carried out at the Materials and Corrosion Technology Department of the Institute for Energy Technology (IFE, Norway) from February 2007 to June 2009. The work was undertaken as a part of the project "Stabilization of Top-of-Line Corrosion rate" under the supervision of Professors Ricardo Pereira Nogueira from Institut Polytechnique de Grenoble and Egil Gulbrandsen [*] from IFE and the Norwegian University of Science and Technology (NTNU). The project was funded by the French Norwegian Foundation, Total, and ConocoPhillips.

[*] Present address: REC Solar As, Norway.

Abstract

In the present work, CO_2 corrosion of API 5L X65 pipeline steel in the presence of acetic acid (HAc) was investigated. The objective of this research was to study a qualitative behaviour frequently found in the case of the so-called top-of-line corrosion (TLC). That is, increasing corrosion rates and steep shrinkage after certain - not predictable - time delay. The focus was on the role of HAc in the growth and stifling of localized attacks in CO_2-containing media. The kinetic behaviours of carbon steel in such brines indicated that the overall effect of HAc is a balance between an enhanced cathodic reaction rate and a slightly inhibited anodic reaction rate. Results also showed that the active dissolution is not directly related to the presence of acetic acid but rather to what is generically referred to as CO_2 corrosion. Zero resistance ammeter (ZRA) measurements on artificial pit electrode assembly, coupled to numerical simulation results, indicated that local HAc concentration gradients sustain the pit growth mechanism to a certain critical depth. Beyond this critical depth, the coupling current sharply drops off and the pit undergoes a process of stifling. However, a substantial effect of the purely ohmic drop on the pit stabilization process appeared unlikely in such conditions. Instead, initiated pits were shown to propagate and stifle mainly according to the counteracting depletions of HAc and CO_2. On the basis of the obtained results, a complete scenario was therefore proposed for the morphological trend of localized attacks, which is in good agreement with field occurring TLC cases.

Keywords: CO_2 corrosion; Top-of-line Corrosion; Localized attacks; Acetic acid; ZRA; Artificial pit electrode; Numerical simulation.

Acknowledgements

Jamel Amri

November 10, 2009

In memory of my beloved father: I hope you are proud of me from over there!

To my beloved mother

BHLAL

"Education is what remains after one has forgotten what one has learned in school. "

Albert Einstein

*"The unknown 22-year old (**Lars Onsager**) from Norway walks into the famous scientist's office with the announcement: "Professor Debye, your theory of electrolytes is incorrect! "*

From E.H. Hauge, Energy 30 (2005) 787.

__Lars Onsager__ is a Norwegian-born American physical chemist and theoretical physicist, awarded the Nobel Prize in chemistry for establishing the "reciprocity relations" in irreversible thermodynamics.

List of Publications

The work described in this doctoral thesis has been published in four refereed journal articles, and presented in two international conferences. The journal articles are listed at the end of this dissertation.

Journal Papers

- J. Amri, E. Gulbrandsen, R.P. Nogueira, "Numerical Simulation of a Single Corrosion Pit in CO_2 and Acetic Acid Environments", Corrosion Science, 52 (2010) 1728.

- J. Amri, E. Gulbrandsen, R.P. Nogueira, "Propagation and Arrest of Localized Attacks in CO_2 Corrosion of Carbon Steel in the Presence of Acetic Acid", Corrosion, 66 (2010) 035001-1.

- J. Amri, E. Gulbrandsen, R.P. Nogueira, "Pit Growth and Stifling on Carbon Steel in CO_2-containing Media in the Presence of HAc", Electrochimica Acta, 54 (2009) 7338.

- J. Amri, E. Gulbrandsen, R.P. Nogueira, "The Effect of Acetic Acid on the Pit Propagation in CO_2 Corrosion of Carbon Steel", Electrochemistry Communications, 10 (2008) 200.

Conference Papers

- J. Amri, E. Gulbrandsen, R.P. Nogueira, "Computational Model of a Localized Attack in CO_2 Corrosion in the Presence of Acetic Acid", EUROCORR (2008), Edinburgh/ UK.

- J. Amri, E. Gulbrandsen, R.P. Nogueira, "Effect of Acetic Acid on Propagation and Stifling of Localized Attacks in CO_2 Corrosion of Carbon Steel", CORROSION/09, Paper no. 09284, NACE (2009), Atlanta/ USA.

.

Table of Contents

I.1. Introduction
I.2. CO₂ Corrosion
I.3. Internal Corrosion of Gas Pipelines in Stratified Flow Regime
I.4. Top-of-Line Corrosion
I.5. Context of this Work
I.6. Research Objective
I.7. Basic Principles of Electrochemical Corrosion
I.8. Dissertation Outline
References

II.1. Introduction
II.2. Physical-Chemistry of Carbonic Species
II.3. CO₂ Corrosion
II.4. Top-of-Line Corrosion
II.5. TLC Models
II.6. Mitigation and Control Techniques
II.7. Conclusions
References

List of Figures

--- Chapter I ---

--- Chapter II ---

--- Chapter V ---

--- *Chapter VI* ---

List of Tables

--- Chapter VI ---

Table VI.1. List of the chemical reactions considered in this model and their respective thermodynamic and kinetic constants at 25 °C.

Table VI.2. List of aqueous species considered in the model along with their diffusion coefficients and initial concentrations.

Chapter I

General Introduction

Table of Contents

I.1.   Introduction

The petroleum industry is at the cornerstone of the technological-energetic world matrix. One of its main concerns relates to the transportation of oil and gas. Particularly, corrosion phenomenon is at the origin of numerous failure cases encountered in this field with the human, cost and environmental impacts that they may cause. For economical reasons, multiphase well streams are still being sent crude or semi-processed into carbon steel pipelines over long-distances from wells to main platforms, existing installations on neighbouring fields or onshore processing facilities. Carbon dioxide (CO_2) gas is a natural component in oil and gas productions. It can be present with concentrations up to 50 % of the gas phase in certain wells. CO_2 gas is soluble in water or aqueous solutions. Its solubility depends strongly on temperature, applied pressure, and to some extent on the nature of liquids. Dry CO_2 gas is non-corrosive in nature to metals and alloys at moderate temperatures. In petroleum industry, however, CO_2 is hydrated in the co-produced aqueous phase and forms carbonic acid (H_2CO_3), which often impairs structures through the so-called CO_2 corrosion [1-6].

I.2. CO_2 corrosion

CO_2 corrosion, also known as "sweet corrosion", was first discovered in the 1940's [1, 7]. Since then, its severity and cost impact on oil and gas productions have been extensively investigated. CO_2 corrosion has also been paid increasing attention with the advent of enhanced oil recovery techniques, which are based on CO_2 injection into reservoirs and gas wells. To date, this form of corrosion is still a major concern for the petroleum industry, particularly in transportation stages [8, 9]. In addition to CO_2 gas, water and other acidic gases such as hydrogen sulphide (H_2S) and volatile organic acids co-produced with the hydrocarbons constitute often the corrosive environment. CO_2 corrosion is also a major issue in which relates to the application of carbon steels. The latter are indeed widely used in the field for being presently the only economically feasible materials. Being highly vulnerable to CO_2 corrosion, carbon steels can

experience high corrosion rates up to 10 millimeters per year **[10**, **11]** leading to premature failure of installations in the absence of preventive mitigation efforts like injection of corrosion inhibitors **[12]**.

I.3.   Internal Corrosion of Gas Pipelines in Stratified Flow Regime

In wet gas pipelines, the multiphase well stream may be transported in a variety of flow regimes such as annular, slug and (wavy) stratified flow. These regimes depend on the orientation of the pipeline and both the nature and the rate of the individual phase flow. The stratified flow regime is the most common of them (see **Figure I.1**). This is the case where the liquid phase (water, condensed hydrocarbons…) is transported along the bottom of the line, while the gas phase (CO_2, water vapour…), flows along the upper part.
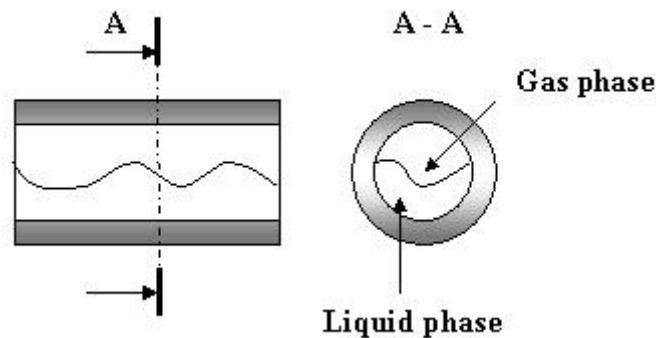
Figure I.1. Schematic of wavy stratified flow regime commonly encountered in wet gas pipelines.

In wet gas transportation, the stratified flow regime is well known to enhance internal corrosion. A broad view would categorize the internal corrosion of the pipe as uniform or localized. Considering the occurrence of internal corrosion, Gunaltun reported that the form of corrosion is correlated to the part of the inner pipe wall **[13]**. The latter is mainly divided into three parts; bottom-of-line, sidewalls, and top-of-line.

I.4. Top-of-Line Corrosion

Top-of-line corrosion (TLC) is recognized as one of the most severe forms of internal corrosion in wet gas transportation **[10]**. **Figure I.2** illustrates a case of TLC encountered in the field. The formation of iron carbonate layer ($FeCO_3$) at the top-of-line is most probably due to the fact that iron-saturated droplets of the condensed water do not fall down under the effect of gravity as the inclination is not sufficient **[13]**. However, if $FeCO_3$ layer does not offer uniform protectiveness (porous or weak layer), the top-of-line can undergo severe localized attacks.
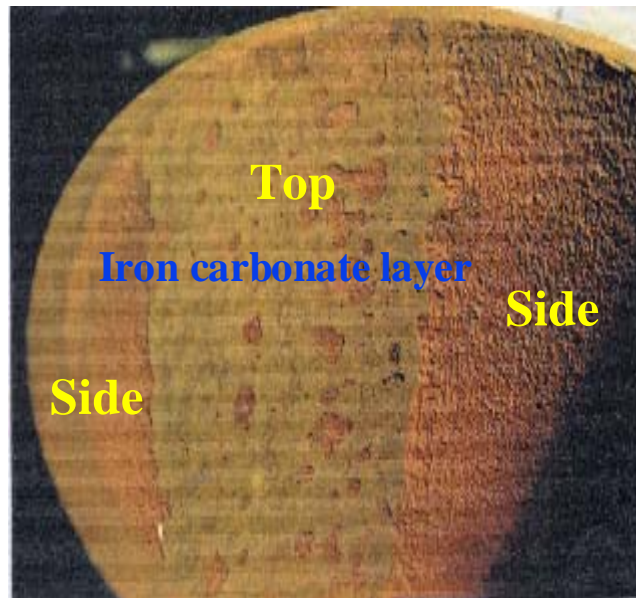
Figure I.2. *Case of top-of-line corrosion [13].*

TLC is typically associated with partially or completely failed (or the absence of) thermal insulation of the pipeline. Due to external cooling that induces large temperature gradients, the co-produced water vapour contained in the gas phase condenses on the whole circumference of the internal walls of the line. In such conditions, the condensed water is in equilibrium with the gas phase and becomes very corrosive when the partial pressure of acidic gases (CO_2, H_2S, organic acids) is high. As most of the condensing water drains under the effect of gravity to the lower part, corrosion is first expected to occur at the bottom-of-line. Under sustained dewing conditions, a thin film of liquid nevertheless forms on the upper parts. In this case, the top-of-line is also subject to corrosion. The key factors involved in TLC phenomenon

are given in **Figure I.3**. Although corrosion mitigation is usually achieved by injection of inhibitors, TLC is still difficult to prevent. Indeed, as TLC occurs in wet gas lines operated in stratified flow regime, corrosion inhibitors remain at the bottom and they are not prone to reach and protect the top-of-line.
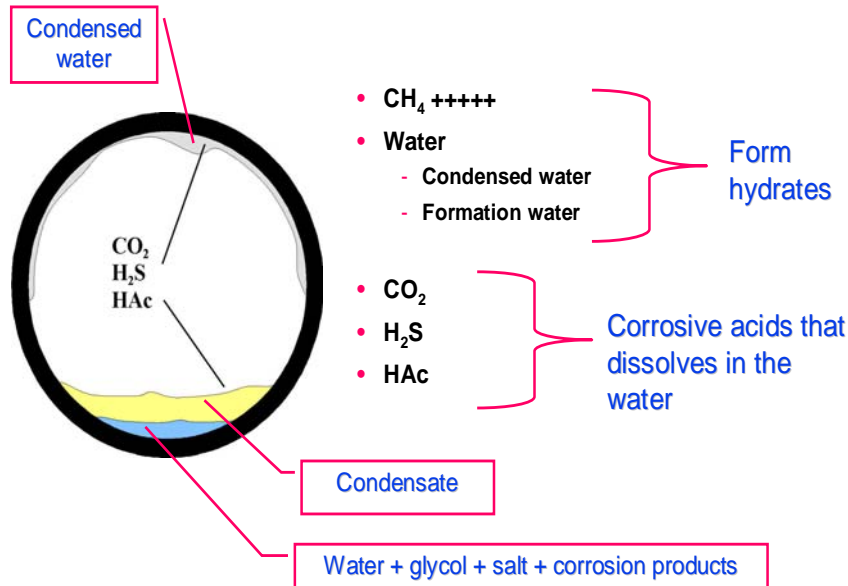
Figure I.3. Key factors involved in TLC phenomenon. Any injected corrosion inhibitor remains at the bottom of the line, and is not able to protect the top of the line.

I.5.   Context of this Work

TLC rate can be particularly high if volatile short chain carboxylic acids are present. Indeed, organic acids lower the pH of the condensed water (below pH 4) and very high localized corrosion rates can take place [13-15]. Acetic acid (CH_3COOH, commonly abbreviated as HAc) is one of the most prevalent organic acids found in oil and gas reservoirs with high concentrations up to thousands of ppm in the co-produced aqueous phase. Results issued from field observations and laboratory studies have shown that HAc causes an additional contribution to the uniform CO_2 corrosion rate [16-18]. Rudimentary understanding however exists regarding its basic role in the propagation of localized attacks. In practice, localized attacks are at the root of most corrosion failures of pipelines. Inspection of pipelines from different gas fields have shown that TLC attacks have, in many cases, slowed down with time and stabilized

after an initial period of high rates **[19]**. Although a significant progress has been achieved over the two last decades to understand TLC phenomenon, the underlying mechanisms controlling the propagation and stifling of localized TLC attacks are still not well understood. This makes TLC attacks difficult to predict, prevent and mitigate in case of need.

I.6.   Research Objective

The present work was undertaken as a part of "Stabilization of TLC rate" Project at the Materials and Corrosion Technology Department at Institute for Energy Technology (IFE) in Norway. The Materials and Corrosion Technology Department has an extensive experience over 25 years in CO_2 corrosion in oil and gas pipelines in general and in TLC in particular. The department is conducting research projects within corrosion area in cooperation with the major international companies operating in oil and gas fields, and has developed advanced laboratory facilities specially designed for such studies.

The present study deals with aqueous CO_2 corrosion in the presence of HAc. The general objective is to identify the key factor(s) and to understand (and quantify) the mechanisms controlling the onset and arrest of localized TLC attacks in wet gas pipelines. Although common behaviours are generally observed, the key factors involved in CO_2 corrosion in the presence of HAc influence the propagation of localized attacks in a complicated way. Understanding the mechanisms involved in the propagation and stifling of localized TLC attacks aims at challenging the petroleum industry to develop optimal methods and strategies for control and mitigation of TLC. Indeed, the consequences of uncontrolled and non predictable TLC attacks in large wet gas pipelines can have a large cost impact if the pipeline has to be repaired, replaced or built in a more resistant but expensive material. Also, both the economical and the environmental impacts are large if a pipeline rupture takes place. Results and data generated during this work could serve to some extent as a basis for further improvements of existing predictive models.

I.7. Basic Principles of Electrochemical Corrosion

I.7.1. Introduction

Aqueous CO_2/ HAc corrosion of carbon steel is a complex phenomenon in which several coupled processes occur simultaneously. Nevertheless, it is fundamentally an electrochemical process that obeys the principles of electrochemistry. It is therefore worthwhile to have a brief look at the basic electrochemistry of aqueous corrosion. Most of these principles will be used later in this work.

I.7.2. Corrosion

Considering the increasing need for long-term performance of engineering structures over a wide size scale, the effective use of any metal as a material of construction must be based on an understanding of their physical, mechanical and chemical properties. These properties cannot however be drawn aside from the environmental conditions prevailing. Indeed, the interaction of a metal with the environment in which it serves is of primary importance. This interaction is commonly referred to as metallic corrosion when it becomes detrimental to the metal. Corrosion may, in many cases, lead to irreversible degradations of the metal by altering its inherent properties that are to be preserved. It follows that any fundamental approach to the phenomena of corrosion must therefore involve consideration of the intrinsic characteristics of the metal, the environmental conditions and the interfacial processes that occur between the metal and its environment. These considerations may thus be summarized as follows [20]:

- *Metal:* elemental composition, atomic structure, microscopic and macroscopic heterogeneities, mechanical properties.

- *Environment*: chemistry, concentrations of reactants involved, deleterious substances, pH, pressure, temperature, hydrodynamics, impingement.

- *Metal-environment interface*: dissolution kinetics of the metal, nature and location of corrosion products, film growth and stability.

I.7.3. Corrosion as a Heterogeneous Chemical Reaction

Considering the aforementioned factors, it is evident that metallic corrosion mechanisms are extremely complex. As a first approach, corrosion can be regarded as a heterogeneous chemical reaction between the metal and its environment. This interfacial reaction involves the metal (M) and its environment (Env) as reactants. Accordingly, corrosion can simply be expressed by the following overall chemical reaction, for which the law for mass action still applies:

$$M + Env \rightleftharpoons M^{'} + Env^{'} \tag{I.1}$$

M' and Env' are respectively the metal and environment after alteration and can therefore be considered as the reaction products. A chemical reaction is a process that results in an interconversion of chemical reactants and in which elements are either added or removed. For a pure chemical reaction, however, none of the reactants undergoes a change in its valence, i.e., no species is either oxidized or reduced **[21]**. Electrochemical reactions are therefore chemical in nature insofar as elements may be added or removed, and in which one reactant or more undergoes a change in the number of its valence electrons. Consider the precipitation reaction of iron carbonate:

$$Fe^{2+} + CO_3^{2-} \rightleftharpoons FeCO_3 \tag{I.2}$$

This reaction is a pure chemical process inasmuch as none of the elements involved has changed its valence. In corrosion context, the ferrous ions are produced by the dissolution of the metallic iron according to the following oxidation reaction:

$$Fe \rightleftharpoons Fe^{2+} + 2e^{-} \tag{I.3}$$

The precipitation reaction of $FeCO_3$ can also be written in a more generalized form that describes the interaction of the metal (Fe) with its environment (CO_2 + water). The overall reaction is therefore as follows [22]:

$$Fe + CO_2 + H_2O \rightleftharpoons FeCO_3 + H_2 \qquad (I.4)$$
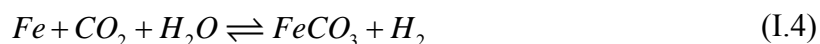
The latter is no longer a pure chemical reaction since the metallic iron Fe (zero valent) is converted into a divalent state. Thus, pure chemical and electrochemical reactions are not widely physically dissociated on the metal surface. Indeed, in many cases, a corrosion process involves a coupling between a pure chemical reaction and a charge-transfer reaction [23].

I.7.4. Requirements for Aqueous Corrosion

Aqueous metallic corrosion occurs when at least two electrochemical half-cell reactions (i.e., oxidation and reduction) take place on the metal (i.e., electrode) surface. The oxidation reaction results in the change of the metal from a metallic state into a non-metallic state, thus rendering it soluble in the aqueous phase. Accordingly, there are four requirements for any aqueous corrosion process: an anodic zone on which oxidation reaction occurs, a cathodic zone on which reduction reaction of a different species occurs, an aqueous solution that insures ionic conduction between the two reaction sites, and an electrical conductor for electrons transfer between the reacting sites. It follows that any successful mitigation effort of corrosion must therefore alter, at least, one of these requirements.

I.7.5. Thermodynamic Driving Force of Corrosion

The driving force of corrosion is defined as the lowering of energy associated with the oxidation of a metal [24]. This driving force is determined from thermodynamic considerations. Indeed, thermodynamics predict whether respectively oxidation and reduction reactions can or cannot occur. It does not however provide any information on how slow or fast the metal corrodes. In fact, the rate at which a metal corrodes is rather a matter of kinetics. As any electrochemical process is fundamentally

a chemical reaction, its thermodynamic is expressed as a correlation between the concentrations of the reacting species and the temperature. In addition and unlike pure chemical reactions, this correlation also takes into consideration the number of electrons transferred or liberated in the oxidation reaction. As an illustrative example, consider the isolated electrochemical process relative to the dissolution of a metal, M, in an aqueous medium to produce metal cations, M^{n+}:

$$M \rightleftharpoons M^{n+} + ne^- \tag{I.5}$$

During this process, the electrons exchanged accumulate at the metal surface, thus inducing an electrical potential difference between the metal and the solution. This potential difference promotes both release of some ions and discharge of some others on the metal surface. Once the metal has reached a characteristic potential relative to the solution, a dynamic equilibrium is then established. At a given temperature, the conditions for this equilibrium are stated by the general expression of the Gibbs free energy change, ΔG:

$$\Delta G = \Delta G^0 + RT.\ln(Q) \tag{I.6}$$

Equation (I.6) is also called Van't Hoff reaction isotherm. Here ΔG^0, R (8.314 J mol^{-1}) and T stand for the standard Gibbs free energy change, the universal gas constant and the absolute temperature (in Kelvin), respectively. The activity quotient (Q) is expressed as follows:

$$Q = \frac{\displaystyle\prod_{products} a_p^{v_i}}{\displaystyle\prod_{reactants} a_r^{\gamma_j}} = \frac{a_p^{v1} \times a_p^{v2} \times ...etc}{a_r^{v1} \times a_r^{v2} \times ...etc} \tag{I.7}$$

where a_p^{vi} is the activity of the produced species i, raised to its stoichiometric coefficient v_i, and $a_r^{\gamma j}$ the activity of the reacting species j, raised to its stoichiometric coefficient γ_i. In the particular case of reaction (I.5), a charge transfer is involved. The Gibbs free energy changes, ΔG and ΔG^0, are hence replaced by the equilibrium electrical potential terms, E and E^0. That is:

$$\Delta G = -nFE \tag{I.8}$$

$$\Delta G^0 = -nFE^0 \qquad \text{(I.9)}$$

where F (96490 C mol^{-1}) is the Faraday`s constant. Similarly, E^0 is referred to as the electromotive force or standard electrode potential. The standard potential is measured against the standard hydrogen electrode (SHE), which is a reference electrode with an arbitrary standard potential equals to zero. The values of the standard potentials are particularly useful in the prediction of galvanic corrosion between dissimilar metals. Rearranging expression (I.6) yields the Nernst equation. Substituting 2.303 log (Q) for ln (Q) and assuming ambient temperature (298 K), Nernst equation is simply expressed as:

$$E = E^0 - \frac{0.059}{n}.\log(Q) \qquad \text{(I.10)}$$

The Nernst equation solves the potential of an electrochemical cell involving a reversible system with fast kinetics and it is valid only at equilibrium and at the electrode surface. This equation is particularly of great interest since it helps mapping the domain of metal stability using Pourbaix (1940) or E-pH diagrams.

In view of the elements argued above, an aqueous corrosion process is a matter of coupling between an anodic reaction (i.e., oxidation) and a cathodic reaction (i.e., reduction) that occur simultaneously. The electrons liberated in the oxidation reaction (I.5) require an electrons-acceptor, and are then transferred to the site, where a soluble oxidant (Ox) is reduced:

$$Ox + ne^- \rightleftharpoons \text{Re}d \qquad \text{(I.11)}$$

The term Red (reductant) denotes here the reduced form of the oxidant. The sum of the two half-cell reactions (I.5) and (I.11) results in the overall corrosion reaction:

$$M + Ox \rightleftharpoons M^{n+} + \text{Re}d \qquad \text{(I.12)}$$
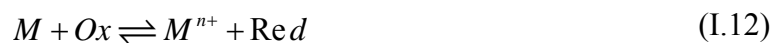
A short-circuited galvanic cell is then naturally setup in which the energy is dissipated by the consumption of oxidant. Applying again Nernst equation to reaction (I.12) yields (the activity of the metal is taken as 1):

$$\Delta E = E_{M/M^{n+}} - E_{Ox/Red} = \Delta E^0 - \frac{0.059}{n} . \log\left(\frac{a_{M^{n+}} a_{Red}}{a_{Ox}}\right) \qquad \text{(I.13)}$$

where ΔE^0 is the difference in standard potentials between the anodic and cathodic reactions. The sign of the difference in equilibrium potentials (ΔE) is the key factor in the prediction of any corrosion reaction. A particular case arises when the equilibrium potential of the metal is lower than the one of the redox couple. As a consequence, the metal liberates electrons through oxidation to increase its equilibrium potential (i.e., lowers its energy) until it reaches the state of a zero net charge exchange. The soluble oxidant present at the metal-solution inferface is simultaneously reduced, thus decreasing its equilibrium potential (i.e., increasing its energy); the metal is said to be experiencing a corrosion process. Thus, the thermodynamic driving force of corrosion is given by (see also **Figure I.4**):

$$\Delta E_{th} = -\Delta E \qquad \text{(I.14)}$$

We saw that although the feasibility of a particular corrosion reaction can be easily determined by evaluating the relative values of the equilibrium potentials of the electrochemical reactions involved, thermodynamics do not predict how fast or slow does a metal corrode. The corrosion rate is of vital importance in the predetermination of the lifetime of engineering structures that are prone to corrosion, and the nature of eventual mitigation attempts. Since the corrosion rate is primarily a matter of kinetics, we therefore propose in the following to briefly summarize the basic principles of electrochemical kinetics frequently applied in corrosion studies.
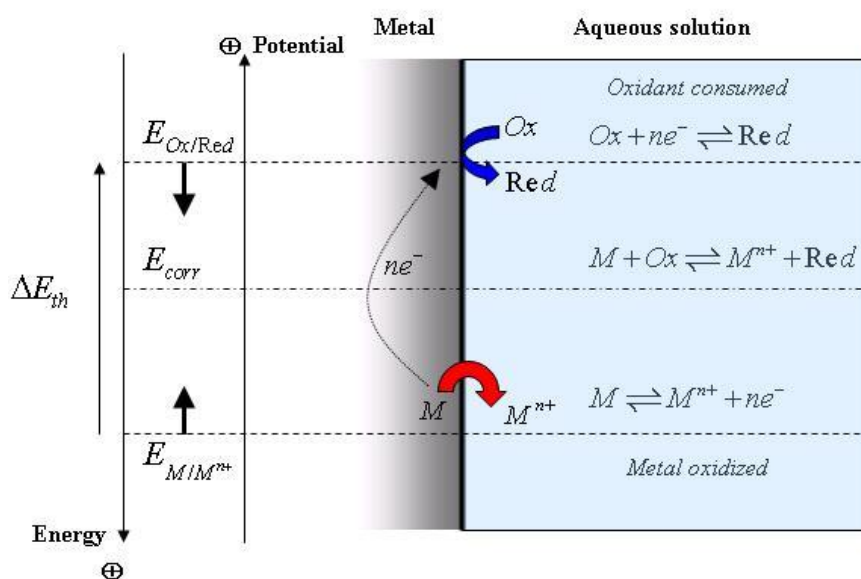
Figure I.4. *Thermodynamic driving force of aqueous metallic corrosion in the presence of a soluble oxidant. The coupling between the two half-reactions occurs at the corrosion potential, E_{corr}. The latter depends on the relative rates of the anodic and cathodic reactions.*

I.7.6.   Kinetics of Corrosion

The rate of an electrochemical reaction occurring at the electrode surface is governed by four major factors: (1) mass transfer of reactants or products to/ from the electrode surface; (2) kinetics of electron transfer; (3) preceding and ensuing reactions, and (4) kinetics of adsorption/desorption. It follows that the slowest process is the rate-determining step.

A.   *Activation Energy*

The rate of an electrochemical reaction is controlled by the magnitude of one or more energy barriers that every entity involved must overcome to be transformed. The energy that must be acquired by this entity to pass these barriers is referred to as the activation Gibbs free energy (ΔG^*). In corrosion context, the latter is the excess energy needed to transform metallic elements into soluble metallic ions (see **Figure I.5**).
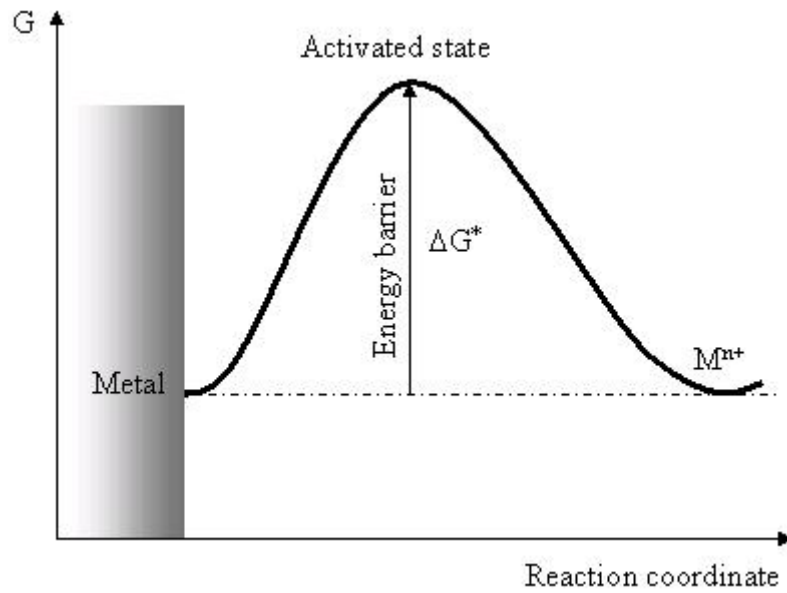
Figure I.5. *Schematic distribution of the free energy. The activation Gibbs free energy ΔG^* is the excess of energy that must be acquired by the metallic element to transform into a soluble metallic ion M^{n+}.*

In general, the rates of electrochemical and chemical reactions can be predicted using both Faraday's (r_F) and Arrhenius' (r_A) equations, respectively:

$$r_F = \frac{iA_{w,j}}{nF} \tag{I.15}$$

$$r_A = k \exp\left(-\frac{\Delta G^*}{RT}\right) \tag{I.16}$$

where i is the current density, $A_{w,j}$ the atomic weight of the species j, and k the chemical reaction constant. At equilibrium, the two rates become equal and the current density can therefore be expressed as:

$$i = \frac{nFk}{A_{w,j}} \exp\left(-\frac{\Delta G^*}{RT}\right) \tag{I.17}$$

For reversible electrode processes at dynamic equilibrium, the current density is simply denoted as the exchange current density ($i = i_0$).

B.   *Electrode Polarization*

For some reasons, it happens that the dynamic equilibrium at the electrode-solution interface is altered. As a consequence, a net current flows across the electrode surface, thus inducing a change in the electrode potential. This phenomenon is referred to as polarization, and the potential difference between the polarized and the unpolarized (equilibrium) electrode potentials is termed the overpotential (η). There are mainly three types of polarization: activation; concentration and resistance polarization.

- Activation Polarization

The dynamic equilibrium at the electrode surface involves simultaneous release of some ions and discharge of some others at equal rates. The partial currents leaving (anodic) and entering (cathodic) the electrode surface, denoted respectively as i_a and i_c, are therefore equal in absolute value but opposite in sign. The activation polarization refers to the charge transfer process, in which a particular electrochemical reaction step becomes a controlling factor of the electron flow rate to and from the electrode surface. The activation polarization manifests in the relative changes in the activation Gibbs free energies when the dynamic equilibrium is disturbed. **Figure I.6** shows a schematic distribution of the free energies for an anodically polarized electrode under activation control. According to equation (I.8), such polarization leads to a positive shift of the metal energy by "$nF\eta_A$" and the activated state by "$\alpha nF\eta_A$". In this case, the activation Gibbs free energy for oxidation of the polarized electrode is decreased by "$(1 - \alpha)nF\eta_A$". Likewise, the activation Gibbs free energy for the opposite reaction is increased by "$\alpha nF\eta_A$". Replacing the activation Gibbs free energy by its new expression in equation (I.17) yields the following expressions for the anodic and cathodic currents:

$$i_a = i_0 \exp\left(\frac{(1-\alpha)nF\eta_A}{RT}\right) \tag{I.18}$$

$$i_c = -i_0 \exp\left(\frac{-\alpha nF\eta_A}{RT}\right) \tag{I.19}$$

Expressing the net current as the sum of i_a and i_c yields the well-known Butler-Volmer equation:

$$i = i_0 \left[\exp\left(\frac{(1-\alpha)nF\eta_A}{RT}\right) - \exp\left(\frac{-\alpha nF\eta_A}{RT}\right) \right] \tag{I.20}$$

For electrode potentials far from the equilibrium, that is $\eta_A \gg 0$ or $\eta_A \ll 0$, equation (I.20) can be written in a very simple and generic form, that is the Tafel's law:

$$\eta_A = a + b\log(i) \tag{I.21}$$

where a and b are constants that can be easily inferred from equation (I.20). The constant b is commonly termed the Tafel slope.
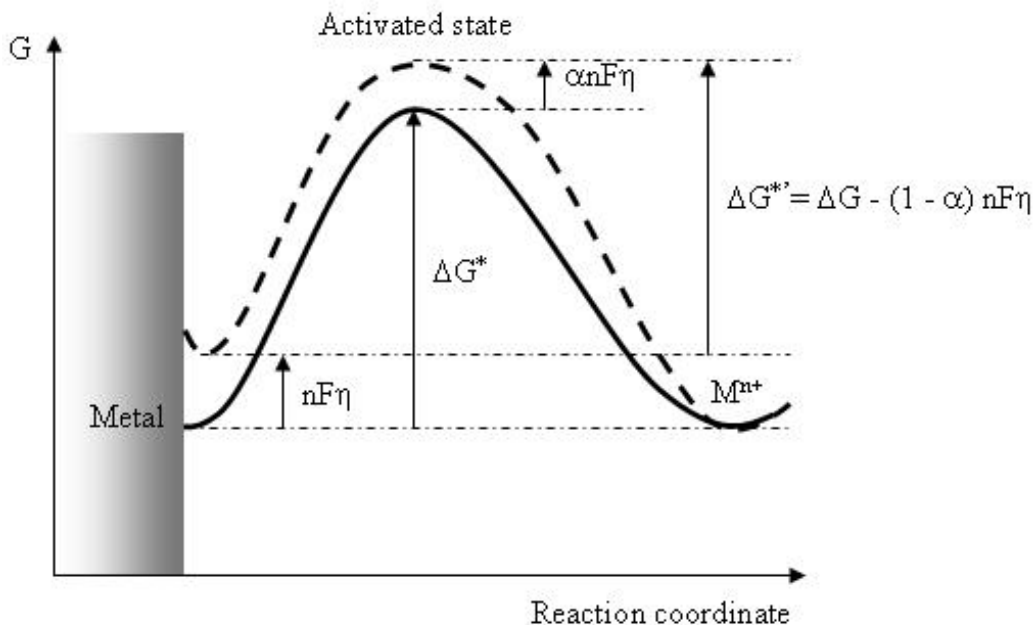
Figure I.6. *Schematic distribution of free energies for an anodically polarized electrode under activation control (overpotential $\eta_A > 0$). The parameter $\alpha \in [0; 1]$ denotes the symmetry factor that defines the position of the activated state in respect with the two minima.*

▪ Concentration Polarization

The activation polarization described by Tafel's law (I.21) is dependent on pure charge transfer process. Complications may arise due to the fact that species involved are sometimes either produced or depleted at the active surface faster than they can diffuse to and from the bulk solution. In this case, the electrochemical process is rather controlled by the rate of mass transfer of these species at a limiting current, i_L. As a consequence, the polarization at i_L becomes larger than that predicted by the Tafel's law. The deviation from pure activation control results in an excess overpotential known as concentration or mass-transport overpotential, η_C. This overpotential is given by the following expression **[25**, **26]**:

$$\eta_C = \frac{RT}{nF} \ln\left(1 - \frac{i}{i_L}\right) \tag{I.22}$$

▪ Resistance Polarization

Under some circumstances, the ohmic resistance may be a limiting factor for the corrosion reaction. This is all the more enhanced when the overall reaction involves the formation of a film on the reacting surface. The total potential drop across such resistance is known as resistance polarization, η_R. Hence, the total polarization is the sum of three major components: activation, concentration and resistance polarization:

$$\eta_T = \eta_A + \eta_C + \eta_R \tag{I.23}$$

C. *Corrosion Rate*

A corrosion process involves at least one anodic reaction (i.e., oxidation) and one cathodic reaction (i.e., reduction) at the metal surface. The two half-reactions couple together at the corrosion potential (E_{corr}) often termed as the mixed potential and at a specific rate called the corrosion current density (i_{corr}). When polarizing the electrode by E from E_{corr}, the anodic and cathodic current densities given respectively by expression (I.18) and (I.19) become:

$$i_a = i_{corr} \exp\left(2.303 \frac{E - E_{corr}}{b_a} \right) \tag{I.24}$$

$$i_c = -i_{corr} \exp\left(-2.303 \frac{E - E_{corr}}{b_c} \right) \tag{I.25}$$

where b_a and b_c are the anodic and cathodic Tafel slopes, respectively. Replacing equations (I.24) and (I.25) into the expression (I.20) yields a more convenient form of Butler-Volmer equation that quantifies the kinetics of the corrosion process:

$$i = i_{corr} \left[\exp\left(2.303 \frac{E - E_{corr}}{b_a} \right) - \exp\left(-2.303 \frac{E - E_{corr}}{b_c} \right) \right] \tag{I.26}$$

It is worth pointing out here that the potential difference E - E_{corr}, commonly denoted as the overvoltage, refers to the polarization of the electrode around the corrosion potential. The overvoltage must then not be confused with the overpotential, η. The latter is indeed related to the reversible potential of the electrode reaction. The polarization resistance R_p can be calculated through derivation of the equation (I.26) at E = E_{corr}. That is Stern-Geary's relationship:

$$R_p = \left(\frac{di}{dE} \right)^{-1}_{E=E_{corr}} = \frac{B_{SG}}{i_{corr}} \quad ; B_{SG} = \frac{b_a b_c}{2.303 (b_a + b_c)} \tag{I.27}$$

The corrosion rate, expressed in terms of penetration rate, is related to the corrosion current density through the following expression:

$$C_R = \frac{A_w}{nF\rho} i_{corr} \tag{I.28}$$

where ρ is the metal density.

I.7.7.   Forms of Corrosion

Corrosion attacks may take several forms that strongly depend on the inherent characteristics of the metal, the environmental conditions in which it serves, and the

kinetics of corrosion processes. Categorization of the corrosion forms aims primarily at approaching in the same way corrosion processes that have similar mechanisms. Although there is no unique classification of these forms, a more focused view would categorize corrosion as uniform or localized. Uniform corrosion, known also as general corrosion, takes place across the entire exposed surface. Nevertheless, the damage caused by this form of corrosion is predictable and can be estimated by the corrosion rate, typically in mm/year. There are many subcategories of this form such as atmospheric, galvanic, hight temperature, and metal-liquid corrosion. Localized corrosion implies that only discrete parts of the metal surface are attacked. Likewise, localized corrosion can be classified as, for example, pitting, crevice, filiform or erosion corrosion. Localized corrosion often results in deep penetration of the metal, thus inducing an impairment of its characteristics. Since this form of attack is stochastic in nature, its control is therefore more difficult than uniform corrosion.

I.8.   Dissertation Outline

Briefly, the present dissertation is structured as follows. In **Chapter II**, the state-of-the art as well as current understanding of CO_2 corrosion in general and TLC in particular are reviewed. The chapter discusses the relative effects of the key factors (CO_2 partial pressure, pH, T…). The most representative experimental studies as well as some well-known models are presented. Common mitigation and control techniques in the field are also mentioned.

The experimental protocol, instrumentations and methods employed in this work are described in **Chapter III**.

The overall macroscopic behaviour of API 5L X65 pipeline steel in 1 bar CO_2-saturated aqueous NaCl in the presence of HAc is investigated and discussed in **Chapter IV**. Experimental data are mainly acquired by potentiodynamic and electrochemical impedance spectroscopy techniques (EIS). Additionally, characterization techniques such as scanning electron microscopy (SEM) and energy dispersive X-ray spectroscopy (EDS) were used to study corrosion product scales and surface states after immersion in CO_2- and HAc- containing media.

In **Chapter V**, experimental investigations were more focused on the effect of HAc. Electrochemical noise technique was used to assess the effect of HAc on pitting in CO_2 corrosion of carbon steel pipelines. Furthermore, the role of HAc in the pit growth was studied by means of artificial pit electrodes. Experimental simulation of the coupling behaviour between the attack and the outer surrounding surface was also undertaken with the help of a split cell setup.

A numerical model of steady-state behaviour of a single localized corrosion attack in mixed CO_2/ HAc brine was developed with Comsol Multiphysics® tools and detailed in **Chapter VI**. The model aimed at overcoming the system complexity and analyzing underlying mechanisms. The model was based on mass-conservation and consisted of 2D axis-symmetric attack in representative working conditions. Electrochemical kinetics occurring on the working surfaces were described by Tafel equations, which were fitted to experimental data obtained on X65 pipeline steel.

On the basis of experimental findings and model predictions, a descriptive scenario was proposed in **Chapter VII** for the propagation mechanism of localized attacks in CO_2 and HAc environments. The main conclusions and the significance of the present work are outlined in this chapter along with some recommendations for future work.

References

[1]   W.F. Rogers, W.A. Shellshear, Ind. Eng. Chem., 29 (1937) 160.

[2]   H.R. Copson, Corrosion, 7 (1951) 123.

[3]   American Peutroleum Institute, Corrosion of Oil- and Gas- well Equipment, API, Dallas, Texas (1958).

[4]   J.W. Graves, E.H. Sullivan, Materials Protection, 5 (1966) 33.

[5]   G. Shmitt, CORROSION\83, Paper no. 43, NACE, 1983.

[6]   S. Nešić, J. Postlethwaite, M. Vrhovac, Corrosion Reviews, 15 (1997) 211.

[7]   J-L. Crolet, N. Thevenot, A. Dugstad, CORROSION\99, Paper no. 24, NACE, 1999.

[8]   R. Nyborg, CORROSION\02, Paper no. 02233, NACE, 2002.

[9]   B.M. Kermani, A. Morshed, Corrosion, 59 (2004) 659.

[10]   C. De Waard, D.E. Milliams, Corrosion, 31 (1975) 177.

[11]   A. Dugstad, L. Lunde, K. Videm, CORROSION\94, Paper no. 14, NACE, 1994.

[12]   S. Nešić, J. Postlethwaite, S. Olsen, Corrosion, 52 (1996) 280.

[13]   Y. M. Gunaltun, D. Supriyatman, J. Achmad, CORROSION\99, Paper no. 36, NACE, 1999.

[14]   M. Estavoyer, "*H2S corrosion in oil and gas production*", NACE publication (1981) 905.

[15]   R. Pailassa, M. Dieumegarde, M. Estavoyer, "*H2S corrosion in oil and gas production*", NACE publication (1981) 860.

[16]   E. Gulbrandsen, K. Bilkova, CORROSION\06, Paper no. 06364, NACE, 2006.

[17]   Y.M. Gunaltun, D. Larrey, CORROSION\00, Paper no. 71, NACE, 2000.

[18]   M. W. Joosten, J. Kolts, J. W. Hembree, M. Achour, CORROSION\02, Paper no. 02294, NACE, 2002.

[19]   M. Thammachart, Y. Gunaltun, S. Punpruk, CORROSION\08, Paper no. 08471, NACE, 2008.

[20]   L.L. Shreir, R.A. Jarman, G.T. Burstein, "*CORROSION - Metal/Environment Reactions*", Vol. 1, Butterworth-Heinemann (1994).

[21]   R. G. Kelly and, J. R. Scully, D. W. Shoesmith, R. G. Buchheit, "*Electrochemical Techniques in Corrosion Science and Engineering*", Marcel Dekker, Inc. (2002).

[22]   S. Nešić, Corr. Science, 49 (2007) 4308.

[23]   A. J. Bard, L. R. Faulkner, "*Electrochemical Methods: Fundamentals and Applications*", John Wiley (1980).

[24] *"Corrosion: Fundamentals, Testing, and Protection"*, Vol. 13A, ASM Handbook (2003).
.

[25] D.A. Jones, *"Principles and Prevention of Corrosion"*, 2nd ed., Macmillan Publishing (1996).

[26] M.G. Fontana, N.D. Greene, *"Corrosion Engineering"*, McGraw-Hill (1978).

Chapter II

Literature Review

II.6.2. Injection of Corrosion Inhibitors
II.6.3. Selection of Materials
II.6.4. Application of Protective Coatings
II.6.5. Cathodic Protection
II.6.6. Other Techniques

II.1.   Introduction

Internal CO_2 corrosion of pipelines is a major concern to the petroleum industry. It is also a serious problem in the application of carbon steel. Indeed, this last is still widely used in the field for being presently the only economically feasible material of construction, although they are highly prone to CO_2 corrosion in absence of remediation efforts. Besides carbon dioxide, water and volatile organic acids are naturally occurring components in oil and gas productions, and constitute a potentially corrosive environment. Under such conditions, carbon steel can experience severe damages leading to premature failures of engineering structures with the well-know repercussions. It is therefore worthwhile to review literature relating to all of these facts. This chapter addresses the following topics:

- Physical-chemistry of carbonic species

- CO_2 corrosion

- Top-of-line corrosion (TLC)

- TLC models

- Mitigation and control techniques

II.2.   Physical-Chemistry of Carbonic Species

II.2.1.   Physical Properties

CO$_2$ gas molecule, also called carbonic anhydride **[1]**, has three vibrational modes; the symmetric stretching mode (λ_1), the bending mode (λ_2), and the asymmetric stretching mode (λ_3). **Figure II.1** diagrams these principal modes. Each vibrational mode has its characteristic quantized energy levels. The energy steps are lowest on the

bending mode, roughly twice as large on the symmetric stretching mode, and even larger on the asymmetric stretching mode **[2]**.
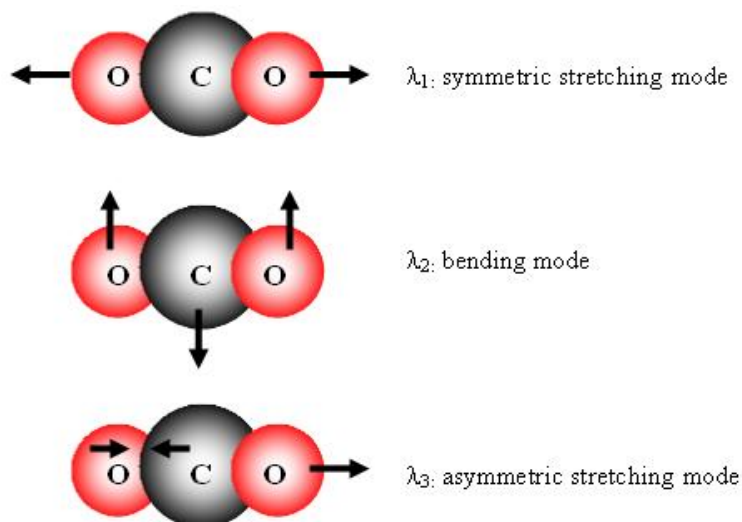
Figure II.1. *Principal vibrational modes of CO_2 gas molecule. The stretching modes stiffen while the bending mode softens with pressure. IR spectra data in literature reported that $\lambda_1 = 1337$ cm^{-1}, $\lambda_2 = 667$ cm^{-1}, $\lambda_3 = 2349$ cm^{-1}.*

II.2.2. Solubility

CO_2 gas is soluble in aqueous solutions and other various liquids (glycol, alcohols, heavy hydrocarbons…). Its solubility strongly depends on temperature (T), partial pressure (P_{CO2}) of CO_2, and to some extent on the nature of the solvent. In water, the mole fraction (x) of dissolved carbon dioxide, CO_2(aq) at 1 bar CO_2 can be represented as a function of temperature over the range 273-353 K **[3]**:

$$R \ln(x) = a + bT^{-1} + c \ln(T) + dT \qquad \text{(II.1)}$$

with a = -1327.8 J K^{-1} mol^{-1}, b = 72611.6 J mol^{-1}, c = 180 J K^{-1} mol^{-1}, and d = -0.009 J K^{-2} mol^{-1}. R denotes the universal gas constant. Equation (II.1) is plotted in **Figure II.2**.
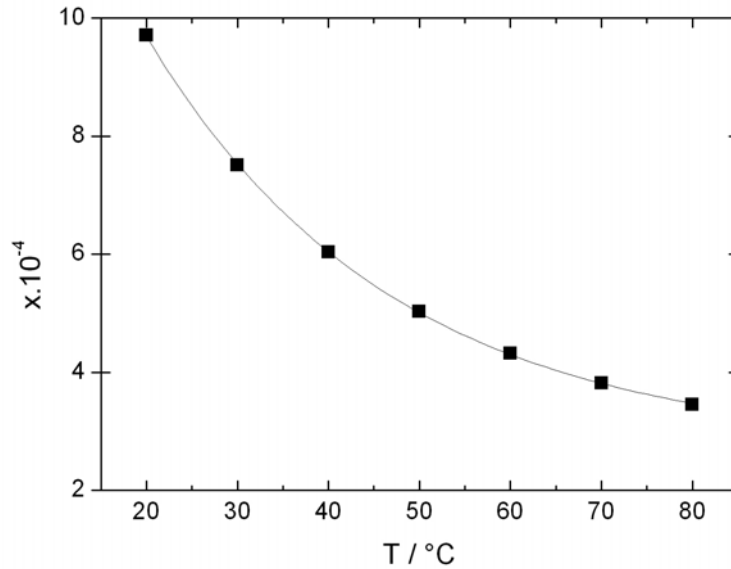
Figure II.2. *Mole fraction of dissolved CO_2 in water vs. temperature at $P_{CO2} = 1$ bar.*

Unless stated otherwise, CO_2 (aq)' is referred hereafter to as the total dissolved carbon dioxide ($CO_2(aq)$ + H_2CO_3). The equilibrium of gaseous CO_2 with $CO_2(aq)$' can be written as follows:

$$CO_2(g) \rightleftharpoons CO_2(aq)'; K_{sol}^{'} \qquad (II.2)$$

In aqueous NaCl solutions, the equilibrium constant varies with T (K) and the ionic strength (I_s) according to the following form [3]:

$$pK_{sol}^{'} = -2385.73T^{-1} + 14.018 - 0.015T + \left(0.286 - 6.167 \times 10^{-4}T\right)I_s \qquad (II.3)$$

where the ionic strength is given by:

$$I_s = \frac{1}{2}\sum_i z_i^2 C_i \qquad (II.4)$$

The terms z_i and C_i are respectively the charge number and the molar concentration of the electroactive species i. **Figure II.3** shows the variation of K_{sol}' with temperature in pure aqueous NaCl at distinct concentrations. It is shown that K_{sol}' decreases substantially with temperature at low and moderates concentrations (i.e., ionic

strengths) of NaCl. At higher concentrations, however, K_{sol}' is low and is practically independent of temperature.
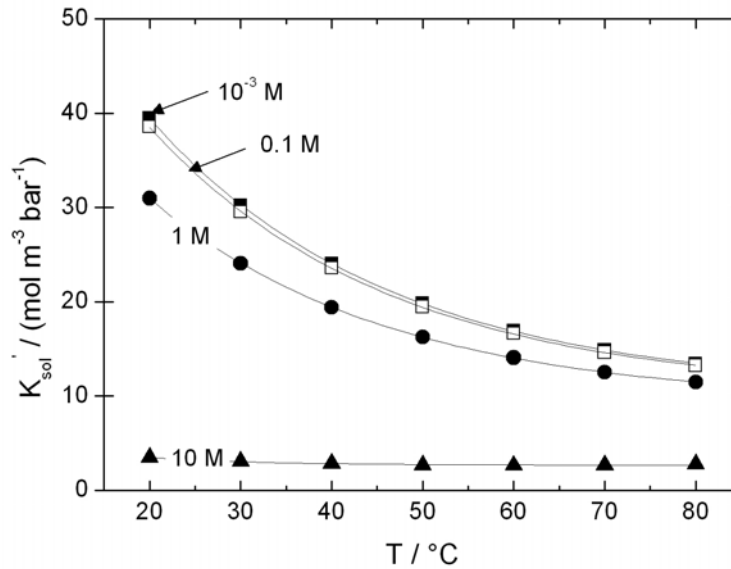
Figure II.3. Variation of the solubility equilibrium constant of dissolved CO_2 with temperature in aqueous NaCl at distinct concentrations.

II.2.3.   Ionization

The existence of carbonic acid (H_2CO_3) has been shown by spectroscopic techniques **[4-6]**. Carbonic acid is a result of a slow chemical reaction between dissolved CO_2 with water. That is:

$$CO_2\left(aq\right) + H_2O \rightleftharpoons H_2CO_3 ; K_{hyd} \tag{II.5}$$
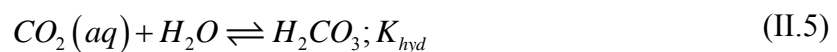
This reaction is likened to a hydration reaction. The equilibrium constant (pK_{hyd}) is 2.58 at 25 °C and 2.63 at 300 °C **[3]**. It is therefore clear that pK_{hyd} varies only slightly with temperature as would be expected for a hydration reaction. As carbonic acid is diprotic, there are therefore two dissociation constants. The first one is related to the dissociation of the parent molecule into proton and bicarbonate ions:

$$H_2CO_3 \rightleftharpoons H^+ + HCO_3^- ; pK_{ca} \tag{II.6}$$

and the second step involves the dissociation of bicarbonate ions into proton and carbonate ions:

$$HCO_3^- \rightleftharpoons H^+ + CO_3^{2-}; pK_{bi} \tag{II.7}$$

The equilibrium constants pK_{ca} and pK_{bi} are respectively 3.5 and 10.33 at 25 °C [7]. The standard Gibbs free energies of formation (G_f^0) of individual species involved in these two reactions are [8, 9]: H^+ (0 kJ mol^{-1}), H_2CO_3 (-623.2 kJ mol^{-1}), HCO_3^- (-586.85 kJ mol^{-1}), CO_3^{2-} (-527.9 kJ mol^{-1}). **Figure II.4** exemplifies a concentration-pH diagram at equilibrium of carbonic species in 1 bar CO_2-saturated water at room temperature.
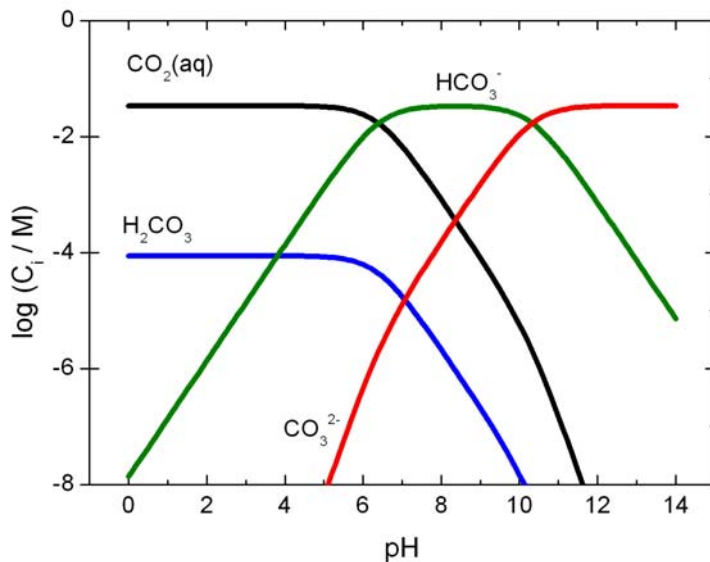
Figure II.4. *Speciation at equilibrium of carbonic species in respect with pH in 1 bar CO₂ saturated-water at ambient temperature (closed system).*

II.2.4. Frequent Confusion

It is worth pointing out that the term "carbonic acid" is often used in literature as a reference to dissolved CO_2 (carbonated water) [10], which has been a source of confusion. The value of pK_{ca} (3.5) shows that H_2CO_3 is a stronger acid than other weak acids such as acetic acid (pK_{ac} = 4.80) or formic acid (pK_{fc} = 3.74). This is expected from the influence of the electronegative oxygen substituent. As it will be discussed hereafter, the concentration of H_2CO_3 is much lower than the CO_2 concentration in

aqueous solutions and the measured acidity is therefore significantly reduced. The overall reaction may be rewritten as the sum of reactions (II.5) and (II.6):

$$CO_2(aq) + H_2O \rightleftharpoons H^+ + HCO_3^-; pK_{ca}' \tag{II.8}$$
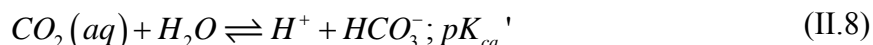
The apparent equilibrium constant pK_{ca}' is 6.36, which is the commonly cited value in literature. Hence, the apparent constant must be referred to as the acidity constant of carbon dioxide. The frequent use of pK_{ca}' instead of pK_{ca} can be attributed to the fact that the first constant is more easily determined from pH measurements or CO_2 analysis than the second one.

II.2.5.   Kinetics

The hydration of CO_2 is not only low, but also not strong acid-catalyzed reaction. These effects were ascribed to the linear structure of the CO_2 molecule [3]. The forward hydration rate constant ($k_{hyd,f}$) was found to vary linearly with the ionic strength, with the relationship being [11, 12]:

$$k_{hyd,f}(s^{-1}) = -(8 \pm 3) \times 10^{-3} I_s + (3.9 \pm 0.5) \times 10^{-2} \tag{II.9}$$

This rate is also expressed as a function of the absolute temperature according to the following [10]:

$$\log\left[k_{hyd,f}(s^{-1})\right] = 329.85 - 110.541 \times \log(T) - 17265.4T^{-1} \tag{II.10}$$

and commonly averaged to 3 x 10^{-2} s^{-1}. Instead, the backward rate constant ($k_{hyd,b}$) was shown to be relatively insensitive to the variation of ionic strength [11]. Carbonic acid is only a small fraction of the total dissolved carbon dioxide that never exceeds 1%. The protolytic dissociation of carbonic acid nevertheless occurs at very high reaction rate ranging between 7.80 x 10^6 s^{-1} and 1.5 x 10^7 s^{-1} [3, 7]. The protonation of bicarbonate anions also occurs at high rate ($k_{bi,b}$) estimated to 6.5 x 10^{10} M^{-1} s^{-1} [13, 14].

II.3.   CO₂ Corrosion

II.3.1.   Introduction

Gaseous carbon dioxide and water vapour are commonly co-produced components in most of oil and gas fields. Although dry CO_2 gas is non-corrosive in nature to steels at moderate temperatures, its hydration in the condensing water forms an aggressive environment that may damage facilities through the so-called CO_2 corrosion or "sweet corrosion". The corrosiveness of such environment depends on pH, temperature and CO_2 partial pressure, beyond the inherent properties of the steel and the hydrodynamic conditions prevailing. The hydration of CO_2 is a slow chemical reaction that can become the controlling step for the overall CO_2 corrosion rate [15]. CO_2 corrosion has been extensively investigated over many decades and a considerable knowledge is now available in literature, particularly in which relates to corrosion-induced failure of oil and gas pipelines [10, 16-28]. CO_2 corrosion is a complex electrochemical phenomenon in which simultaneous coupled processes occur. Although factors that play key roles in CO_2 corrosion has been identified, a satisfactory mechanistic explanation of their mutual interactions has not yet been given.

II.3.2.   CO₂ Corrosion Mechanisms

A.   *Anodic Mechanisms*

The basic mechanisms of CO_2 corrosion of mild steels under varying conditions are now well documented in literature through the works of de Waard et al. [29-32], Dugstad et al. [33], and Nešić et al. [16, 34-37]. In oxygen-free aqueous environments, the overall CO_2 corrosion of carbon steel can be written as:

$$Fe + \left(CO_2 \bullet H_2O \right) \rightleftharpoons \left(Fe^{2+} \bullet CO_3^{2-} \right) + H_2 \qquad \text{(II.11)}$$
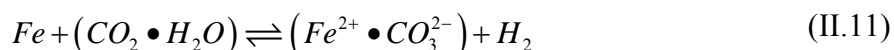
As for any electrochemical process, CO_2 corrosion involves a coupling between at least two half-reactions. The corresponding anodic reaction consists of iron dissolution through the following overall reaction:

$$Fe \rightleftharpoons Fe^{2+} + 2e^{-} \qquad \text{(II.12)}$$

The anodic mechanisms in CO_2 corrosion have however been controversial until recently [16, 38]. It was assumed that the basic mechanism of the active dissolution of iron is little affected by the presence of CO_2. In this case, dissolved CO_2 would only act as a catalyst [39] and the three-step pH-dependent mechanism proposed by Bockris et al. still applies [29, 40-43]:

$$Fe + OH^{-} \rightleftharpoons (FeOH)_{ad} + e^{-} \qquad \text{(II.13)}$$

$$(FeOH)_{ad} \rightleftharpoons FeOH^{+} + e^{-}; RDS \qquad \text{(II.14)}$$

$$FeOH^{+} \rightleftharpoons Fe^{2+} + OH^{-} \qquad \text{(II.15)}$$

The subscript "ad" stands for the adsorbed state. In this case, reaction (II.14) would be the rate-determining step (RDS).This mechanism has however been put into question by later findings [37, 38, 44]. An alternative mechanism that takes into account the effect of dissolved CO_2 on the active dissolution of iron has therefore been proposed by Nešić et al. [44]. In this mechanism, an intermediate ligand (Fe.CO_2) [45] is believed to act as a catalyst instead of OH^{-} as suggested by Bockris' model. Instead of reaction (II.14), the interfacial process whereby adsorbed hydroxyled ligands are released from the steel surface hence becomes the rate-determining step for lower and intermediate pH values. At higher pH (typically pH>5), the steel surface is supplied with hydroxide ions without any restrictive mass-transfer until the determining rate exceeds the rate of charge transfer step. At such pH values, this last step becomes the "new" RDS. A general expression for the anodic current was therefore derived [44]:

$$\log(i_a) = \frac{\eta}{b_a} + a_1 pH + a_2 \log(P_{CO_2}) + a_3 \qquad \text{(II.16)}$$

Here a_1, a_2 and a_3 are constant. The other parameters have their usual meanings. The orders of reaction are dependent on pH and the partial pressure of CO_2, respectively (see **Table II.1**). It is worth noticing that according to equation (II.16) the anodic current

does not depend on pH at values higher than 5 ($a_1 = 0$), which is in line with other works [43, 46].

Table II.1. List of values for reactions orders as well as apparent transfer coefficient in respect with pH and partial pressure of CO_2 at moderate temperatures [44].

	pH<4		4<pH<5		pH>5	
	$P_{CO2}<1$	$P_{CO2}>1$	$P_{CO2}<1$	$P_{CO2}>1$	$P_{CO2}<1$	$P_{CO2}>1$
a_1	2		1		0	
a_2	1	0	1	0	1	0
b_a (mV dec^{-1})	30		30-120		120	

B.   *Cathodic Mechanisms*

In acidic solutions, the reduction of protons is the prevailing cathodic reaction. At pH values (typically pH>4), the availability of protons is significantly restricted in the vicinity of the surface. The reaction rate is therefore governed by the diffusion rate at which the reacting surface is supplied with H^+ ions from the bulk. This would be the case in the presence of weak acids such as carbonic acid. Although it is only a small fraction of the total dissolved carbon dioxide (less than 1%), carbonic acid is acknowledged to enhance cathodic reaction rate and thus the overall corrosion rate at a much higher rate than would be found in solutions of completely dissociated acids [16]. Nevertheless, the high corrosivity of carbonic acid remained unexplained until the 1970's.

In 1975, de Waard and Milliams investigated the corrosion of X52 carbon steel by means of weight loss and polarization resistance measurements in CO_2-saturated aqueous NaCl solutions under varying conditions of pressure and temperature [29]. They found that the relation between the corrosion rate and the CO_2 partial pressure is significantly different from that expected for strong acids (HCl). Upon their theoretical analysis, de Waard and Milliams demonstrated that the hydrogen evolution reaction in CO_2 corrosion occurs in a "catalytic" way via the direct reduction (II.17) of adsorbed molecules of undissociated carbonic acid. They also suggested that the protonation of bicarbonate anions (II.19) can become rate-controlling through a cathodic shift in

potential. This mechanism was corroborated later by the works of Schmitt et al. **[47-51]** and Eriksrud et al. **[52]**, although they proposed a different RDS:

$$\left(H_2CO_3\right)_{ads} + e^- \rightleftharpoons H_{ads} + HCO_3^-; RDS \qquad (\text{II.17})$$

$$H_{ads} + H_{ads} \rightleftharpoons H_2 \qquad (\text{II.18})$$

$$H^+ + HCO_3^- \rightleftharpoons H_2CO_3 \qquad (\text{II.19})$$
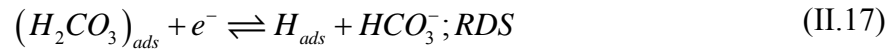
Efforts had been made by Schmitt et al. to study in further details the direct reduction of H_2CO_3 **[47-51]**. Their polarization experiments on rotating disk electrodes in oxygen-free carbonic acid solutions revealed that the cathodic limiting current is the sum of two distinct contributions: the diffusion-controlled proton reduction limiting current and the chemical-controlled H_2CO_3 reduction limiting current. Accordingly, they suggested that the direct reduction of carbonic acid is controlled by the preceding slow heterogeneous hydration of adsorbed aqueous CO_2.

$$\left(CO_2\right)_{ads} + H_2O \rightleftharpoons \left(H_2CO_3\right)_{ads} \qquad (\text{II.20})$$

Later work of Gray et al. confirmed these respective contributions to the overall cathodic limiting current **[41]**. However, the heterogeneous nature of the reaction control remained questionable until the work of Gray et al. Since similar cathodic limiting currents were observed on metals as different as platinum and iron, Gray et al. suggested that the homogeneous hydration of carbon dioxide in the bulk (reaction II.5) is rather the controlling step in the direct reduction of carbonic acid. Homogeneous control is now well accepted **[16, 52]**. According to them, the electron transfer-controlled reduction of bicarbonate anions (II.21) also becomes the prevailing cathodic reaction at pH higher than 5 **[42]**. The effect of this particular reaction on the overall hydrogen evolution is however difficult to experimentally distinguish from the reduction reactions of respectively protons and carbonic acid. Direct reduction of water is commonly omitted since this reaction occurs at lower potentials and can become important only at pH > 5 and partial pressures of CO_2 far below 1 bar **[37, 53]**. Such conditions do not indeed reflect practical CO_2 corrosion situations **[8]**.

$$HCO_3^- + e^- \rightleftharpoons \frac{1}{2}H_2 + CO_3^{2-} \qquad \qquad \text{(II.21)}$$

A more general expression was thereafter derived from Vetter's model by Nešić et al. for the superposition of the diffusion and chemical reaction controlled limiting currents in aqueous CO_2 corrosion [36]. A flow factor was introduced to account for the effect of hydrodynamic conditions on the reaction cathodic limiting current. The interaction between diffusion and chemical reactions appeared to be significant at temperatures lower than 40 °C and flow velocities higher than 1 m s^{-1}. Nešić et al. also found that at such conditions the mass transfer layer is as thick as the chemical reaction layer.

II.3.3.   Key Factors in CO₂ Corrosion

Considering the increasing need for long-term performance of metallic structures in oil and gas fields over a wide size scale, the effective use of any steel must be based on the understanding of its interaction with environmental conditions prevailing, along with its intrinsic properties. Having briefly outlined CO_2 corrosion mechanisms, one can anticipate that there are many key factors that affect CO_2 corrosion in oil and gas industry. A non-exhaustive list of such factors as well as their respective roles in CO_2 corrosion are presented and discussed hereafter.

A.   *CO₂ Partial Pressure*

In scale-free CO_2 corrosion, there seems a general consensus that the corrosion rate increases with the CO_2 partial pressure (P_{CO2}). The commonly accepted explanation is that the concentration of H_2CO_3 is substantially increased with P_{CO2}, thus accelerating the cathodic part reaction rate [16]. The effect of P_{CO2} was first expressed in 1975 [29] in the aforementioned study of de Waard et al. and reviewed in 1993 [31]. According to this study, the corrosion rate was found to increase proportionally to P_{CO2} raised to the power 0.67. Since then, similar power laws between corrosion rates and P_{CO2} with the exponent ranging from 0.5 to 0.8 were reported in literature [28, 31, 33, 53, 54]. The relationship developed by de Waard et al. was generally accepted in laboratory studies

for quantitative prediction of corrosion rates of bar steel under varying conditions of pressure and temperature with the prerequisite that scale build-up does not occur **[51**, **52**, **56**, **57]**. This relationship also showed a satisfactory agreement with some practical situations in low pressure and temperature conditions **[58]**. **Figure II.5** illustrates a good agreement between three predicted P_{CO2} effects on the corrosion rate **[37]**.
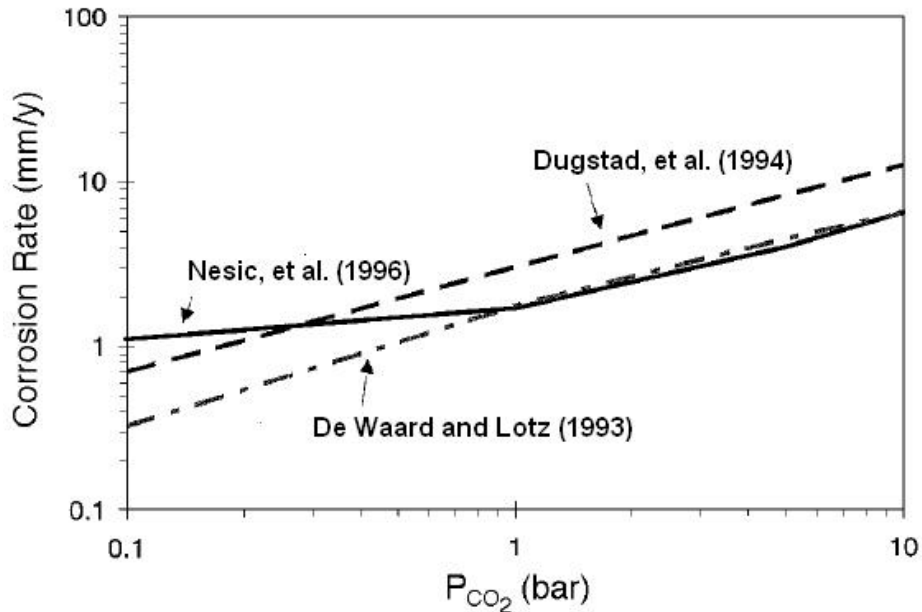
Figure II.5. *Comparison of predicted P_{CO2} effects on the corrosion rate at pH 4 and 20 °C [37].*

The model of de Waard et al. is however valid for operating pressures and temperatures that are often far below the conditions generally encountered in oil and gas fields, and the practical application of this relationship is therefore very limited. Limiting conditions of CO_2 partial pressure and temperature for the validity of this model were set in 1984 and are summarized in **Table II.2**. On the other hand, an increase of P_{CO2} at higher pH leads to higher concentrations of bicarbonate and carbonate anions. These are favourable conditions for precipitation and corrosion scaling **[59]**.

Table II.2. *Limiting conditions of CO_2 partial pressure and temperature set for the validity of de Waard et al. model.*

	P_{CO2} (bar)	T (°C)
Schmitt **[48]**	< 2	< 60
Eriksrud **[52]**	1	20
Ikeda **[56]**	2	60
Murata **[57]**	70	60

B. ***Temperature***

Temperature has an accelerating effect on all the major processes involved in CO_2 corrosion: electrochemical and chemical (by increasing reaction rates), and mass transport (by increasing the diffusion coefficient). It is generally agreed that at low pH, CO_2 corrosion rate steadily increases with temperature until a certain temperature is reached. Beyond this temperature the solubility of iron carbonate is exceeded and protective surface films are formed (particularly at high pH), thus hindering the corrosion rate. This is in good agreement with several studies, where the corrosion rate was shown to peak somewhere in between 60 - 80 °C. On the basis of their prediction results, de Waard and Lotz reported that the corrosion rate increases with temperature and reaches successive maxima at different threshold temperatures depending on the applied partial pressure of CO_2 **[31]**. Other studies also showed that at temperatures beyond 60 °C, the corrosion rate is controlled by the formation of protective scales **[27**, **33**, **52**, **54**, **57**, **60]**. Below this temperature, films build-up may still proceed. However, these films are often unprotective due to their open porous and detached structure **[8**, **16**, **61]**.

C. **pH**

In CO_2-saturated aqueous solutions, pH is dependent on the two aforementioned factors. Typical pH in the field is about 4 or somewhat less **[16]**. At such pH, the second dissociation reaction of carbonic acid (II.7) is neglected and proton concentration is hence equal to that of bicarbonate anions in pure CO_2-water systems. According to Henry's law, the concentration of carbonic acid is proportional to the CO_2 partial pressure. It follows that:

$$pH = -\frac{1}{2}\log\left(P_{CO_2}\right) + \frac{1}{2}\left(pK_{ca} + pK_{sol}\right) \qquad \text{(II.22)}$$

Both K_{ca} and K_{sol} are temperature-dependent constants. A linear relation between pH and temperature was also obtained at 1 bar CO_2 **[29]**. Incorporating this relation into the above equation yields:

$$pH = -\dfrac{1}{2}\log\left(P_{CO_2}\right) + 4.17 \times 10^{-3}T(°C) + 3.71 \qquad \text{(II.23)}$$

Plots of the solution pH under varying conditions of pressure and temperature are depicted in **Figure II.6**. According to equation (II.23), the effect of pH on the overall CO_2 corrosion would be a simple extrapolation from the respective effects of pressure and temperature. At pH 4 or below, it is generally accepted that the reduction of protons dominates the cathodic part reaction rate, particularly at low partial pressures of CO_2. Beyond pH 5 and at high partial pressures of CO_2, the direct reduction of carbonic acid however becomes more significant [37, 62]. High pH also decreases the solubility of iron carbonate, thus resulting in a favourable condition for precipitation and scaling tendency [59, 63, 64]. Both the composition and the nature of surface films can also be indirect effects of pH [16].
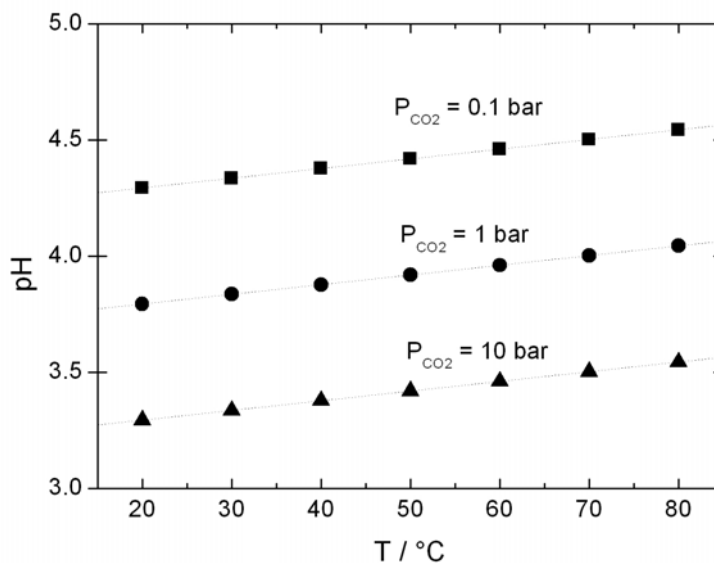
Figure II.6. *Graphical illustration of a pH-T-P_{CO2} diagram in pure CO_2-water systems according to equation (II.23).*

D. *Speciation of the Aqueous Solution*

The chemistry of the aqueous solution is one of the most influential factors in CO_2 corrosion. In practice, this chemistry is as complex as CO_2 corrosion itself. Indeed, a large number of chemical species are found in oilfield brines [16]. Short chain organic

acids are often co-produced as volatile compounds with hydrocarbons. Amongst these acids, acetic acid appears to be the most abundant. The role of acetic acid in CO_2 corrosion is usually addressed in relation with the so-called top-of-line corrosion, and will accordingly be treated in the section dedicated to this phenomenon. For instance and except the fact that they can be directly involved in the electrochemical processes, these numerous species can be more or less influential via their effects on the following factors:

- pH

- Ionic strength

- Viscosity

- Wettability

- Growth and stability of surface scales

It follows that accurate calculations of the solution speciation are an essential pre-requisite for a good prediction of CO_2 corrosion rate.

E. *Corrosion Scales*

CO_2 corrosion mechanisms are strongly dependent on corrosion product scales formed on the steel surface at certain conditions. The nature, protectiveness and kinetics of scales are affected primarily by the environmental conditions prevailing, along with the composition and microstructure of the corroding steel. It follows that any fundamental approach to CO_2 corrosion processes must involve the identification and study of these corrosion scales. It is known that the formation of corrosion scales can slow down initial corrosion rates by as much as three orders of magnitude. Indeed, protective scales act as a diffusion barrier for species involved in the corrosion processes or/and block a portion of the reacting surface. Accordingly, scales-induced mass transfer to and from the steel surface can become the rate-controlling factor instead of hydrogen evolution [51, 52, 56, 60]. The stability, protectiveness, growth rate

and the anchoring of scales are also key parameters that determine whether corrosion is uniform or localized. Scales are formed on the steel surface through the precipitation reaction when the solubility of corrosion products is exceeded. Precipitation of corrosion products can nevertheless proceed in the condition of undersaturation, thus suggesting that the micro-environment in the immediate vicinity of the steel surface is a favourable condition (high Fe^{2+} concentration) for earlier precipitation. As mentioned above, scales are protective and present a good anchoring on the steel surface at high temperatures and high CO_2 partial pressures. At lower temperatures and lower pressures, the formation of scales may still occur. However, such scales often exhibit weak protectiveness due to their open porous structure and poor adherence to the steel surface. In CO_2 corrosion of mild steels, most of the research efforts indicate that iron carbide or cementite (Fe_3C) and iron carbonate ($FeCO_3$) are the two main components of corrosion product scales. Other authors suggested that the good protectiveness and adherence of scales are rather due to the presence of iron bicarbonate, $Fe(HCO_3)_2$ **[65]**. Iron carbide is a naturally occurring component in ferritic-pearlitic steels. It consists of the uncorroded portion of the steel, and it is generally left as lamellas once metallic iron is leached out. This role is briefly discussed in the section hereafter. Corrosion scale may also include iron oxide and hydroxide products **[51**, **65**, **66]**.

Unlike iron carbide, iron carbonate is a "pure" corrosion product. When the concentrations of ferrous ions and carbonate ions are large enough so that the solubility product (K_{sp}) is exceeded, solid iron carbonate precipitates or deposits on the steel surface according to the following slow heterogeneous reaction:

$$Fe^{2+} + CO_3^{2-} \rightleftharpoons FeCO_3(s); K_{sp} \qquad \text{(II.24)}$$
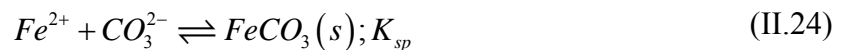
The precipitation reaction is therefore a sink for Fe^{2+} and CO_3^{2-}, and this influences the fluxes and concentrations gradients of ferrous ions and all the carbonic species in the vicinity of the reacting surface, accordingly. The solubility product of iron carbonate is given by:

$$K_{sp} = \left[Fe^{2+} \right]\left[CO_3^{2-} \right] \tag{II.25}$$
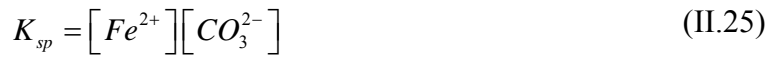
In free-oxygen carbonated water, precipitation reaction of iron carbonate is thermodynamically a stable product at a potential as lower as the potential of all iron oxides **[67**, **68**, **69]**. This explains why iron carbonate is the most common type of scale encountered in CO_2 corrosion. At 25 °C, pK_{sp} is generally given an average value between 10 and 11 **[70**, **71]**. Several research efforts have been made to investigate the effect of temperature on the solubility product **[72-75]**. A comparison between some proposed pK_{sp}-T relationships is illustrated in **Figure II.7**.
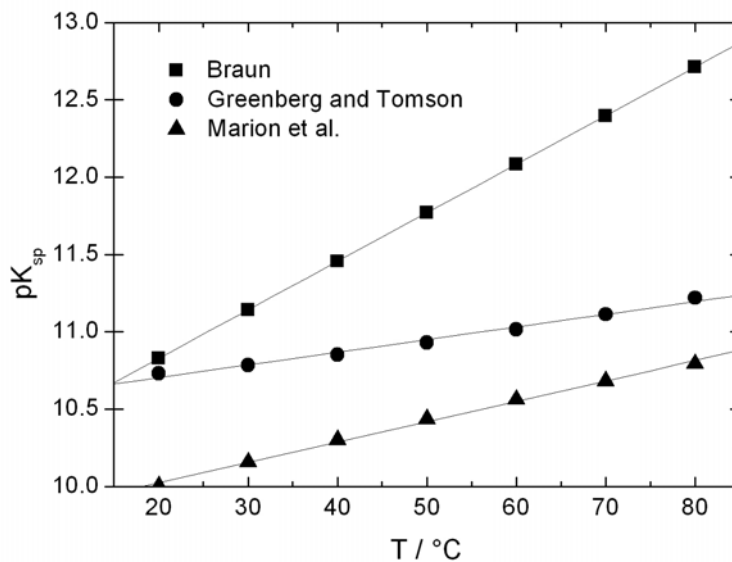
Figure II.7. *Variation of the solubility product with temperature.*

The effect of the ionic strength on K_{sp} has also been a subject for a number of studies **[76**, **77]**. At the Istitute for Energy Technology, the solubility product for iron carbonate has been modelled as a function of temperature and ionic strength:

$$pK_{sp} = 10.13 + 0.0182T(°C) - \log\left[f\left(I_s \right) \right] \tag{II.26}$$

where $f(I_s)$ is given by:

$$f\left(I_s\right)=\frac{1}{0.0115I_s^{-0.6063}};\text{for } I_s > 0.17\text{M} \tag{II.27}$$

$$f\left(I_s\right)=\frac{1}{1-5.6517I_s};\text{for } I_s \le 0.17\text{M} \tag{II.28}$$

The equation (II.26) is based on the IUPA formula **[78]** for the effect of temperature and in-house calculations of the solubility product as a function of ionic strength performed with Thermo-Calc program.

The precipitation reaction kinetics of iron carbonate is well documented in literature. Johnson and Tomson suggested that the precipitation rate of iron carbonate is proportional to the supersaturation (S) **[79]**. That is:

$$P_R = k_{gr}\frac{A}{V}K_{sp}\left(S^{\frac{1}{2}}-1\right)^2 \tag{II.29}$$

where A/V is the surface to volume ratio. The supersaturation is defined as:

$$S = \frac{\left[Fe^{2+}\right]\left[CO_3^{2-}\right]}{K_{sp}} \tag{II.30}$$

The proportionality factor (k_{gr}) is the crystal growth rate constant, which depends on temperature. The relationship between k_{gr} and temperature is expressed in Arrhenius' law-like form:

$$k_{gr} = e^{B-\frac{E_a}{RT}} \tag{II.31}$$

where B and E_a are experimentally determined constants and have the values of 54.8 and 123 kJ/mole (the activation energy), respectively. Five years later, Van Hunnik et al. **[80]** proposed a slightly different expression for the precipitation rate. This expression showed a better agreement with experimental results, particularly at higher supersaturation:

$$P_R = k_{gr} \frac{A}{V} K_{sp} \left(S - 1 \right)\left(1 - S^{-1} \right)$$

<div align="right">(II.32)</div>

and they obtained the values B = 52.4 and E_a = 119.8 kJ/mole, accordingly.

F.   Steel Composition and Microstructure

The severity of CO_2 corrosion strongly depends on the composition and microstructure of the steel in use. These inherent characteristics influence corrosion rates in a complicated manner. A number of studies were nevertheless devoted to understand this influence. It was reported in early study that localized attacks at the upset ends of oil well tubing are ascribed to selective corrosion of spheroidized carbides, and that the spherodization damages the lamellar pearlite grain structure [81]. This last is believed to strengthen the adherence of protective films to the substrate [81, 82]. Investigations of the structural characteristics of iron carbonate showed that the steel microstructure also have an effect on the thickness of corrosion product layers [82]. A corrosion process and a growth mechanism of $FeCO_3$ were therefore proposed for ferritic-pearlitic steels [82, 83]. This corrosion process is schematically shown in **Figure II.8**. For such steels, ferrite corrodes away and cementite lamellas (Fe_3C) are left behind. Being electrically conductive, these lamellas were however shown to enhance hydrogen evolution [84, 85] and thus increase the corrosion rate [83-90]. Results obtained from experiments on sixteen distinct steels clearly showed that the corrosion rate increases with the carbon content, which is a direct consequence of the described effect of cementite [83]. Other works reported that ferritic-pearlitic steels are less prone to localized corrosion at temperature below 80 °C than martensitic materials [91-94]. Morphological observations of deposited corrosion products also showed that ferritic-pearlitic steels are efficient substrates for the formation of homogeneous layers, while porous $FeCO_3$ layers were found to develop on martensitic specimens [95]. In some cases, the steel composition rather than the microstructure was shown to be responsible for a better resistance to CO_2 corrosion [96]. A number of low carbon steels containing micro-alloying elements appear to be 3 to 10 times more resistant to CO_2 corrosion than conventional grades. As an example, it is known that chromium provide

a mechanical strengthening of the surface films, although it is sometimes detrimental to certain corrosion inhibitors **[83]**. Other constituting elements such as vanadium can also have influential and complementary roles in the prevention of CO_2 corrosion. However, how these elements prevent CO_2 corrosion is not clearly understood. Further research efforts are therefore required in this area.
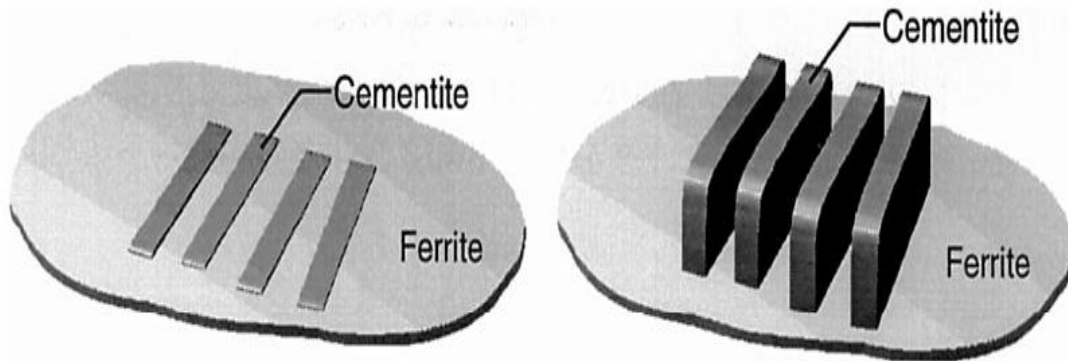
Figure II.8. *Illustration of the corrosion process for ferritic-pearlitic steels as proposed in Refs. [82, 83]. Left: freshly ground surface. Right: corroded surface. Figure taken from Ref. [83].*

II.3.4.   Forms of CO_2 Corrosion

In CO_2-containing aqueous media, corrosion attacks may take several forms that strongly depend on the inherent characteristics of the metal, the environmental conditions prevailing, and the kinetics of the interfacial corrosion processes. There are mainly two forms of corrosion often encountered in the field, namely uniform and localized corrosion.

A.   *Uniform Attacks*

Uniform corrosion, known also as general corrosion, takes place across the entire exposed surface. Nevertheless, the damage caused by this form of corrosion is predictable. Uniform corrosion is also by far the most widely studied form of attack in oil and gas industry. A number of predictive models have been devoted to this form of corrosion over the last two decades. A comparison of the respective performances and accuracies of these models has been reported in literature **[97-99]**. Recently, Nyborg has

published a detailed overview on the major models used in the field **[100, 101]**. The history and mathematical schemes has also been summarized **[102]**.

B.   Localized Attacks

Localized corrosion is known to be more severe and more difficult to both predict and control than uniform corrosion due respectively to its latent incubation, quick propagation and stochastic nature. This form of attack implies that only discrete parts of the metal surface are attacked. Localized corrosion often results in deep penetration of the metal, thus inducing an impairment of its characteristics. In practice, localized corrosion is at the root of most corrosion failures of facilities encountered in oil and gas fields. This is particularly observed at low fluid velocities for flowing systems or in stagnant conditions. A rational explanation would be that a pre-initiated localized attack is prone to grow in such conditions due to local electrochemical concentration gradients between the attack and the outer surrounding surface. Due to its severity, localized CO_2 corrosion attacks have been given an increasing attention **[65, 103-106]**. Modelling approaches were also used to tackle the stochastic nature of this phenomenon **[107]**.

Under corrosion scaling condition, particular localized attacks known as mesa attacks can develop. These attacks are particularly observed at high fluid velocities. For this reason, the phenomenon of mesa attacks is generally categorized as flow-induced or flow-assisted localized corrosion. The prerequisite for the formation of mesa attacks is that partially protective corrosion scales must form first. Mesa attacks are typically characterized by deep and often flat-bottomed cavities. The mechanisms for initiation and growth of mesa corrosion attacks have not been given a satisfactory explanation until the work of Nyborg **[108-110]**. The mechanism suggested by Nyborg is sketched in **Figure II.9**. Some other efforts have been made to better understand this phenomenon **[111-113]**. Since mesa attacks are localized, their occurrence is also unpredictable.
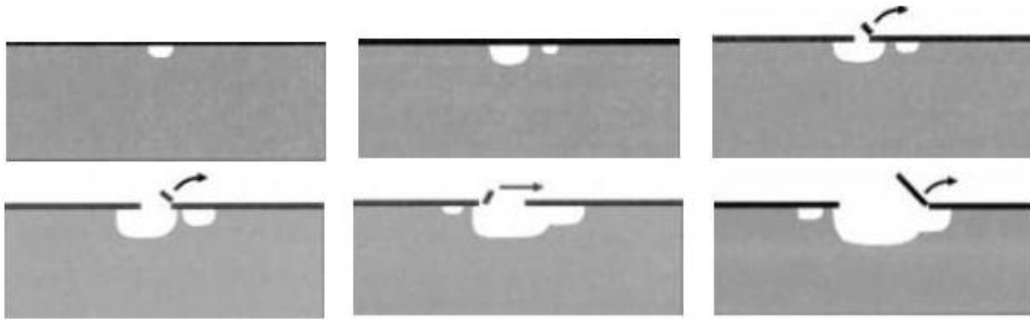
Figure II.9. *Mechanism for initiation and growth of mesa attacks according to Nyborg [110].*

II.4. Top-of-Line Corrosion

II.4.1. Introduction

In natural gas production, a common practice to mitigate sweet corrosion in carbon steel pipelines carrying wet CO_2-containing gas consists in drying the gas prior to its transport. For economical reasons, well gas streams are still being sent unprocessed into carbon steel pipelines over long-distances from wells to main platforms, existing installations on neighbouring fields or onshore processing units. Due to injection of corrosion inhibitors, transportation of natural gas under wet conditions or even in the presence of a water phase at the bottom the pipeline has been successfully practised over the world. However, it must be made certain that the active inhibitor reaches all parts of the pipeline under all transport conditions. At high gas flow rates, injected inhibitors are dispersed as a spray, and the micro-droplets are carried along the line, thus producing a protective film on over the internal parts of the pipeline. This is no more possible under stratified (-wavy) flow regime when injected inhibitors drain downward under gravity and collect at the bottom of the line. Under these conditions, the upper pipeline surface is not sufficiently supplied with inhibitors, and is therefore subject to sweet corrosion. Such phenomenon is commonly referred to as top-of-line corrosion (TLC).

II.4.2.   Flow Patterns in Wet Gas Pipelines

In wet gas pipelines, the multiphase downstream may be transported in a variety of flow patterns. These depend on the orientation of the pipeline and both the nature and the rate of the individual phase flow. The three common types of them are mist flow, annular (-mist) flow, and stratified (-wavy) flow regimes **[114**, **115]**. These regimes are schematically illustrated in **Figure II.10**. The mist flow regime is typically observed at low quantity of liquid and at very high velocities of the gas flow. The liquid co-produced with hydrocarbons is sprayed as micro-droplets and entrained in the vapour phase. In annular (-mist) flow regime, the liquid phase is swept up until it wets the entire circumference of the pipe with a gas core in the middle. This is particularly achieved when the gas velocity is high. A mist is often present in the gas core. In practice, an annular liquid film is however difficult to occur and a crescent shaped film is often observed at the bottom half of the pipe with liquid flowing as streaks along the the top surface **[114]**. Stratified (-wavy) flows are the most common patterns encountered in wet gas transportation, particularly at moderate velocities of the gas flow. This is the case where the liquid phase, a brine of water and condensed hydrocarbons, flows down the internal pipeline while the gas phase is carried along the internal upper part. Some liquid is dispersed into micro-droplets that are then entrained in the vapour phase. The micro-droplets can coalesce under favourable conditions on the top surface of the pipe and form thin liquid films, in which gaseous CO_2 and other acidic gases, for instance hydrogen sulphide, are readily hydrated. In combination with organic acids, these condensates become potentially very aggressive and cause the upper part to corrode. It follows that TLC is relevant for wet gas pipelines, and more specifically for wet gas transportation in stratified flow regimes **[116]**.
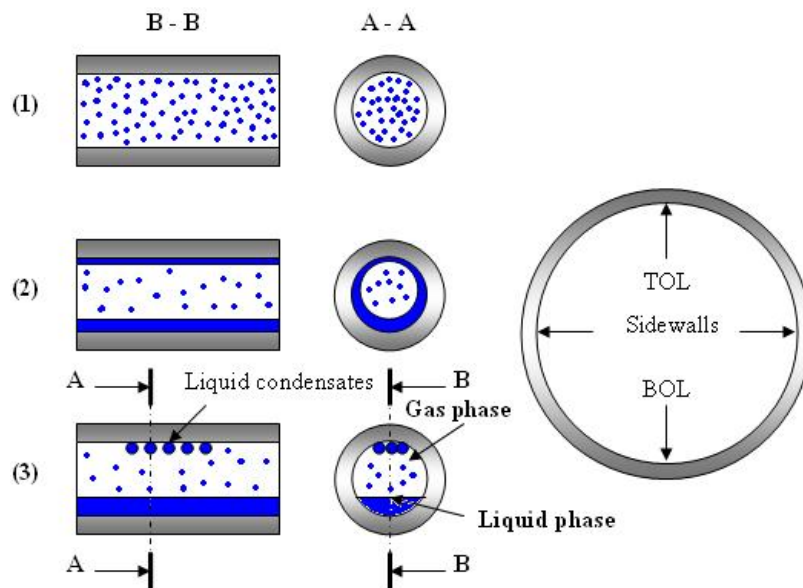
Figure II.10. Main patterns of gas flow encountered in wet gas pipelines. (1) Mist flow regime; (2) Annular (-mist) flow regime; (3) Stratified flow regime. This last is the most common type, particularly observed at moderate velocities of the gas flow.

II.4.3.   Basic Mechanism of TLC

Top-of-line corrosion is fundamentally CO_2 corrosion. Therefore, the mechanisms of the underlying reactions in sweet systems still apply. In most of cases, TLC occurs in multiphase stratified flow or during wet gas transportation. It is typically associated with partially or completely failed thermal insulation of the pipeline. Due to the external cooling that induces large temperature gradients between the internal medium and the surrounding environment, the water vapour co-produced with hydrocarbons condenses on the whole circumference of the internal walls of the line. In such conditions, the condensed water is in equilibrium with the gas phase, thus allowing the hydration of gaseous carbon dioxide. The internal environment can become even much more corrosive when sweet conditions are associated with high partial pressures of other acidic gases such as hydrogen sulphide. Since most of the condensing water drains downward under the effect of gravity, CO_2 corrosion is first expected to occur at the bottom of the line. Under sustained dewing conditions, a continuous thin film of liquid nevertheless forms on the internal top surface and this last is also subject to sweet corrosion. Although corrosion mitigation is usually achieved by injection of inhibitors,

TLC is still difficult to prevent and control. Indeed, as TLC occurs in wet gas lines often operated in stratified flow regime, corrosion inhibitors remain at the bottom and are not prone to reach and protect the top of the line.

II.4.4.   Key Factors in TLC

The first case of TLC was reported in 1960 at a sour gas field in France, where severe localized TLC attacks with a penetration rate of around 5 mm/year were observed in the gas gathering system. Although laboratory studies were already initiated in early 1990 to provide a rational explanation for TLC phenomenon, it was only in 1999 that a complete description of TLC case was made on the basis of field data and inspections results **[117]**. Since then, the issues related to TLC phenomenon have increasingly caught up the attention of the major industries in oil and gas fields. In practice, the majority of TLC cases are met offshore. Several field cases are nevertheless related to onshore gas gathering. The factors affecting top-of-line corrosion in sweet conditions are now identified. These factors have been extensively addressed in literature. The condensation rate, temperature and organic acids (mainly acetic acid) are by far the most influential parameters in TLC phenomenon. All of these factors influence the corrosion rate in a complicated way, but common behaviours are generally observed. These are briefly outlined hereafter. Since TLC phenomenon is fundamentally CO_2 corrosion, the same observations can be made concerning the metallurgical effects.

A.   *Condensation Rate*

Great research efforts have been undertaken to study the top-of-line corrosion and how the TLC rate is affected by the condensation rate. Most of the published experimental work has been performed at IFE in Norway and Ohio University in USA with Total as an active partner at both institutions. In simple cases, the TLC rate can be estimated from the water condensation rate and the concentration of ferrous ions that accumulate in the condensing water. The condensed water is pure and, due to the hydration of CO_2, has typically a pH < 4. When the water condensation rate is low, the water film is not renewed. Corrosion products hence accumulate rapidly in the

condensed water and raise the local pH until the water is saturated with iron carbonate. Once the supersaturation is exceeded, precipitation reaction does occur and a protective scale of iron carbonate is formed. The top-of-line corrosion is therefore limited by the amount of ferrous irons that can be released and transported with the condensed water. On the other hand, fresh condensed water will dissolve the already formed iron carbonate scale. This implies that a minimum corrosion is required to increase iron content in the condensed water phase to at least the saturation point $[Fe^{2+}]_{sat}$. In such condition, the corrosion rate (C_R) is simply expressed as follows [80]:

$$C_R = f_{corr}.V_{cond}.\left[Fe^{2+}\right]_{sat} \tag{II.33}$$

where V_{cond} is the condensation rate in liters per second. The conversion of one mole of Fe^{2+} per liter into mm/year may be achieved by using the correction factor (f_{corr}). At very high condensation rates, the supersaturation of the condensed water becomes very difficult to reach and unprotective iron carbonate layer is formed. As a consequence, the equation (II.3) is no longer valid and the corrosion rate is simply determined as a free-scaling C_R. One can therefore assume that there exists a critical condensation rate beyond which no saturation of the condensed water by corrosion products can be reached.

B.   *Gas Temperature*

The temperature of the flowing gas influences TLC in a complex way. Since TLC occurs primarily in sweet conditions, the aforementioned effects of temperature on both CO_2 corrosion kinetics and the formation of product scales still nevertheless apply.Temperature evenly plays other major role related to the condensation rate, and thus has an indirect effect on the overall TLC rate. As the temperature increases, more water is condensed on the top surface of the pipe. Beyond a certain temperature, protective -and hard to undermine- films are formed. TLC rate is hence governed by the counteracting actions of temperature and condensation rate. Further scenarios concerning the counteracting roles of these two parameters in sweet dewing conditions were suggested by Olsen and Dugstad [118].

C. **CO$_2$ Partial Pressure**

CO$_2$ partial pressure is also an influential parameter in TLC conditions. Top-of-line corrosion rate increases with CO$_2$ partial pressure. This is however less pronounced than in the uninhibited bottom of the line. This is particularly true, respectively at low temperatures and high condensation rates, or at high temperatures and low condensation rates [118, 119]. At high temperatures and large condensation rates, the effect of CO$_2$ partial pressure on the corrosion rate can become substantial. In both cases, the same reasoning adopted to explain the effects of temperature and condensation rate still applies.

D. *Gas Velocity*

Under dewing conditions, the corrosion rate is not directly proportional to the gas velocity [120]. Instead, the influence of the gas velocity is primarily related to the condensation rate. High gas velocities indeed enhance mass transfer and heat exchange, thus resulting in an increase in the condensation rate. One may go further by assuming that the overall TLC rate could be influenced via the impact of the gas velocity on the following parameters:

▪ *Water layer thickness* – Depending on the gas velocity, condensates are spread on the top surface of the pipe with a varying thickness of the water layer. This case is similar to the one reported at low condensation rates (effect on the water supersaturation).

▪ *Condensate forms* – At very low gas velocities, condensates may, for example, take the form of stagnant droplets. In such condition, one would deduce that TLC is different from the one occurring under thin liquid films.

▪ *Galvanic coupling* – Once localized corrosion attacks have initiated, the condensed water may remain inside the cavity due to flowing gas. On the other hand, the growing external layer of the condensed water at the gas-liquid interface is carried away by the flowing gas at high velocities.

E. *Acetic Acid*

Sweet TLC is often associated with the presence of short chain organic acids. These are naturally occurring compounds in unprocessed oilfield brines besides carbon dioxide. **Table II.3** shows some organic acids frequently found in formation water.

Table II.3. *List of some short chain organic acids commonly found in formation water [121].*

Acid	Concentration (mM)	Concentration (mg/l)
Acetic acid	10.1	609
Propanoic acid	1.5	113
Formic acid	0.3	14
1-butanoic acid	0.3	27
Malonic acid	0.2	21
Oxalic acid	0.1	9

Amongst these organic acids, acetic acid (commonly abbreviated as HAc) appears to be the most prevalent short chain carboxylic acids. It can be present with concentrations ranging from a few hundreds up to several thousands of ppm in the co-produced aqueous phase. **Table II.4** lists some relevant information about the physicochemical properties of pure HAc.

Table II.4. *Some physicochemical properties of pure HAc.*

F_w	M_w (g mol^{-1})	ρ_{liquid} (g cm^{-3})	ρ_{solid} (g cm^{-3})	T_{melt} (°C)	T_{boil} (°C)	pK_{ac}	Viscosity (mPa s)
CH_3COOH	60.05	1.049	1.266	16.5	118	4.80	1.22

Since acetic acid is a weak acid (pK_{ac} = 4.80 at 25 °C), it partially dissociates into hydrogen ions and acetates according to the following reaction:

$$HAc \rightleftharpoons H^+ + Ac^-; K_{ac} \qquad (II.34)$$

This dissociation is very fast with the forward reaction constant ($k_{ac,f}$) estimated to 3.2 x 10^5 s^{-1} **[122]**. The equilibrium constant depends on temperature. The following expression for the pK_{ac} – T relationship is generally used in literature **[123]**:

$$pK_{ac} = 6.661 - 0.013T(K) + 2.378 \times 10^{-5} T(K)^2 \qquad \text{(II.35)}$$

One matter of confusion was frequently encountered in literature concerning the effect of acetic acid, namely that HAc would be a stronger acid than H_2CO_3 ($pK_{ca} = 3.5$). This has been elucidated by Gulbrandsen and Bilkova in 2006 [10]. In CO_2/ HAc brine, each of the two acids is a proton supplier. Carbonic acid becomes the main source of protons only when it is present at a concentration at least equal to acetic acid's. This is particularly achieved at very high partial pressures of CO_2.

The knowledge of the role of HAc in sweet systems is as old as that of CO_2 corrosion itself [124]. The effect of HAc on the corrosion rate of carbon steel in CO_2-containing media has been extensively investigated over a wide range of conditions since the 1980's [125-127]. That is to say much later since the presence of carboxylic acids was discovered in the early 1940's. Literature relating to the role of HAc in CO_2 corrosion in oil and gas industry has been systematically reviewed. The most recent was provided by Gulbrandsen and Bilkova [10]. Their work throws light on literature addressing the effect of HAc over the period 1983-2006. Field experience shows that HAc is a key factor in the occurrence of localized TLC attacks in gas-condensate pipelines [128]. Crolet and Bonis [125] reported that the presence of HAc in unprocessed oil and gas brine could substantially increase the corrosion rate of carbon steel, even in small amounts [124]. This was corroborated sixteen years later by the work of McVeigh [129]. Since then, this fact has been generally acknowledged. There also seems a consensus that HAc entails a significant enhancement of the cathodic part reaction rate in two undistinguishable mechanisms. HAc acts as a proton supplier, with the subsequent buffering effect suggested by Crolet [124] et al. and also by Joosten et al. [130]. By analogy with carbonic acid, a direct cathodic reduction of undissociated HAc molecules is also assumed to occur:

$$HAc + e^- \rightleftharpoons \frac{1}{2} H_2 + Ac^- \qquad \text{(II.36)}$$
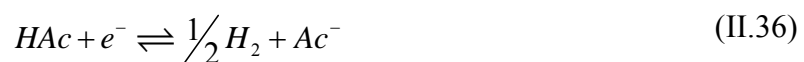
This seems to be in line with the extensive cyclic voltammetry studies of Garsany et al. [131-134] and also by later work [135]. Due to the rapidity of HAc dissociation, distinguishing the direct reduction of HAc from the conventional reduction of protons

appears, however, to be a difficult experimental task. Some laboratory results on HAc corrosion in sweet conditions have nevertheless showed that acetic acid is particularly detrimental in its undissociated form [16, 136, 137]. The anodic inhibition effect was also observed in other studies on iron and steel corrosion in HAc-containing media [124, 135, 138]. This is still not elucidated, and a deep insight is then required into this area. Thermodynamically speaking, the precipitation of ferrous di-acetate complexes could occur via the following reaction:

$$Fe^{2+} + 2Ac^{-} \rightleftharpoons FeAc_2; K_{ia} \qquad (II.37)$$

The formation of protective FeAc_2 layer is generally ignored. Indeed, the solubility of ferrous di-acetate is so much higher than iron carbonate's that precipitation of FeAc_2 is unlikely to be driven in practical situations (see **Figure II.11**). At pH higher than 6 and high acetate concentrations (typically several thousands ppm), nearly 60 % of divalent iron could be present as acetate complexes [10]. The precipitation of ferrous di-acetate products is no longer negligible, accordingly.
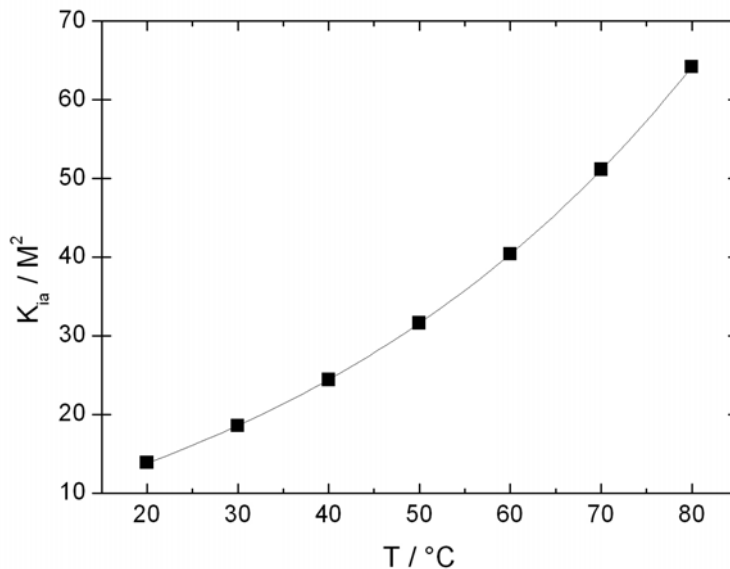
Figure II.11. *Variation of ferrous acetate's solubility with temperature in 0.3% NaCl. Data were obtained by polynomial fitting of those reported by Palmer and used later by Gulbrandsen and Bilkova [3, 10].*

II.5. TLC Models

II.5.1. Introduction

Several empirical and semi-empirical models have been proposed in literature to predict the occurrence of sweet TLC. Some others have also been developed from more mechanistic considerations. Five of them are briefly reviewed hereafter.

II.5.2. de Waard et al. Model (1993)

The model of de Waard and Milliams is probably one of the most well-known and referenced models. Based on their experimental results, the authors developed an empirical correlation allowing the prediction of CO_2 corrosion rate in natural gas pipelines [139]. The model was upgraded in 1991 [30]. In 1993, de Waard and Lotz adapted the last version of the model for systems operating under dewing conditions by introducing a correction factor for the condensation rate (F_{cond}). The authors proposed a correction value of 0.1 for a condensation rate below 0.25 g m^{-2} s^{-1} [31]. Quantification of the influence of environmental parameters besides condensation rate such as scaling tendency and pH was also made by applying other correction factors. The generic formula is written in its following expression for uniform corrosion:

$$\log\left[C_R\left(mm\,/\,year\right)\right] = 5.8 \times \log\left(F_{cond}\right) - \frac{1710}{273 + T\left(°C\right)} + 0.67 \times \log\left[P_{CO_2}\left(bar\right)\right] \qquad \text{(II.38)}$$

II.5.3. Andersen and Valle Model (1993)

The authors postulated that the TLC rate depends primarily on the CO_2 partial pressure, the bulk temperature in the gas stream (T_{bulk}), and the condensation rate if the presence of hydrocarbons can be neglected. They accordingly proposed the following predictive expression for the corrosion rate [140]:

$$C_R\left(mm/year\right)=\left[\sum_{i=0}^{4}t_i T_{bulk}^i\left(°C\right)\right]V_{cond}P_{CO_2}^{0.3}$$

(II.39)

The polynomial coefficients (t_i) were obtained experimentally by curve fittings. Although it involves the main influential factors in TLC, this model is exclusively valid in scale-free corrosion.

II.5.4. Van Hunnik et al. Model (1996)

Van Hunnik et al. noticed that the already developed models often over-predict the sweet corrosion rate in wet gas and oil systems. They argued that the observed inaccuracy is due mainly to the fact that corrosion scaling is not properly taken into account. Based on an evaluation of in-house and literature data, the authors developed equation (II.33), which is specific to practical situations where iron carbonate scaling is chosen as a control option of TLC [80]. At very high condensation rates, equation (II.33) is however no longer valid since in such conditions $FeCO_3$ films are very unlikely to be protective.

II.5.5. Pots and Hendriksen Model (2000)

In order to tackle the conservatism present in the de Waard et al. model, Pots and Hendriksen developed a new correlation for TLC prediction. The so-called iron supersaturation model describes the competitive effects of iron discharge via the water condensation rate and the precipitation rate of iron carbonate. The model uses the Van Hunnik et al. expression [141] for $FeCO_3$ precipitation. Under supersaturation condition, the corrosion rate is given by:

$$C_R\left(mm/year\right)=2.26\times10^8\times\frac{V_{cond}}{\rho_w}\times\left[Fe^{2+}\right]_{supersat}$$

(II.40)

ρ_w stands for the water density. Predictions were likened to experimental results obtained by Olsen and Dugstad [118], and also to field data reported by Gunaltun [117]. A good agreement was obtained.

II.5.6.   Gunaltun et al. Model (2000)

In 1999, Gunaltun et al. **[117]** published a case history of TLC in multiphase wet gas flowlines of Tunu field (Indonesia). One year later **[128]**, Gunaltun and Larrey evaluated the condensation rates in sealines of four fields. The calculated condensation rates were thereafter correlated to the thickness losses measured by inspection of the Tunu case. The authors used a computational module for the simulation of the multiphase flow all along wet gas pipelines. The model included thermodynamics, hydrodynamics, and thermal exchange packages. In steady-state flow regime, the radial heat transfer in a pipeline was calculated via the integration of the following expression:

$$dQ = 2\Pi R_0 U_0 \left(T_{fluid} - T_{ext} \right) \times dL \qquad (II.41)$$

where:

dQ: differential radial heat loss

dL: elementary pipe length

U_0: overall radial heat transfer coefficient (referred to R_0)

R_0: arbitrary radius taken as reference

T_{fluid}: bulk fluid temperature

T_{ext}: external temperature

II.5.7.   Other Models

During the period 2002-2007, several other models have been developed. However, this exceeds the scope of the present review, and the interested reader is invited to see the related references **[119, 121, 142, 143]**.

II.6. Mitigation and Control Techniques

II.6.1. Introduction

There are four requirements for any aqueous corrosion process: an anodic zone on which oxidation reaction occurs, a cathodic zone on which reduction reaction of a different species occurs, an aqueous solution that insures ionic conduction between the two reaction sites, and an electrical conductor for electrons transfer. It follows that any successful mitigation effort of corrosion must alter, at least, one of these requirements. Many control techniques have been developed and used in oil and gas industry to prevent and mitigate CO_2 corrosion phenomena. These techniques include chemical inhibition, selection of more corrosion-resistant metals and alloys (eventually non-metallic materials), protective coatings, cathodic protection etc…A short overview of these techniques is given hereafter. The same measures apply for sweet TLC.

II.6.2. Injection of Corrosion Inhibitors

Corrosion inhibitors have been shown to be very effective in CO_2 corrosion condition and are therefore extensively used in oil and gas production. Since the 1940's, the use of inhibitors has indeed slowed down the corrosion rates by a factor ranging from 4 to 15 [144]. Amines and their derivatives are the most commonly used commercial inhibitors. These are nitrogen-based organic surfactants with a long dipolar chain. Some inorganic inhibitors are also used. The corrosion protection is achieved through the physical adsorption and chemisorption of inhibitors onto the reacting surface. It follows that the inhibition (or the protection) efficiency is directly proportional to the fraction of the steel surface covered by the inhibitor [16]. Corrosion inhibitors can be generally classified into two principal groups according to the manner by which they are applied: continuous injection, and batch (intermittent) injection inhibitors. A more focused view would categorize inhibitors according to their basic roles or according to the electrochemical process being controlled: anodic, cathodic, film forming, passivating, and neutralizing. In addition to external injection of inhibitors, some naturally occurring components of crude oil are known to slow down CO_2 corrosion rates either by wetting effect [145] or inhibitive effect [146-148].

II.6.3.   Selection of Materials

Control and mitigation of CO_2 corrosion can evenly be done upstream by suitable choice of the material. This implies the use of more corrosion-resistant metals and alloys such as stainless steels [149, 150]. These are indeed less prone to CO_2 corrosion. Their application is nevertheless still limited to highly corrosive environments in petroleum industry due to their cost impact. Non-metallic materials can also be used. In some practical situations, however, this can prove to be detrimental to the mechanical properties of facilities particularly under extreme conditions of temperature and pressure. The use of metallic materials is therefore recommended in such conditions.

II.6.4.   Application of Protective Coatings

Corrosion alleviation is, in some cases, achieved by application of organic coatings. These, if properly applied, may extend the lifespan of engineering structures a few years [151]. However, coatings do not remain holiday-free for very long in saltwater service. Effective use of coatings should therefore be supplemented with cathodic protection.

II.6.5. Cathodic Protection

Cathodic protection provides a method of protecting large steel structures such as pipelines by supplying an electron flow to the active steel to reduce or eliminate oxidation reactions. This can be accomplished either by applying a cathodic potential (impressed potential) or by impressing a cathodic current (impressed current) from a DC generator across the steel-environment interface. This last is commonly used to supplement internal coatings and the injection of inhibitors. An alternative method of producing a similar effect is to couple a less noble metal (sacrificial anode) to the metal of interest.

II.6.6.   Other Techniques

Reduction of corrosion rates in sweet systems can also be performed through the control of the environmental conditions prevailing. A number of wet gas steel pipelines use glycol for hydrate prevention and the pH-stabilization technique **[152]**. This consists in adding alkaline chemicals such as aqueous sodium hydroxide (NaOH) or methyldiethanolamine (MDEA) to the corrosive environment in order to increase its pH, and thus improving the protectiveness of corrosion films **[153]**. In sweet systems, the control of other environmental factors such as temperature was also found to be beneficial in some practical cases **[154]**. Last but not least, upstream optimization of the design for engineering structures can result in less corrosion-induced damages, particularly in which relates to localized attacks or galvanic coupling when dissimilar metals are involved.

II.7.   Conclusions

The above bibliographical analysis shows that CO_2 corrosion phenomena cannot be satisfactorily explained only on the basis of the acid character of carbonated water. Hence, it clearly appears that carbonic species are directly involved in the elementary cathodic processes. However, the underlying mechanism whereby these species are involved is still a subject of controversial theories. Besides the buffer effect of carbonic acid, the least controversial explanation would be that the acid molecules are directly reduced. This means that the respective reactions of proton reduction and carbonic acid reduction are independent, and that the overall cathodic process is the sum of both. In practice, internal CO_2 corrosion of pipelines is even more complex. This is due to the interacting effects of the environmental conditions prevailing as well as the metallurgical properties of the corroding steel.

Under sweet conditions, TLC is not more than a particular case of CO_2 corrosion and the same observations can therefore be made concerning the effects of all these parameters. A relative difference lies in the fact that sweet TLC occurs in wet gas lines operated in stratified flow regime, which enables the water condensation rate to play a major role in the overall corrosion process. At very high condensation rates and

very low gas velocities (i.e. stagnant conditions), however, a thick water layer can be formed on the top surface of the pipe, and TLC phenomenon can thus be treated in the same way as a "pure" CO_2 corrosion phenomenon. For convenience, this approach was used in this work. Sweet TLC is commonly associated with the presence of weak organic acids. These are naturally occurring compounds in unprocessed oil and gas brine besides carbon dioxide. Amongst these organic acids, acetic acid appears to be the most abundant.

The effect of acetic acid on CO_2 corrosion has been a poorly understood issue until recently. Since then, a significant progress has been achieved in understanding the effect of acetic acid on the uniform CO_2 corrosion. Rudimentary understanding however exists regarding its basic role in the propagation of localized attacks, and no model has been proposed on this topic thus far. In practice, localized attacks are at the origin of most corrosion failures of pipelines. The consequences of uncontrolled and non-predictable attack of large wet gas pipelines will have a large economical impact if the pipeline has to be replaced or built in a more expensive material or if the field has to close down before the field has been fully exploited. The environmental impact can also be substantial if a rupture takes place. Hence, understanding localized corrosion in such conditions is an important precondition for challenging the major actors in oil and gas industry to find the optimal techniques for mitigation and control. The present work comes within the scope of this major stake. It is anticipated that the results of this research effort provide an essential insight into the mechanism of localized attacks of carbon steel pipeline in the presence of acetic acid, namely in which concerns the stifling of growing pits often encountered in TLC conditions. Nevertheless, an investigation of the macroscopic behaviour of carbon steel in CO_2/HAc aqueous solutions is worth the detour, and will be addressed in **Chapter IV**. By then, the experimental protocol, instrumentations and methods employed in this work are outlined in the next chapter.

References

[1] *"Handbook of Chemistry and Physics",* 85th ed., CRC Press LLC, USA (2000).

[2] C. B. Hitz, J. J. Ewing, J. Hecht, *"Introduction to Laser Technology"*, 3rd ed., John Wiley & Sons, USA (2001).

[3] D.A. Palmer, R.V. Eldik, Chem. Rev., 83 (1983) 651.

[4] A.R. Davis, B. G. Oliver, J. Sol. Chem., 1 (1972) 329.

[5] G.R. Anderson, J. Phys. Chem., 81 (1977) 273.

[6] R. Kruse, E.U. Franck, Ber. Bunsenges.Phys. Chem., 86 (1982) 1036.

[7] J. Tidblad, T.E. Graedel, J. Electrochem. Soc., 144 (1977) 2676.

[8] S. Nešić, M. Nordsveen, R. Nyborg, A. Stangeland, CORROSION\01, Paper no. 40, NACE, 2001.

[9] W. Moore, *"Basic Physical Chemistry"*, Prentice-Hall, Inc., USA (1983).

[10] E. Gulbrandsen, K. Bilkova, CORROSION\06, Paper no. 06364, NACE, 2006.

[11] D.J. Poulton, H.W. Baldwin, Can. J. Chem., 45 (1967) 1045.

[12] R.C. Patel, R.J. Boe, G.J. Atkinson, J. Sol. Chem., 2 (1973) 357.

[13] M. Eigen, Angew. Chem., 75 (1963) 489.

[14] W. Knoche, *"Biophysics and physiology of carbon dioxide"*, Springer-Verlag, Germany (1980) 3.

[15] K.D. Kern, J. Chem. Edu., 37 (1960) 19.

[16] S. Nešić, Corr. Science, 49 (2007) 4308.

[17] G. Schmitt, M. Hörstemeier, CORROSION\06, Paper no. 06112, NACE, 2006.

[18] M.B. Kermani, A. Morshed, Corrosion, 59 (2003) 659.

[19] S. Nešić, J. Postlethwaite, M. Vrhovac, Corrosion Reviews, 15 (1997) 211.

[20]   M.B. Kermani, D. Harrop, SPE Production & Facilities, 11 (1996) 186.

[21]   J.L. Dawson, C.C. Shih, P.K.N. Bartlett, European Federation of Corrosion (EFC) 13, (1994).

[22]   J.L. Dawson, C.C. Shih, P.K.N. Bartlett, *"Progress in the Understanding and Prevention of Corrosion"*, UK, 1 (1993) 513.

[23]   J.-L. Crolet, European Federation of Corrosion (EFC) 13, (1994).

[24]   J.-L. Crolet, *"Progress in the Understanding and Prevention of Corrosion"*, UK, 1 (1993) 473.

[25]   P.A. Burke, A.I. Asphahani, B.S. Wright, *"Advances in CO_2 Corrosion"*, NACE (1985).

[26]   L.E. Newton, R.H. Hausler, *"CO_2 corrosion in oil and gas production – selected papers, abstracts, and references"*, NACE (1984).

[27]   R.H. Hausler, H.P. Godard, *"Advances in CO_2 Corrosion"*, NACE (1984).

[28]   G. Schmitt, CORROSION\83, Paper no. 43, NACE, 1983.

[29]   C. de Waard, D.E. Milliams, Corrosion, 31 (1975) 131.

[30]   C. de Waard, U. Lotz, D.E. Milliams, Corrosion, 47 (1991) 976.

[31]   C. de Waard, U. Lotz, CORROSION\93, Paper No. 69, NACE, 1993.

[32]   C. de Waard, U. Lotz, A. Dugstad, CORROSION\95, Paper No. 128.

[33]   A. Dugstad, L. Lunde, K. Videm, CORROSION\94, Paper No. 14, NACE, 1994.

[34]   S. Nešić, L. R. Lunde, CORROSION\93, Paper No. 640, NACE, 1993.

[35]   S. Nešić, G.T. Solvi, J. Enerhaug, Corrosion, 51 (1995) 773.

[36]   S. Nešić, B.F.M. Pots, J. Postlethwaite, N. Thevenot, J. Corr. Sci. and Eng., 1, Paper 3, 1995.

[37]   S. Nešić, J. Postlethwaite, S. Olsen, Corrosion, 52 (1996) 280.

[38]   S. Nešić, N. Thevenot, J.-L. Crolet, CORROSION\96, Paper no. 3, NACE, 1996.

[39]   T. Hurlen, S. Gunvaldsen, R. Tunold, F. Blaker, P.G. Lunde, J. Electroanal. Chem., 180 (1984) 511.

[40]   J.O.M. Bockris, D. Drazic, A.R. Despic, Electrochim. Acta, 4 (1961) 325.

[41]   L.G.S. Gray, B.G. Anderson, M.J. Danysh, P.G. Tremaine, CORROSION\89, Paper no. 464, NACE, 1989.

[42]   L.G.S. Gray, B.G. Anderson, M.J. Danysh, P.R. Tremaine, CORROSION\90, Paper no. 40, NACE, 1990.

[43]   K. Videm, European Corrosion Congress (ECC) 10, 1 (1993) 513.

[44]   S. Nešić, J.-L. Crolet, D.M. Drazic, CORROSION\96, Paper no. 3, NACE, 1996.

[45]   D.M. Drazic, C. Shen Hao, Bulletin de la Société Chimique Beograd, 11 (1982) 649.

[46]   H. Davies, G. T. Burstein, Corrosion, 36 (1980) 385.

[47]   G. Schmitt, "*Advances in CO$_2$ Corrosion*", R.H. Hausler and H.P. Godard (ed.), NACE (1984) 1.

[48]   G. Schmitt, "*Advances in CO$_2$ Corrosion*", R.H. Hausler and H.P. Godard (ed.), NACE (1984) 10.

[49]   G. Schmitt, B. Rothmann, "*CO$_2$ Corrosion in Oil and gas production – selected papers, abstracts and reference*", ed. NACE Task Group T-1-3 (1984) 154.

[50]   G. Schmitt, B. Rothmann, "*CO$_2$ Corrosion in Oil and gas production – selected papers, abstracts and reference*", ed. NACE Task Group T-1-3 (1984) 163.

[51]   G. Schmitt, B. Rothmann, "*CO$_2$ Corrosion in Oil and gas production – selected papers, abstracts and reference*", ed. NACE Task Group T-1-3 (1984) 167.

[52]   E. Eriksrud, T. Sontvedt, "*Advances in CO$_2$ Corrosion*", R.H. Hausler and H.P. Godard (ed.), NACE (1984) 20.

[53]   P. Delahay, J. Am. Chem. Soc., 74 (1952) 3497.

[54]   A. Ikeda, M. Ueda, S. Mukai, CORROSION\83, Paper no. 45, NACE, 1983.

[55]   A. Ikeda, M. Ueda, S. Mukai, "*Advances in CO$_2$ Corrosion*", R.H. Hausler and H.P. Godard (ed.), NACE (1985) 1.

[56]   A. Ikeda, M. Ueda, S. Mukai, "*Advances in CO$_2$ Corrosion*", R.H. Hausler and H.P. Godard (ed.), NACE (1984) 39.

[57]   T. Murata, E. Sato, R. Matsuhashi, "*Advances in CO₂ Corrosion*", R.H. Hausler and H.P. Godard (ed.), NACE (1984) 64.

[58]   P.E. Townsend, G.T. Colegate, T.L. Van Waart, "*CO₂ Corrosion in Oil and gas production – selected papers, abstracts and reference*", ed. NACE Task Group T-1-3 (1984) 501.

[59]   S. Nešić, K.J. Lee, CORROSION\02, Paper no. 237, NACE, 2002.

[60]   A.K. Dunlop, H.L. Hassell, P.A. Rhodes, "*Advances in CO₂ Corrosion*", R.H. Hausler and H.P. Godard (ed.), NACE (1984) 52.

[61]   K. Videm, A. Dugstad, "*Materials Performance*", 28 (1989) 64.

[62]   S. Nešić, J. Postlethwaite, S. Olsen, CORROSION\95, Paper no. 131, NACE, 1995.

[63]   K. Chokshi, W. Sun, S. Nešić, CORROSION\05, Paper no. 285, NACE, 2005.

[64]   F. De Moraes, J.R. Shadley, J. Chen, E.F. Rybicki, CORROSION\00, Paper no. 30, NACE, 2000.

[65]   Z. Xia, K.C. Chou, Z. Szklarska-Smialowska, Corrosion, 45 (1989) 636.

[66]   S. Shah, CORROSION\93, Paper no. 361, NACE, 1993.

[67]   M. Pourbaix, "*Atlas d'équilibres électrochimiques*", Gauthier-Villars (1963).

[68]   G.I. Ogundele, W. E. White, Corrosion, 42, (1986) 71.

[69]   B.R. Linter, G. T. Burstein, Corr. Science, 41, (1999) 117.

[70]   J.L. Mora-Mendoza, S. Turgoose, Corr. Science, 44 (2002) 1223.

[71]   E.B. Castro, J.R. Vilche, A.J. Arvia, Corr. Science, 32 (1991) 37.

[72]   J. Greenberg, M. Tomson, Appl. Geochem., 7 (1992) 185.

[73]   D.K. Nordstrom, L.N. Plummer, D. Langmuir, E. Busenberg, H.M. May, B.F. Jones, D.L. Parkhurst, Revised chemical equilibrium data for major watermineral reactions and their limitations, ACS Symp. Ser, (1990), 416, 398.

[74]   G.M. Marion, D.C. Catling, J.S. Kargel, Geochimica et Cosmochimica Acta, 67 (2003) 4251.

[75]   R. D. Braun, Talanta 38 (1991) 205.

[76]   C.A.R. Silva, X. Liu, F.J. Millero, J. Sol. Chem., 31 (2002) 97.

[77]   Norsok Standard, http://www.nts.no/norsok.

[78]   E. Högfeldt, "*Stability Constants of Metal-Ion Complexes*", IUPAC Chemical Data Series No 21, Part A: Inorganic Ligands Pergamon Press, USA (1979).

[79]   M.L. Johnson, M.B. Tomson, CORROSION\91, Paper no. 268, NACE, 1991.

[80]   E.W.J. Van Hunnik, B.F.M. Pots, E.L.J.A. Hendriksen, CORROSION\96, Paper no. 6, NACE, 1996.

[81]   R.W. Manuel, Corrosion, 3 (1947) 197.

[82]   C.A. Palacios, J.R. Shadley, Corrosion, 47 (1991) 122.

[83]   E. Gulbrandsen, R. Nyborg, T. Loland, K. Nisancioglu, CORROSION\00, Paper no. 00023, NACE, 2000.

[84]   D.N. Staicopolous, J. Electrochem. Soc., 110 (1963) 1121.

[85]   M. Ueda, H. Takabe, CORROSION\99, Paper no. 13, NACE, 1999.

[86]   E. Gulbrandsen, S. Nešić, A. Stangeland, T.Burchardt, B.Sundfaer, S.M.Hesjevik, S.Skjerve, CORROSION\98, Paper no. 13, NACE, 1998.

[87]   R. Jasinsky, Corrosion, 43 (1987) 214.

[88]   J.-L. Crolet, N. Thevenot, S. Nešić, CORROSION\96, Paper no. 4, NACE, 1996.

[89]   A. Dugstad, L. Lunde, K. Videm, CORROSION\91, Paper no. 473, NACE, 1991.

[90]   S. A1-Hassan, B. Mishra, D.L. Olson, M.M. Salama, Corrosion, 54 (1998) 480.

[91]   M.W. Joosten, T. Johnsen, A. Dugstad, T. Walmann, T. Jassang, P. Meakin, J. Feder, CORROSION\94, Paper no. 3, NACE, 1994.

[92]   J. –L. Crolet, CORROSION\94, Paper no. 4, NACE, 1994.

[93]   S.D. Kapusta and S.C. Canter, CORROSION\94, Paper no. 10, NACE, 1994.

[94]   G.B.Chitwood, R.L. Hilts, CORROSION\94, Paper no. 20, NACE, 1994.

[95]   M. Ueda and A. Ikeda, CORROSION\96, Paper no. 13, NACE, 1996.

[96]   A. Dugstad, H. Hemmer, M. Seiersten, CORROSION\00, Paper no. 24, NACE, 2000.

[97]   M.B. Kermani, L.M. Smith, European Federation of Corrosion (EFC), no. 23, (1997).

[98]   S. Srinivasan, CORROSION\00, Paper no. 473, NACE, 2000.

[99]   H. Wang, C.J.Y. Hongwei, W.P. Jepson, CORROSION\02, Paper no. 238, NACE, 2002.

[100]   R. Nyborg, CORROSION\02, Paper no. 233, NACE, 2002.

[101]   R. Nyborg, A. Dugstad, Proceedings of the International Conference on Offshore Mechanics and Arctic Engineering-OMAE 4, 125-132, 2002.

[102]   S.D. Kapusta, B.F.M. Pots, I.J. Rippon, CORROSION\04, Paper no. 633, NACE, 2004.

[103]   M. H. Achour, J. Kolts, A.H. Johannes, G. Liu, CORROSION\93, Paper no.87, NACE, 1993.

[104]   Y. Sun, K.George, S. Nešić, CORROSION\03, Paper no. 327, NACE, 2003.

[105]   Y. Sun, S. Nešić, CORROSION\04, Paper no. 380, NACE, 2004.

[106]   J. Kvarekval, CORROSION\07, Paper no. 659.

[107]   Y. Xiao, S. Nešić, CORROSION\05, Paper no. 57, NACE, 2005.

[108]   R. Nyborg, A. Dugstad, CORROSION\98, Paper no. 29, NACE, 1998.

[109]   R. Nyborg, A. Dugstad, CORROSION\03, Paper no. 642, NACE, 2003.

[110]   R. Nyborg, CORROSION\98, Paper no. 48, NACE, 1998.

[111]   K. Videm, A. Dugstad, CORROSION\87, Paper no. 42, NACE, 1987.

[112]   A.M.K. Halvorsen, T. Søndtvedt, CORROSION\99, Paper no. 42, NACE, 1999.

[113]   G. Schmitt, C. Bosch, M. Mueller, G. Siegmund, CORROSION\00, Paper no. 49, NACE, 2000.

[114]   D. Vedapuri, C. Kang, D. Dhanabalan and M. Gopal, CORROSION\00, Paper no. 43, NACE, 2000.

[115]   Y.H. Sun, T. Hong, W.P, Jepson, CORROSION\01, Paper no. 1034, NACE, 2004.

[116]   NACE publication, "*H₂S corrosion in oil and gas production*", NACE publications (1981) 905.

[117]   Y.M. Gunaltun, D. Supriyatman, J. Achmad, CORROSION\99, Paper no. 36, NACE, 1999.

[118]   S. Olsen, A. Dugstad, CORROSION\91, Paper no. 472, NACE, 1991.

[119]   F. Vitse, S. Nešić, Y. Gunaltun, D. Larrey de Torreben, P. Duchet-Suchaux, CORROSION\03, Paper No. 03633, NACE, 2003.

[120]   R. Nyborg, CORROSION\07, Paper No. 07555, NACE, 2007.

[121]   T.R. Andersen, A.M.K, Halvorsen, A. Valle, G.P. Kojen, A. Dugstad, CORROSION\07, Paper No. 07312, NACE, 2007.

[122]   K.J. Vetter, "*Electrochemische Kinetics*", Springer-Verlag (1960) 406.

[123]   Y.K. Kharaka, W.D. Gunter, P.K. Aggarwaal, E.H. Perkins, J.D. DeBraal, "*Solmineq 88: A Computer Program for Geochemical Modelling of Water-Rock Interactions*", Alberta Research Council, Menlo Park, California, 1989.

[124]   J.-L. Crolet, N. Thevenot, A. Dugstad, CORROSION\99, Paper no.24, NACE, 1999.

[125]   J.-L. Crolet, M.R. Bonis, CORROSION\83, Paper no. 160, NACE, 1983.

[126]   M.R. Bonis, J.-L. Crolet, CORROSION\89, Paper no. 466, NACE, 1989.

[127]   J.-L. Crolet, M.R. Bonis, "*Prediction of the Risk of CO₂ Corrosion in Oil and Gas Wells*", 22nd Offshore Technology Conference, Houston, Texas, 1990.

[128]   Y.M. Gunaltun, D. Larrey, CORROSION\00, Paper no. 71, NACE, 2000.

[129]   B. Hedges, L. McVeigh, CORROSION\99, Paper no. 21, NACE, 1999.

[130]   M. Joosten, J. Kolts, J.W. Hembree, M. Achour, CORROSION\02, Paper no. 02273, NACE, 2002.

[131]   Y. Garsany, D. Pletcher, B. Hedges, CORROSION\02, Paper no. 02273, NACE, 2002.

[132]   Y. Garsany, D. Pletcher, B. Hedges, J. Electroanal. Chem., 538-539 (2002) 285.

[133]   Y. Garsany, D. Pletcher, B. Hedges, CORROSION\03, Paper no. 03324, NACE, 2003.

[134] Y. Garsany, D. Pletcher, D. Sidorin, Corrosion, 60 (2004) 1155.

[135] R. De Marco, Z.T. Jiang, D. John, M. Sercombe, B. Kinsella, Electrochim. Acta, 52 (2007) 3746.

[136] S. Wang, K. George, S. Nešić, CORROSION\04, Paper no. 375, NACE, 2004.

[137] K. George, S. Wang, S. Nešić, CORROSION\04, Paper no. 623, NACE, 2004.

[138] G. Bech-Nielsen, Electrochim. Acta, 19 (1974) 821.

[139] C. de Waard, D.E. Milliams, "*Prediction of Carbonic Acid Corrosion in Natural Gas Pipelines*", 1st International Conference on the Internal and External Protection of Pipes, Paper F1, University of Durham, UK, 1975.

[140] T.R. Andersen, A. Valle, CORROSION\93, Paper no. 73, NACE, 1993.

[141] BF.M. Pots, E.L.J.A. Hendriksen, CORROSION\00, Paper no. 31, NACE, 2000.

[142] F. Vitse, Y. Gunaltun, D. Larrey de Torreben, P. Duchet-Suchaux, CORROSION\02, Paper No. 02245, NACE, 2002.

[143] Z. Zhang, D. Hinkson, M. Singer, H. Wang, S. Nešić, CORROSION\07, Paper no. 07556, NACE, 2007.

[144] L.E. Fisher, CORROSION\93, Paper no. 537, NACE, 1993.

[145] J. Cai, S. Nešić, C. de Waard, CORROSION\04, Paper no. 663, NACE, 2004.

[146] C. Mendez, S. Duplat, S. Hernandez, J. Vera, CORROSION\01, Paper no. 44, NACE, 2001.

[147] S. Hernandez, S. Duplat, J. Vera, E. Baron, CORROSION\01, Paper no. 293, NACE, 2001.

[148] S. Hernandez, J. Bruzual, F. Lopez-Linares, J. Luzon, CORROSION\03, Paper no. 330, NACE, 2003.

[149] P.W. Rice, CORROSION\93, Paper no. 151, NACE, 1993.

[150] M.J. Schofield, R.D. Kane, CORROSION\93, Paper no.165, NACE, 1993.

[151] "*Corrosion in the Petrochemical Industry*", ASM Publication (1994).

[152] J.-L. Crolet, J.P. Samaran, CORROSION\93, Paper no. 102, NACE, 1993.

[153] J. Kvarekval, A. Dugstad, CORROSION\06, Paper no. 06646, NACE, 2006.

[154] H.G. Byars, J.M. Galbraith, "*Advances in CO$_2$ Corrosion*", R.H. Hausler and H.P. Godard (ed.), NACE (1984) 103.

Chapter **III**

Materials & Methods

Table of Contents

III.1.   Introduction

The present work was performed using the facilities available at MetLab Laboratory at The Institute for Energy Technology (IFE, Kjeller) in Norway. This chapter presents both experimental conditions and methods used in this work. The first part deals with the protocol followed in the preparations of working electrodes and test solutions. The second part lists the different electrochemical instrumentations and techniques. For each method, the basic principle is briefly reviewed. The reader can refer to Chapter I for more details. The last part of this chapter is devoted to characterization methods. Their basic principles are also shortly described.

III.2.   Electrodes and Solutions

The electrodes used in this work were made from API 5L X65 pipeline steel. The nominal chemical composition of the steel is given in **Table III.1**.

Table III.1. The nominal chemical composition of API 5L X65 pipeline steel (wt. %). Microstructure: ferrite-pearlite.

C	Si	Mn	S	P	Cr	Ni	Mo	Cu	Al	Fe
0.08	0.25	1.54	0.001	0.019	0.04	0.03	0.01	0.02	0.038	Bal.

The microstructure of the steel is depicted as an optical micrograph in **Figure III.1-(a)** and as SEM image in **Figure III.1-(b) [1]**. The SEM image reveals lamellar cementite typical of pearlite for API 5L X65 steel. The pearlite is more or less anisotropically oriented. In many ferritic-pearlitic steels, we see a pearlite sheet structure, the sheets being parallel to the pipe surface. For this reason we have systematically aimed to have the samples machined to be parallel to the inner pipe wall as illustrated in **Figure III.2**. The unexposed faces and edges of the working electrodes were coated with epoxy resin to prevent crevice corrosion leading to erroneous results. Prior to each corrosion test, the working surfaces were wet-ground with SiC papers up to 1200 grit finish, rinsed with distilled water and degreased with acetone.
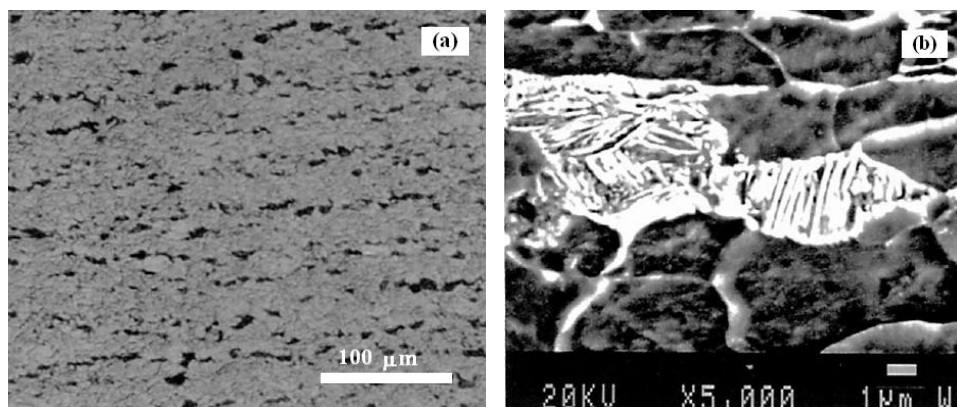
Figure III.1. *Microstructure of API 5L X65 pipeline steel after 30 s etch in 2% Nital solution. (a) optical micrograph. (b) SEM image [1].*
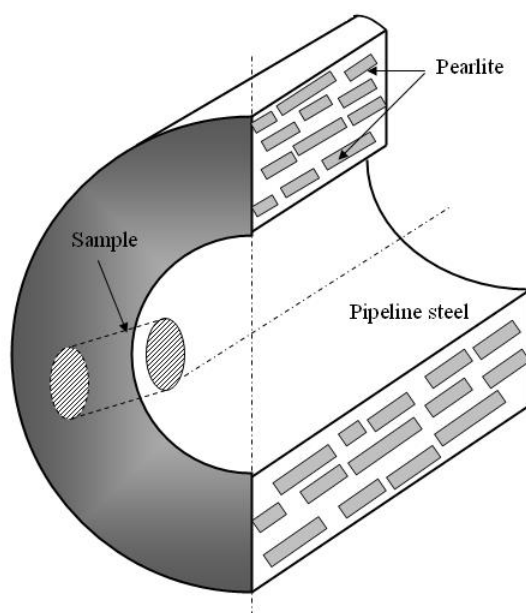
Figure III.2. *Radial cut of samples from X65 pipeline steel.*

All test solutions were prepared from analytical grade reagents and deionized water (18 MΩ cm in resistivity). They consisted of aqueous NaCl solutions de-aerated and saturated by purging CO_2 gas (>99.99%) at 1 bar for 2 hours. The electrodes were then installed through the pre-designed holders. The CO_2 gas flow was maintained over the test solution throughout the measurement to prevent oxygen ingress. Different amounts of HAc within the range 0 to 1000 ppm were also added to the test solution prior to each experiment. All tests were performed at room temperature. In this work, most of the experiments were performed at free pH. Experiments dealing with the pH effect were

however conducted by achieving the desired solution pH through minute adjustments using droplets of HCl or NaOH, respectively.

III.3.   Electrochemical Measurements

III.3.1.   Instrumentations

Electrochemical records were monitored using PCI4/750 Potentiostat from Gamry Instruments installed in Intel Pentium 4-based workstation. The PCI4 Potentiostat is a research electrochemical instrument, which consists of two printed circuit cards; the Potentiostat card and the Controller card. It can operate as potentiostat, galvanostat, or a precision zero resistance ammeter (ZRA). Data acquisition and analysis were performed using Gamry`s software support for the PCI4. They include the modules Gamry Framework and ESA 400. A brief listing of their corresponding applications and analysis software used in this work is given in **Table III.2**.

Table III.2. *Brief listing of the modules and their corresponding applications and analysis software used in this work.*

Module	Applications	Analysis software
Gamry Framework	Potentiodynamic; EIS	Echem Analyst
ESA 400	Acquisition & analysis of EN data	ESA Analysis

III.3.2.   Potentiodynamic Polarization Measurements

Electrochemical reaction kinetics is essential in evaluating the corrosion rate of a given metal exposed to the environment of interest. Although thermodynamics may predict the possibility of corrosion, it does not provide information on how slow or fast corrosion processes occur [2]. A characterization of electrochemical kinetics can be achieved by evaluating at least three polarization parameters, such as corrosion current density, i_{corr}, corrosion potential, E_{corr}, and Tafel slopes, b_a and b_c. For a corroding electrode at its open circuit potential E_{corr} (net current = 0), as well as for IR-compensated data in polarized conditions, the interfacial electrochemical processes can

be described in terms of current-potential relationships, namely Butler-Volmer equation:

$$i = i_{corr} \left[\exp\left(2.303 \; \frac{E - E_{corr}}{b_a} \right) - \exp\left(- 2.303 \; \frac{E - E_{corr}}{b_c} \right) \right]$$

(III.1)

In this case, any anodic polarization induced by an anodic overvoltage, that is to say $E > E_{corr}$, is referred to as an electrochemical process in which an electrode surface corrodes by losing electrons. Inversely, any cathodic polarization requires that electrons must be supplied to the electrode surface at a negative overvoltage which implies that $E < E_{corr}$. In this work, potentiodynamic polarization measurements were performed in a conventional three-electrode cell shown in **Figure III.3**.

Figure III.3. *Experimental setup. 1 (RE): reference electrode; 2: pH probe; 3: thermostatically controlled heating plate; 4: pH-meter; 5: temperature probe; 6: specimen holder; 7: bubble flask; CO_2 IN: CO_2 gas inlet; CO_2 OUT: CO_2 gas outlet.*

All potentials were measured against a saturated calomel electrode (SCE) being used as the reference electrode connected to the test solution through a Luggin capillary probe. A coiled titanium wire was used as a counter-electrode (CE). Prior to each

measurement, the specimen was kept in solutions during 2 h until a stable corrosion potential was reached. Both the anodic and the cathodic polarization curves were scanned separately at a rate of 1 or 5 mV s^{-1} from ±10 mV versus the corrosion potential in the cathodic-to-anodic direction for the anodic sweep and in the inverse direction for the cathodic sweep.

III.3.3. EIS Measurements

Electrochemical Impedance Spectroscopy is essentially a steady-state technique, which is capable of providing valuable and reliable information about interfacial kinetic and mechanistic phenomena with relaxation times varying over many orders of magnitude [3]. The advantage of EIS lies in the fact that the steady-state regime permits the use of signal averaging methods within a single experiment to reach the desired level of precision while the wide frequency range permits a wide range of interfacial processes to be disclosed. EIS technique consists of applying periodic signals of small amplitudes to perturb an electrode-electrolyte interface and measuring the cell response while varying the frequency. In corrosion experiments, it is common to apply a sinusoidal potential perturbation with amplitude ranging from 10 to 50 mV$_{rms}$ to a corroding electrode interface and measure the resulting current signal occurring at the same excitation frequency. In this case, the relationship between potential and current signals is simply expressed in Ohm's law-like form in the frequency domain:

$$Z(\omega) = \frac{E(\omega)}{I(\omega)}$$

(III.2)

Here, the term $Z(\omega)$ stands for the complex impedance and accounts for the relationship between the amplitudes of the voltage and current signals as well as the phase shift between them. The spectroscopic character of EIS technique results from the fact that $Z(\omega)$ is measured over a range of discrete frequencies. The interpretation of EIS diagrams allows one to determine the electrochemical parameters that are useful to acquire information about corrosion process and mechanism. In corrosion context, the high-frequency end of the measurement domain is determined by the frequency required to short-circuit the interfacial capacitance [4]. In this case, only the electrolyte resistance is

prevailing. As the frequency is lowered, both interfacial resistances and capacitances will contribute to the complex impedance. Local electrochemical phenomena including adsorption/desorption and diffusion associated with corrosion processes are commonly detected at frequencies lower than 10 Hz. In this work, EIS measurements were performed with a sinusoidal potential excitation of 10 mV$_{rms}$ amplitude in the 50 kHz – 10 mHz frequency range. Unless stated otherwise, all EIS measurements were carried out in open-circuit conditions.

III.3.4.   EN Measurements

Electrochemical noise is referred to the spontaneous current or potential fluctuations. The study of these fluctuations for the characterization of corrosion processes has received considerable attention over the recent years. In corrosion context, EN phenomena are considered as the result of stochastic processes that can arise from various sources such as time-related uniform or localized corrosion activities taking place on the surface of a corroding metal. Valuable information about the corrosion mechanisms can be obtained from EN data **[5]**. EN measurements can be acquired in a conventional manner using electrochemical instruments configured as potentiostat and galvanostat. Reliable EN-based information are obtained by analyzing the spontaneous fluctuations in the potential record of a freely corroding electrode. Since the electrode is maintained in an entirely natural state, it is possible to obtain results with very high accuracy. A preferred alternative and non-invasive technique consists of combining the potential record with the measurement of the coupling current flowing between two freely corroding electrodes by a sensitive ZRA without any external perturbation, thus closely simulating ambient real-world conditions. The ZRA has become an integral part of EN measurements. On the basis of solid state electronics, it achieves simultaneous time records of the spontaneous changes in coupling current with low resistance and potential with high impedance. **Figure III.4** illustrates the basic principle of ZRA measurements. The biased ZRA mode also offers the possibility to apply a bias voltage between two electrodes that allows the anodic corrosion processes to occur on the positively polarized electrode. It also provides a useful way to electrochemically stress a material to measure its resistance to localized corrosion. EN

measurements were performed within the PCI4/750 Potentiostat in ZRA mode. Two specimens made from the same steel were used as the working electrodes. Before recoding, the specimen was kept in the test solution during 2 hours until a steady-state regime is reached. The electrochemical current noise was measured as the coupling current between the coupled states kept at the same potential. EN data were simultaneously recorded during 12 hours with a sampling frequency of 1 or 10 Hz.
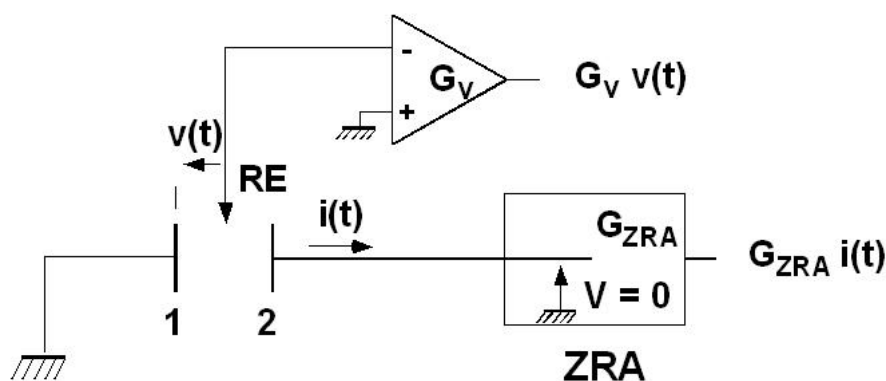
Figure III.4. *Basic principle of ZRA measurements.*

III.3.5. Artificial Pit Measurements

Under certain circumstances, a metal surface exposed to an aggressive environment may undergo corrosion attack at discrete sites. Considering the area ratio between the attacked sites and the total exposed surface, the metal is said to be experiencing localized corrosion when this ratio is much smaller than unity **[6]**. In this situation, the dissolution rate is much higher at these sites than at the rest of the surface, either because of inherent characteristics of the corroding metal or because of environmental factors at the time of attack. Localized corrosion includes various forms of attacks such as pitting, crevice corrosion and stress corrosion cracking. Localized corrosion is also known to be more severe and more difficult to both predict and control than uniform corrosion due respectively to its latent incubation, quick propagation **[7]** and stochastic nature. Indeed, the highly localized damage can render the equipment unserviceable even if the attack on the rest of the exposed surface is negligible. In practice, localized corrosion is at the root of most corrosion failures of facilities encountered in oil and gas fields. One of the most destructive forms of attack is pitting

corrosion. In general, localized corrosion is categorized into three basic stages: initiation, growth and stabilization. Although much experimental data were gathered and considerable progress was made in the understanding of pitting phenomena, many issues still need to be cleared up, particularly in which concerns the initiation stage.

Once they have initiated, pits propagate at a rate that strongly depends on intrinsic properties of the material (composition, microstructure …), pit electrolyte composition, and potential gradient along the pit. Local mass-transport characteristics also influence pit growth kinetics through the pit electrolyte concentration. In order to better understand pit growth and stability, it is essential to ascertain the rate-determining factors. As for any electrochemical reaction, pit growth can be governed by the same limiting factors: charge-transfer processes, ohmic drop effects, mass-transport considerations, or some combination of these factors. The unpredictability and random nature associated with pitting corrosion make it extremely difficult to both identify and understand the mechanisms controlling the pit behaviour and their respective interactions by classical electrochemical techniques. The current measured from a corroding electrode may indeed come from several pits with unknown active pit surface area. In order to alleviate this ambiguity, an alternative technique consists of studying a single attack in naturally simulated pit environments **[8-10]**. Multiple pits are therefore avoided, and only the dissolution kinetics of the active pit is probed. This was achieved in this work by using "artificial pit electrode" assembly schematically illustrated in **Figure III.5**. The potential and the net coupling current flowing between the two coupled electrodes were monitored with a ZRA, which was connected in such a way that any positive current was indicative of an anodic behaviour of the working electrode simulating the attack. The working surfaces were the cross sections of concentric, mutually insulated rods of 2 and 20 mm diameter for the artificial pit and the outer big surface, respectively. Pre-initiated pits were simulated by adjusting the inner electrode down to a given depth within the range 0 to 20 mm. More views of the assembly are given in appendix (see **Figures III.A1a** and **III.A1b**).
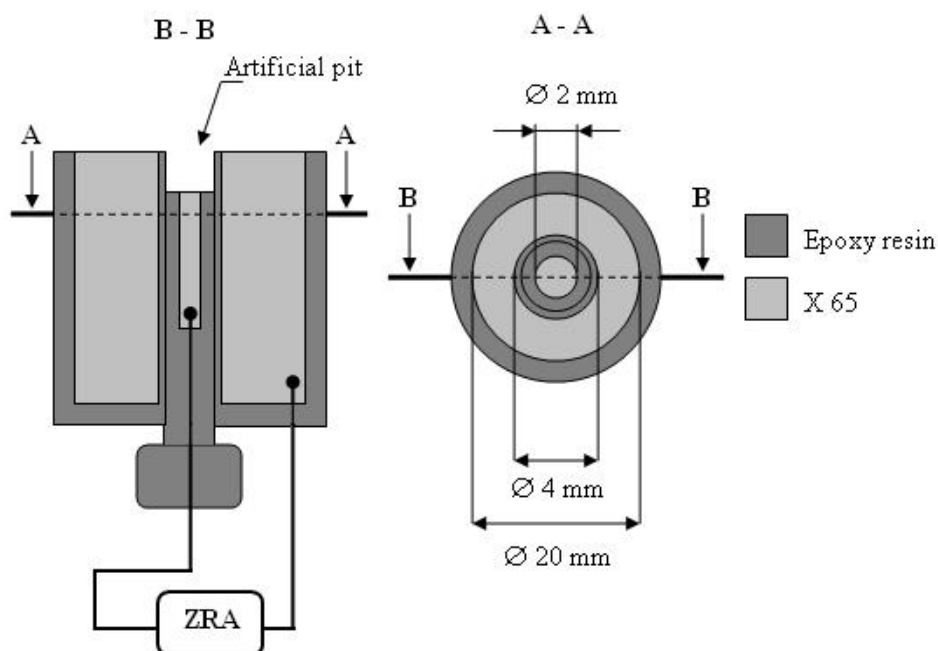
Figure III.5. *Schematic diagram of the artificial pit electrode assembly.*

III.3.6. Split Cell Measurements

Difficulty in studying localized corrosion arises due to the presence of both cathodic and anodic reactions occurring on the same nominal surface area of the corroding metal. Additional information about the coupling behaviour between the attack and the outer surface might be obtained by partial or complete segregation of the anodic and cathodic reactions. This approach involves two working electrodes in separate compartment cells, with one electrode acting as a net cathode (outer surface) and the other as a net anode (attack). By employing separate coupled electrodes, the coupling current may be studied as related to the individual reactions. The experimental setup used to simulate the coupling behaviour between the attack and the outer surface is illustrated in **Figure III.6**.
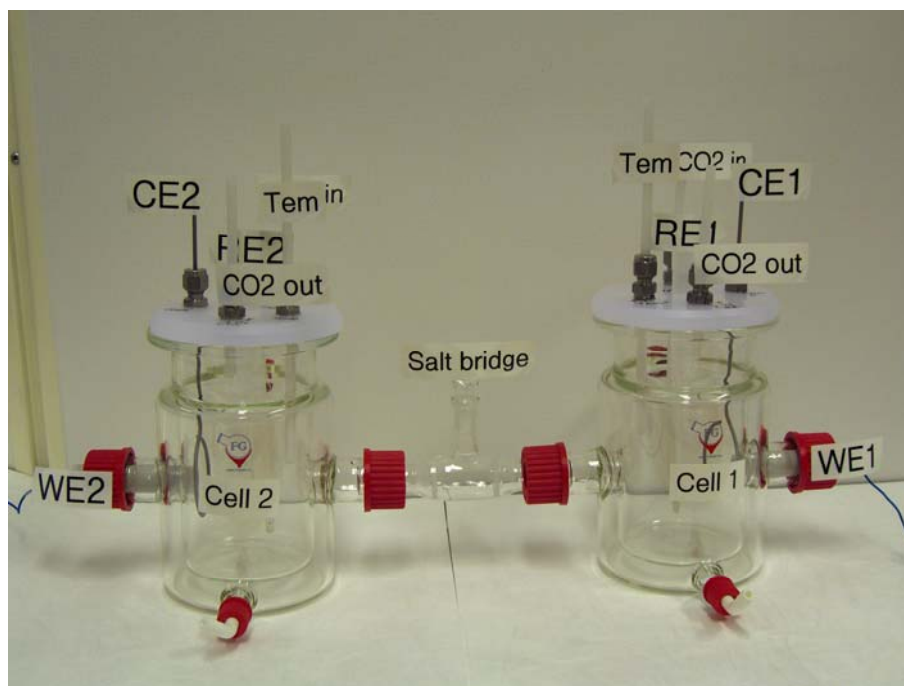
Figure III.6. *View of the split cell assembly.*

It consisted of a split cell where the two working electrodes of the same exposed area ($\approx$ 1 cm^2) were machined from API 5L X65 pipelines steel and immersed into two separate compartment cells connected to each other with a salt-bridge. The latter is connected to both compartment cells through porous glass frits that allow ion migration but restrict bulk mixing of the two solutions. Thanks to this setup configuration, the environments of the two compartment cells may be altered independently, thus allowing for more selective control of the anodic and cathodic reactions. All potentials were measured against a SCE through a Luggin capillary located in the cathodic compartment cell, which is assumed to simulate the bulk environment. It is finally worth pointing out that a potential drop existed between the two compartment cells; however the small current ($\sim \mu A$) and good electrolyte conductivity limited the extent of the ohmic drop to less than 2 mV.

III.4.   SEM and EDS Characterizations

Scanning Electron Microscopy is a technique, which is used for the observation and characterization of materials on a nanometer to micrometer scale **[11]**. This

technique requires conductive samples to avoid charging effects. The latter occur if a nonconductive or poor conductive sample is exposed to an electron beam. This imparts a negative charge that cannot be dissipated in non-conductive components. Coating samples with a thin layer of conductive material helps to overcome these problems. The basic principle of SEM consists of bombarding the sample surface to be examined under vacuum with a finely focused beam of electrons. The electron beam may be either scanned in a raster across the surface to obtain images or static for single position analyses. Interactions of the incident beam with the sample yield different types of signals including secondary electrons, backscattered electrons, characteristic X-rays and other photons at various energy levels. These signals are obtained from specific emission volumes within the sample. The intensity of the emitted signals depends mainly on the surface relief features (surface topography) and atomic weight and crystallographic arrangement of elements constituting the surface.

Hereafter, surface and cross-sectional examinations were performed using S-4800 Hitachi apparatus equipped with EDS detector. Data visualization and handling were thereafter made using Noran System Six software. The samples of interest were prepared according to the following experimental protocol. Prior to each examination, the samples were stored during 24 hours at least into a drying oven at 70 °C in order to remove unwanted liquid that could vaporize while in SEM vacuum. For cross-sectional examinations, the samples were mounted in epoxy resin. After mounting, the samples were sequentially wet-ground on a series of SiC papers with grit sizes of 80, 500, 1000 and 4000, respectively. The grinded samples were then polished using alumina polishing powder suspended in distilled water down to 0.05 μm to produce a mirror-like surface. In order to prevent charging effects, thin carbon films of about 5 nm were deposited on the substrates using the CED 030 Carbon Thread Evaporation Device by flash evaporation process of carbon threads (BAL-TEC). The threads were kept to standard clamps. Each thread degassing was performed at room temperature during 5 seconds under a pressure of 0.02 mbar and with a current value of 2.5 A. During the degassing process, the substrate was shielded by a shutter to prevent excessive heating and deposit of impure carbon. Subsequent flash evaporation (after shutter removal) was performed with a current value of about 16 A under a pressure of 0.02 mbar.

References

[1]   E. Gulbrandsen, R. Nyborg, T. Løland, K. Nisancioglu, CORROSION\2000, Paper no. 00023, NACE, 2000.

[2]   N. Perez, *"Electrochemistry and Corrosion Science"*, Kluwer Academic Publishers (2004).

[3]   D.D. Macdonald, *"Application of electrochemical impedance spectroscopy in electrochemistry and corrosion science"*, R. Varma, J.R. Selman (Eds.), Techniques for Characterization of Electrodes and Electrochemical Processes, John Wiley & Sons (1991).

[4]   R. G. Kelly and, J. R. Scully, D. W. Shoesmith, R. G. Buchheit, *"Electrochemical Techniques in Corrosion Science and Engineering"*, Marcel Dekker, Inc. (2002).

[5]   W. P. Iverson, J. Electrochem. Soc., 115 (1968) 617.

[6]   S. M. Sharland, Corr. Science, 27 (1987) 289.

[7]   D. A. Jones, *"Principles and Prevention of Corrosion"*, Macmillan Publishing Company (1992).

[8]   D. W. Buzza and H. C. Alkire, J. Electrochem. Soc., 142 (1995) 1104.

[9]   H. C. Newman and E. M. Franz, Corrosion, 40 (1984) 325.

[10] H. H. Strehblow and J. Wenners, Z. Phys. Chem. Neue Folge, 98 (1975) 199

[11] J. Goldstein, D. Newbury, D. Joy , C. E. Lyman, P. Echlin, E. Lifshin, L. Sawyer, J. Michael, *"Scanning Electron Microscopy and X-Ray Microanalysis"*, Kluwer Academic/Plenum Publishers (2003).

Appendix
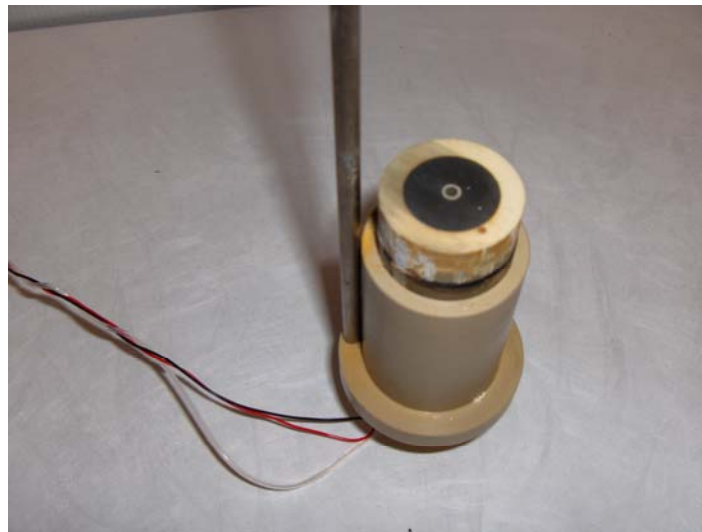
Figure III.A1a. *Face view of the artificial pit device.*
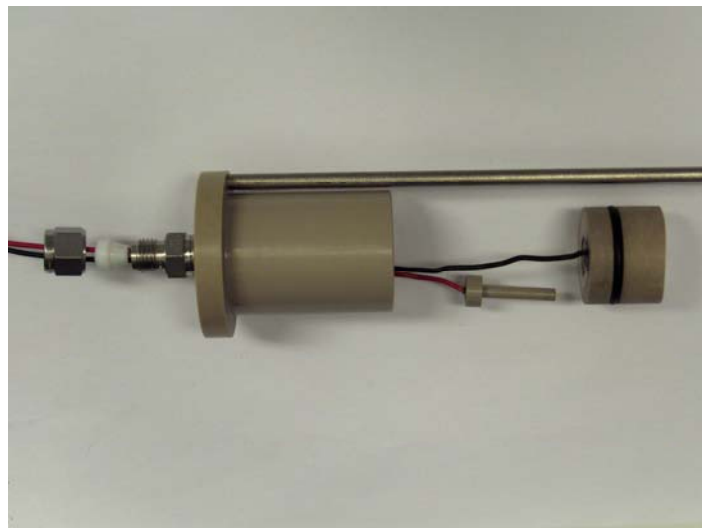
Figure III.A1b. *Detailed side view of the artificial pit device.*

Chapter *IV*

Role of HAc in CO$_2$ Corrosion

Table of Contents

IV.1.   Introduction

CO$_2$ corrosion is often associated with the presence of some other acidic gases or volatile short chain carboxylic acids usually co-produced with unprocessed hydrocarbons. Acetic acid appears to be one of the most prevalent organic acids found in oil and gas reservoirs with high concentrations up to thousands of ppm in the produced aqueous phase. The effect of HAc on the corrosion rate of carbon steel in CO$_2$-containing media has been extensively investigated over a wide range of conditions during the last few years. To date, however, the fundamental role of acetic acid in CO$_2$ corrosion of carbon steel has been the subject of apparent controversies, particularly in which concerns the eventual electroactive participation of this compound in the cathodic mechanism. The effect of HAc on the overall kinetic behaviour of carbon steel and corrosion scaling was addressed by means of electrochemical measurements and SEM examinations. Whether HAc acts as a specific cathodic reactant or just as a proton source is the central idea of the present chapter.

IV.2.   Chemical Equilibria and Electrode Reactions

IV.2.1.   Equilibrium Speciation of CO$_2$/HAc Brine

In oil and gas industry, CO$_2$ and HAc gases readily dissolve into the condensed water. The latter has typically a pH lower than 4 and the concentration of carbonates is hence very low. It follows that the formation of a protective iron carbonate layer can be omitted in a first approach. This simplification is further supported by the fact that FeCO$_3$(s) precipitation is very slow at moderate temperatures, and the formation of protective layers at such temperatures takes weeks even under conditions of artificially elevated pH [1, 2]. Assuming ideal-homogenous water chemistry, CO$_2$/HAc system can be adequately described by the following set of chemical equilibria.

Table IV.1. *List of chemical reactions associated with CO$_2$/HAc system.*

Water dissociation	$H_2O \rightleftharpoons H^+ + OH^-$; K_w (IV.1)
Solubility of CO$_2$ gas in water	$CO_2(g) \rightleftharpoons CO_2(aq)$; K_{sol} (IV.2)
CO$_2$ hydration	$CO_2(aq) + H_2O \rightleftharpoons H_2CO_3$; K_{hyd} (IV.3)
H$_2$CO$_3$ dissociation	$H_2CO_3 \rightleftharpoons H^+ + HCO_3^-$; K_{ca} (IV.4)
HCO$_3^-$ dissociation	$HCO_3^- \rightleftharpoons H^+ + CO_3^{2-}$; K_{bi} (IV.5)
Solubility of HAc gas in water	$HAc(g) \rightleftharpoons HAc$; K_H (IV.6)
HAc dissociation	$HAc \rightleftharpoons H^+ + Ac^-$; K_{ac} (IV.7)

At high concentrations, however, the infinite dilution theory does not hold anymore and concentrations must be replaced by activities to represent the solution non-ideality. The activity coefficients can be accurately calculated by considering the combination of long-range and short-range electrostatic interactions between cations and anions. This however exceeds the extent of this work and the interested reader is invited to see the related references [3]. On the other hand, acetic acid gas is strongly soluble in water with the Henry's constant being $K_H = 4.1 \times 10^3$ M bar^{-1} [4, 5]. The equilibrium partial pressure of HAc over 1 mM (60 ppm) HAc solution is less than 1 Pa at temperatures up to 100 °C [6]. This means that the gas phase over the aqueous solution is not a big reservoir for HAc as it is the case for CO$_2$. For this reason, acetic acid will be regarded only in its aqueous form (HAc), and the reaction (IV.6) is accordingly ignored. The pH of the brine was determined with a relative tolerance of 10^{-6} using Comsol Reaction Engineering Lab$^{©}$ module. **Figure VI.1** shows the simulated variation of pH with the total amounts of HAc initially added to the simulated 17 mM (1 g/l or 0.1 wt-%) aqueous NaCl solution saturated with 1 bar CO$_2$ at 25 °C. It is assumed that the brine is continuously loaded with carbon dioxide gas so that the level of aqueous CO$_2$ (also H$_2$CO$_3$) is always kept constant throughout the liquid phase (open system). The ratio between acetates and the total amounts of HAc was also plotted. It is seen that acetates concentration is only a small fraction of less than 8 % of the total acetic species. In such a range of pH, acetic acid is clearly shown to be present mainly in its undissociated form (free HAc).
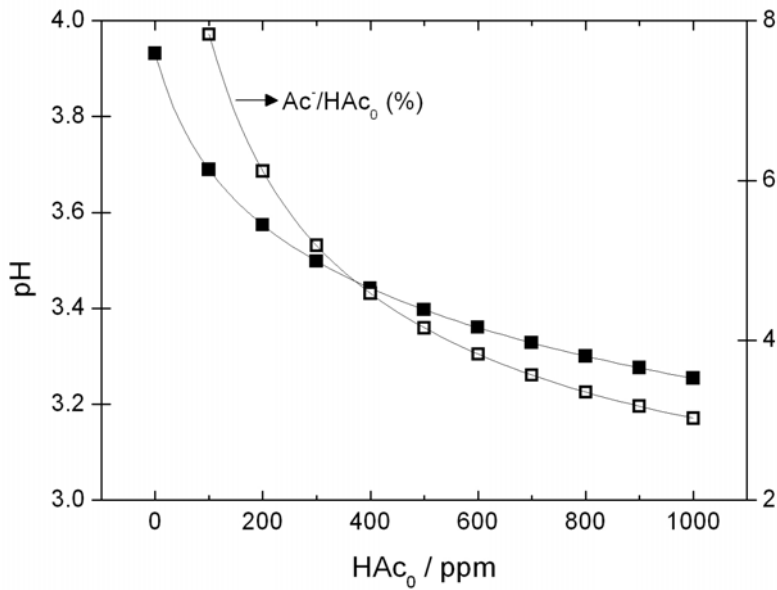
Figure IV.1. *Simulated variation of pH with initial HAc concentration in simulated 17 mM aqueous NaCl solution saturated with 1 bar CO₂ at 25 °C (open system). In such a range of pH, acetic acid is clearly shown to be present mainly in its undissociated form (free HAc).*

By substituting the calculated concentration of H^+ ions into equations IV.4, IV.5 and IV.7, a complete speciation of the system was then obtained. **Table IV.2** lists the calculated concentrations at various initial concentrations of total acetic acid.

Table IV.2. *Calculated speciation at 25 °C as a function of the initial concentration of acetic acid. 17 mM NaCl, 1 bar CO₂ (open system). Except for HAc_0 and HAc, all concentrations are expressed in mol l^{-1}.*

HAc_0 ppm	pH	HAc ppm	Ac^-	HCO_3^-	CO_3^{2-}
0	3.931	0	0	1.17×10^{-4}	4.67×10^{-11}
100	3.689	92.079	1.37×10^{-4}	6.69×10^{-4}	1.53×10^{-11}
200	3.574	187.591	2.15×10^{-4}	5.13×10^{-4}	8.99×10^{-12}
300	3.498	284.246	2.74×10^{-4}	4.31×10^{-4}	6.35×10^{-12}
400	3.442	381.473	3.23×10^{-4}	3.79×10^{-4}	4.90×10^{-12}
500	3.397	479.272	3.66×10^{-4}	3.4×10^{-4}	3.99×10^{-12}
600	3.360	577.071	4.04×10^{-4}	3.14×10^{-4}	3.36×10^{-12}
700	3.328	674.870	4.4×10^{-4}	2.9×10^{-4}	2.90×10^{-12}
800	3.300	773.241	4.72×10^{-4}	2.74×10^{-4}	2.56×10^{-12}
900	3.276	871.040	5.03×10^{-4}	2.58×10^{-4}	2.28×10^{-12}
1000	3.254	969.411	5.32×10^{-4}	2.46×10^{-4}	2.06×10^{-12}

A related graph is also provided in **Figure IV.2**. For the sake of readability, the respective concentrations of hydroxide ions and carbonate ions were not shown in this figure.
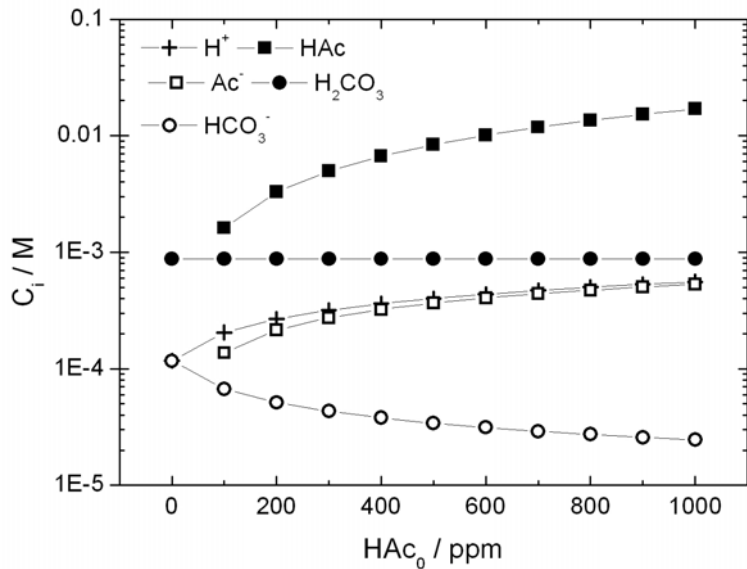
Figure IV.2. *System speciation at 25 °C as a function of the initial concentration of acetic acid. 17 mM NaCl, 1 bar CO₂ (open system).*

IV.2.2. Equilibrium Potentials

The overall corrosion process of carbon steel in such conditions can be described by the electrode reactions listed in **Table IV.3**. As mentioned in the previous chapter, the direct reduction of water occurs at low potentials and can become influential only at pH > 5 and at partial pressures of CO_2 far below 1 bar **[7, 8]**. Such conditions, however, do not reflect practical CO_2 corrosion situations and this reaction was therefore not included in the overall electrochemical process. For each electrochemical reaction of **Table VI.3**, the standard electrode potential was calculated using the following expression for the standard Gibbs free energy change combined to equation (I.9) of Chapter I:

$$\Delta G^0 = \sum_i v_i G_{f,i}^0 \left(\text{products} \right) - \sum_i v_i G_{f,i}^0 \left(\text{reactants} \right) \qquad \text{(IV.16)}$$

where v_i is the stoichiometric coefficient of species i.

Table IV.3. *List of the corresponding electrode reactions associated with carbon steel corrosion in the system of Table IV.1.*

Anodic reactions	$Fe \rightleftharpoons Fe^{2+} + 2e^-; \quad E_1^0, E_1 \quad (\text{IV.8})$
	$Fe + H_2CO_3 \rightleftharpoons FeCO_3 + 2H^+ + 2e^-; \quad E_2^0, E_2 \quad (\text{IV.9})$
	$Fe + HCO_3^- \rightleftharpoons FeCO_3 + H^+ + 2e^-; \quad E_3^0, E_3 \quad (\text{IV.10})$
	$Fe + 2H_2O \rightleftharpoons Fe(OH)_2 + 2H^+ + 2e^-; \quad E_4^0, E_4 \quad (\text{IV.11})$
Cathodic reactions	$2H^+ + 2e^- \rightleftharpoons H_2; \quad E_5^0, E_5 \quad (\text{IV.12})$
	$H_2CO_3 + e^- \rightleftharpoons HCO_3^- + \frac{1}{2}H_2; \quad E_6^0, E_6 \quad (\text{IV.13})$
	$HCO_3^- + e^- \rightleftharpoons CO_3^{2-} + \frac{1}{2}H_2; \quad E_7^0, E_7 \quad (\text{IV.14})$
	$HAc + e^- \rightleftharpoons Ac^- + \frac{1}{2}H_2; \quad E_8^0, E_8 \quad (\text{IV.15})$

The standard Gibbs free energies of formation of individual species (G_f^0) are listed in the following table.

Table IV.4. *Standard Gibbs free energies of formation of individual species.*

Species	G_f^0(kJ mol⁻¹)	References
H^+	0	**[9, 10]**
H_2O	-237.18	**[11]**
H_2CO_3	-623.2	**[9, 10, 12]**
HCO_3^-	-586.85	**[9, 10, 12]**
CO_3^{2-}	-527.9	**[9, 10, 12]**
HAc	-390.2	**[9]**
Ac-	-369.3	**[9]**
Fe^{2+}	-91.5	**[11]**
$Fe(OH)_2$	-492	**[11]**
$FeCO_3$	-681	**[12]**

At 25°C, the corresponding values of E^0 as well as the relative expressions for the equilibrium electrode potentials are given below in **Table VI.5**. The equilibrium potential of iron oxidation (IV.8) requires that the concentration of ferrous ions must be known. This issue could be overcome by considering that the presence of ferrous ions in the solution is only due to the anodic processes by which these species are released from

the active surface, i.e. $[Fe^{2+}]_{t=0} = 0$. On the other hand, the self-dissociation of the acid molecules can be neglected in the buffer region, and a weak acid HA is converted to its conjugate base A⁻ upon the overall corrosion reaction [6]:

$$2HA + Fe \rightleftharpoons Fe^{2+} + 2A^- + H_2 \tag{IV.17}$$

Thus:

$$\left[Fe^{2+}\right] \approx \frac{\left[HCO_3^-\right] + \left[Ac^-\right]}{2} \tag{IV.18}$$

Table IV.5. *Calculated standard equilibrium potentials as well as Nernst equations of the electrode reactions (ref. Table IV.2) associated with carbon steel corrosion in simulated 17 mM aqueous NaCl solution saturated with CO₂ at 25 °C. All potentials are expressed in volts versus a saturated calomel electrode (SCE).*

$E_1^0 = -0.682$	$E_1 = -0.682 + 0.029 \times \log\left[Fe^{2+}\right]$
$E_2^0 = -0.541$	$E_2 = -0.423 - 0.029 \times \log\left(P_{CO_2}\right) - 0.059 \times pH$
$E_3^0 = -0.729$	$E_3 = -0.509 - 0.029 \times \log\left(P_{CO_2}\right) - 0.059 \times pH$
$E_4^0 = -0.332$	$E_4 = -0.332 - 0.059 \times pH$
$E_5^0 = -0.241$	$E_5 = -0.241 + 0.059 \times pH$
$E_6^0 = -0.618$	$E_6 = -0.411 - 0.059 \times pH$
$E_7^0 = -0.851$	$E_7 = -0.241 - 0.059 \times pH$
$E_8^0 = -0.457$	$E_8 = -0.176 - 0.059 \times pH$

IV.3. Kinetic Behaviour of X65 Steel in CO₂/HAc Brine

IV.3.1. Introduction

In order to evaluate the contribution of HAc to the overall CO₂ corrosion process of X65 pipeline steel independently from what could be related to the pH effect, three sets of potentiodynamic measurements were performed at constant pH while varying HAc concentration. At a constant pH, indeed, the concentration of protons is fixed, and the effect of acetic acid on the anodic and cathodic reactions can be straightforwardly distinguished. The concentration of the undissociated HAc, HAc_u, at equilibrium is

determined by considering the partial dissociation of the weak acid (IV.7) and the condition for mass conservation of total acetic species (IV.19), HAc_0. That is to say:

$$HAc_0 = HAc_u + Ac^-$$ (IV.19)

Combining (IV.7) and (IV.19) yields:

$$HAc_u = HAc_0 \left(1 + \frac{K_{ac}}{[H^+]} \right)^{-1}$$ (IV.20)

The total amounts of acetic species initially added to the test brine were 60, 180 and 600 ppm. After each measurement, the working electrode was wet-ground according to the experimental protocol described in paragraph III.2 of Chapter III. The desired solution pH was achieved through minute adjustments using droplets of HCl or NaOH. **Figure IV.3** shows the calculated equilibrium concentration of undissociated HAc as a function of pH at room temperature for different total amounts of acetic species.
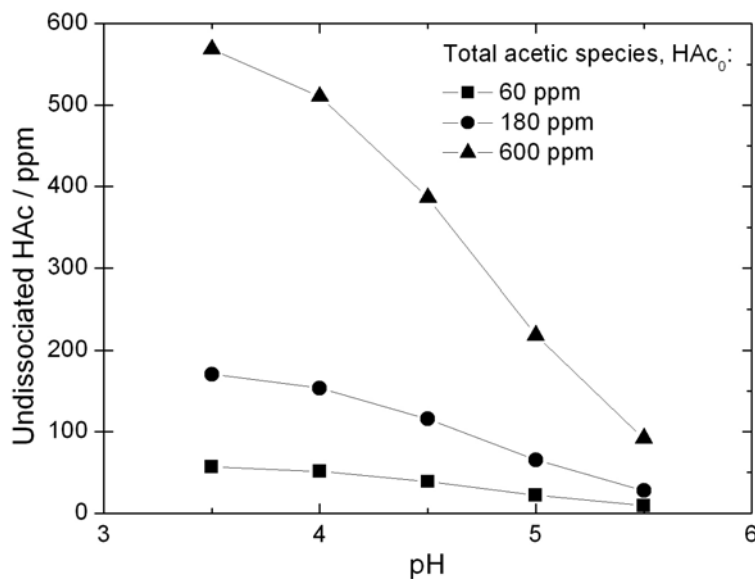
Figure IV.3. *Calculated concentrations of undissociated HAc as a function of pH at room temperature for various total amounts of acetic species initially added to the test solution.*

It is worth pointing out here that the HAc concentration range was selected so that it reflects near-realistic service conditions.

IV.3.2. Polarization Curve Measurements

The IR-compensated polarization curves are depicted in **Figures IV.4** - **IV.6**. The values (A-D) are the calculated equilibrium concentrations of undissociated HAc corresponding to the total amounts of acetic species reported in **Figure IV.3**. Despite the four solutions had the same concentration of free proton for each pH, the responses were clearly different with the most prominent differences occurring at cathodic polarization. In all cases, characteristic active dissolution behaviour was more or less evident on the anodic branch. Upon the increase of the concentration of undissociated HAc, the cathodic part reaction rate was remarkably enhanced and well-defined limiting current plateaus were generally observed at high cathodic polarization. In HAc-free solutions, the limiting current density appears to be consistent with the diffusion of protons formed by the slow hydration of CO_2 and followed by the dissociation of H_2CO_3 molecules. Instead, the appearance of different limiting current plateaus in the presence of acetic species at constant pH suggests that the diffusion of undissociated HAc becomes the rate-controlling step at high cathodic polarization.
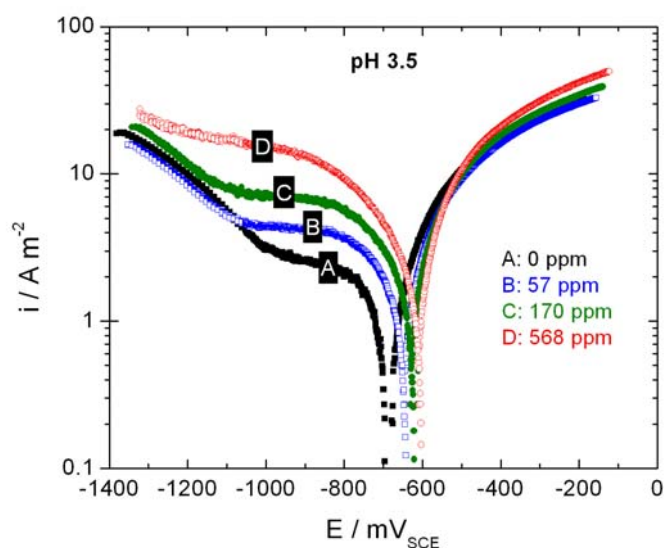
Figure IV.4. *Polarization curves of X65 pipeline steel at room temperature in 1 bar CO_2-saturated 17 mM NaCl solutions containing various amounts of free HAc (A-D) at pH 3.5.*
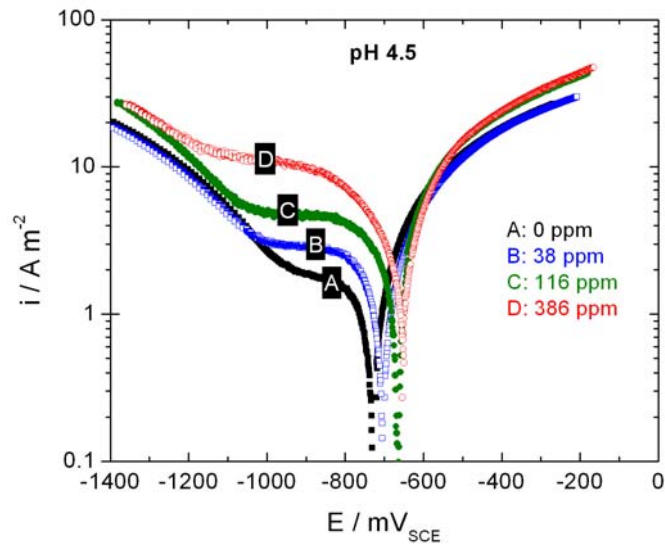
Figure IV.5. Polarization curves of X65 pipeline steel at pH 4.5. The experimental conditions are those of Figure IV.4.
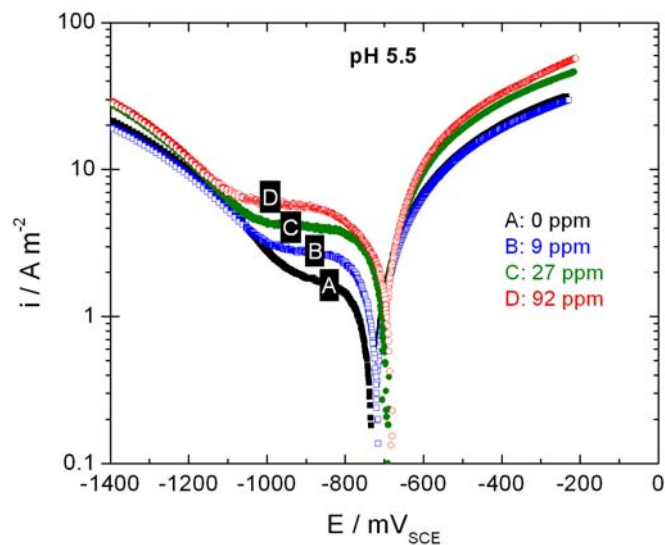
Figure IV.6. Polarization curves of X65 pipeline steel at pH 5.5. The experimental conditions are those of Figure IV.4.

IV.3.3. Cathodic Limiting Current vs. Corrosion Current

Figure IV.7 shows the respective plots of the cathodic limiting current density and the corrosion current density vs. the concentration of undissociated HAc for such a range of pH. The corrosion current densities were determined using the linear

polarization resistance technique for a potential ramp of $\pm$ 10 mV vs. the corrosion potential with the Stearn-Geary factor B_{SG} estimated to 20 mV (see equation I.27).
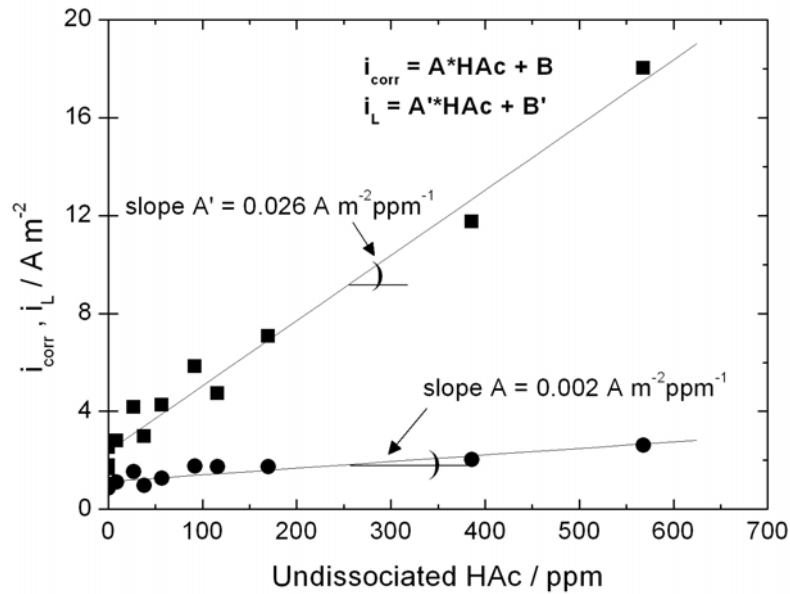
Figure IV.7. *Respective variations of the cathodic limiting current density* (■) *and the corrosion current density (●) with the concentration of undissociated HAc for a pH within the range 3.5 – 5.5. Data were obtained for X65 pipeline steel corroding in 1 bar CO₂-saturated 17 mM NaCl solutions at room temperature.*

It can be clearly seen that the limiting current density increases substantially with increasing the concentration of undissociated HAc and, indeed, the dependence is linear with a slope evaluated to 0.026 A m^{-2} ppm^{-1}. The other feature to be noticed here is the significant intercept B (2 - 2.5 A m^{-2}) on the limiting current density axis in HAc-free medium. In earlier work of Garsany et al. **[13-17]**, this intercept has been interpreted as the kinetically controlled current arising from the slow formation of carbonic acid. The corrosion current density also proved to evolve linearly but very slightly with the concentration of undissociated HAc with a slope being 10 times smaller than the one for the cathodic limiting current density. Also, in pure CO₂ corrosion or at very low concentrations of HAc, the corrosion current density was systematically shown to be of the same order of magnitude as the limiting current density, thus suggesting a mixed charge/ chemical control **[18]** (e.g. branches A in **Figures IV.4 - IV.6**). With the further increase of undissociated HAc concentration, the limiting current density becomes

much more significant than the corrosion current density, thus indicating a pure (or at least a dominating) charge-transfer control at low cathodic polarizations. This is also corroborated by the fact that the limiting current plateau is retarded at high concentrations of undissociated HAc, for instance the cathodic branch of curve D in **Figure IV.4**.

IV.3.4. Corrosion Potential

The fact that the corrosion current density remained practically unchanged even in the presence of HAc rationalizes the general trend observed for the polarization curves. The kinetic behaviour in the vicinity of E_{corr} depicted in **Figures IV.4 - IV.6** indicates that the overall effect of the HAc is a balance between a boosted cathodic branch and a depressed anodic one. The inhibition behaviour observed on the anodic part reaction rate, which is commonly reported in literature [19-21], must however be taken with an extreme caution regarding the relation of cause and effect in the presence of HAc. One possible explanation would be that the inhibition effect is a direct consequence of the substantial increase of the cathodic reaction rate with the concentration of undissociated HAc. Subsequently, the large changes observed for the partial cathodic current lead to an upward shift of the corrosion potential as featured by **Figure IV.8**. This upward shift means that the metal becomes nobler (more positive). On the other hand no clear sign appears thus far concerning an electroactive participation of undissociated HAc in the vicinity of E_{corr}, and more particularly in the cathodic process. An insightful look at **Figures IV.4 - IV.6** did not indeed reveal any significant change in what could be assimilated to the Tafel lines (low polarizations) for any of the conditions tested. The anodic Tafel slope was respectively found to be 50 mV/decade in HAc-free solutions and 75 mV/decade in the presence of HAc. Instead, the cathodic Tafel slope was the lesser affected by the presence of HAc with an average value of -120 mV/decade. This means that in each case the corrosion mechanism is almost the same, and that only the partial reaction rates are affected by the presence of undissociated HAc.
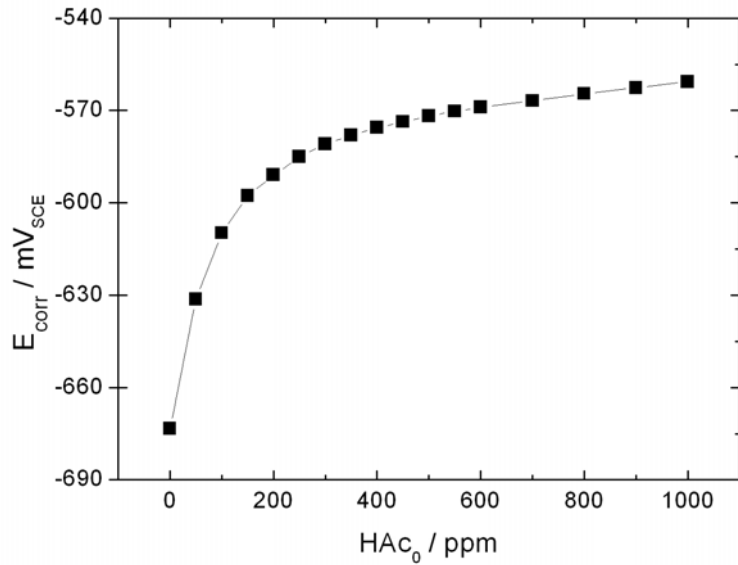
Figure IV.8. *Corrosion potential of X65 pipeline steel in 1 bar CO₂-saturated 17 mM NaCl as a function of total HAc concentration at free pH. Room temperature.*

IV.3.5.   Identification of the Possible Anodic Reaction Branches

According to mixed potential theory, only reactions with more negative equilibrium potentials than the steady-state E_{corr} are likely to be thermodynamically anodic processes. The measured corrosion potentials of **Figure IV.8** were likened to the calculated equilibrium potentials (see **Table IV.4**) of the anodic reactions listed in **Tables IV.2** for various concentrations of the total acetic species. The results are depicted in **Figure IV.9**. The filled area under E_{corr} curve denotes the region, where anodic reactions are thermodynamically possible. Except for reaction (IV.11), the proposed anodic reactions prove to be thermodynamically possible regardless of the HAc concentration. The results also show that the formation of iron carbonate scale is unlikely to be driven via reaction (IV.9) at HAc concentration typically lower than a threshold of 30 ppm. In this exceptional case, $FeCO_3$ film is likely to form rather according to reaction (IV.10), and, to some extent, according to the precipitation reaction $Fe^{2+} + CO_3^{2-} \rightarrow FeCO_3$ if ferrous and carbonate ions are such that the saturation limit is exceeded. Above the threshold of 30 ppm HAc, the formation of iron carbonate

scale would therefore be the result of either two mechanisms below the saturation level or three mechanisms under saturation condition.
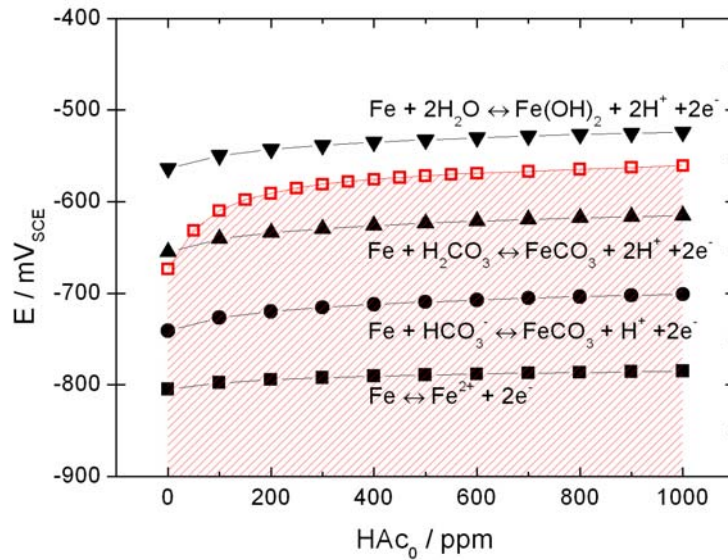
Figure IV.9. Comparison between the measured corrosion potentials of X65 pipeline steel (red unfilled-square symbols) and the calculated equilibrium potentials of anodic reactions (see Tables IV.2 and IV.4) for various concentrations of total HAc at free pH. 1 bar CO$_2$, 17 mM NaCl, room temperature.

IV.3.6.   Identification of the Possible Cathodic Reaction Branches

Likewise, **Figure IV.10** diagrams the calculated cathodic equilibrium potentials versus the measured corrosion potentials for various amounts of total acetic species. Generally, only those with less negative equilibrium potentials than the measured corrosion potentials are thermodynamically possible to be cathodic reactions. The filled area under E$_{corr}$ curve denotes the region, where cathodic reactions are thermodynamically unlikely. With an exception made for the direct reduction of H$_2$CO$_3$ (reaction IV.13), all the cathodic reactions proposed are thermodynamically possible in such system. According to **Figures IV.9** and **IV.10**, an electroactive participation of carbonic acid molecules is expected only at very low concentrations of HAc. One would also anticipate that carbonic acid dominates over HAc at high CO$_2$ partial pressures. The results of **Figure IV.10** also show that the cathodic reduction of free proton has the least negative equilibrium potential, and appears to be at present the prevailing cathodic

reaction. Even though no sign of any electroactive participation has appeared thus far, the results nevertheless indicate a potential occurrence of the direct reduction of HAc molecules.
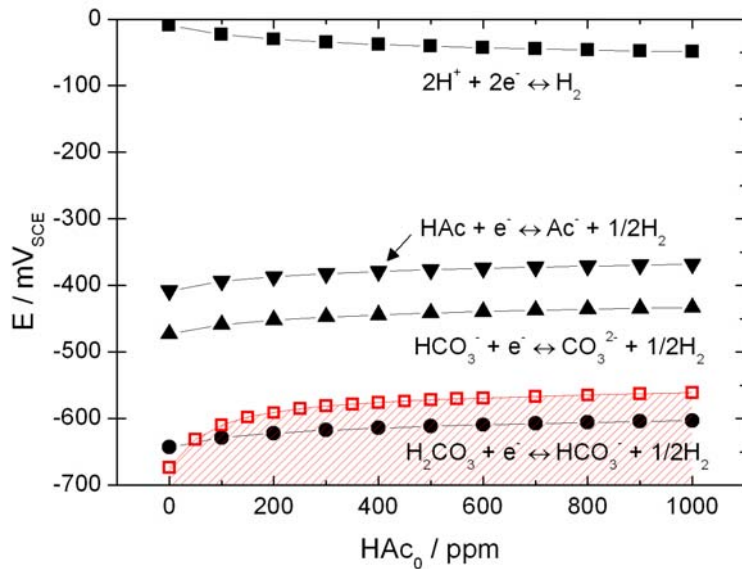
Figure IV.10. Comparison between the measured corrosion potentials of X65 pipeline steel (red unfilled-square symbols) and the calculated equilibrium potentials of cathodic reactions (see Tables IV.2 and IV.4) for various concentrations of total HAc at free pH. 1 bar CO₂, 17 mM NaCl, room temperature.

IV.3.7. EIS Measurements

IR-compensated Nyquist plots for 17 mM NaCl solutions containing 0 and 600 ppm of total acetic species at pH 3.5 are given in **Figure IV.11**. The respective values of the polarization resistance (R_p), as evaluated from the polarization curves A and D of **Figure IV.4** according to Stern-Geary's relationship (equation I.27 in Chapter I), are also shown in the same figure. These values are pretty consistent with those estimated from the Nyquist plots. In both cases, the impedance diagrams exhibit a flattened semi-circle at high frequencies, with a virtual center located under the real axis. This behaviour is typical for solid electrodes that show frequency dispersion of the impedance data. Influential factors such as the surface roughness and the current distribution were suggested to be at the origin of the depressed high-frequency loop **[22,**

23]. This last is indicative of a charge-transfer process through the double-layer capacitance.
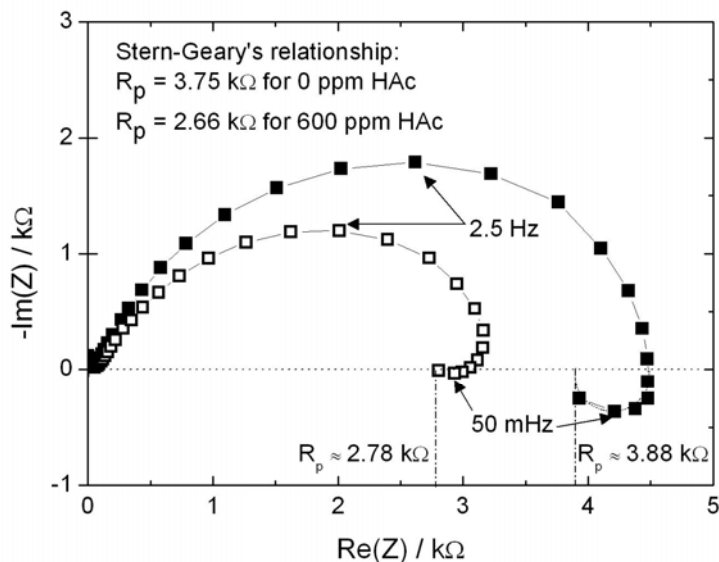
Figure IV.11. *Nyquist plots obtained for a 2 mm diameter X65 electrode at the corrosion potential in 1 bar CO_2-saturated 17 mM NaCl solution for 0 ppm (■) and 600 ppm (□) of total HAc. pH 3.5, room temperature.*

It is also important to mention that the low-frequency inductive loops revealed by the Nyquist diagrams, which can be ascribed to multi-step dissolution processes and the relaxation of adsorbed species or reaction intermediates **[24**, **25]** are not straightforwardly related to the presence of HAc, but to the presence of CO_2, as seen in **Figure IV.12**. Indeed, no clear inductive loop appears in CO_2-free solutions. The shapes of the Nyquist diagrams as well as the characteristic frequencies remain roughly invariant regardless of the presence of HAc. The uniform dissolution of carbon steel in these conditions would then be more liable to be a matter of what is generically referred to as CO_2 corrosion, with HAc mainly being a proton source.
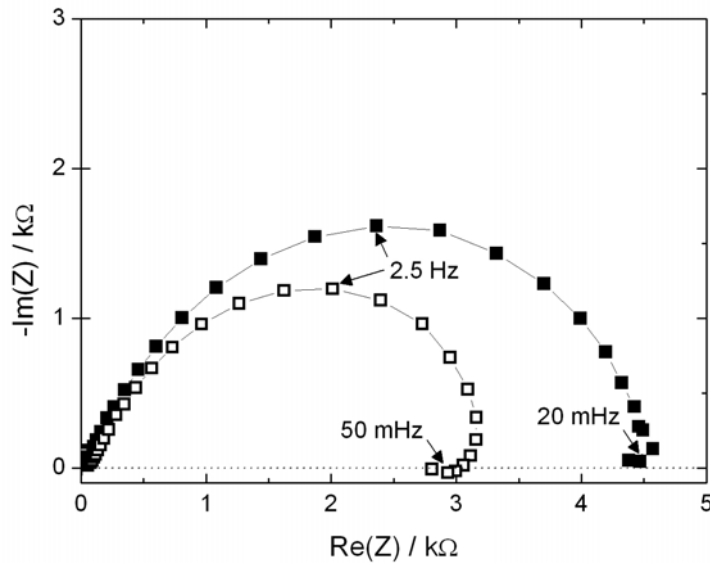
Figure IV.12. *Nyquist plots obtained for a 2 mm diameter X65 electrode at the corrosion potential in respectively CO$_2$-free (■) and 1 bar CO$_2$-saturated (□) solutions. 17 mM NaCl, 600 ppm of total HAc, pH 3.5, room temperature.*

IV.4. Adsorption of Acetic Acid on X65 Steel

IV.4.1. Introduction

The results of **Figure IV.11** also reveal that the decrease of the polarisation resistance in the presence of acetic acid is accompanied by a less pronounced inductive loop. The fact that the obtained results have not showed any direct implication of HAc in the overall dissolution reaction thus far has prompted us to attribute this behaviour to the screen effect of adsorbed HAc molecules. These last would act as a barrier and cancel the interaction of the main actors in the dissolution reaction (i.e. carbonic species) with the metal surface at adsorption sites, which is also consistent with the slight inhibition of the anodic branch observed in the vicinity of E$_{corr}$ in the presence of HAc.

IV.4.2. Surface Coverage

Figure IV.13 is an illustration of the adsorption isotherm of undissociated HAc molecules onto the electrode surface. The surface coverage (θ),which accounts for the slight inhibition effect of the addition of HAc as shown in the anodic branches of the polarization curves in the vicinity of E_{corr}, was estimated according to the following correlation [26]:

$$\theta = 1 - \frac{I}{I_0} \tag{IV.21}$$

where I and I_0 are the currents measured in HAc-containing and HAc-free solutions, respectively. It is seen that the adsorption of HAc fits the Temkin logarithmic isotherm as found elsewhere [26, 27]. It was argued that the Langmuir isotherm cannot be applied in this situation considering the deviations from the ideal behaviour of chemisorption [26]. These deviations can be ascribed to the non-homogeneity of the electrode surface and the presence of mutual interactions between adsorbed molecules.
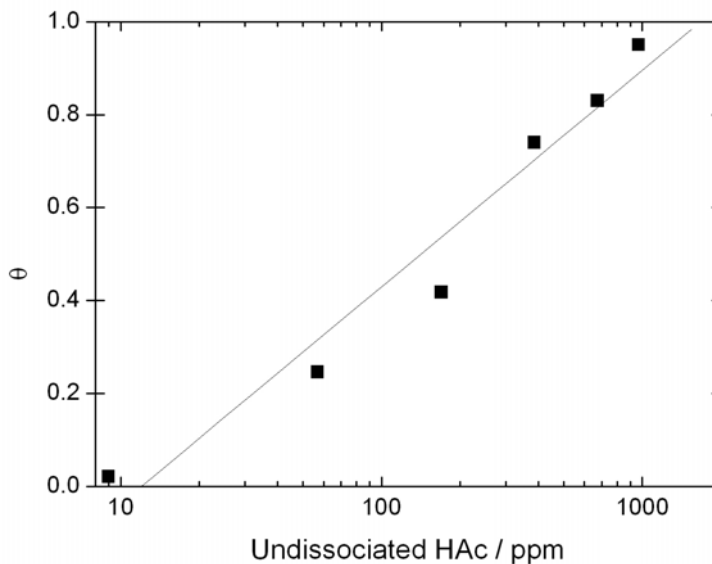
Figure IV.13. *Adsorption isotherm of undissociated HAc molecules on X65 carbon steel electrodes in 1 bar CO₂-saturated 17 mM NaCl solutions at E = -600 mV_{SCE}. pH 3.5, room temperature.*

The adsorption isotherm of undissociated HAc appears to be in conformity with the general trend of the corrosion potential observed in **Figure IV.8** with the subsequent inhibition of the anodic part reaction rate. Which of acetate or undissociated HAc is at the origin of this behaviour is however a question that may arise. In order to dissipate this ambiguity, the corrosion potentials were recoded at constant pH for various concentrations of total acetic species. As featured in **Figure IV.14**, the corrosion potential was systematically shown to increase linearly with the concentration of undissociated HAc regardless of the solution pH.
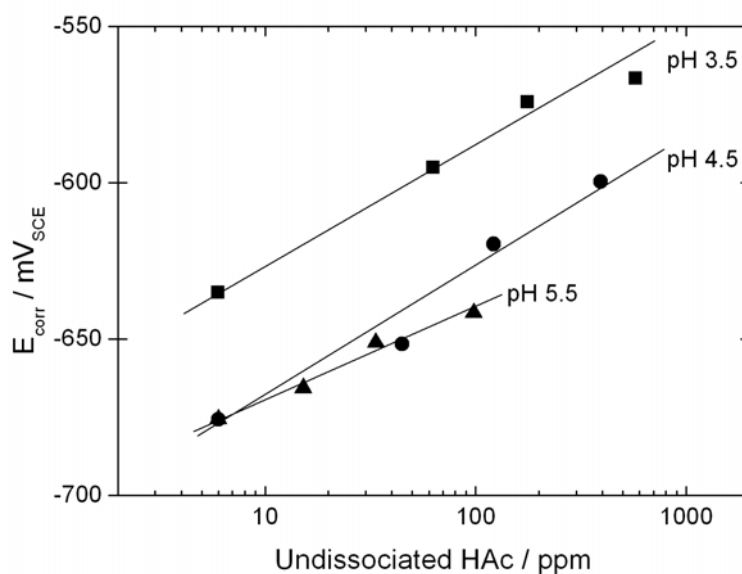
Figure IV.14. *Linear dependence of the corrosion potential on the concentration of undissociated HAc at constant pH in 1 bar CO₂-saturated 17 mM NaCl solutions. Room temperature.*

Furthermore, the evolution of the corrosion potential was found to be linear even when acetates dominate over the undissociated molecules of HAc, for instance at pH 5.5. Such observation can be considered as evidence that Ac⁻ ions are at least much less active than the undissociated HAc in the adsorption onto the electrode surface. Similar observations were also made concerning the adsorption of acetic acid onto other metals [27]. One possible rationalization of the lack of large adsorption of acetates even at high pH is that the surface binding of acetates is significantly prevented by a more competitive formation of hydroxyl-containing adsorbed species, as also suggested by other authors [28]. Also, it is worth pointing out that even though the presence of a

strong electric field across the double layer is likely to enhance the dissociation rate of HAc molecules, this effect could not be high enough so that the Ac$^-$ to HAc$_u$ ratio is affected in a decisive way **[27]**. Overall, the above observations suggest that the large change in the corrosion potential is closely connected to the adsorption of undissociated HAc onto the steel surface.

IV.4.3. Effect of Hydrodynamic Conditions

Thus far, the results have dealt with the adsorption of HAc under unstirred conditions. One simple way to assess the effect of hydrodynamic conditions on the adsorption of HAc molecules would thus consist in measuring the corrosion potential in stirred electrolytes. **Figure IV.15** pictures the variation of the corrosion potential with the rotation rate of the magnet stirrer.
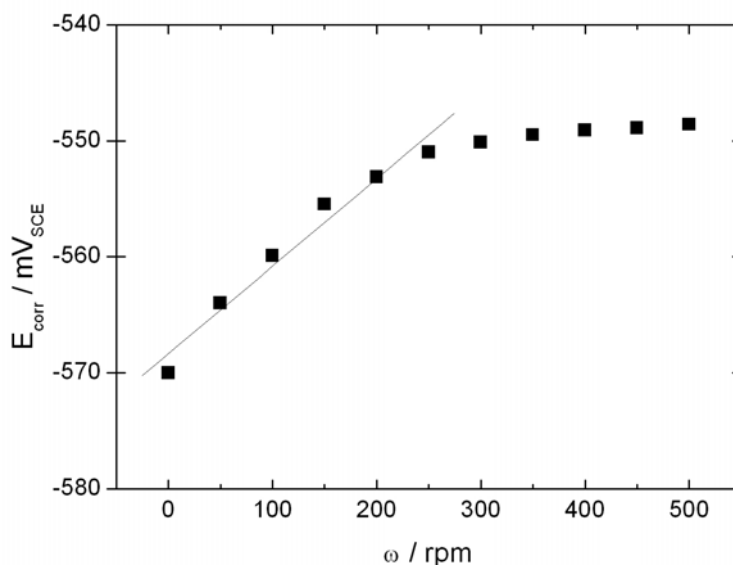
Figure IV.15. *Corrosion potential of X65 pipeline steel at various rotation rates of the magnet stirrer in 1 bar CO$_2$-saturated 17 mM NaCl solution containing 600 ppm of total HAc. pH 3.5, room temperature. rpm = rotation per minute.*

It is seen that the corrosion potential underwent an upward shift upon the increase of the rotation speed. A similar behaviour on rotating disk electrode was also reported very

recently **[29]**. Starting from the static condition ($\omega = 0$ rpm), the corrosion potential was shown to evolve in a roughly linear manner to level off thereafter. In view of the elements argued above, the monotonic evolution of E_{corr} with the rotation rate can be inferred to the increased HAc adsorbates onto the electrode surface. On the other hand, the deviation from the linear trend observed at higher rotation rates is likely to be a sign of a surface saturation with HAc adsorbates. Stirring of the solution is therefore a stimulating factor for the adsorption rate of HAc molecules, which also indicates that the kinetics of adsorption is diffusion-controlled under such conditions. The number of adsorbed HAc molecules can otherwise be estimated via the surface concentration, Γ.

IV.4.4. Surface Concentration

Assuming a linear diffusion process, the maximum concentration of HAc adsorbates onto the electrode surface should obey the following equation **[27]**:

$$\Gamma_{max} = \frac{2N_A \left(HAc_u \right)_{bulk}}{\theta R_f} \sqrt{\frac{D_{ac}t}{\pi}}$$

(IV.22)

where N_A is the Avogadro constant and R_f is the roughness factor. D_{ac} is the diffusion coefficient of HAc estimated to 1.24×10^{-5} cm^2 s^{-1} at room temperature **[9]**. The roughness factor is defined as the real surface area to the geometric surface area ratio. In the present study, all the working surfaces were ground with SiC papers up to 1200 grit finish, which approximately corresponds to a roughness factor of 5. The maximum surface concentration was evaluated one second ($t = 1$ s) after the steady-state condition is achieved. This was made by incorporating the values of the surface coverage of **Figure IV.13** into equation (IV.22). The results are featured in **Figure IV.16**. It is unsurprising that the number of adsorbed HAc molecules is markedly increased with the bulk concentration of the same compound, which is in agreement with the important enhancement of the cathodic reaction rate revealed by the potentiodynamic results. The respective trends of the isotherm and the surface concentration also indicate that a monolayer adsorption of HAc molecules is most likely taking place, i.e. contact adsorption **[27]**. The adsorption of acetic acid in its undissociated form on top of adsorbed water molecules was also envisaged **[27, 30]**. This alternative adsorption

process would involve water hydrogen-bonding interaction with the carbonyl group of the HAc molecule.
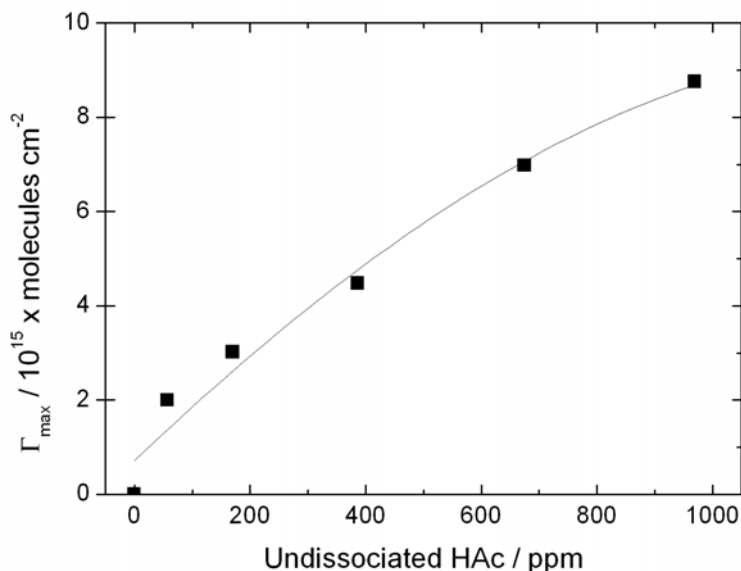
Figure IV.16. *The dependence of the maximum surface concentration of undissociated HAc on the bulk concentration of this compound in 1 bar CO$_2$-saturated 17 mM NaCl solutions at E = -600 mV$_{SCE}$. pH 3.5, room temperature. Unstirred conditions.*

IV.5. Role of Acetic Acid in the Overall Cathodic Reaction

IV.5.1. Acetic acid Acting as a Buffer

The fact that the cathodic polarization behaviour was fairly similar in the vicinity of E$_{corr}$ regardless of the presence of acetic acid indicates that the adsorption is not accompanied by a "direct" charge transfer process between the HAc molecules and the electrode surface. It was also found that the presence of HAc even at high concentrations does not cause the hydrogen suppression, thereby meaning that the rate of HAc chemisorption in the hydrogen region is a very slow process [27]. Similarly, no (or negligible) charge transfer was detected between the chemisorbed molecules of HAc and the active surface. In view of the elements discussed thus far, undissociated HAc would therefore not act more than a buffer via its ability of proton-delivering compound, and thus preserving the pH at the electrode surface [31]. The resistance to

pH change, particularly in the vicinity of the corroding surface, is quantitatively measured via the buffer capacity of acetic acid. In the present range of pH, the buffer capacity of HAc can be approximated by [32]:

$$C_{buffer} = 2.303 \times \left[H^+ \right] \times \left(1 + \frac{K_{ac} HAc_0}{\left(K_{ac} + \left[H^+ \right] \right)^2} \right)$$

<div align="right">(IV.23)</div>

As an illustration, **Figure IV.17** shows how the buffer capacity varies with pH for 600 ppm of total acetic species. Theoretically, a relative maximum of resistance to pH change is obtained when acetate and undissociated HAc are equimolar, i.e. pH = pK_{ac}. At pH typically lower than 4, acetic acid is mainly present in its undissociated form. Accordingly, the presence of HAc adsorbates with sufficient amounts onto the steel surface enables hydrogen evolution at much higher rates.
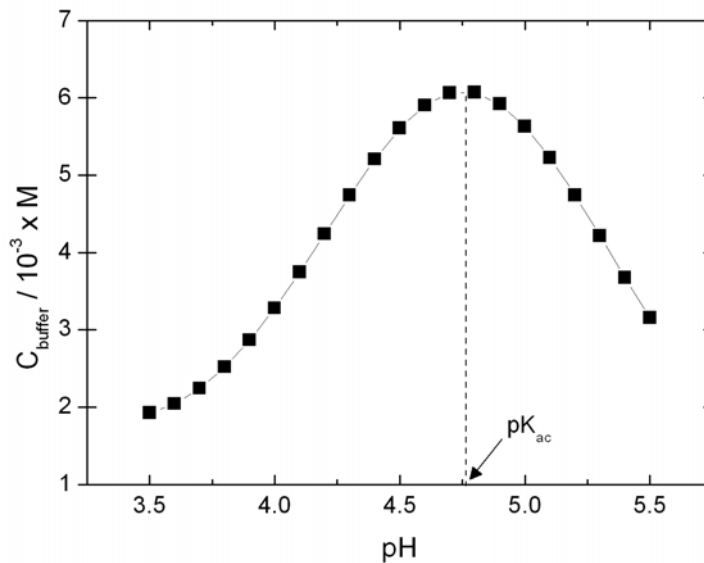
Figure IV.17. *Variation of the buffer capacity for 600 ppm of total acetic species with pH at room temperature.*

This interpretation is in line with the pure charge-transfer control observed at low cathodic polarizations (see comparison between i_L and i_{corr}, **Figure IV.7**), on the one hand, and with the retardation of the limiting current plateau at high concentrations of undissociated HAc (see curve D in **Figure IV.4**), on the other hand. The present

observations are also in agreement with a previous study of Singh and Gupta [33]. Indeed, the authors found that the cathodic reaction was fundamentally unaffected by changing either the concentration of the weak acid or the temperature of the system. They accordingly suggested a mechanism for hydrogen evolution reaction in HAc-containing solutions that was adopted in a later work [34]. According to their mechanism, Singh and Gupta interpreted the observed upward shift of the cathodic reaction rate in terms of the increase in molecular concentration of HAc. However, the proposed mechanism tacitly involves an electroactive participation of HAc, and an alternative route is therefore required.

IV.5.2.   Proposal for a Mechanism

Following a classical approach, the hydrogen evolution reaction is assumed to occur via a pathway that initially involves the discharge of a soluble oxidant on an active site of the surface, i.e. Volmer step. Since in HAc-containing medium the discharge of HAc molecule is unlikely, an apparent Volmer step would be rather preceded by the fast dissociation of the adsorbed HAc molecule. Garsany et al. argued that HAc dissociation can be too fast to allow the distinction of the reduction of free proton from the direct reduction of HAc [13]. Once the H^+ ion has been reduced, the Volmer step can be followed by either an electrochemical desorption (Heyrovsky step) or a recombination of two adsorbed hydrogen atoms (Tafel step). It follows that the rate-determining step is established by the strength of the H_{ad}–metal surface bond, and the energetic balance of the overall mechanism is determined by the nature of the substrate [35]. The mechanism proposed by Singh and Gupta considers Tafel step rather than the Heyrovsky step. The recombination of adsorbed hydrogen atoms does not involve any charge-transfer, thus implying a chemical control. This recombination process however appears to hold only at very low concentrations of HAc, where a mixed charge/chemical control was observed. On the other hand, the recombination process becomes a controlling step only if the degree of coverage of the surface by hydrogen atoms remains small. This is unlikely since the influence of the overvoltage upon the Volmer step leads to an increase of the degree of coverage in order to reach the steady-state condition [36]. When HAc is present in the medium with reasonable

concentrations, Tafel step can be disregarded and the overall cathodic reaction is likely to follow Volmer-Heyrovsky route instead of Volmer-Tafel route proposed by Singh and Gupta. In addition, the hydrogen evolution reaction via Volmer-Heyrovsky route has a theoretical Tafel slope of -118 mV/decade at room temperature [37], which agrees well with the experimental b_c. The Volmer-Heyrovsky route could hence be the following:

$$\left(HAc\right)_{ad} \rightleftharpoons H^+ + Ac^- \overset{+e^-}{\rightleftharpoons} H_{ad} + Ac^-; \ Volmer \ step \tag{IV.24}$$

$$H_{ad} + H^+ + e^- \rightleftharpoons H_2; \ Heyrovsky \ step \tag{IV.25}$$
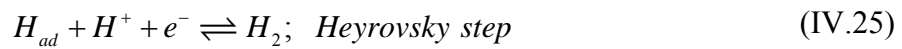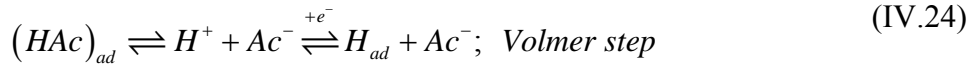
IV.6. Corrosion Scaling in CO₂/HAc Brine

One of the difficulties that may arise when predicting CO_2 corrosion rate is related to the formation of corrosion scales. In oxygen-free CO_2 saturated medium, most of the research efforts indicate that solid iron carbonate is the main compound of corrosion product scales. Protectiveness as well as growth rate of $FeCO_3$ film are factors that depend primarily but not exclusively on the environmental conditions prevailing. At elevated temperature, precipitation of solid $FeCO_3$ proceeds at high rates and very dense and protective films can be formed even at low supersaturation. The "worst case" for CO_2 corrosion is obtained when poorly protective iron carbonate films are formed. In this case, the corrosion process undermines the newly growing film faster than precipitation can follow. This is particularly encountered at room temperature when precipitation rate is very slow, thus leading to the formation of porous and unprotective films even at high levels of supersaturation. The growth rate of iron carbonate in units of meter per second can be predicted by rearranging the rate equation of Van Hunnik et al. (Eq. II.32, Chapter II):

$$R_{gr} = \frac{M_{FeCO_3}}{\rho_{FeCO_3}}.k_{gr}.K_{sp}.\left(S-1\right)\left(1-S^{-1}\right) \tag{IV.26}$$

Here M_{FeCO3} and ρ_{FeCO3} stand for the molar mass (116 g mol^{-1}) and the density (3800 kg m^{-3}) of solid iron carbonate, respectively. In the above equation, the solubility product is expressed in molality units, i.e. mole^2 kg^{-2}.

In order to assess whether HAc influences the protectiveness and morphology of FeCO$_3$ corrosion product film, two identical X65 coupons of 2.5 cm x 2.5 cm were left corroding freely during 30 days in respectively HAc-free and 600 ppm HAc- containing solutions under 1 bar of CO$_2$. The pH of the two solutions (150 mL) was initially adjusted to 3.5. No HAc replenishment was made thereafter. Iron (II) content was determined by spectrophotometry at 508 nm as ortho-phenanthrolin complex. The results are featured in **Figure IV.18**.
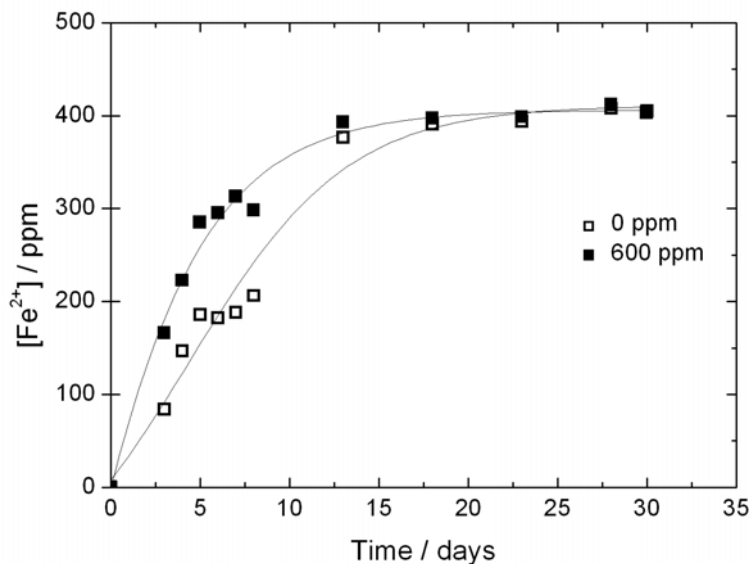
Figure IV.18. *Experimental iron (II) content-time curves in respectively HAc-free and 600 ppm HAc-containing solutions saturated with 1 bar CO₂. 17 mM NaCl, initial pH 3.5, room temperature. No HAc replenishment was made thereafter.*

The two iron (II) content-time curves exhibit a similar general trend regardless of the presence of HAc. Once again, the dissolution of carbon steel in these conditions seems to be rather a matter of what is generically referred to as CO$_2$ corrosion. It is also seen that the two curves level off at roughly 400 ppm up from the second half of the test duration, thus indicating saturation behaviour. At the end of the experiment, the

measured pH of the two solutions was about 4, which corresponds to a supersaturation of 43. A rough calculation by means of equation (IV.26) would predict an average growth rate of $FeCO_3$ film of 0.1 mm/year, accordingly.

Figures IV.19 and **IV.20** show SEM front view images of the two samples before and after removing the corrosion product layers. These layers were stripped using inhibited HCl solution. In both cases, the resulting films were soft and easily peeled off from the sample surface. Even though the both corrosion layers exhibited a poor protectiveness, the film formed in HAc-containing medium was nevertheless shown to be much less porous than the one formed in the absence of HAc. One could therefore postulate that HAc caused corrosion products to precipitate as fine grain particles. This is a case which is commonly observed in acidic solutions **[38]**. Preserving the pH of the environment adjacent to the steel surface due to the buffer capacity of adsorbed HAc could be at the origin of this prominent difference. On the other hand, visual inspection showed that the film formed in HAc solution did not a priori present cracks right after having removed the sample from the test solution. It was therefore concluded that the cracks observed in **Figure IV.19 (b)** were simply formed upon drying in the oven, and that the pronounced porous microstructure of the film formed in HAc-free medium prevented the formation of such cracks. Examination of the samples after removing the corrosion layers showed a rough and uniformly corroded surface in both cases.

(a)	(b)
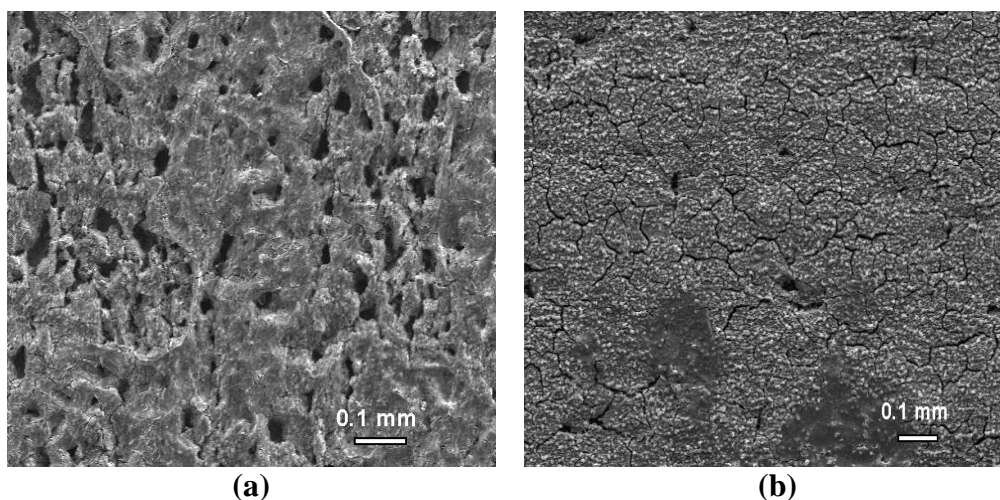
Figure IV.19. SEM front view images of X65 samples after 30 days immersion in HAc-free (a) and 600 ppm HAc-containing (b) solutions saturated with 1 bar CO₂. 17 mM NaCl, initial pH 3.5, room temperature. Magnification = 50X.

(a)   **(b)**
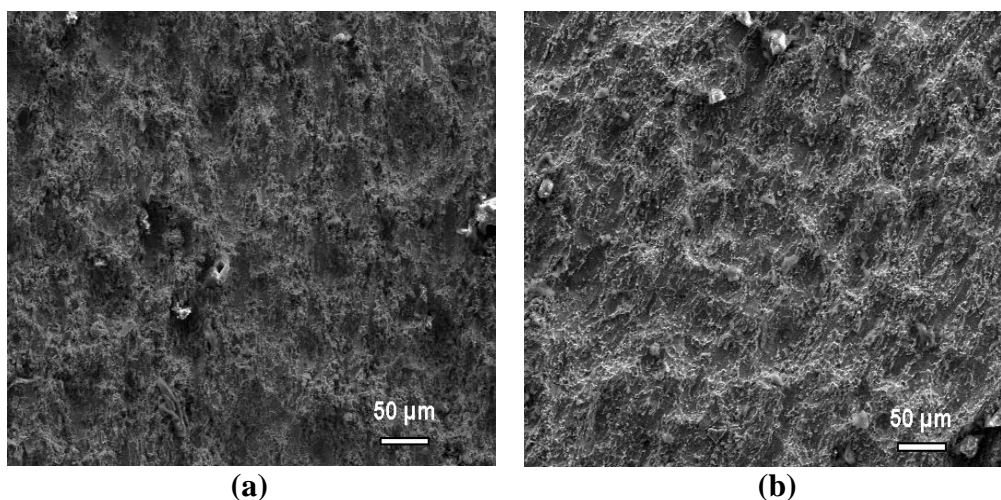
Figure IV.20. SEM front view images of sample surfaces after removing the corrosion product layers. 1 bar CO_2-saturated 17 mM NaCl with 0 ppm (a) and 600 ppm (b) of HAc, initial pH 3.5, room temperature. Magnification = 100X.

Cross-sectional analyses as well as the corresponding EDS patterns of the two corrosion films are shown in **Figures IV.21** and **IV.22**, respectively.

(a)   **(b)**
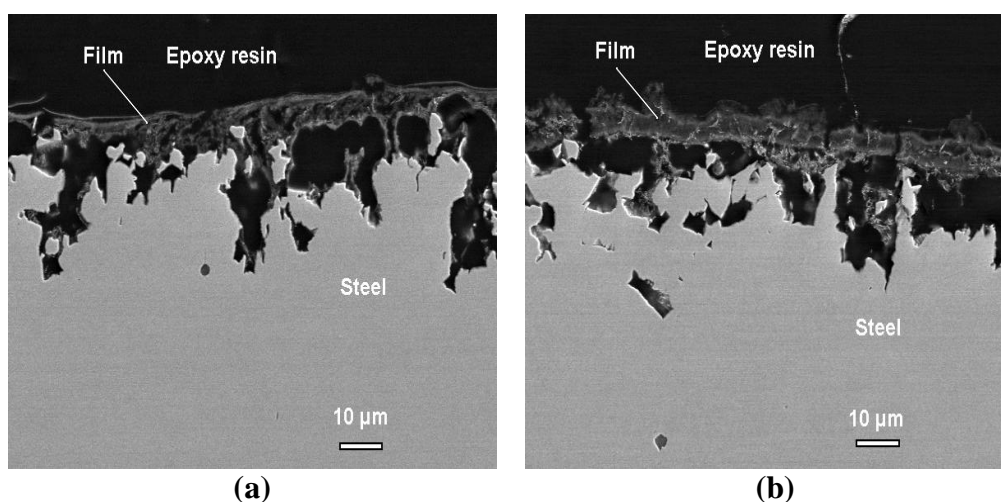
Figure IV.21. SEM images of sample cross-sections. 1 bar CO_2-saturated 17 mM NaCl with 0 ppm (a) and 600 ppm (b) of HAc, initial pH 3.5, room temperature. Magnification = 500X.

A rather thin film with a thickness estimated to 8 μm (i.e. 0.09 mm/year) was observed in both cases. This is in good agreement with the predicted growth rate (0.1 mm/year). Also, one would anticipate from EDS patterns that iron carbonate is the main compound of the resulting films. A very small quantity of calcium (Ca) was also found in the film formed in HAc solution. Overall, no appreciable effect of HAc on the composition of

the corrosion film was observed at least in the experimental conditions of the present study.
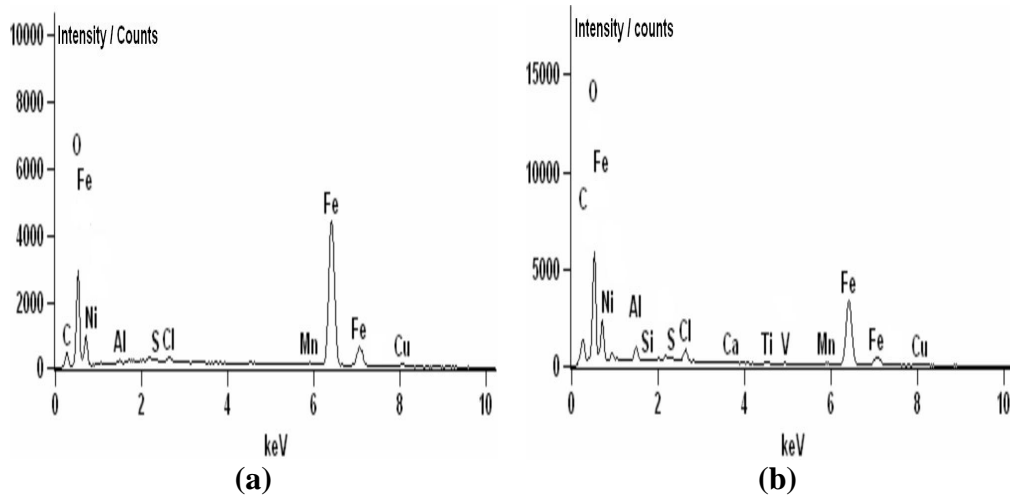
Figure IV.22. *EDS patterns of the two corrosion films. 1 bar CO₂-saturated 17 mM NaCl with 0 ppm (a) and 600 ppm (b) of HAc, initial pH 3.5, room temperature.*

None of the above surface examinations revealed pitting tendency. However, few but deep pits were systematically observed in the presence of HAc at higher initial pH. For instance, **Figure IV.23** shows typical pitting morphologies observed on X65 sample immersed during 30 days in 600 ppm HAc solution at an initial pH of 5.5.
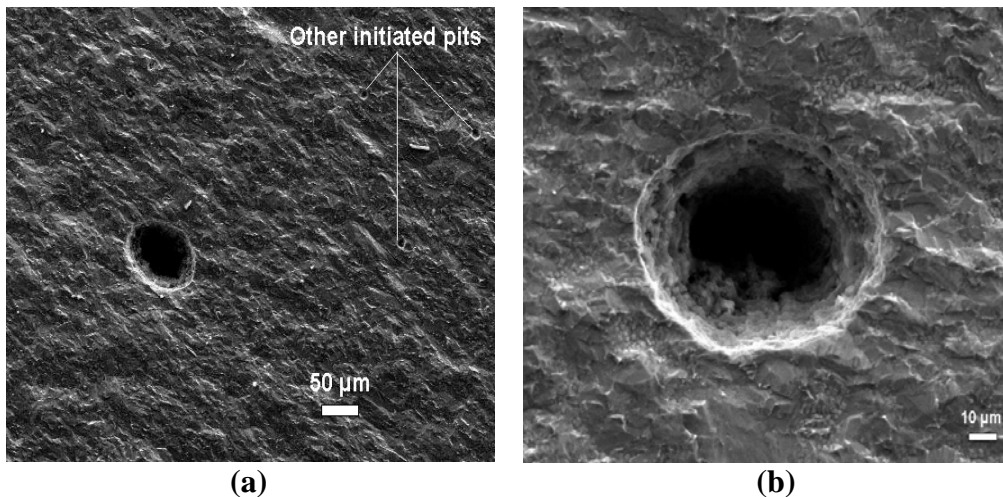
Figure IV.23. *Pitting morphologies on X65 sample immersed during 30 days in 600 ppm HAc-containing solution. 1 bar CO₂-saturated 17 mM NaCl, initial pH 5.5, room temperature. Magnification = 100X (a), 500X (b).*

This seems to agree with other observations reported in the literature concerning the pitting behaviour of X65 pipeline steel, where HAc was found to promote the formation of deep corrosion pits at room temperature to the detriment of an inhibition of the general corrosion [6].

IV.7. Conclusions

Although the direct reduction of acetic acid was thermodynamically shown to be a potential cathodic reaction, the electrochemical results of the present study did not show a clear sign of an electroactive participation of adsorbed HAc molecules. The significant increase of the cathodic reaction rate observed in the presence of acetic acid appears to be rather related to the cathodic reduction of free proton. Adsorbed HAc molecules would therefore act as a local proton reservoir. This is likely to preserve the pH of the micro-environment adjacent to the steel surface by minimizing the limiting current induced by the mass transfer of H^+ from the bulk solution. The buffering effect of HAc also seemed to have an effect on the compactness of corrosion product films as revealed by SEM analyses. On the other hand, neither polarization curves nor EIS measurements did show any appreciable effect of HAc on the anodic reaction mechanism. The present results cannot give a direct answer concerning the inhibited rate of the anodic reaction observed in the vicinity of E_{corr} in the presence of HAc, but suggest that the adsorbed HAc molecules render the steel surface less accessible for carbonic species to drive the anodic dissolution. In these conditions, the uniform dissolution of carbon steel would then be more liable to be a matter of what is generically referred to as CO_2 corrosion.

In summary, the kinetic behaviour of carbon steel in such brine indicates that the overall effect of the HAc is a balance between a boosted cathodic rate and an inhibited anodic one without any significant increase of the uniform corrosion current. This scenario seems then to be consistent with either field observations or laboratory studies of localized attack of carbon steel in the presence of both CO_2 and HAc. It is also conceivable that non-uniformly adsorbed molecules of HAc induce a substantial difference in pH between anodic and cathodic sites. The acting potential gradient, i.e.

the driving corrosion force, between the two sites could therefore be large enough to allow the formation of deep pits as observed in the present study. The pitting behaviour particularly observed in the presence of HAc has prompted us to study the role of this organic compound in the mechanisms of propagation and stifling of localized attacks. This issue will be insightfully addressed in the next chapter.

References

[1]   R. Nyborg, CORROSION\02, Paper no. 02233, NACE, 2002.

[2]   A. Dugstad, R. Nyborg, M. Seiersten, CORROSION\03, Paper no. 03314, NACE, 2003.

[3]   A. Anderko, R. Young, CORROSION\99, Paper no. 31, NACE, 1999.

[4]   I. Khan, P. Brimblecombe, S. Clegg, J. Atmospheric Chem., 22 (1995) 285.

[5]   B.J. Johnson, E.A. Betterton, D. Craig, J. Atmospheric. Chem., 24 (1996) 113.

[6]   E. Gulbrandsen, K. Bilkova, CORROSION\06, Paper no. 06364, NACE, 2006.

[7]   S. Nešić, J. Postlethwaite, S. Olsen, Corrosion, 52 (1996) 280.

[8]   P. Delahay, J. Am. Chem. Soc., 74 (1952) 3497.

[9]   S. Nešić, M. Nordsveen, R. Nyborg, A. Stangeland, CORROSION\01, Paper no. 40, NACE, 2001.

[10]   W. Moore, *"Basic Physical Chemistry"*, Prentice-Hall, Inc., USA (1983).

[11]   G.H. Kelsall, R.A. Williams, J. Electrochem. Soc. 138 (1991) 931.

[12]   R. Reffas, R. Sabot, C. Savall, M. Jeannin, J. Creus, P. Refait, Corr. Sc., 48 (2006) 709.

[13] Y. Garsany, D. Pletcher, B. Hedges, CORROSION\02, Paper no. 02273, NACE, 2002.

[14] Y. Garsany, D. Pletcher, B. Hedges, J. Electroanal. Chem., 538-539 (2002) 285.

[15] Y. Garsany, D. Pletcher, B. Hedges, CORROSION\03, Paper no. 03324, NACE, 2003.

[16] Y. Garsany, D. Pletcher, D. Sidorin, Corrosion, 60 (2004) 1155.

[17] Y. Garsany, D. Pletcher, D. Sidorin, Corrosion, 63 (2007) 285.

[18] K.S. George, S. Nešić, Corrosion, 63 (2007) 178.

[19] G. Bech-Nielsen, Electrochim. Acta, 19 (1974) 821.

[20] J.-L. Crolet, N. Thevenot, A. Dugstad, CORROSION\99, Paper no.24, NACE, 1999.

[21] R. De Marco, Z.T. Jiang, D. John, M. Sercombe, B. Kinsella, Electrochim. Acta, 52 (2007) 3746.

[22] D. MacDonald, M.C.H. McKubre, J.O.M. Bockris, B.E. Conway, R.E. White, "*Modern Aspects of Electrochemistry*", Vol. 14, Plenum Press (1982).

[23] E. McCafferty, J. Corr. Science and Eng., 39 (1997) 243.

[24] F. Huet, R.P. Nogueira, B. Normand, H. Takenouti, ASM Handbook, "*Corrosion: Fundamentals, Testing and Protection*", Vol. 13A, ASM International, Materials Park, OH, 2003, p. 52.

[25] M. Keddam, O.R. Mattos, H. Takenouti, J. Electrochem. Soc., 128 (1981) 257.

[26] R.S. Gonçalves, N.M. Coradini, W.X. Olivera, Corr. Science, 33 (1992) 1667.

[27] A. Wieckowski, J. Sobkowski, P. Zelenay, K. Franaszczuk, Electrochim. Acta, 26 (1981) 1111.

[28] T. Takahashi, J.A. Bardwell, B. MacDougall, M.J. Graham, Electrochim. Acta, 37 (1992) 477.

[29] G.A. Zhang, Y.F. Cheng, Corr. Science, 51 (2009) 87.

[30] D.S. Corrigan, E.K. Krauskopf, L.M. Rice, A. Wieckowski, M.J. Weaver, J. Phys. Chem., 92 (1988) 1596.

[31]   T. Hurlen, S. Gunvaldsen, F. Blaker, Electrochim. Acta, 29 (1984) 1163.

[32]   A. Hulanicki, "*Reactions of acids and bases in analytical chemistry*", Ellis Horwood series, Halsted Press, Translation editor, M.R. Masson, 1987.

[33]   M.M. Singh, A. Gupta, Corrosion, 56 (2000) 371.

[34]   M.A. Veloz, I. González, Electrochim. Acta, 48 (2002) 135.

[35]   A.N. Correia, S.A.S. Machado, L.A. Avaca, Electrochem. Commun., 1 (1999) 600.

[36]   J. Koryta, J. Dvorak, L. Kavan, "*Principles of Electrochemistry*", 2nd ed., John Wiley & Sons (1993).

[37]   Y.-H. Xu, G.-R. He, X.-L. Wang, Intern. J. of Hydrogen Energy, 28 (2003) 961.

[38]   S. Tebbal, N. Hakerman, Corr. Science, 34 (1993) 1787.

Chapter V

Attack Behaviour in CO$_2$/HAc Brine

Table of Contents

V.1.   Introduction

Despite comprehensive studies have been devoted to the effect of HAc on the uniform corrosion in CO$_2$-containing media, rudimentary understanding however exists regarding the basic role of this organic compound in localized corrosion. This is of particular interest in the case of the so-called TLC which is recognized as the most severe form of internal corrosion encountered in wet gas transportation. The underlying mechanisms controlling TLC attacks are still not well understood, and this makes TLC phenomenon even more difficult to predict. The purpose of the present chapter is to go deeper in the analysis of the qualitative behaviour often found in actual situations of TLC phenomenon, that is, increasing corrosion rates and steep shrinkage after certain-not predictable - time delay. The focus is on how acetic acid influences the mechanisms of growth and stifling of localized corrosion attacks.

V.2.   Analysis of Electrochemical Noise

V.2.1.   Introduction

In practice, localized corrosion is at the root of most corrosion failures of facilities encountered in oil and gas fields. Pitting is one of the most destructive forms of localized corrosion that occurs at discrete sites of the metal surface exposed to an aggressive environment. While the rest of the exposed surface can remain largely free of corrosion, narrow pits are formed. This form of attack is more difficult to both predict and control than uniform corrosion due respectively to its stochastic nature, latent incubation and quick propagation. Indeed, initiated pits can propagate deeply into the metal and impair its properties that are to be preserved, thus rendering the equipment unserviceable. The stochastic nature (both in space and time) of pitting corrosion makes the phenomenon even more complex to study. With respect to this complexity, the electrochemical noise technique has been promoted as a tool for both corrosion science and corrosion engineering with unparalleled advantages compared with other classical

techniques. Electrochemical noise refers to the spontaneous fluctuations of current or potential. The study of these fluctuations has provided information about pitting phenomena. In particular, analysis of individual noise transients can give valuable insight into fundamental corrosion mechanisms.

V.2.2. Features of Potential and Current Fluctuations

Typical time records of the potential and current fluctuations generated on freely corroding carbon steel are shown in **Figures V.1** and **V.2**. The tests were performed in HAc-free and HAc-containing solutions of 17 mM NaCl saturated with 1 bar CO$_2$ at pH 3.5 and room temperature. The patterns were measured in flat configuration (i.e., zero pit depth) using the assembly of **Figure III.5** after 2 hours immersion. In the absence of HAc, the noise signals were found to exhibit stochastic fluctuations with low frequency and small amplitudes. No sharp potential or current transients were however observed.
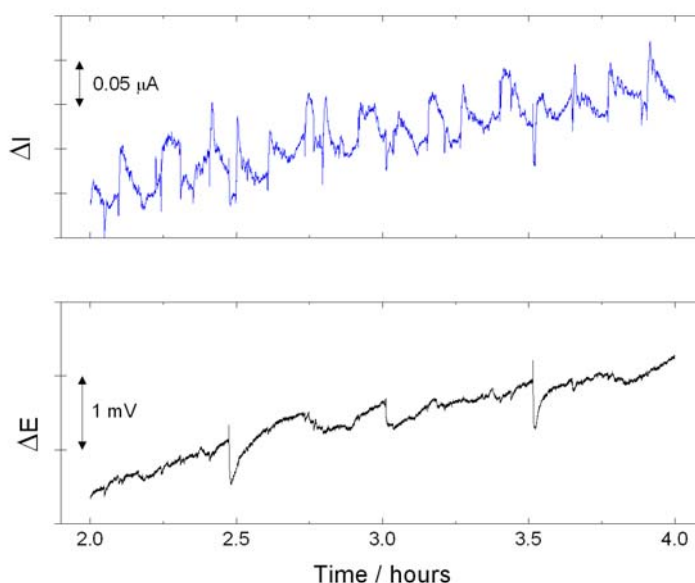
Figure V.1. *Time records of current and potential for a freely corroding X65 electrode in 17 mM NaCl solution saturated with 1 bar CO$_2$ at pH 3.5 and room temperature.*

Upon addition of HAc, the noise signals fluctuated in more irregular patterns with higher frequency and amplitudes, thus suggesting a higher local electrochemical activity.
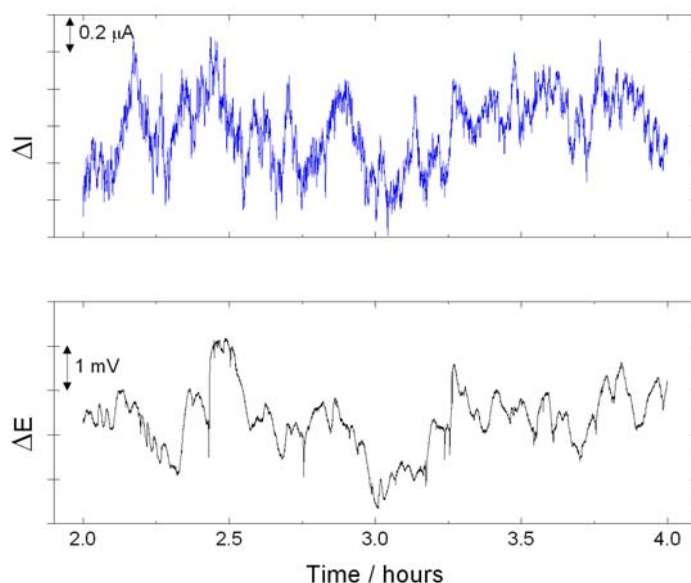
Figure V.2. *Time records of current and potential for a freely corroding X65 electrode in 17 mM NaCl and 600 ppm HAc solution saturated with 1 bar CO₂ at pH 3.5 and room temperature.*

V.2.3.   Analysis in the Time Domain

Metastable pitting is generally associated with the appearance of typical current transients that are well described by current growth laws. Regardless of the presence of HAc, careful examination of a large population of metastable pitting events showed that transients did not all have the same time evolution. Most of the events decayed rapidly, but there were also a significant number of events, which decayed more slowly, or were virtually rectangular in form. Typical current transients generated on freely corroding X65 steel in CO_2/HAc brine are shown in **Figure V.3**. Analysis of the shape variability nevertheless revealed a pattern that was the most frequently observed in the present conditions. Also, shown in **Figure V.3** is an expanded time scale featuring an individual metastable pit current spike. The latter is characterized by a quick rise followed by an exponential recovery to the baseline current. Such electrochemical noise signature was reported for A516 carbon steel in a brine of sodium bicarbonate and sodium chloride, and is known to display the typical shape of metastable events on carbon steel **[1]**. This also indicates that metastable pitting on carbon steel is quiet different from that

observed on iron and stainless steels **[2]**. The localization of the dissolution inherent in localized corrosion implies a spatial separation of the anodic and cathodic reactions, which leads to the formation of a galvanic couple. Since the two electrodes were coupled through a ZRA with a zero bias voltage applied between them, the observed current transients were consequently the galvanic currents induced by the steel surface condition and local chemistry differences between the two electrodes. It has been shown that the sharp rise of the current is indicative of a pit initiation **[3, 4]**. According to the principle of galvanic coupling, the total charge (Q_{pit}) generated during the pit initiation must be simultaneously consumed by the cathodic reaction occurring on the boldly exposed surface. However, the exponential recovery of the current suggests that the charge balance is not immediately fulfilled. A first explanation would be that the freshly initiated pit undergoes a progressive repair due to a change in the chemistry inside the pit, thereby implying a mass transport control. A second rationalization would be that the cathodic reaction is not fast enough to consume all the charge released from the freshly initiated pit, thus suggesting an IR-drop control. It is therefore anticipated that a part (i.e., non-faradaic charge) of the total charge is used for the charging of the double layer capacitance. The slow discharging of this last would then explain the slow current decay observed in **Figure V.3**. The overall charge balance must hence obey the following balance **[1]**:

$$\underbrace{Q_{pit}}_{\text{pit charge}} = \underbrace{Q_{cath}}_{\text{cathodic charge}} + \underbrace{C_{dl}.\Delta E}_{\text{capacitive charge}} \qquad (V.1)$$

In the above equation, C_{dl} and ΔE denote the double layer capacitance and the potential drop, respectively. When a metastable growth is involved, the total charge consumed during the time period between the pit initiation and the peak pit current can be calculated by integrating the current-time curve. The metastable pit size is then estimated using a faradaic relationship assuming hemispherical pit morphology:

$$r_{pit} = \sqrt[3]{\frac{3A_w}{2\pi nF\rho} . \int_{t_0}^{t_{peak}} \left(I(t) - I_{baseline} \right) dt} \qquad (V.2)$$

where r_{pit} is the pit radius, t_0 is the time at which the pit initiates, and t_{peak} is the time at which the peak current is reached. The peak pit current, denoted hereafter as I_{peak}, is

defined as the maximum pit current minus the baseline current. Faradaic calculations done on metastable current data of **Figures V.1** and **V.2** yielded pit radii at the peak pit current ranging between 0.1 and 6 μm. For instance, integration of the linear portion of the current-time curve shown in the inset of **Figure V.3**, gave a pit radius at the peak current of 3.25 μm.
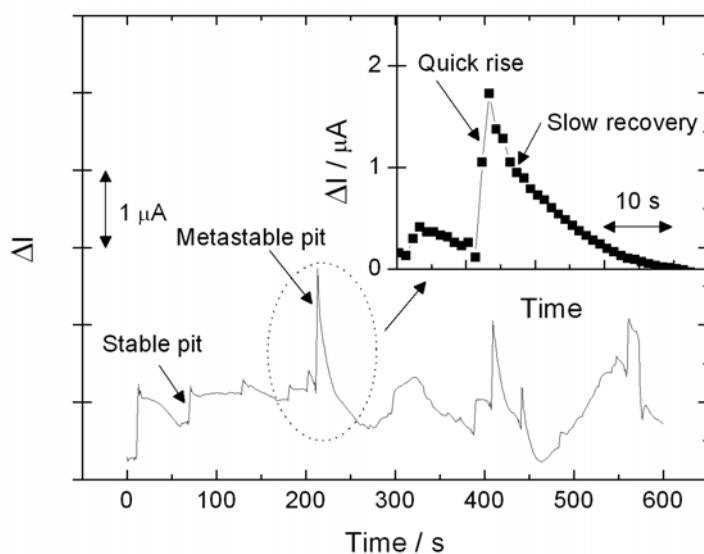
Figure V.3. Typical current transients generated on freely corroding X65 electrode in CO₂/HAc brine at room temperature. Also shown is an expanded time scale featuring an individual metastable pit current spike.

V.2.4. Analysis in the Frequency Domain

From the expanded time scale of **Figure V.3**, it can be seen that the elapsed time from the peak pit current to the baseline current is typically much larger than the elapsed time from the pit initiation to the peak pit current. Also, the current rise is so fast so that it is difficult to discern the pit initiation from its metastable growth. This observation has prompted us to consider the growth stage as overlapped by the initiation stage. Over the lifetime of such elementary transient, the following mathematical relationships can therefore adequately describe the current fluctuation:

$$I(t) = 0 \ ; \ t < 0 \qquad\qquad (V.3)$$

$$I(t) = I_{peak} . \exp\left[-\frac{t}{\tau} \right] \ ; \ t \geq 0 \qquad\qquad (V.4)$$

where τ is the recovery time. The Fourier transform of the above fluctuation into the frequency domain can be written as:

$$F(f) = \int_{-\infty}^{+\infty} I(t) . \exp(-j2\pi ft) . dt \qquad\qquad (V.5)$$

with f being the frequency in Hertz. Supposing that pits are uniformly distributed along the metal surface, that is, considering that the number of metastable pits N(T) observed during a period T evolves linearly with the area of the exposed surface (S), the power spectrum density ψ_I, also denoted as PSD, is simply given by [5, 6]:

$$\Psi_I(f) = 2 . \lim_{T \to +\infty} \frac{N(T) . |F(f)|^2}{T} = \frac{2\lambda S I_{peak}^2 \tau^2}{1 + 4\pi^2 \tau^2 f^2} \qquad\qquad (V.6)$$

Here, λ denotes the average initiation rate of metastable pits per unit area or the fluctuation rate. At frequencies typically far below $1/2\pi\tau$, ψ_I becomes independent of the frequency and the noise spectrum is referred to as "white" noise. That is:

$$\Psi_I = 2\lambda S I_{peak}^2 \tau^2 \qquad\qquad (V.7)$$

Inversely, when the frequency is far larger than $1/2\pi\tau$, then:

$$\Psi_I(f) = \frac{\lambda S I_{peak}^2}{2\pi^2} . f^{-2} \qquad\qquad (V.8)$$

The roll-off frequency (f_c) is calculated by equating expressions (V.7) and (V.8), that is $f_c = 1/2\pi\tau$. More generally, the power spectrum density exhibits f^α behaviour. The parameter α is commonly called the roll-off slope, which depends on the transient pattern and is believed to reflect the type of corrosion attack [7-9]. For such a type of transient as represented in **Figure V.3**, equation V.7 indicates a theoretical slope of -2.

To examine quantitatively the influence of HAc on the susceptibility of carbon steel to metastable pitting, the current noise data were transformed into the frequency domain using Fourier Power Spectrum transform (FPS). Data de-trending was performed by a linear fitting method prior to each FPS conversion to exclude eventual DC components. **Figure V.4** shows the respective current PSD plots of the electrochemical noises of **Figures V.1** and **V.2**. On the whole, the current PSD increased in the presence of HAc as a result of the higher fluctuation rate (λ) and the higher transient amplitude (I_{peak}) observed in the time domain. In both cases, the noise spectra were shown to exhibit f^α behaviour in the high frequency range with the values of α in agreement with the theoretical slope. Since the two slopes of the PSD were fairly the same, it is likely that the pit initiation kinetics did not change remarkably in the presence of HAc. The other feature to be noted is the significant increase of the recovery time upon addition of HAc to the corrosive medium. Indeed, f_c values showed a shift of τ from 12 s in HAc-free solution to 24 s in the presence of 600 ppm of HAc. The recovery time is indicative of the rate at which the metastable current decays to its baseline value. Regardless of whether the exponential recovery bears on the pit repair or the discharging of the interfacial capacitance, the increase of the transient variable τ suggests that metastable pitting events are more sustained in the presence of HAc.
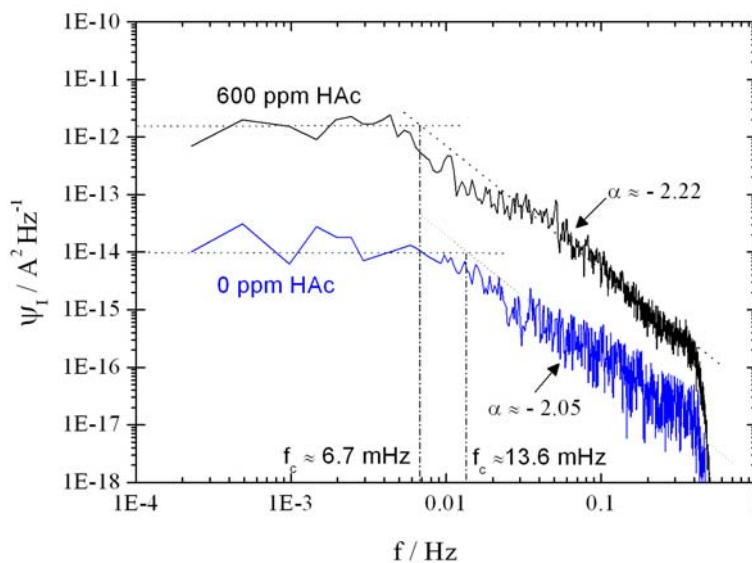
Figure V.4. *The current PSD plots calculated from the noise data of Figures V.1 and V.2.*

V.3. Kinetic Behaviour of a Single Pit in CO₂/HAc Brine

V.3.1. Introduction

The current measured from a corroding electrode may come from several pits with unknown active pit surface area. This fact points to the need for other approaches to alleviate this ambiguity. One alternative technique consists of studying a single attack in naturally simulated pit environments. Multiple pits are therefore avoided, and only the dissolution kinetics of the active pit is investigated. In the section hereafter, stable pit growth has been emphasized much more directly and quantitatively. A thorough investigation was undertaken using artificial pit electrode assembly to probe the effect of acetic acid on pit behaviour. The focus was on how acetic acid hinders pit growth. Another important goal was to better define whether pit growth is kinetically, ohmically, mass transport controlled or some combination thereof may emerge.

V.3.2. Foreword on the Artificial Pit Setup

Unless specifically mentioned, the set of measurements consisted of pit propagation experiments performed using the asymmetric assembly schematically illustrated by **Figure III.5**. The specimen was positioned vertically in the test cell with the electrode surfaces facing upwards. All measurements were carried out in a large 2 liters cell to prevent any significant depletion of either free proton or undissociated HAc in the bulk. It must be emphasized that the lateral walls inside the pit consisted of insulating epoxy resin; only the pit bottom was then made of steel. The electrochemical measurements were carried out on the large outer surface and the inner artificial pit electrodes connected through the ZRA by applying a zero-voltage difference between them. Real-time records of the current flowing between the coupled electrodes as well as their coupled potential measured against a saturated calomel reference electrode with the help of a Luggin capillary probe located at the pit mouth were then simultaneously measured. The electrical connections of the ZRA setup were kept in such a way that a net anodic current to the inner electrode is reported as positive. Due to the 100 fold surface ratio, the potential of the couple was approximately equal to that of the outer large one, which means that whenever the electrodes were coupled by the ZRA, the

potential value sensed was assimilated to the corrosion potential of the outer large electrode. In Chapter IV, we have emphasized that the kinetic behaviour of X65 carbon steel in CO$_2$/HAc brine indicates that the overall effect of acetic acid is a balance between a boosted cathodic branch and a depressed anodic one, with no uniform corrosion current increase related to the presence of HAc. As a consequence, the corrosion potential was shown to increase monotonically with HAc concentration. The constant supply of fresh solution indeed yielded a larger range of potential shift. This scenario appears to be consistent with field and laboratory observations of localized attack of carbon steel in the presence of both CO$_2$ and HAc. For the aims of the present section, the important effect of the presence of HAc is the shift of the corrosion potential to less negative values.

V.3.3.   Effect of Acetic Acid on Pit Growth

The role of HAc on the pit growth has been evaluated taking advantage of the specific experimental arrangement described above. If no preferential attack of the artificial pit takes place, the current is expected to remain close to zero, because of the 0 V applied by the ZRA. This is what was actually observed in the absence of HAc even in the case of pre-initiated pits as shown in **Figure V.5**. In comparison, the introduction of HAc even at small concentrations induced an always positive current, monotonically increasing with the acid concentration. The fact that the pre-initiated pit did not start growing in the absence of HAc is strong evidence that geometric constraints only are not enough to trigger pitting in CO$_2$ environments, at least in the experimental conditions of the present study. On the other hand, even small quantities of HAc seem to be sufficient to trigger and sustain pit growth. This can be ascribed to the combined effect of geometric constraints and the presence of HAc. As seen in the previous chapter, the presence of HAc strongly enhanced the cathodic activity. Inside the pre-initiated pit, the acid is more rapidly depleted because of mass transport limitations that establish a HAc concentration gradient between the artificial pit surface and the outer one. This is confirmed from **Figure V.5**, since the current is lower for higher magnet rotation speeds that increased HAc supply to the artificial pit, hence reducing the potential difference between the pit and the outer surface. It is worth noticing that a

coupled current density of about 1-2 A m^{-2} can be inferred from **Figure IV.4** for the fully depleted 0 ppm and the 600 ppm HAc solutions (I ≈ 3-6 μA for a 0.03 cm^2 surface as that of the artificial pit). This is about the order of magnitude of the values given in **Figure V.5**, which indicates that the artificial pit assembly gives reliable results.
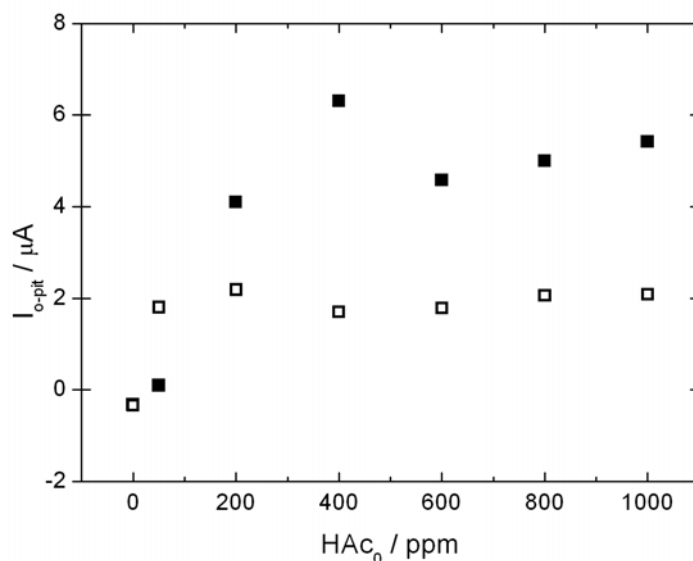
Figure V.5. Average values after 12 h of exposure, of the current flowing to a pre-initiated 2 mm depth artificial pit as a function of HAc concentration. 17 mM NaCl and 1 bar CO₂. (■) ω = 100 rpm. (□) ω = 200 rpm.

V.3.4.   Distribution of the Coupling Current

The idea that the HAc depletion inside the pit is at the origin of the pit growth leads to an important issue related to the monotonic evolution of the corrosion potential with HAc concentration. Shallow pits must be more easily fed by mass transport of HAc than deep ones. This entails that the potential difference, and hence the current should increase with the pit depth till a certain critical value for which the HAc depletion is complete inside the pit. Results shown in **Figure V.6** indicate that the pit growth is self-sustained only to a certain critical depth, beyond which the dissolution current vanishes. One of the possible reasons of this behaviour is the ohmic potential drop between the electrodes. For very deep pits, where the supply of HAc is strongly restrained, the ohmic drop may be a major component and the current would then be expected to

decrease, which is in agreement with the experimental results. After reaching a maximum at about 8 mm, however, the current drops too sharply to be only ascribed to the ohmic drop. This has been the matter of repeated experiments that always yielded the typical profile of **Figure V.6**. Another possible explanation would be the accumulation of corrosion products, or the presence of small hydrogen bubbles trapped inside the pit **[10, 11]**, which could act as a gas-cavity **[12]**. The described pit growth mechanism hence deviates in several ways from that of stainless steels and other passive metals. The pit growth is self-sustained only to a certain depth, and it occurs under anaerobic acid corrosion conditions, with no acidic cations present. The pK_a of the first hydrolysis step of Fe^{2+} is 9.6, compared to 2.2 for Fe^{3+} **[13]**. Since the acid is consumed inside the pit, a local alkalinisation is rather expected to occur, which would also contribute to hinder the dissolution at the pit bottom as a result of $FeCO_3$ precipitation. These results suggest that a real pit may grow spherically until a certain radius is reached, followed by opening of the pit mouth and lateral growth, which is the morphology observed in laboratory tests **[14]** and in actual TLC cases **[15]**.
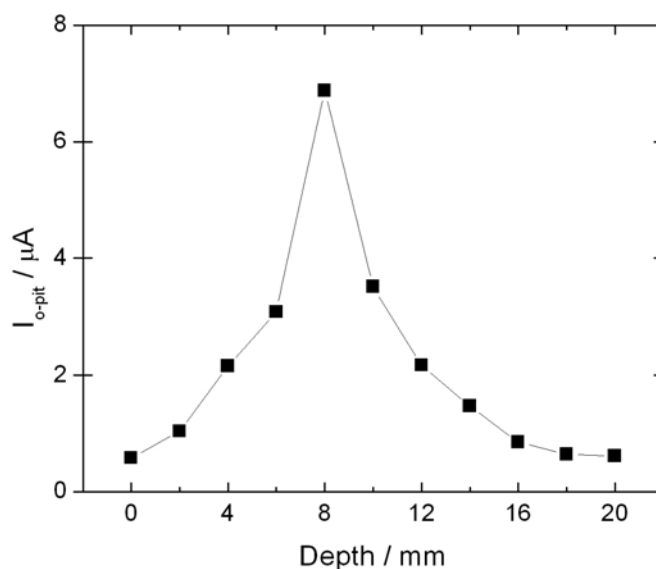
Figure V.6. *Average coupling current vs. pit depth in 17 mM NaCl, 600 ppm HAc and 1 bar CO₂.*

V.3.5.   Distribution of the Potential Drop

The two electrodes depicted in **Figure III.5** being of the same material and exposed to the same electrolyte, the corrosion potential is a priori expected to be the same for the outer and the inner electrodes so that a mean current value close to zero is supposed to be sensed by the ZRA setup. This is what effectively happens for zero pit depths or even shallow pits. Nevertheless, for deeper pits (typically > 1 mm), a net current different from zero was always and reproducibly sensed. Furthermore, this current being always positive indicated that the small inner electrode was anodically polarized by the outer one. This means that the anodic polarization inside the pit is actually changed in the sense of easier dissolution, this change being caused by the local fluctuations of the environment inside pit. The potential difference between the outer and the inner electrodes is not straightforwardly accessible since the ZRA imposes a zero bias voltage between the two electrodes. It can nevertheless be evaluated by intermittently disconnecting the ZRA for short time intervals, as illustrated in **Figure V.7** taking as an example the case of an 8 mm depth artificial pit.
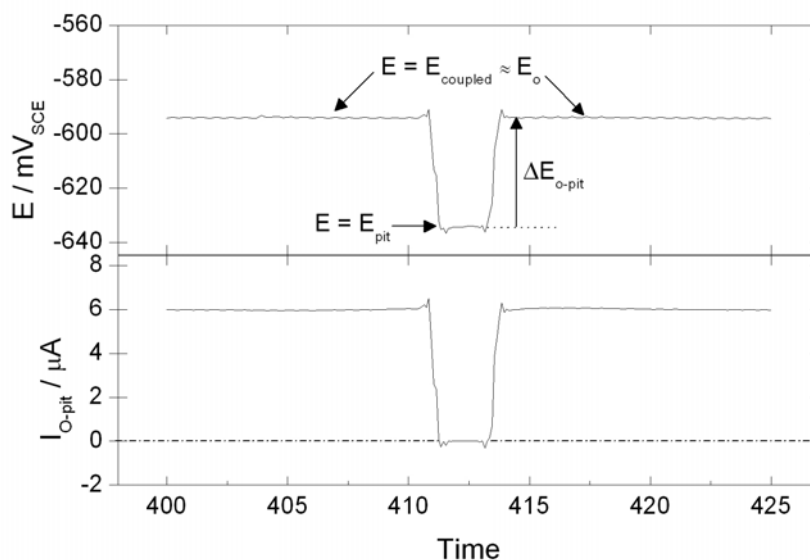
Figure V.7. *Interrupting the ZRA connection for the determination of the potential difference between the outer large electrode (O) and the inner artificial pit electrode (pit) for the case of a 8 mm depth pit after 2 hours of immersion in 17 mM NaCl, 600 ppm HAc and 1 bar CO₂. Arbitrary time origin.*

During disconnection, the outer large electrode was kept out of the circuit and the system directly measured the potential difference between the reference electrode and the small inner one. This overall procedure allowed hence the potential difference between the pit bottom (as mentioned before, lateral walls were insulated) and the outer surface to be monitored as well as the current flowing between them. Since the interruption is short (few seconds), the concentration profiles approximate those of the coupled state, and the measured potential difference is not other than the polarization of the inner electrode plus the IR-drop. As expected, immediately after uncoupling the electrodes, the current fell to zero and the potential of the artificial pit dropped about 45 mV in respect with the coupled state in the case illustrated by **Figure V.7**. It is interesting to see that applying the 45 mV found in **Figure V.7** to the pH 3.5 curve in **Figure IV.14** would effectively correspond to a strong ca 15-fold depletion of HAc inside the pit. This is consistent with results from other works, where the concentration of free HAc, rather than pH, was shown to be a critical factor in CO_2 corrosion of X65 steel **[16**, **17]**. These results seem to be a sound although indirect corroboration of the basic idea that the potential drop illustrated in **Figure V.7** can be ascribed to the HAc depletion inside the artificial pit due to hindered hydrodynamic conditions. This scenario is expected to be dependent on the pit depth due to the increasing difficulty of supplying the reactant the deeper the pit is. One should hence expect an in principle monotonic increase of the potential difference till a given limit depth beyond which the acid would be completely depleted and the potential difference should reach a maximum. This issue is illustrated in **Figure V.8**. It can be seen that the potential difference (measured in each case after two hours of exposure to the corrosive solution) does not increase indefinitely. It goes through a maximum at 8 mm depth before slightly decreasing again. This seems consistent with the previous results of **Figure V.6**, where the dissolution rate has been shown to reach its maximum value at about 8 mm beyond which it sharply drops off. Similar behaviours have also been reported for iron **[18]** and steel **[19]** in NaAc/HAc buffer solution.
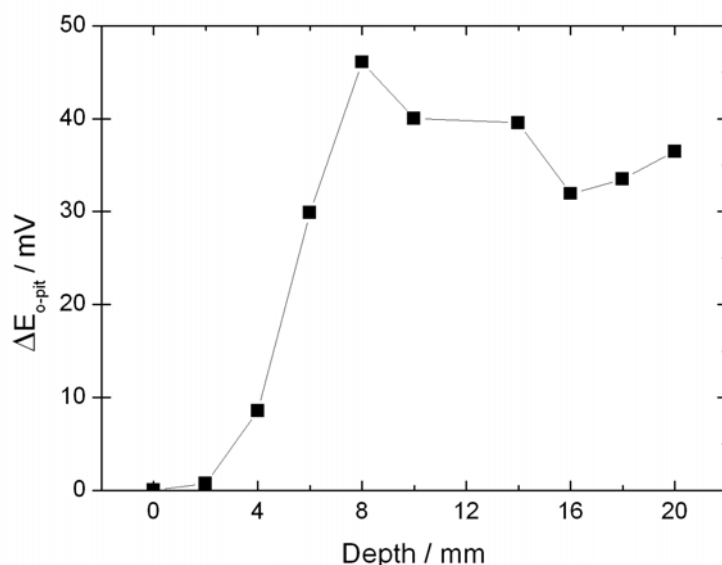
Figure V.8. *Potential difference between the outer large electrode and the artificial pit electrode as a function of the pit depth in 17 mM NaCl, 600 ppm HAc and 1 bar CO₂.*

V.3.6.   HAc Depletion - Experimental Validation Using Split Cell Technique

To validate the hypothesis of HAc depletion as the key parameter behind the electrochemical asymmetry between the inner and the outer electrodes, some specific measurements were carried out with a split-cell (see **Figure III.6**) in which two identical electrodes were placed in two identical compartments separated by a salt bridge, so that no geometric differences were present. The salt bridge is connected to both compartments through porous glass frits that allow ion migration but restrict bulk mixing of the two solutions. One of the compartments was filled with the same base solution of that in previous measurements, that is, CO_2 saturated (1 bar CO_2) 17 mM NaCl aqueous solution containing 600 ppm of HAc, the second being filled with different electrolytes depending on the experiment. **Figure V.9** depicts the current flow between the two electrodes in distinct conditions simulating no depletion (solutions were strictly the same in both compartments) and total depletions (no HAc was added in the second compartment). Also shown in the inset is the current flow in the condition of total depletion of HAc in both compartments. To simulate the pH gradient expected in the case x = 0, the pH of one of the two solutions was adjusted to 3.5. Results clearly

point out a net anodic polarization -resulting in a net anodic current - of the electrode exposed to the electrolyte simulating depleted conditions as seen in the figure (x = 0). It is worth noticing that regardless of the pH gradient, an expected ca zero current was also found between the two electrodes when the HAc concentration was set to the same value in both compartments, which is also consistent with the idea of HAc concentration gradient triggering the current flow.
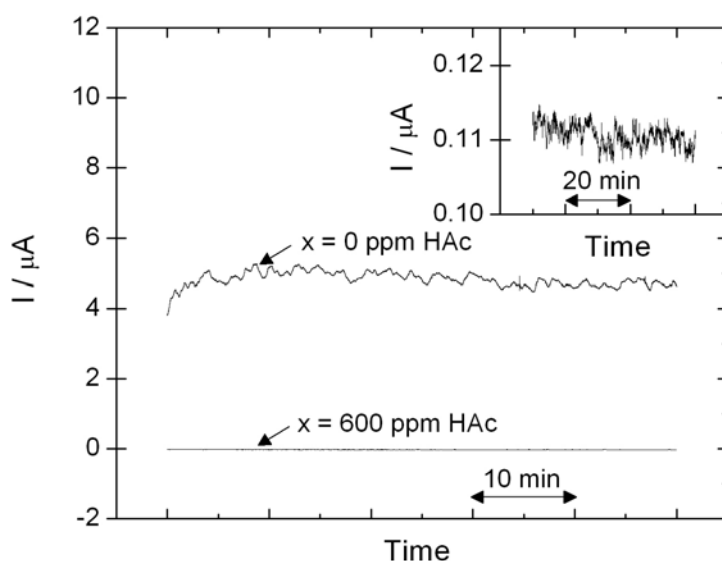
Figure V.9. *Current flow between two identical electrodes in a split-cell composed of two identical compartments separated by a high conductivity salt bridge. One of the compartments contained the base CO₂ saturated (1 bar CO₂) 17 mM NaCl aqueous solution containing 600 ppm. The other compartment simulated distinct conditions of no depletion (x = 600 ppm) and total depletion (x = 0 ppm) of HAc. Also shown in the inset is the current flow in the condition of total depletion of HAc in both compartments (1 bar CO₂, 17 mM NaCl). For the results shown in the inset, the pH gradient expected in the case x = 0, was simulated by adjusting the pH of one of the two solutions to 3.5.*

V.3.7.   Relationship between the Potential Drop and the Coupling Current

Before analyzing the relationship between the potential difference and the current flow between the outer surface and the artificial pit, **Figure V.10** shows their time evolution for two cases, 8 mm and 20 mm depth artificial pits. As well as in **Figure V.8**, potentials were measured after 2 hours of exposure. Unlike the coupled

potential, which was stable over the whole period of the experiment, the potential at the pit bottom increased slightly but gradually with time. As a consequence, the potential difference decreased monotonically during several hours before reaching a steady behaviour as seen in **Figure V.10-A**, which is consistently followed by a decreasing tendency of the current flowing between the outer surface and the pit, as shown in **Figure V.10-B**. This slow evolution may be ascribed to the concentration changes due to the consumption of reactants and production of reaction products coupled to the restricted mass transfer.
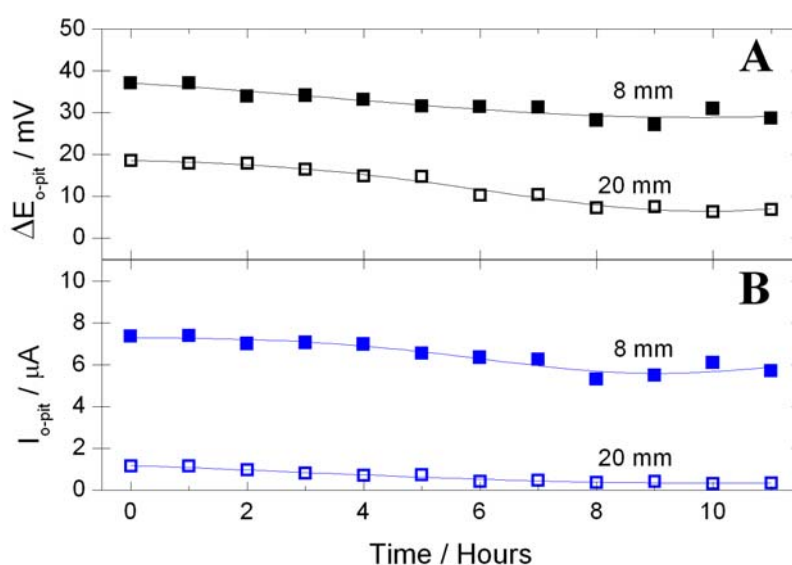
Figure V.10. *Typical time evolution of the potential difference (A) and the coupling current flow (B) between the outer large electrode and the artificial pit electrode for 8 mm and 20 mm depths in 17 mM NaCl, 600 ppm HAc and 1 bar CO₂.*

It is worth noticing that the coupling current and the potential difference behaved in a very reproducible way reflecting the intrinsic kinetic behaviour of the coupled interface. Indeed, while rearranging the results depicted in **Figure V.10**, it appeared that the joint evolution of the potential difference and the coupling current between the two electrodes follows a linear trend as seen in **Figure V.11** for the 8 and 20 mm depth artificial pits, respectively. This linear correspondence appeared for all pit depths not only when following their time evolution, as done in the case of **Figure V.10**, but also

when computing values issued from different experiments performed in similar conditions.
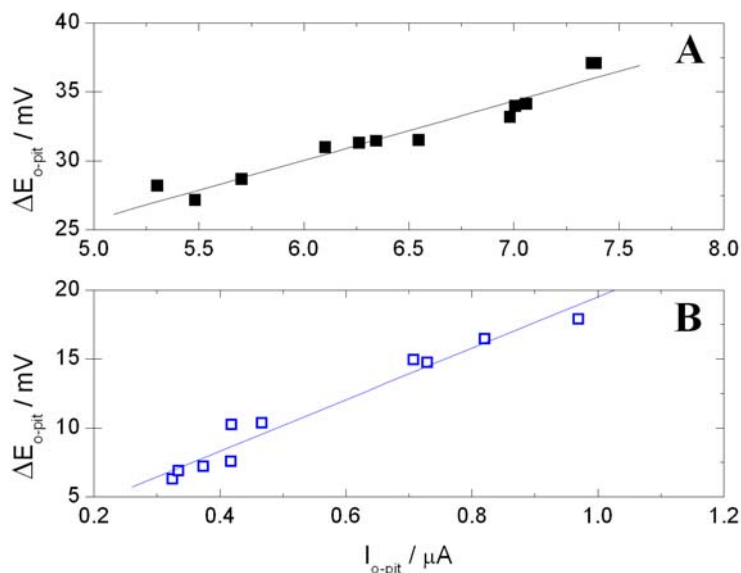
Figure V.11. *Potential-current relationship for 8 mm (A) and 20 mm (B) pit depth during the time evolution of the potential difference and the coupling current between the outer large surface and the artificial pit as depicted in Figure V.10. 17 mM NaCl, 600 ppm HAc and 1 bar CO₂.*

V.3.8. Distribution of the Overall Macroscopic Resistance

The persistence of this current-potential linearity brings to the forefront of the problem the idea of a macroscopic overall resistance that controls this behaviour, at least in steady-state conditions as discussed in this work. **Figure V.12** shows the evolution with the pit depth of the slope R, directly obtained from the E − I plots like those in **Figure V.11**. It is interesting to see that the curve goes through a minimum value at the same 8 mm depth for which the maximum current flowing between the two electrodes is reached as shown in **Figure V.6**. This indicates that this current behaviour is not merely a coincidence but is clearly related to the intrinsic kinetic behaviour of the interface illustrated by **Figure V.11**. Previously, the steep decrease of the current for deeper pits was tentatively ascribed to the increase of the electrolyte resistivity ρ inside the pit. The validity of such hypothesis can be verified by incorporating in **Figure V.12** the linear evolution of the theoretical electrolyte resistance, R_s, calculated by applying

the measured electrolyte conductivity ρ at different pH values to a perfect cylindrical pit of a length L and a cross-sectional area S:

$$R_s \approx \rho \frac{L}{S}$$

(V.9)

It appears hence that the pure electrolyte resistance, being always smaller than the slope R, cannot account for the overall ohmic behaviour of the pit electrode.
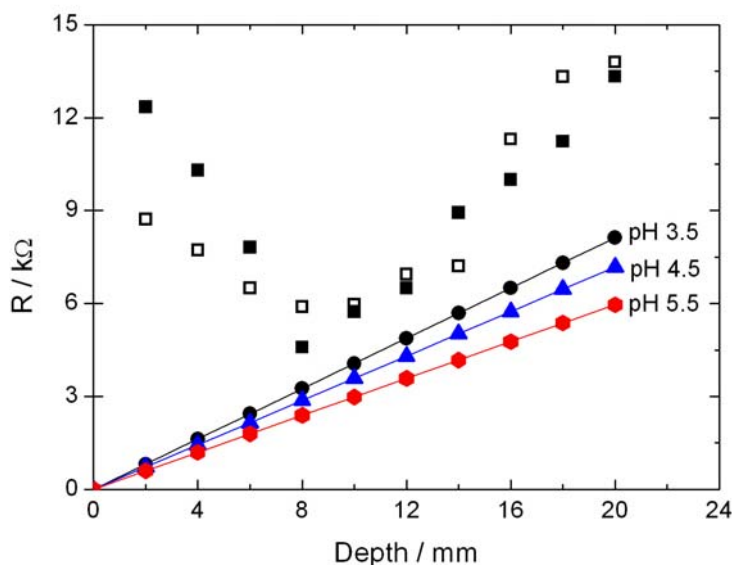
Figure V.12. *Experimental values of the slope R of the potential-current linear relationship as shown in Figure V.11 as a function of the pit depth (■); theoretical electrolyte resistance R$_s$ at different pH values for a perfect cylindrical geometry (solid lines) and R values computed from equation (V.13) with R$_s$ and R$_{p, pit}$ obtained from electrochemical impedance measurements (□), see Figure V.14 below.*

In order to assess the role of HAc in the pit propagation stage independently from the IR-drop effect, potentiodynamic measurements were performed on the uncoupled inner at different depths. **Figure V.13** shows the IR-compensated data obtained at three depths in the base solution. Increasing the depth unsurprisingly yielded a downward shift of the polarization curves, which indicates that the deeper the attack, the more anodically polarized will it be when coupled to the large outer surface. The effect of the pit depth on the local kinetics is in line with the general trend observed for the corrosion potential while varying the concentration of HAc. Furthermore, the fact that the

corrosion potential dropped significantly even at moderate depths constitutes strong evidence that the local depletion of HAc is mainly at the origin of this behaviour. It is worth noticing, however, that the results shown in **Figure V.13** are only representative of the uncoupled condition, which may be biased by starting the scan at high cathodic polarization. In comparison, the procedure described in **Figure V.7** appears to be a better approximation for the description of the attack behaviour in the coupled state.
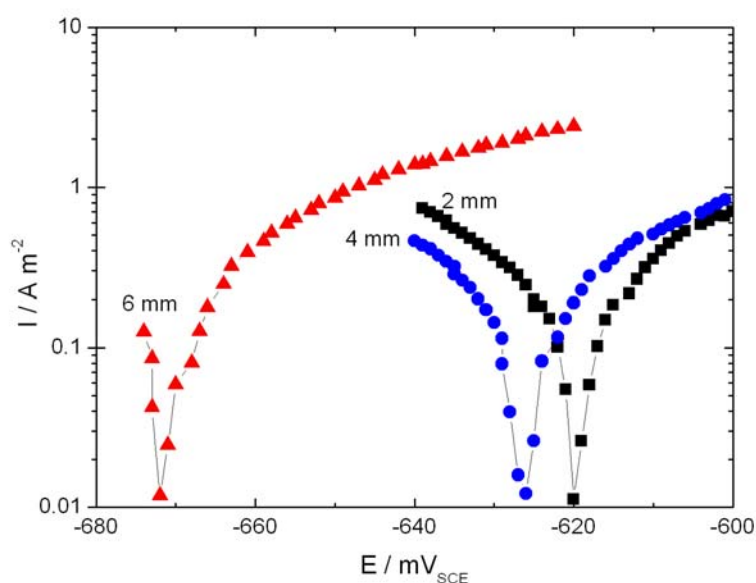
Figure V.13. IR-compensated polarization curves of the uncoupled inner electrode of Figure III.5 at different depths in 17 mM NaCl, 600 ppm HAc and 1 bar CO₂.

V.3.9. Equivalent Circuit of the Coupled Interface

The general behaviour of the slope R in **Figure V.12** must thus be addressed by considering that the small potential differences involved in the coupled measurements (typically less than 50 mV as seen in **Figures V.8** and **V.10**) allow the current-potential curves to be investigated with the help of a simple linear equivalent circuit analysis in the frequency domain **[20]**, **[21]** according to **Figure V.14** that yields

$$I_{o-pit} = \frac{\Delta E_{o\text{-}pit}}{\left(Z_o + R_s + Z_{pit} \right)} \quad\quad \text{(V.10)}$$

where Z_o and Z_{pit} account for the electrochemical impedances of the outer large surface and the artificial pit, respectively. R_s is the actual resistance of the narrow electrolyte path inside the pit. Since we were interested only in the steady values of both the potential difference and the current flow obtained under stationary conditions, the electrochemical impedance of each electrode can be assimilated to its polarization resistance:

$$R_p = \lim_{\omega \to 0} Z(\omega) \quad\quad \text{(V.11)}$$

$$\Delta E_{o\text{-}pit}$$
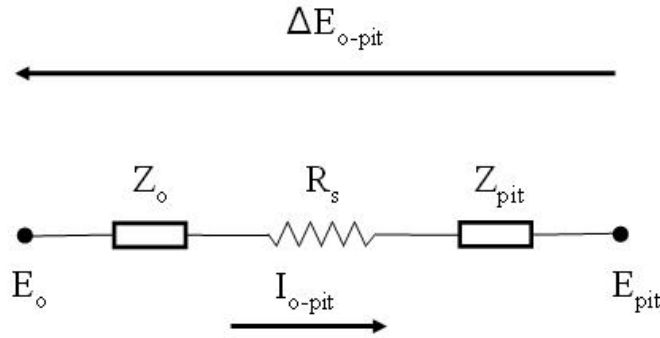
Figure V.14. Equivalent circuit for the asymmetric artificial pit electrode assembly of Figure III.5.

Besides, taking into account the 100-fold surface ratio, one can estimate the polarization resistance of the inner electrode, $R_{p,pit}$, to be 100 times larger than that of the outer one:

$$I_{o-pit} \approx \frac{\Delta E_{o\text{-}pit}}{R_s + R_{p,pit}} \quad\quad \text{(V.12)}$$

Accordingly, the slope R of the current-potential curves as those in **Figure V.11** is hence given by:

$$R = R_s + R_{p,pit} \tag{V.13}$$

This hypothesis was evaluated with the help of electrochemical impedance measurements, shown in **Figure V.15**, performed on the smallest electrode at different depths in the range 2-20 mm. The electrode was DC polarized to the coupled potential
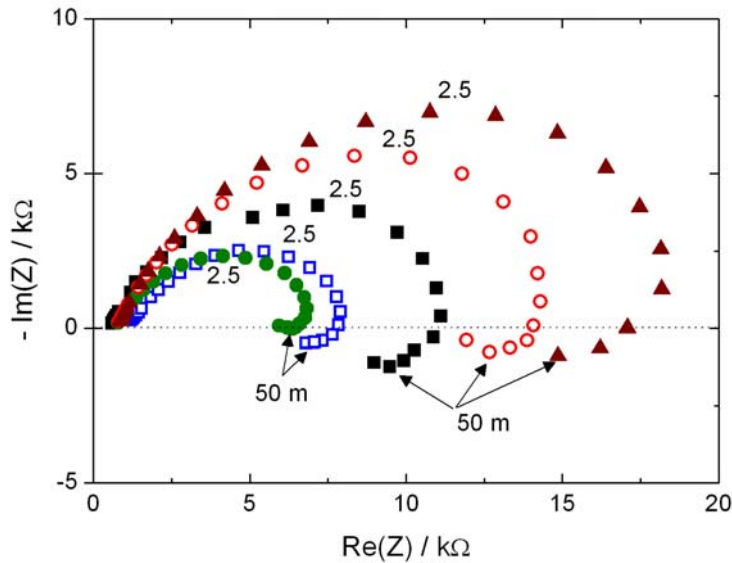
Figure V.15. *Nyquist plots of the electrochemical impedance of artificial pits at different depths in 17 mM NaCl, 600 ppm HAc and 1 bar CO₂. (■) 2 mm; (□) 6 mm; (●) 10 mm; (O) 16 mm ; (▲) 18 mm. Frequency values in Hz.*

prior to and during the EIS measurements in order to establish the actual concentration profiles inside the pit. It must be noticed that we were interested in the goodness of equation (V.13) to describe the overall macroscopic behaviour and not in the deep analysis of the impedance behaviour that is beyond the aim of the present study and is not discussed here accordingly. The impedance modulus decreased with depth till the critical 8 mm value beyond which it increased again, which reflects very well the qualitative behaviour of the coupling current observed in **Figure V.6**. For the sake of comparison, the values of R obtained from the Nyquist diagrams according to equation (V.13) were also plotted in **Figure V.12**. A good general agreement between these values and those issued from the overall kinetic behaviour appearing from the ZRA measurements and illustrated in **Figure V.11** indicates that equation (V.13) represents a

good approximation for the description of the macroscopic behaviour of the artificial pit at different depths. It must be noticed that the R_s values obtained from the Nyquist diagrams are smaller than those predicted by the theoretical curves for deeper pits, probably because of changes in the composition of the confined electrolyte. This confirms that purely ohmic effect related to R_s is not the only factor contributing to the inversion of the curve tendency beyond 8 mm.

V.4.　　Morphological Trend - Proposal for a Scenario

In view of the elements argued above, the role of HAc is likely to be related to the pit growth. The complete scenario can then be described as follows: the coupling current is related to the potential difference induced by the HAc depletion inside the pit. The inner electrode is hence anodically polarized and corrodes according to its polarization resistance for shallow pits, for which the depletion and hence the potential difference between the electrodes is not too high and the electrolyte resistance can be neglected. As the pit goes deeper towards the critical depth, the depletion and hence the anodic polarization increases yielding a strong decrease of the polarization resistance. Beyond the critical depth the decreasing current may tentatively be explained by a further depletion of HAc and CO_2, which leads to a decrease of the corrosiveness and thus an increase of the polarization resistance. However, the solution resistance does not seem to contribute substantially to the overall resistance at this stage. It must be emphasized however, that these results were obtained with inert, electrically insulating lateral walls of the artificial pit, which is obviously not a realistic configuration. In this sense, experiments were also performed on artificial pits with corroding steel walls, and with the same geometrical proportions as that in **Figure III.5**. The corroding lateral walls were part of the external electrode, while the inner electrode was located in the bottom of the pit as before. The results showed that the peak in the coupling current occurred at present closer to the pit mouth (2 instead of 8 mm critical depth as seen **Figure V.16**), thus minimizing the polarization of the deeper portions **[22]**.
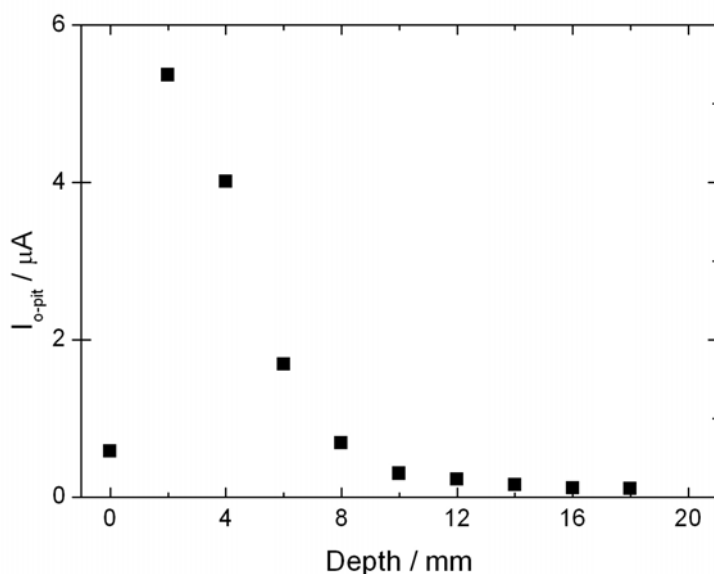
Figure V.16. *Average coupling current versus pit depth with corroding steel sidewalls in 17 mM NaCl, 600 ppm HAc and 1 bar CO₂.*

This also suggests that the concentration gradients were steeper due to the increased area of the corroding steel inside the pit. The results have nonetheless yielded a similar qualitative dependence for the coupling current versus the pit depth. This justifies to some extent the extrapolation of the results obtained with non-reactive wall pits to undertake our following reasoning on the morphological trend of the growing pit. For a pre-formed artificial pit but with corroding lateral walls, the vanishing coupling current beyond a critical depth as shown in **Figure V.16** would confine the high dissolution region to the sidewalls around this critical depth with a concomitant rapid slowdown of the growth rate at the pit bottom as the pit grows deeper. This would then trigger the lateral growth of the pit, which leads to an important issue related to the morphological trend of actual growing pits. In that case, a possible scenario, schematically represented in **Figure V.17**, would be such that at the first stages, the pit bottom would increasingly dissolve as and when HAc is depleted and not sufficiently fed because of diffusion constraints. As the critical depth is approached, the faster dissolving region is shifted to the lateral walls and moves gradually towards the pit mouth. The pit should therefore progressively become hemispherical and the pit mouth would widen to the extent where mass transport is no more seriously limited, the concentration gradient and consequently

the potential difference between the pit mouth and bottom vanishes as well as the driving force for the pit growth: the pit is then stifled.
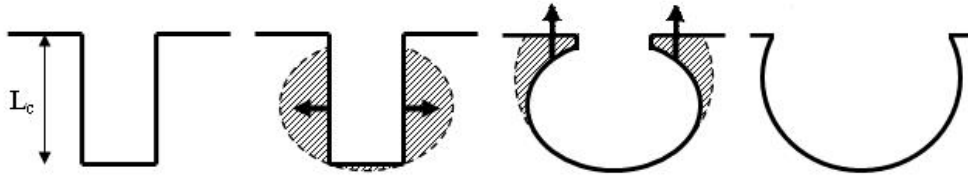
Figure V.17. *Schematic illustration of the hemispherical morphology trend of the propagating attack after an initial period of growing down till the critical depth L_c. From the left to the right, the scheme illustrates the pre-initiated attack, the lateral growth, the mouth opening and the final shape. Once the attack undergoes a sufficient mouth widening (step 3), the growth process may stifle due to increased convection and inward mass transfer. Clustering of attacks may also be envisaged.*

This morphological trend is in good agreement with the typical hemispherical shape observed for localized attacks as illustrated in **Figure V.18**, and the further development into mesa attacks, which is commonly reported from laboratory studies and field observations, and particularly found in actual situations of TLC.
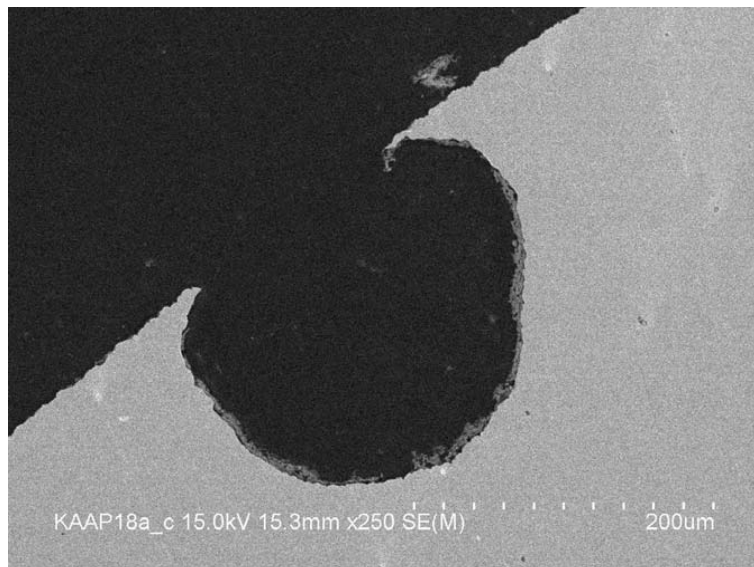
Figure V.18. *SEM image of a pit cross-section showing a hemispherical morphology typically observed for attacks on carbon steel in CO₂/HAc brine at room temperature. 0.051 M NaCl, 1 bar CO₂, 600 ppm HAc. Magnification = 250X.*

V.5.   Conclusions

Analyses of the current fluctuations generated on carbon steel in the experimental conditions of the present study showed that the noise signals fluctuated in more irregular patterns with higher frequency and amplitudes in the presence of HAc, thus suggesting a higher local electrochemical activity. Regardless of the presence of HAc, insightful examination of the shape variability suggested that the initiation of metastable pits is characterized by a sharp and stochastic current fluctuation with the typical transient of a quick rise preceding an exponential decay to the baseline level. In view of the results acquired subsequently using artificial pit measurements, this exponential decay is likely to bear on a progressive repair of the freshly initiated pit due to a change in the local chemistry (i.e., mass transport control) rather than a slow discharging of the double layer capacitance. On the other hand, analyses in the frequency domain indicated that HAc does not affect appreciably the initiation kinetics, but sustains metastable pitting events.

ZRA measurements on an artificial pit electrode assembly showed that HAc triggers and sustains the pit growth through a galvanic coupling between the pit bottom and the outer surface. Consumption of HAc inside the pit, in combination with restricted convection and the extended diffusion path gives rise to a HAc concentration gradient along the occluded geometry. That is, a HAc differential concentration cell is formed. Since the corrosion potential increases with HAc concentration, this differential cell establishes a potential difference so that the pit bottom is anodically polarized by the outer surface. This scenario would predict a monotonic increase of the corrosion rate as long as the organic compound is depleted. Nevertheless, measurements of the coupling current flowing between the pit base and the outer surface at different depths within the range 0-20 mm evidenced the existence of a critical depth below which the coupling current increases and beyond which it sharply drops off as it effectively occurs in actual TLC cases. The peak value of the coupling current reached at this critical depth suggested a total depletion of HAc for which the potential difference between the pit base and the outer surface is maximum. On the basis of the obtained results, a scenario was therefore proposed for the morphological trend of localized attacks, which is in

good agreement with laboratory studies and field observations. The results of the present study also showed that the IR-drop formalism is unlikely to operate for localized corrosion of carbon steel in CO_2/HAc brine, thereby suggesting that the process of stifling is rather induced by other influential factors. In order to elucidate the origin of the abrupt current-pit depth profile, this issue as well as the inferred alkalinization inside the pit will be the matter of numerical modelling and simulation in the next chapter.

References

[1]   Y. F. Cheng, M. Wilmott, J.L. Luo, Corr. Science, 41 (1999) 1245.

[2]   P.C. Pistorius, Corrosion, 53 (1997) 273.

[3]   D.E. Williams, C. Westcott, M. Fleischmann, J. Electrochem. Soc., 132 (1985) 1796.

[4]   M. Hashimoto, S. Miyajima, T. Murata, Corr. Science, 33 (1992) 885.

[5]   C. Gabrielli, M. Keddam, Corrosion, 48 (1992) 794.

[6]   Y.F. Cheng, J.L. Luo, M. Wilmott, Electrochim. Acta, 45 (2000) 1763.

[7]   J.C. Uruchurtu, J.L. Dawson, Corrosion, 43 (1987) 19.

[8]   P.R. Roberge, R. Beaudoin, V.S. Sastri, Corr. Science, 29 (1989) 1231.

[9]   Y.F. Cheng, J.L. Luo, J. Electrochem. Soc, 146 (1999) 970.

[10]   H.W. Pickering, Mater. Sci. Eng., A198 (1995) 213.

[11]   B.G. Ateya, H.W. Pickering, J. Electrochem. Soc. 122 (1975) 1018.

[12]   C. Gabrielli, F. Huet, R.P. Nogueira, Electrochim. Acta, 50 (2005) 3726.

[13]   R.M. Smith, A.E. Martell, "*Critical Stability Constants*", vol. 6, Plenum Press (1989).

[14]   E. Gulbrandsen, K. Bilkova, CORROSION\06, Paper no. 06364, NACE, 2006.

[15]   Y.M. Gunaltun, D. Larrey, CORROSION\00, Paper no. 71, NACE, 2000.

[16]   Y. Garsany, D. Pletcher, B. Hedges, J. Electroanal. Chemistry, 538-539 (2002) 285.

[17]   Y. Garsany, D. Pletcher, D. Sidorin, W.M. Hedges, Corrosion, 60 (2004) 1155.

[18]   M. Vankeerberghen, M. Abdulsalam, H. Pickering, J. Deconinck, J. Electrochem. Soc., 150 (2003) B445.

[19]   E. A. Nystrom, J. B. Lee, A. A. Sagüés, H. W. Pickering, J. Electrochem. Soc., 141 (1994) 358.

[20]   A. Bautista, U. Bertocci, F. Huet, J. Electrochem. Soc., 148 (2001) B412.

[21]   A. Aballe, F. Huet, J. Electrochem. Soc. 149 (2002) B89.

[22]   J.A. Beavers, N.G. Thompson, Corrosion, 43 (1987) 185.

Chapter VI

Numerical Simulation of a Single Corrosion Pit

Table of Contents

VI.1.   Introduction

In the previous chapter, acetic acid has been identified as a driving factor that triggers and sustains the growth of localized attacks through galvanic coupling effect. Although common behaviours are generally observed, the key factors involved in CO_2 corrosion of carbon steel in the presence of HAc influence the pitting behaviour in a complex way. It was therefore worthwhile to develop a computational model that could help overcoming this complexity by solving the large set of equations of tightly coupled and non-linear nature, thereby enabling a complementary analysis and a better understanding of the underlying mechanism of pit growth. The present chapter covers a numerical model of steady-state behaviour of a single corrosion pit in CO_2-containing media in the presence of HAc. The model was based on mass-conservation statement and consisted of 2D axis-symmetric attack in representative working conditions. The kinetics of the electrochemical reactions occurring on the electrode surface was described by Tafel equations fitted to the experimental data obtained on X65 pipeline steel. We anticipated that the simulation results provide an essential insight into both the chemistry and electrochemistry inside the active pit. Particular attention was paid to the effect of HAc on the coupling behaviour between the attack base and the outer surrounding surface.

VI.2.   Localized Corrosion - Brief Review

VI.2.1.   Introduction

Pitting and crevice corrosion are two of the most destructive forms of localized corrosion. These two forms of attack are different in the sense that a pit generates the required geometry spontaneously instead of relying on an outside former as in crevice corrosion. Despite this difference, there are many mechanistic similarities associated with the self-sustaining nature of the growth process of established pits and crevices. Foremost among these is the formation a locally occluded region which causes high rate

localized attack. It has been suggested that pitting is a (special) form of crevice corrosion on a smaller scale, with either micropores or surface heterogeneities acting to form the crevice [1, 2]. It is becoming increasingly clear that much can be understood about the fundamental mechanisms of pitting and crevice corrosion by considering them as manifestations of the same set of basic phenomena. No particular distinction between established pits and crevices will then be made in the next subsections.

VI.2.2.   Theories of Localized Corrosion - Propagation Mechanism

Modern theories of localized corrosion ensue from the active dissolution theory developed in the 1960's [3, 4]. According to this theory, the local conditions become substantially aggressive so that the metal dissolving inside the cavity is in the active state. This implies that the potential drops inside the cavity and lies often in the active region of the polarization curves [5]. The active dissolution theory was further challenged by the later observations of large potential drops as high as 1 V [6-9]. A competing theory based on IR-drop concept was therefore formulated. The IR theory assigns paramount importance to electrical change (instead of compositional change) as the factor controlling both the rate and the location of attack.

A.   *Compositional Change Theory*

It is generally accepted that in all cases the activation of established pits or crevices stems from the driving force induced by the environmental difference between the localized corrosion site and its surrounding [3, 10, 11]. The compositional change theory stipulates that the paramount role of the occluded geometry is to act as a barrier to chemical fluxes by restricting mixing of the cavity solution with the bulk. The change in the electrolyte composition includes metal ion concentration cell [12], differential aeration cell [13, 14], inhibitor concentration cell [15], pH [16, 17], and chloride ion concentration cell [18, 19]. Each of all these chemical gradients may drive the active dissolution of the metal inside the occluded region at a much higher rate than on the boldly exposed surface. This also supposes that the cavity solution must reach a critical degree of aggressiveness to trigger the active dissolution. The concept was originally

proposed by Mears and Evans [14], and it has become known as the critical crevice solution criterion (CCS). Oldfield and Sutton [20-22] were the first to develop a mathematical model based upon the CCS concept explicitly formulated by Fontana and Greene [3]. Even though it was developed specifically for crevice corrosion of stainless steel in neutral halide solutions, the Fontana and Greene concept has nevertheless been adapted with minor modifications for most alloys. Basically, the concept identifies four stages. In the first stage, the metal dissolves over the entire surface. The cathodic reaction occurs both inside the cavity and on the boldly exposed surface. However, owing to the restricted mass transport to the occluded site, the oxidant is progressively depleted inside the cavity until the spatial separation of the anode and cathode becomes effective. The cavity then corrodes as being galvanically coupled to the outer surface. This marks the onset of the second stage. The accumulation of metallic cations M^{n+}, enhanced by the mass transport restrictions inherent in the geometry, is concomitantly balanced by the electromigration of aggressive X^- anions into the cavity from the bulk solution. Upon reaction with metallic cations, some of X^- anions are tied up in instable complexes (MX_n), which are then quickly hydrolyzed. The hydrolysis lowers the local pH through the production of hydrogen ions, thereby increasing the dissolution current inside the cavity. Likewise, the increase of the dissolution current leads to a further ingress of X^- into the crevice with the subsequent decrease in pH. For passive metals, the third stage is characterized by the breakdown of the passive film inside the cavity once the CCS criterion is achieved (critical pH and critical [X^-]). In a later stage, the large cathode-to-anode area ratio and the self-sustaining nature of the process stabilizes the active dissolution by exceeding the rate at which the Fickian driving force can upset the established balance. Overall, a self-sustained growth mechanism of any established form of localized corrosion must meet three requirements; the CCS, the spatial separation of anode and cathode, and the stability of these two processes.

All the mechanisms based on the compositional change theory were however questioned by Vetter and Strehblow [23]. The authors stipulated that the deterministic factors of pitting should be influential during all the stages of pit growth even for the detectable pits as small as one micron in diameter, and that such compositional changes would be initially meaningless to be considered at the origin of pitting phenomena.

B.   IR-drop Theory

The inability of the compositional change theory to rationalize some observed cases of active dissolution in the absence of local acidification or large influx of aggressive anions (anions build-up), which are the two pre-requisites for the Fontana and Greene model, has prompted Pickering et al. to propose the IR-drop theory **[8**, **9**, **24**, **25]**. Unlike the former theory, the IR-drop mechanism ascribes primacy to the electrical changes inside the occluded site. Once the oxidant is totally depleted inside the cavity, the spatial separation of the anode and cathode becomes effective, thus resulting in net current flowing through the resistive electrolyte path towards the boldly exposed surface. The basic feature of the theory is that the ohmic drop in the cavity electrolyte causes the local electrode potential to become less oxidizing than the electrode potential at the outer surface until it lies in the active region of the polarization curve. In this case, the cavity dissolves actively at a much higher rate than the outer surface. However, the effect of the resulting potential drop strongly depends on the electrochemical kinetics of the metal. For a metal exhibiting anodic Tafel behaviour, a potential drop is always protective as it lowers the driving force for the active dissolution. The IR-drop mechanism does therefore operate only for passive metals exhibiting an active peak on the anodic branch. By analogy with the CCS theory, Pickering et al. conceptualized the critical potential drop IR^* as a pre-requisite for the onset of active dissolution inside the cavity. Since then, the IR^* criterion, defined as the difference between the (corrosion or applied) potential at the outer surface and the passivation or Flade potential **[8**, **24]**, has lent its name to the entire theory. According to the critical potential drop concept, the cavity potential must therefore be below the Flade potential for a stable local cell (pit crevice, or crack) to exist, i.e. $IR > IR^*$.

One of the aspects that Pickering and co-authors have emphasized is the ability of the IR-drop theory to anticipate and rationalize the morphological trend of corrosion attacks **[25**, **26]**. Since the potential inside the cavity is being continuously shifted towards the less noble direction, the expected morphology would be related to the polarization curve as a function of the position inside the cavity. The concept thus anticipates the existence of a critical depth around which the active dissolution is confined. The maximum dissolution rate at the critical depth corresponds to the active

peak on the anodic branch of the polarization curve. Both the amount of IR-drop needed to shift the electrode potential into the active region and the location inside the cavity at which the IR* criterion is attained strongly depend on the cavity geometry and the local chemistry (e.g. conductivity). Although they are not necessary for stability, both of these factors evolve during active dissolution and can influence the local cell processes. For instance, acidification of the local solution induces an upward shift of the Flade potential and, therefore, the criterion IR > IR* is more readily met. Overall, the IR-drop mechanism is not other than a direct consequence of the compositional change theory in poorly conductive electrolytes.

VI.2.3.   Modelling Localized Corrosion

A.   *Motivation*

Despite the technical challenges posed by the geometric constraints, a considerable progress has been made concerning the experimental characterization of single corrosion pits. Because of these constraints, however, experimental measurements can only be performed at discrete points in time and space, and can therefore only provide limited information about the key factors controlling the pit behaviour.There are many difficulties associated with the experimental characterization of the local conditions inside corrosion pits. Pit dimensions are exceedingly tight and the insertion of probes can influence the corrosion process, thereby rendering the measured values unrealistic. Also, there is a small solution inside a pit available for analysis. As a result, a number of mathematical pitting models have been developed over the last years. Mathematical modelling can bridge the gaps between experimental values and allows prediction of the impact of a range of variables, helping to provide a more complete framework of the pit behaviour. One of the major advantages of modelling is also its ability to uncouple factors that in practice cannot be separated. Indeed, the implementation of virtual experiments with only a subset of gathered data can sometimes be used to gain a valuable insight into the interrelations between experimentally inseparable factors.

B.   Common Simplifying Assumptions

To date, most of modelling and simulation approaches of localized corrosion attacks have been fundamentally based on Newman's mass transport theory for dilute electrolytes **[27**, **28]**. From a broad point of view, modelling localized corrosion must involve consideration of the environmental conditions and the interfacial processes that occur between the metal and its environment. These considerations include; chemical equilibria, mass transport modes, and interfacial kinetics. In most cases, however, the governing processes are described by a large set of equations of tightly coupled and non-linear nature. A number of models in literature have therefore had recourse to simplifying assumptions to make the problem easier to solve. Also, the scarce of either theoretical or experimental data does not permit use of the complete solution and making assumptions may prove to be essential in certain cases. The simplifying assumptions that are commonly made in the area of modelling localized corrosion can be categorized into four broad groups:

- *Thermodynamic variables:* The attack to be modelled is often assumed to remain at constant temperature and pressure; standard conditions are usually considered. This is justified by the fact that the attack is not supposed to undergo substantial fluctuations in these variables in practical situations.

- *Chemistry effects:* The governing processes are usually described according to the mass transport theory for dilute electrolytes. Long-range and short-range electrostatic interactions between solute ions are often ignored so that the mass transport coefficients (diffusion and mobility) are independent of the electrolyte chemistry. Also, in the absence of stirring or hydrodynamic transport, the natural convection is assumed to be largely overlapped by diffusional and electromigrational components, and the convection term is therefore rarely included in the modelling approaches (stagnant condition). Precipitation and accumulation of corrosion products are also not taken into account in circumstantial cases, particularly in a short-term context.

- *Potential effects:* One of the major assumptions often encountered in this area concerns the charge neutrality condition, thereby implying a uniform repartition

of the space charge density in the electrolyte. Recall that the electrostatic potential in the electrolyte is related to the charge separation that is inherent to the difference in the respective diffusion rates of solute ions. Simplified representations of the boundary conditions are also systematically used, particularly in which relates to the potential-current relationship.

- *Dimensionality (time and space):* A number of models assume that the reaction mechanisms are fast enough so that the system reaches its steady-state shortly. In this way, computations are performed for steady-state corrosion conditions. Also, for the sake of minimizing the computation speed, geometrical simplifications are often made. The cavity is usually reduced to two- or even one-dimensional pattern, so a high degree of symmetry is possible.

C.   *Few Illustrative Models*

Most of pit and crevice corrosion models have been developed on the basis of infinite dilution theory. A few illustrative examples of steady-state models are presented hereafter. Comprehensive literature reviews of a variety of models have nevertheless been proposed by Evitts **[29]** and Stewart **[30]**, and the interested reader is invited to refer to their respective works.

In a series of papers, Galvele **[31]**, **[32]**, and Galvele and Gravano **[33]** developed three CCS pitting corrosion models. Unlike the two first models, where mass transport was assumed to occur exclusively via the diffusion mode, the final model included the electromigration term and the electroneutrality condition was applied. The results were drawn in terms of concentration profiles as a function of the parameter "depth x current" for a unidirectional pit. The authors attributed the pit activation to the local acidification arising from the metal ions hydrolysis with the major change occurring near the pit opening. Sharland and Tasker **[34]** simulated the propagation stage of a pit on carbon steel. The pit was modelled as a parallel-sided slot in a dilute sodium chloride solution. Mass transport process was described in terms of diffusion and electromigration and convection was neglected. The authors also assumed the electroneutrality condition. An extension to the model incorporated the effect of precipitation of ferrous hydroxide. The

model predicts the steady-state chemistry and kinetics inside the active cavity as a function of many parameters such as external electrode potential and cavity dimensions. A comparison was made between pits with reactive and non-reactive sidewalls, respectively. The one-dimensional pit model developed by Walton [35] was based on dilute electrolyte theory. It accounted for the mass transport in acetic and sulphuric solutions by diffusion and electromigration. The condition for the local charge neutrality was applied and the concentrations were assumed to be constant at the pit mouth. The model was drawn in a general form to accommodate various techniques for evaluating the current density. Predictions were in good agreement with experimental results of Valdes-Mouldon [36]. Upon a dimensional analysis of the governing equation, Walton concluded that the condition inside the corrosion cell is no other than a consequence of the counteracting effects of mass transport and species generation. By analogy with the "severity factor" of Bernhardsson [37], Walton determined the "geometry factor" (depth^2/width) as a key indicator of the solution aggressiveness inside the cavity. A transient version of this model was also presented later by Walton et al. [38].

VI.3.   Pit Model - Conceptual Description

VI.3.1.   Theoretical Background

In aqueous environments, mass transfer of species from one location to another is driven either by differences in electrical or chemical potential between the two locations or by motion of a volume element of the electrolyte. The modes of mass transfer are thus:

- *Migration (also called electromigration):* motion of charged species subjected to an electric field, i.e. electrical potential's gradient.

- *Diffusion:* motion of species subjected to a concentration gradient, i.e. chemical potential's gradient.

- Convection: motion of species occurs under the influence of stirring or hydrodynamic transport, i.e. forced convection or advection. In natural

convection, the motion of volume elements of the electrolyte is induced by the density gradient. More generally, the fluid flow is characterized by stagnant regions, laminar flow, and turbulent flow.

This underscores the need for the concept of the electrochemical potential ($\tilde{\mu}_j$) that obeys the same criteria at equilibrium as the chemical potential. In a stagnant electrolyte subjected to diffusion and migration, where mass transfer phenomena due to the convective forces are relatively small so that they can be ignored, the net molar flux of a species j is written in a functional form of the electrochemical potential:

$$N_j = -u_j C_j \nabla\left(\tilde{\mu}_j\right) \qquad\qquad (VI.1)$$

where u_j is the mobility and C_j is the concentration. The electrochemical potential is formally the sum of the chemical potential (μ_j) and the contribution from charged species described by the electrostatic potential (V) in the electrolyte:

$$\tilde{\mu}_j = \mu_j + z_j FV \qquad\qquad (VI.2)$$

with z_j being the charge number and F being the Faraday's constant. Since,

$$\mu_j = \mu_{j0} + RT \ln\left(\gamma_j C_j\right) \qquad\qquad (VI.3)$$

Then,

$$N_j = -D_j \nabla C_j - u_j z_j C_j F \nabla\left(V\right) \qquad\qquad (VI.4)$$

Here, γ_j and μ_{j0} denote the activity coefficient and the standard chemical potential, respectively. The diffusion coefficient varies with the mobility according to the following correlation:

$$D_j = u_j RT\left(1 + \frac{\partial \ln\gamma_j}{\partial \ln C_j}\right) \qquad\qquad (VI.5)$$

The above equation still holds even under the influence of long-range and short-range electrostatic interactions between cations and anions. For electrolytes that are

sufficiently diluted so that the infinite dilution theory may apply, the expression in the brackets is close to 1. That is,

$$\lim_{C_j \to 0} \frac{\partial \ln \gamma_j}{\partial \ln C_j} = 0 \tag{VI.6}$$

In equation (VI.4), the first term on the right hand side represents the diffusion contribution arising from a concentration gradient while the second term represents the migration contribution induced by the electric field in the electrolyte. Assuming a mass-conservation condition, the full transport-reactive phenomena may be fundamentally described by:

$$\frac{\partial C_j}{\partial t} + \nabla \left(N_j \right) = R_j \tag{VI.7}$$

R_j stands for the reaction rate including both the production and the consumption parts. Substituting N_j in equation (VI.7) yields the following general form:

$$\frac{\partial C_j}{\partial t} = D_j \nabla^2 \left(C_j \right) + z_j u_j F \nabla \left[C_j \nabla \left(V \right) \right] + R_j \tag{VI.8}$$

The second order gradient of the electrostatic potential is related to the space charge density (ρ) in the electrolyte via Poisson's equation that operates on a much faster time scale than electromigration and diffusion:

$$\nabla^2 \left(V \right) = - \frac{\rho}{\varepsilon_0 \varepsilon_r} = - \frac{F}{\varepsilon_0 \varepsilon_r} \sum_j z_j C_j \tag{VI.9}$$

where ε_0 and ε_r denote the vacuum permittivity and the relative permittivity of the electrolyte, respectively. The solution conductivity (σ) is given by:

$$\sigma = \frac{F^2}{RT} \sum_j z_j^2 D_j C_j \tag{VI.10}$$

VI.3.2. Assumptions

The model consisted of a single pit in a dilute electrolyte. All the diffusion coefficients were assumed isotropic and constant. A major geometrical simplification was made by assuming the pit as a perfect cylindrical hole with a base diameter of 2 mm and a finite depth within the range 0-20 mm. Note that the pit dimensions were selected so that a comparison between the simulation results and the experimental findings was feasible (see **Figure VI.2** and **Figure III.5** for comparison). Thanks to the cylindrical symmetry, the model was reduced to a two-dimensional pattern. The axial symmetry also allowed the consideration of only the one-half of the model, thus reducing substantially the resolution time. On the other hand, it was assumed that natural convective forces were sufficiently large so that the homogeneity and equilibrium conditions were ascertained in the bulk. As illustrated in **Figure VI.1**, the calculation domain for the outer electrode was then set within the Nernst diffusion layer of a thickness δ estimated to 300 μm for natural convection conditions **[39]**. Inside the cavity, however, this mode of mass transfer was neglected due to the geometrical restrictions. According to Poisson's equation (VI.9), the term $\left(\varepsilon_0\varepsilon_r\right)^{-1}$ is sufficiently large ($\sim 10^9$) so that any slight deviation from the charge neutrality would induce very large electrical restoring forces **[40, 41]**. These forces tend to remove the charge gradients on a much faster time scale than those associated with pure electromigration or diffusion processes **[34]**. The issue was actually circumvented by considering the motion of charged species so fast so that the condition for the local charge neutrality of volume elements is met at any time. That is,

$$\sum_j z_j C_j = 0 \qquad\qquad (VI.11)$$
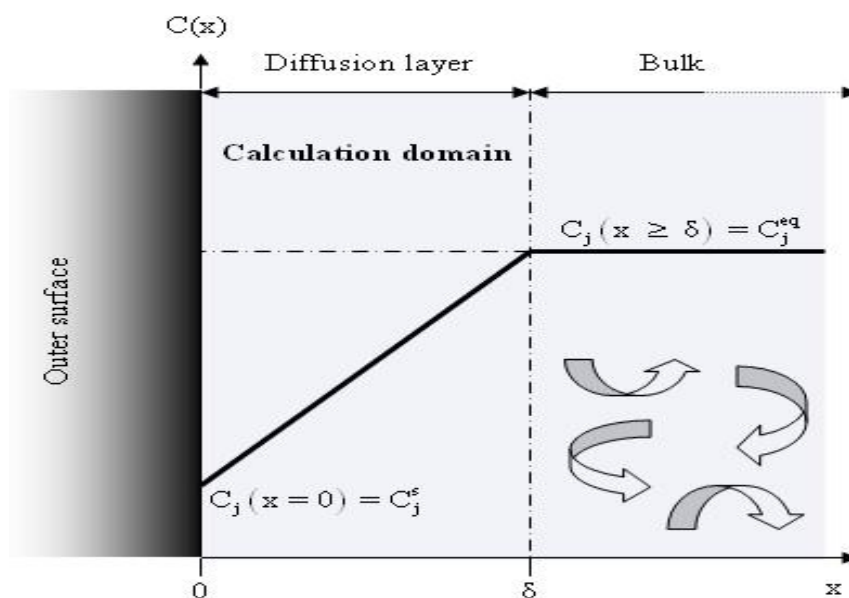
Figure VI.1. *Concentration profile for a species j as a function of the distance from the outer surface in steady-state diffusion - convection regime. The terms* C_j^{eq} *and* C_j^s *stand for the equilibrium and surface concentrations, respectively.*

VI.3.3. Boundary Settings

The boundary settings are particularly important since they describe both the chemical and electrochemical processes occurring at the metal-electrolyte interface. The molar fluxes are proportional to the overall current density generated by the cathodic (i_a) and anodic (i_c) reactions at the metal surface through Faraday's law:

$$i = i_a + i_c = F \sum_j z_j N_j \qquad (VI.12)$$

A dimensional description of the model and the corresponding boundary settings are schematically represented in **Figure VI.2**. To allow for the comparison between the predictions and the experimental results, the simulations were performed on a single attack with non-reactive and electrically insulating sidewalls.
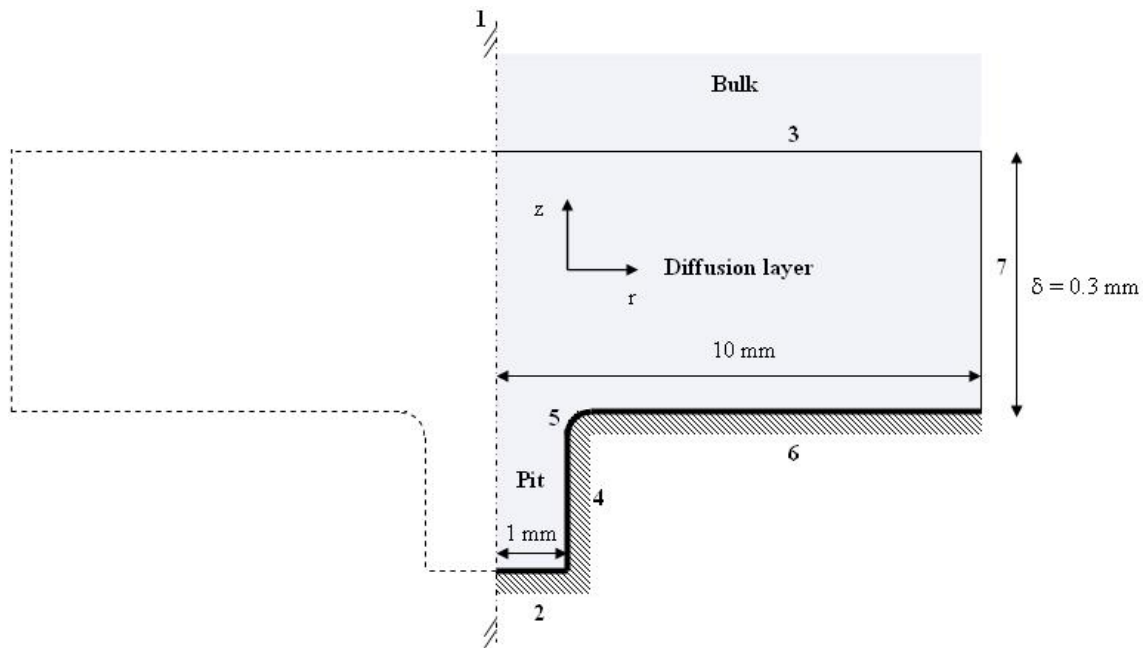
Figure VI.2. *Dimensional description of the 2D-axisymmetric pit and the corresponding boundary settings. 1- Axial symmetry; 2- Pit bottom: $i = i_a + i_c$; 3- $C_j = C_j^{eq}$; 4- Pit sidewall: Electric insulation; 5- Chamfer: Electric insulation; 6- Outer surface: $i = i_a + i_c$; 7- Electric insulation. The chamfer (boundary 5) was used to smooth the straight corner, thereby simplifying the numerical grid pattern.*

The kinetics of electrochemical reactions occurring on the electrode surface is essential for determining the corrosion rate of a metal exposed to a corrosive medium. These reactions strongly depend on the electrode potential, E:

$$E = \varphi_{WE} - \varphi_{RE} \tag{VI.13}$$

where φ_{WE} and φ_{RE} are the Galvani potentials of the working electrode and the reference electrode, respectively. For a freely corroding electrode (net current = 0) at its open circuit potential, E_{corr}, as well as for IR-compensated data in polarized conditions, the interfacial electrochemical processes can be described in terms of the current-potential relationships, for instance Tafel equations if appropriate (equation III.1). To simulate the galvanic coupling effect, the sum of the partial currents integrated over the area of the pit base must balance the total current integrated over the area of the boldly exposed surface. In the finite-element calculations, both the potential and the current distributions are rather calculated in the electrolyte domain according to the configuration (B) of **Figure VI.3**.
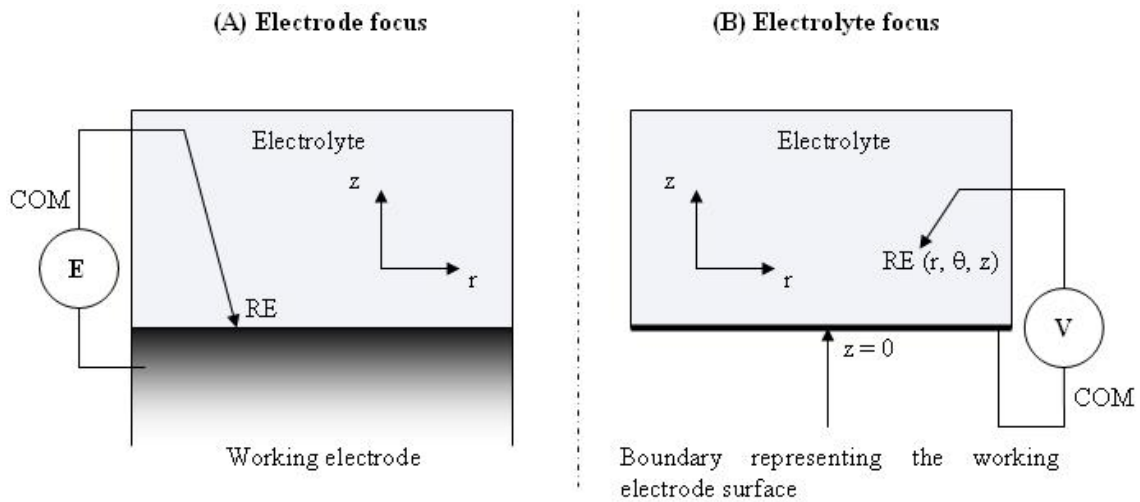
Figure VI.3. *Determination of the electrode potential according to the experimental approach (A) and the modelling approach (B). RE = reference electrode.*

In this case, the working electrode is just represented as a boundary condition describing the current-potential relationship at the metal-electrolyte interface. This underscores the need for a new formalism that relates to the electrolyte domain. Instead, an alternative concept, which is directly related to the experimental measurements, can be adopted by expressing the potential V(r, θ, z) of a reference electrode versus the corroding electrode. That is,

$$V\left(r,\theta,z\right) = \varphi_{RE}\left(r,\theta,z\right) - \varphi_{WE} \qquad (VI.14)$$

with r, θ and z being the cylindrical coordinates. The potential V(r, θ, z = 0) at a given point of the boundary representing the working electrode surface as well as the new open circuit potential V_{corr} are hence given by:

$$V\left(r,\theta,0\right) = - E \qquad (VI.15)$$

$$V_{corr} = - E_{corr} \qquad (VI.16)$$

Here E denotes the IR-compensated potential of the working electrode versus the reference electrode located at a given point of the active surface. Note that the new electrode polarization ΔV remains unchanged as if it would have been obtained in a more conventional manner according to the scheme (A) of **Figure VI.3**:

$$\Delta V = V_{corr} - V\left(r,\theta,0\right) = \left(-E_{corr}\right) - \left(-E\right) = E - E_{corr} \qquad (VI.17)$$

VI.3.4. Model Application

The electrochemical kinetics was described by Tafel equations fitted to the experimental data obtained on X65 pipeline steel in CO_2-containing media in the presence of HAc. In Chapter IV, the corrosion potential has been shown to increase monotonically with HAc concentration. In the present model, we accordingly used the E_{corr} data reported in **Figure IV.8**. Likewise, a similar fitting of i_{corr} - HAc data was used (see **Figure IV.7**). The anodic and cathodic Tafel slopes were experimentally found to be fairly independent of HAc concentration. For the purpose of this model, these parameters were assumed constant with a b_a value of 50 mV/decade and a b_c value of -120 mV/decade. Since proton reduction and iron dissolution were the only electrochemical reactions considered in this model, the net fluxes of H^+ and Fe^{2+} at the metal boundaries were given by equation (VI.12); the fluxes for all other species were hence assumed zero. The simulated electrolyte consisted of 17 mM aqueous NaCl containing different amounts of HAc and saturated with 1 bar CO_2. The chemical reactions as well as their respective equilibrium (K_j) and reaction rate (k_j) constants at 25 °C are listed in **Table VI.1**.

Table VI.1. *List of the chemical reactions considered in this model and their respective thermodynamic and kinetic constants at 25 °C. The subscripts "b" and "f" stand for backward and forward (reactions), respectively. All the reaction rate constants are in s^{-1} units, except for $k_{w,b}$ expressed in units of $M^{-1}s^{-1}$.*

Chemical reaction	pK_j	k_j	References
1. $H_2O \rightleftharpoons H^+ + OH^-$	14	$k_{w,b} = 7.85 \times 10^{10}$	**[42]**
2. $CO_2(g) \rightleftharpoons CO_2(aq)$	1.468	-	**[43, 44]**
3. $CO_2(aq) + H_2O \rightleftharpoons H_2CO_3$	2.588	$k_{hyd,f} = 3 \times 10^{-2}$	**[43, 44]**
4. $H_2CO_3 \rightleftharpoons HCO_3^- + H^+$	3.5	$k_{ca,f} = 7.80 \times 10^6$	**[43-45]**
5. $HCO_3^- \rightleftharpoons CO_3^{2-} + H^+$	10.33	$k_{bi,f} = 6.07$	**[45-47]**
6. $HAc \rightleftharpoons H^+ + Ac^-$	4.80	$k_{ac,f} = 3.20 \times 10^5$	**[45, 48]**

In addition to water, these reactions involved eleven aqueous species. They are reported in **Table VI.2** along with their diffusion coefficients and initials concentrations. The sodium and chloride ions do not take part in the chemical reactions, but help preserving the local charge neutrality. A further simplification of the model was made by omitting

the formation of iron carbonate layers. This simplification sounds reasonable since $FeCO_3$ precipitation is very slow at room temperature [45, 49], and the formation of protective layers takes weeks at such temperatures even under conditions of artificially elevated pH [49].

Table VI.2. List of aqueous species considered in the model along with their diffusion coefficients and initial concentrations. (*) pH; (**) calculated from K_j; (***) calculated using the condition for mass conservation of total acetic species. The concentration of undissociated HAc is expressed in ppm units and corresponds to 600 ppm of total acetic species (HAc + Ac⁻) at pH 3.38.

Species										
Na^+	Cl^-	H^+	OH^-	Fe^{2+}	CO_2	H_2CO_3	HCO_3^-	CO_3^{2-}	HAc	Ac^-
Diffusion coefficients at 25 °C in units of 10^{-9} m² s⁻¹										
1.3	2	9.3	5.3	0.7	1.96	2	1.1	0.92	1.2	1.1
Initial conditions										
17 mM	17 mM	3.38*	**	0	1 bar	**	**	**	578	***

VI.4. Simulation Results

VI.4.1. Pit Chemistry

Since no moving boundaries were involved in the model, each calculation was therefore carried out independently in a static geometry (i.e., at a given depth) using Comsol Multiphysics$^©$ with a convergence criterion of 10^{-4}. The predicted steady-state composition of the pit electrolyte is shown in **Figure VI.4**. Large quantities of ferrous ions are generated by the metal dissolution with concentrations exceeding 100 mM deeper into the cavity. At such concentrations, the dilution theory still nevertheless applies. The major impact of high ionic concentrations is through the IR-drop in electrolyte. Within this range, the maximum error in the calculation of the electrostatic potential is less than 1 %. Also, most of the ionic flux within the pit is diffusive. The effect that this error would have on the rate of ionic transport through the electromigration mode is hence negligible. The increasing positive charges of metallic cations are balanced by a large migration of chloride ions from the bulk electrolyte and the formation of bicarbonate and acetate anions. **Figure VI.4** also indicates that the

model keeps all reactions at equilibrium and ensures the local charge neutrality throughout the pit electrolyte. The relatively high concentration observed for bicarbonate anions is likely to ensue from a high dissociation rate of carbonic acid as it will be confirmed later by the simulated pH profile.
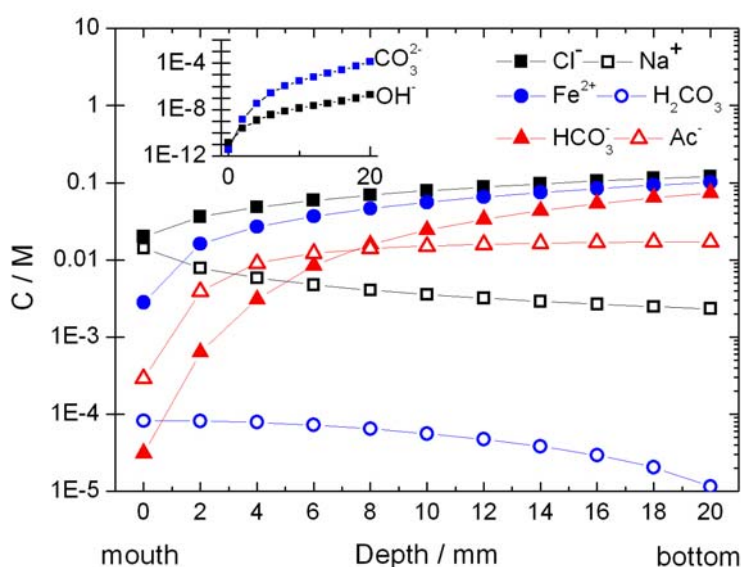
Figure VI.4. *Simulated steady-state composition of the electrolyte along the pit depth.*

VI.4.2.   CO₂ Depletion

According to the Law of Mass Action, a high dissociation rate of carbonic acid should boost the hydration reaction of carbon dioxide (reaction 3, **Table VI.1**). Moreover, the geometric constraints would limit the ability of aqueous carbon dioxide to move into the pit so that CO_2 depletion occurs faster than diffusion can follow. This is what was actually observed as shown in **Figure VI.5**. The predicted depletion of CO_2 is of major importance regarding the steep decrease of the coupling current beyond a certain depth (**Figure V.6**). Beyond a critical depth, the depletion of CO_2 should in principle lead to a decrease of the corrosiveness and thereby an increase of the polarization resistance. To validate the hypothesis of CO_2 depletion as the key parameter behind the process of stifling observed in **Figure V.6**, some specific measurements were performed with the help of the split-cell setup described in Chapter

III (see **Figure III.6**). One of the compartments was filled with the same base solution of that in previous measurements, that is, CO_2
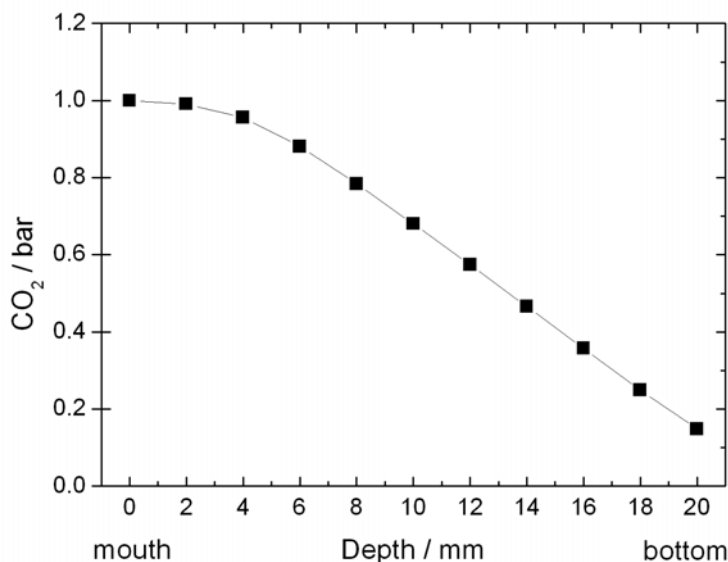
Figure VI.5. Simulated steady-state profile of CO_2 concentration, reported as equilibrium partial pressure.

saturated (1 bar CO_2) 17 mM NaCl aqueous solution containing 600 ppm of HAc, the second being filled with HAc-free solutions of 17 mM NaCl saturated with x bar CO_2. **Figure VI.6** depicts the current flow between the two electrodes in distinct conditions simulating no depletion (x = 1) and total depletion (x = 0) of CO_2. For the latter case, the solution was de-aerated by purging nitrogen for 2 hours prior to each experiment, and the nitrogen gas flow was maintained over the solution throughout the measurement to prevent oxygen ingress. In order to make the comparison feasible, the pH difference that would have been established between the two compartments in the case of x = 1 was reproduced in the situation of total depletion by adjusting the pH to the same value as in the situation of no depletion. Results clearly point out a net anodic polarization induced by the HAc depletion -resulting in a net anodic current - of the electrode exposed to the electrolyte simulating no CO_2 depletion (x = 1). In comparison, a significant shrinkage of the coupling current was found between the two electrodes in CO_2 depleted conditions, that would make the solution less aggressive. This is consistent with the idea of CO_2 depletion causing the stifling of pit growth. In this case,

pits would thus propagate and stifle mainly according to the counteracting depletions of acetic acid and CO_2.
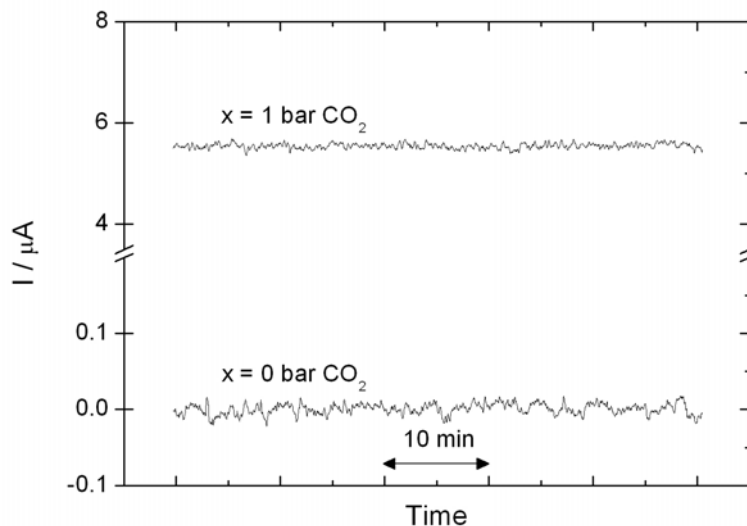
Figure VI.6. *Current flow between two identical electrodes in a split-cell composed of two identical compartments separated by a high conductivity salt bridge. One of the compartments contained the base CO_2 saturated (1 bar CO_2) 17 mM NaCl aqueous solution containing 600 ppm HAc. The other compartment was filled with HAc-free solution of 17 mM NaCl saturated with x bar CO_2, thus simulating distinct conditions of no depletion (x = 1) and total depletion (x = 0) of CO_2.*

As demonstrated in Chapter IV, the onset of the active dissolution is not straightforwardly related to the presence of HAc, but rather to the presence of CO_2. A SEM cross-section of a pre-initiated pit after immersion during three months in 17 mM NaCl and 600 ppm HAc showed that propagation did not occur in CO_2 free-solutions regardless of the presence of HAc as illustrated by **Figure VI.7**, which also agrees well with the results of **Figure VI.6**. This suggests that the potential difference induced by HAc differential concentration cell, only, is not enough to trigger the active dissolution inside the pit in the absence of CO_2. In such case, pit activation would be a matter of interfacial interactions of carbonic species with the metal (anodic control), with HAc concentration gradient being a supplementary driving force.

Figure VI.7. *SEM cross-section of 2 mm-depth attack on X65 sample after immersion during 3 months in 17 mM NaCl and 600 ppm HAc (0 bar CO_2). The solution was continuously purged with nitrogen to prevent oxygen ingress.*

VI.4.3.   HAc Depletion

The other important feature of the steady-state behaviour of the pit is related to the variation of undissociated HAc concentration between the bulk electrolyte and the cavity as depicted in **Figure VI.8**. The simulated profile clearly shows a depletion of HAc inside the pit. This depletion is not only due to the consumption of protons by the cathodic reaction at the pit base but also to mass transfer limitations induced by the geometric constraints. Shallow pits are indeed more easily fed by mass transport of HAc than deep ones. The acid depletion inside the pit induces a concentration gradient in respect with the bulk. That is, HAc differential concentration cell is formed. The depletion of HAc is also an important factor since the corrosion potential decreases with decreasing HAc concentration as reported in the previous chapter. The differential cell thus establishes a potential difference so that the pit is anodically polarized by the outer large surface. This result is in good agreement with the experimental findings, where HAc (coupled to CO_2 as discussed before) was clearly found to trigger and sustain pit growth via galvanic coupling mechanism.
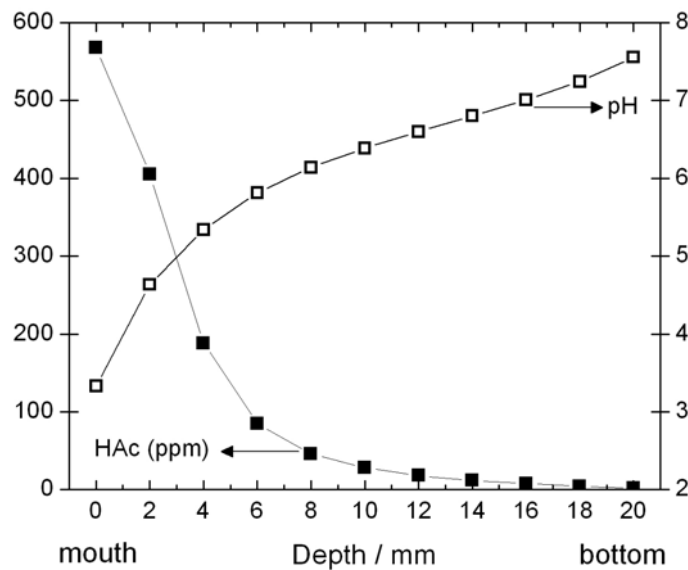
Figure VI.8. *Simulated steady-state profiles of HAc concentration and pH as predicted by simulation results.*

SEM cross-sections of two pre-initiated pit immersed during 3 months in HAc-containing and HAc-free solutions indeed showed that propagation is appreciably enhanced in the presence of HAc (**Figures IV.9** and **IV.10**). As HAc depletion goes on deeper into the attack, CO_2 corrosion is expected to become prevailing, thus resulting in a local alkalinization as evidenced by the simulated steady-state pH profile of **Figure VI.8**. In a similar way to the aforementioned study, a complementary investigation was performed by means of the split-cell technique to assess the effect of HAc on the coupling behaviour. One of the two compartments was filled with CO_2 saturated (1 bar CO_2) 17 mM NaCl aqueous solutions containing x ppm of HAc, the second contained a CO_2 saturated (1 bar CO_2) 17 mM NaCl aqueous solution and simulated a total depletion of HAc.
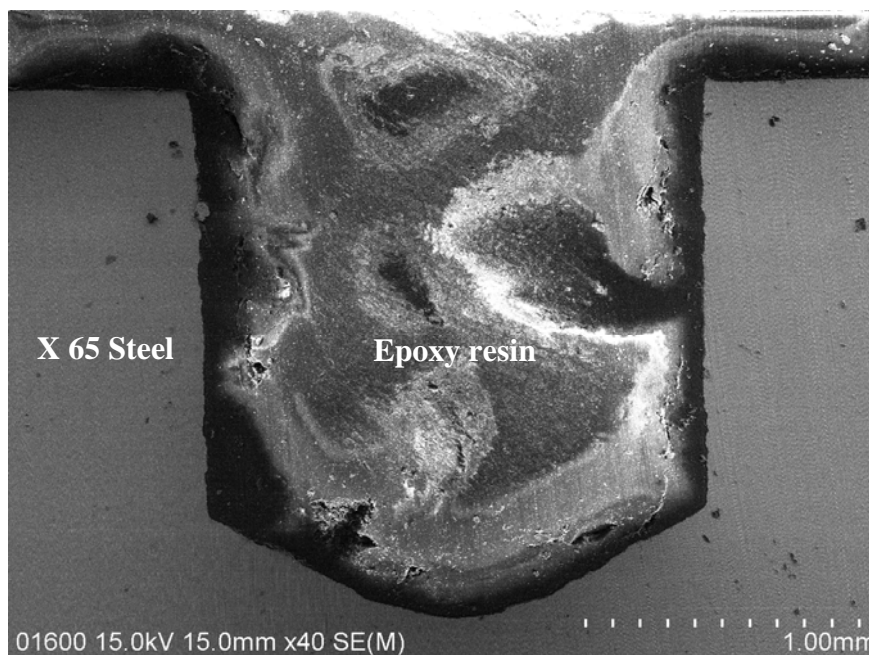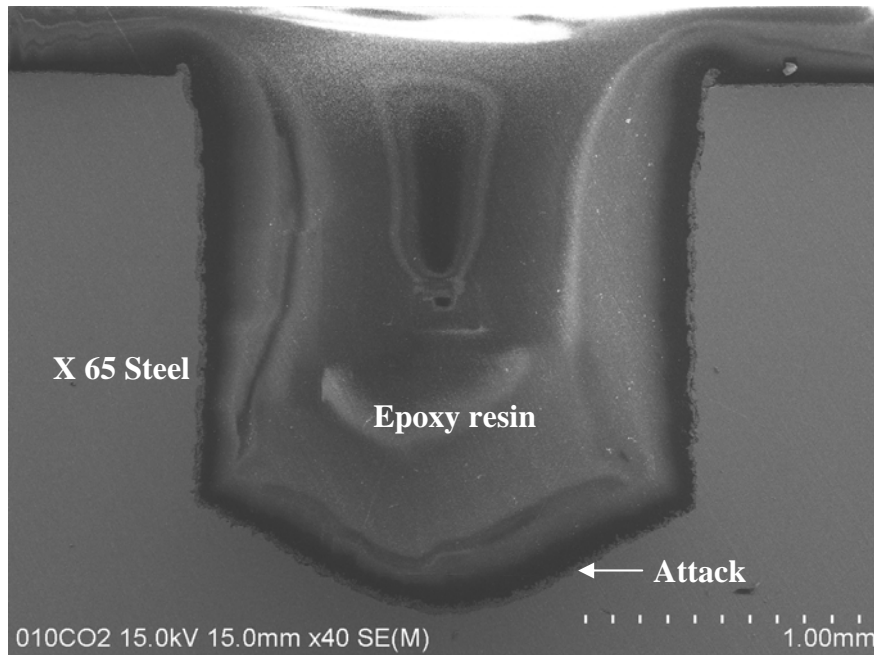
Figure VI.9. *SEM cross-section of 2 mm-depth attack on X65 sample after immersion during 3 months in 17 mM NaCl and 0 ppm HAc saturated with 1 bar CO_2.*
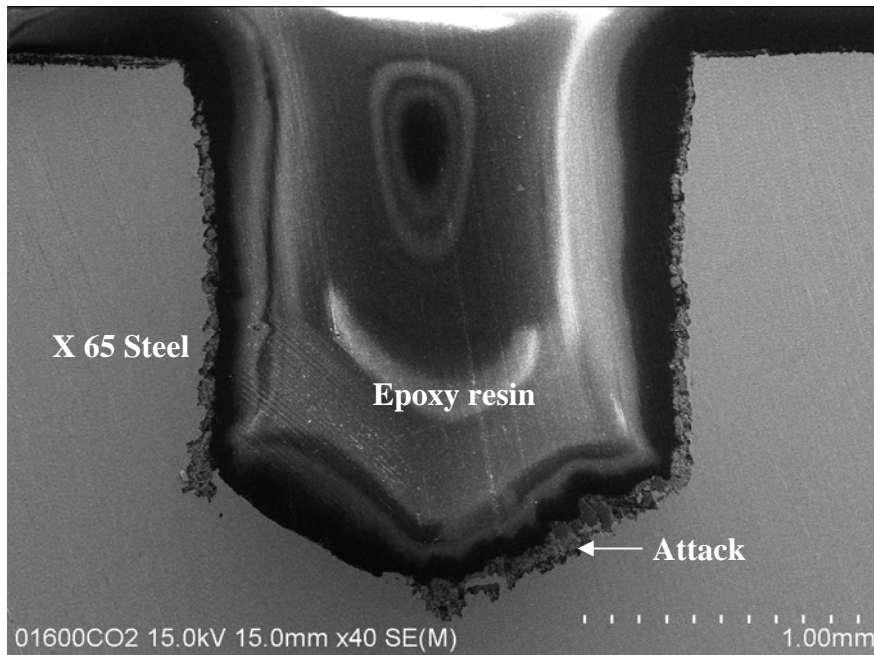
Figure VI.10. *SEM cross-section of 2 mm-depth attack on X65 sample after immersion during 3 months in 17 mM NaCl and 600 ppm HAc saturated with 1 bar CO_2.*

The variation of the current flow between the two electrodes as a function of HAc concentration is featured in **Figure VI.11**. Considering the E_{corr}-HAc relationship,

increasing HAc concentration was unsurprisingly shown to enhance the net anodic polarization -resulting in an increase of the net anodic current - of the electrode exposed to the electrolyte simulating depleted conditions. Results also show that the current levels off towards high concentrations of the organic compound, thereby suggesting a saturation of the electrode surface with HAc adsorbates as also discussed in Chapter IV.
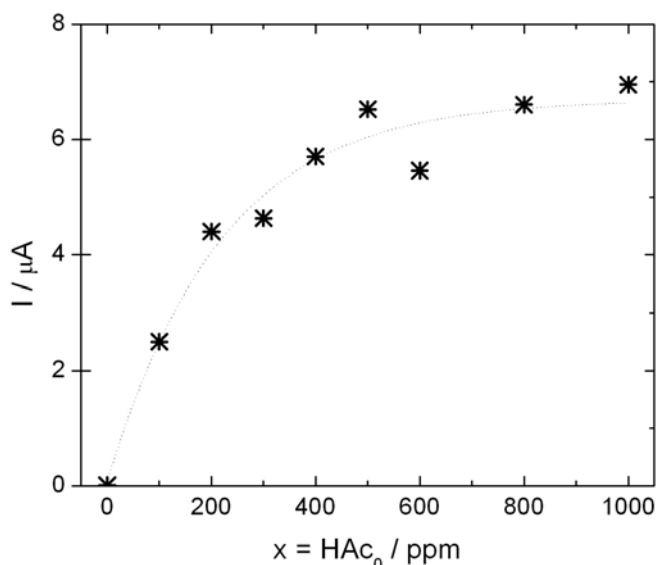
Figure VI.11. Current flow between two identical electrodes in a split-cell composed of two identical compartments separated by a high conductivity salt bridge. One of the compartments contained the base CO_2 saturated (1 bar CO_2) 17 mM NaCl aqueous solution containing x ppm of HAc. The other compartment was filled with HAc-free solution of 17 mM NaCl saturated with 1 bar CO_2.

VI.4.4. Comparison of Model Predictions with Experimental Data

The simulated values of the IR-uncompensated potential difference between the outer surface and the pit base at distinct positions inside the cavity were likened to the previous experimental data of **Figure V.8**. As indicated by **Figure VI.12**, the agreement between the model predictions and the experimental results is very good. In both cases, the potential difference was shown to increase monotonically with pit depth until it levels off for deeper pits. This is unsurprising considering the monotonic depletion of HAc depicted in **Figure VI.8**, on the one hand, and the close relationship between the organic compound and the corrosion potential evidenced in Chapter IV, on the other

hand. Also shown in **Figure VI.12** is an inset featuring a comparison between predicted and measured values of the pure ohmic resistance of the narrow electrolyte path inside the pit. The predicted R_s values were calculated via equation (VI.10). In the previous chapter, it was demonstrated that the IR-drop mechanism does not operate for localized corrosion of carbon steel in CO_2/HAc brine. It was therefore concluded that the process of stifling might be induced by other factors rather than the IR-drop. This assumption was actually corroborated by the low values of R_s. In combination with the results of **Figures VI.5 - VI.7**, the R_s profile also suggests that the local depletion of CO_2 is the main cause of stifling.
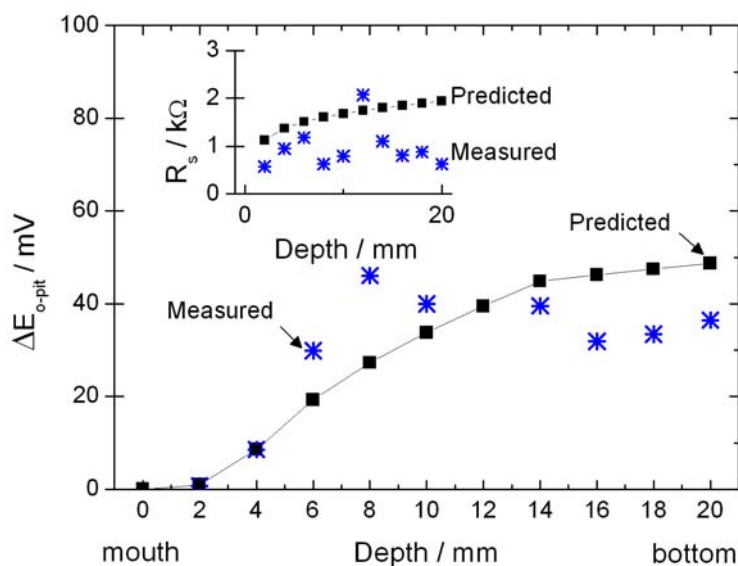
Figure VI.12. Simulated and measured IR-uncompensated distributions of the potential difference between the outer large surface and the pit base. Also shown in the inset is a comparison between predicted and measured values of the ohmic resistance of the narrow electrolyte path inside the pit.

The simulated distribution of the coupling current between the pit bottom and the outer large surface is depicted in **Figure VI.13**. Recall that the coupling current is the sum of the individual current densities integrated over the area of the exposed surface. The model reveals that the current reaches a maximum at 12 mm. The calculated distribution corroborates the experimental results obtained with the help of ZRA and artificial pit electrodes. Indeed, typical distributions of the coupling current flowing between the actively corroding attack bottom and the outer large surface clearly

showed the existence of a transition depth at 8 mm below which the current increases and beyond which it sharply drops off. It is also worth noticing that the magnitude of the calculated current is in fair agreement with the experimental data of **Figure V.6**. The predicted current-depth peak however seems not as sharp as that found experimentally. This may be ascribed to the fact that the measured electrochemical data implemented in the present model are limited to $pH \leq 5.5$ and $P_{CO2} = 1$ bar. Implementation of data for higher pH and lower P_{CO2} would probably give a sharper current-depth peak. Nevertheless, the model helps us to identify a need for further experimental data within the predicted ranges. This will be a matter of recommendations for future work. At 2 mm depth, however, the partial pressure of CO_2 is practically 1 bar (see **Figure VI.5**) and the pH is almost 4.5 (see **Figure VI.8**). This gave a good agreement between predicted and experimental results as illustrated by **Figure VI.14**.
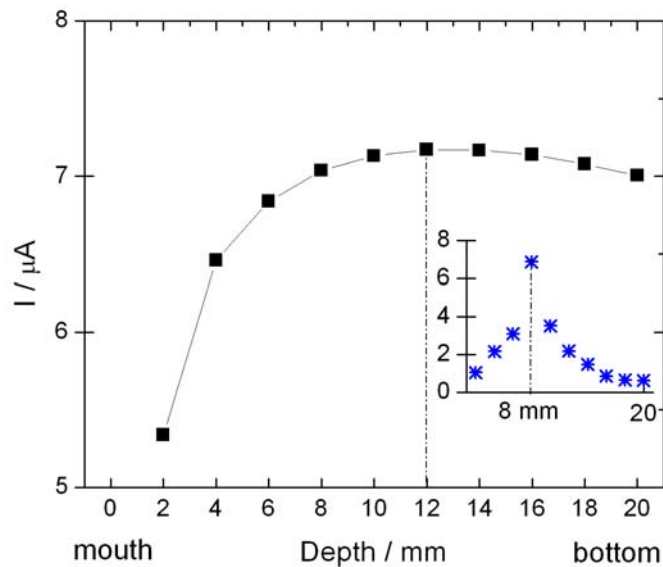
Figure VI.13. *Simulated and measured distributions of the coupling current.*
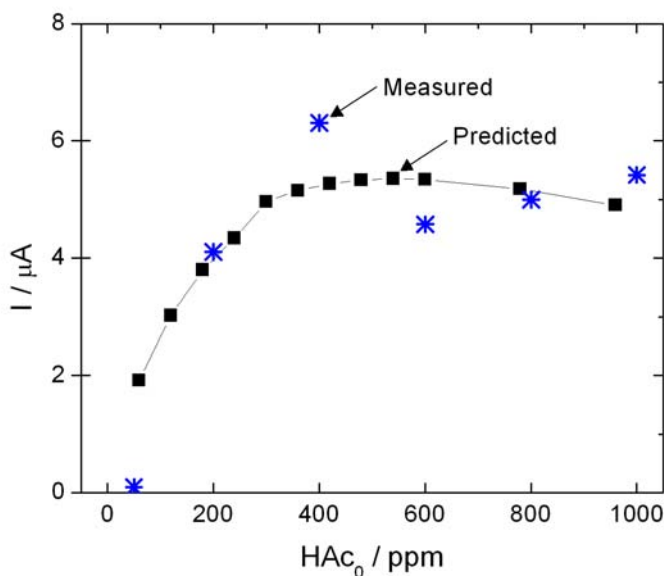
Figure VI.14. *Simulated and measured coupling currents vs. the initial concentration of HAc for a pit of 2 mm diameter and 2 mm depth in 17 mM NaCl and 1 bar CO_2.*

VI.5.   Conclusions

A flexible and predictive model of steady-state behaviour of a single pit was developed and applied to X65 pipeline steel in CO_2/HAc media. The model is general in form, thus allowing extension and application to a variety of systems. A promising agreement was obtained between the model predictions and experimental data acquired with the help of artificial pit measurements. This agreement gave complementary evidence about the major role played by HAc in the growth mechanism of actively corroding pits through galvanic coupling effect. The predicted results clearly showed a local depletion of HAc, which is due not only to the consumption of protons by the cathodic reaction inside the pit but also to mass transport restrictions that are inherent to the occluded geometry. Shallow pits were indeed found to be more easily fed by mass transport of HAc than deep ones. The model also predicted a progressive depletion of CO_2 inside the pit. The depletion of CO_2 should in principle lead to a decrease of the corrosiveness and thereby an increase of the polarization resistance as indicated by the general trend of the overall resistance in the previous chapter. This finding is of a major importance in the sense that it rationalizes the steep decrease observed for the coupling

current towards deeper pits. In view of all these elements, established pits propagate according to the counteracting depletions of HAc and CO_2. As indicated by the predicted pH-depth profile, a local alkalinization is therefore expected rather than an acidification, which would also contribute to hinder the active dissolution inside the pit as a result of $FeCO_3$ precipitation. In agreement with experimental observations, the simulated distribution for the coupling current versus depth relation showed the existence of a transition depth beyond which the pit is no more self-sustained. The magnitude of the predicted coupling current was in fair agreement with experimental data. The predicted current-depth peak was however not as sharp as that found experimentally. The overestimation of the coupling current, particularly for deep pits, was ascribed to the restricted range of experimental data implemented in the model. This will be a matter of recommendations for future work in the next chapter, notwithstanding the fact that for shallow pits, simulations and experiments were in very good agreement. Overall, even though a certain similarity with the compositional change theory can be inferred from the described pit growth mechanism, the latter deviates nevertheless in several ways from that of stainless steels and other passive metals. The IR-drop formalism is hence unlikely to operate in such conditions.

References

[1]   S.M. Sharland, C.P. Jackson, A.J. Diver, Corr. Science, 29 (1989) 1149.

[2]   R. G. Kelly and, J. R. Scully, D. W. Shoesmith, R. G. Buchheit, *"Electrochemical Techniques in Corrosion Science and Engineering"*, Marcel Dekker, Inc. (2002).

[3]   M.G. Fontana, N.D. Greene, *"Corrosion Engineering"*, McGraw-Hill, New York, 41 (1967).

[4]   J. Tousek, *"Theoretical Aspects of the Localized Corrosion of Metals"*, Trans. Tech. Publications, Switzerland (1985).

[5] H.J. Engell, Electrochim. Acta, 22 (1977) 987.

[6] H.W. Pickering, Mat. Science and Eng., A198 (1995) 213.

[7] C.M. Chen, F.H. Beck, M.G. Fontana, Corrosion, 27 (1971) 234.

[8] H.W. Pickering, Corr. Science, 29 (1989) 325.

[9] A. Valdes, H.W. Pickering, *"Advances in Localized Corrosion"*, H. Isaacs, U. Bertocci, J. Kruger, Z. Szklarska-Smialowska, (Eds.), NACE-9, NACE, Houston, TX. 1990.

[10] L.L. Shreir, *"Corrosion"*, Vol.1, Newnes-Butterworths, 1976.

[11] F. Dabosi, G. Beranger, B. Baroux, *"Corrosion Localisée"*, Les Editions de Physique, les Ulis, 1994.

[12] R.J. McKay, Trans. Electrochem. Soc., TESOA, 41 (1972) 201.

[13] U.R. Evans, J. Inst. Metals, 30 (1923) 239**.**

[14] R.B. Mears, U.R. Evans, Trans. Faraday Soc., 30 (1934) 417.

[15] U.R. Evans, L.C. Bannister, S.C. Britton, Proc. Roy. Soc. A131, 4131 (1931) 355.

[16] I.L. Rosenfeld, I.K. Marshakov, Corrosion, 20 (1964) 115t.

[17] W.D. France, N.D. Greene, Corrosion, 24 (1968) 247.

[18] I.B. Ulanovskii, J. Appl. Chem., 39 (1966) 768

[19] J. Mankowski, Z. Szklarska-Smialowska, Corr. Science, 15 (1975) 493.

[20] J.-L. Crolet, J.M. Defranoux, L. Seraphin, R. Tricot. Mem. Sci. Rev. Metall., 71 (1974) 797.

[21] J.W. Oldfield, W.H. Sutton. Brit. Corr. J., 13 (1978) 13.

[22] J.W. Oldfield, W.H. Sutton. Brit. Corr. J., 13 (1978) 104.

[23] K.J. Vetter, H.H. Strehblow, *"Localized Corrosion"*, B.F. Brown, J. Kruger, R.W. Staehle, A. Agarwal (Eds.), NACE-3, NACE, Houston, TX, 1974.

[24] H.W. Pickering, Corrosion, 42 (1986) 125.

[25] H.W. Pickering, *"Advances in Localized Corrosion"*, H. Isaacs, U. Bertocci, J. Kruger, Z. Szklarska-Smialowska, (Eds.), NACE-9, NACE, Houston, TX.

1990.

[26]   Y. Xu, M. Wang, H.W. Pickering, J. Electrochem. Soc., 140 (1993) 3448.

[27]   J.S. Newman, *"Localized Corrosion"*, B.F. Brown, J. Kruger, R.W. Staehle, A. Agarwal (Eds.), NACE-3, NACE, Houston, TX, 1974.

[28]   J.S. Newman, *"Advances in Localized Corrosion"*, H. Isaacs, U. Bertocci, J. Kruger, Z. Szklarska-Smialowska, (Eds.), NACE-9, NACE, Houston, TX. 1990.

[29]   R.W. Evitts, Ph.D. Thesis, University of Saskatchewan (1997).

[30]   K.C. Stewart, Ph.D. Thesis, University of Virginia (1999).

[31]   J.R. Galvele, J. Electrochem. Soc., 124 (1976) 464.

[32]   J.R. Galvele, Corr. Science, 21 (1981) 551.

[33]   J.R. Galvele, J.R. Gravano, Corr. Science, 24 (1984) 517.

[34]   S.M. Sharland, P.W. Tasker, Corr. Science, 28 (1988) 603.

[35]   J.C. Walton, Corr. Science, 30 (1990) 915.

[36]   A. Valdes-Mouldon, Ph.D. Thesis, The Pennsylvania State University (1987).

[37]   S. Bernhardsson, L. Eriksson, J. Oppelstrup, I. Puigdomenech, T. Wallin, 9th Scandinavian Corrosion Congress (1984).

[38]   J.C. Walton, G. Cragnolino, S.K. Kalandros, Corr. Science, 38 (1996) 1.

[39]   S. Nešić, B.F.M. Pots, J. Postlethwaite, N. Thevenot, J. Corr. Sci. and Eng., 1, Paper 3, 1995.

[40]   S.M. Sharland, Corr. Science, 27 (1987) 289.

[41]   A. Turnbull, *"Modelling Aqueous Corrosion: From Individual Pits to System Management"*, NATO Science Series, Vol. 266 (1993).

[42]   P. Delahay, J. Am. Chem. Soc., 74 (1952) 3497.

[43]   S. Nešić, M. Nordsveen, R. Nyborg, A. Stangeland, CORROSION\01, Paper no. 40, NACE, 2001.

[44]   D.A. Palmer, R.V. Eldik, Chem. Rev., 83 (1983) 651.

[45]   E. Gulbrandsen, K. Bilkova, CORROSION\06, Paper no. 06364, NACE, 2006.

[46]   M. Eigen, Angew. Chem., 75 (1963) 489.

[47]   W. Knoche, *"Biophysics and physiology of carbon dioxide"*, Springer-Verlag, Germany (1980) 3.

[48]   K.J. Vetter, *"Electrochemische Kinetics"*, Springer-Verlag (1960) 406.

[49]   A. Dugstad, R. Nyborg, M. Seiersten, CORROSION\03, Paper no. 03314, NACE, 2003.

Chapter **VII**

Conclusions and Future Direction

VII.1. Main Conclusions

Although a considerable development of mitigation and control strategies has been achieved over the last few decades, internal CO_2 corrosion of pipelines is still a major concern to the petroleum industry that relates to the transportation of crude or semi-processed well streams. CO_2 corrosion is often associated to the presence of some other acidic gases and volatile short chain carboxylic acids usually co-produced with hydrocarbons. Acetic acid is one of the most prevalent organic acids found in oil and gas reservoirs with high concentrations up to thousands of ppm in the co-produced aqueous phase. Comprehensive studies have been devoted to the effect of HAc on the uniform corrosion in CO_2-containing media. However, the basic role of this organic compound in the initiation and growth of localized attacks is still a poorly understood issue. This is of particular interest in the case of the so-called top-of-line corrosion, which is the most severe form of internal corrosion encountered in wet gas lines operated in stratified flow regime. The main objective of this thesis has been the analysis of the qualitative behaviour often found in actual cases of TLC, that is, increasing corrosion rates and steep shrinkage after certain - not predictable- time delay. The focus has been on understanding and quantifying the underlying mechanisms controlling the growth and stifling of localized corrosion attacks in CO_2 and HAc environment and providing a complete scenario for the morphological trend.

The macroscopic kinetic behaviour of carbon steel in such brine indicated that the overall effect of the HAc is a balance between a boosted cathodic rate and an inhibited anodic one without any significant increase of the uniform corrosion current. The dissolution processes are therefore not straightforwardly related to the presence of acetic acid but rather to what is generically referred to as CO_2 corrosion. Also, the electrochemical results of the present study did not show a clear sign of an electroactive participation of adsorbed HAc molecules. The significant increase of the cathodic reaction rate observed in the presence of acetic acid appears to be rather related to the cathodic reduction of free protons. In this case, adsorbed HAc molecules would therefore act as a local proton reservoir. This is likely to preserve the pH of the micro-

environment adjacent to the steel surface by minimizing the limiting current induced by the mass transfer of H^+ from the bulk solution. Although the present results cannot give a direct answer concerning the inhibited rate of the anodic reaction observed in the vicinity of the corrosion potential in the presence of HAc, they nevertheless suggest that the adsorbed HAc molecules render the steel surface less accessible for carbonic species to drive the anodic dissolution. Further investigations are however required to elucidate this issue.

Careful examination of the shape variability in the current fluctuations generated on carbon steel in the experimental conditions of the present work showed that metastable pitting events are characterized by a quick rise followed by an exponential decay to the baseline level. It was suggested that the slow decay bears on a progressive repair of the freshly initiated pit due to a change in the local chemistry (i.e., mass transport control) rather than a slow discharging of the double layer capacitance. This was corroborated by both artificial pit measurements and simulation results where the effect of the purely ohmic drop on the pit growth mechanism was shown to be unlikely. On the other hand, analyses in the frequency domain indicated that the presence of HAc does not affect appreciably the initiation kinetics of metastable pitting events. Instead, the role of HAc in localized corrosion appears to be related to the growth mechanism. HAc was indeed shown to trigger and sustain the pit growth through a galvanic coupling between the pit bottom and the outer surface. Consumption of HAc inside the pit, in combination with the restricted convection and the extended diffusion path, gives rise to HAc concentration gradient between the pit bottom and the bulk solution. That is, HAc differential concentration cell is formed. Considering the monotonic evolution of the corrosion potential with HAc concentration, a potential difference induced by HAc depletion inside the pit is established between the occluded geometry and the boldly exposed surface. This implies that as long as HAc is depleted, the pit is galvanically coupled to the outer surface and propagates according to its polarization resistance for shallow pits, for which the depletion and hence the potential difference between the two environments is not too high and the electrolyte resistance can be neglected. Furthermore, the observed distribution for the coupling current versus depth relation indicated that the pit growth is self-sustained only to a certain pit depth, beyond which the dissolution current at the pit bottom vanished as it effectively occurs in actual

TLC cases. The steep decrease of the coupling current towards deeper pits, i.e. the mechanism of stifling, was rationalized on the basis of the progressive depletion of carbon dioxide as revealed by the simulated steady-state distribution of CO_2 along the cavity. Indeed, the depletion of CO_2 leads to a decrease of the corrosiveness and thereby an increase of the polarization resistance as indicated by the general trend of the overall resistance. Accordingly, established pits propagate and stifle according to the counteracting depletions of HAc and CO_2. This complete scenario is schematically featured in **Figure VII.1**. The proposed scenario has an important consequence for the pit morphology. The anticipated development will then be a radial growth from the pit mouth till the critical depth, whereupon the lateral growth and opening of the pit mouth will dominate. After a sufficient widening, the pit growth process may increasingly stifle due to enhanced mass transfer to the occluded site. This morphological trend is in line with field observations of TLC. Clustering of attacks may also be envisaged.
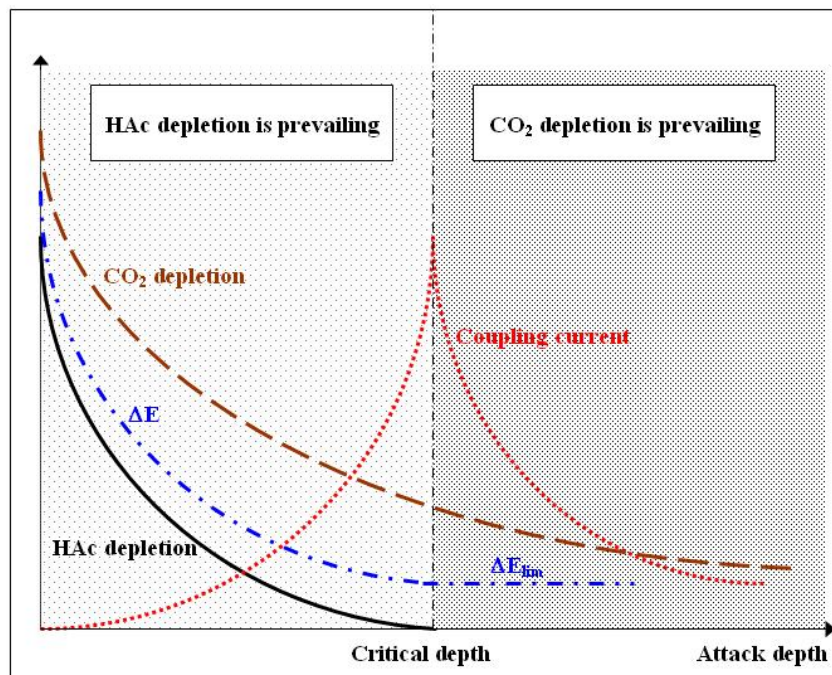
Figure VII.1. *Schematic illustration for the mechanisms of growth and stifling of localized corrosion attacks according to the counteracting depletions of HAc and CO_2. ΔE = potential difference.*

While likening artificial pit measurements for pits with electrically insulating sidewalls and with corroding sidewalls, the coupling current was unsurprisingly shown to be

lower in the latter case, since also the sidewalls become anodic. Furthermore, the critical depth of self-sustained pit growth is smaller than for the pit with insulated walls. Even though the pit with reactive sidewalls is the most realistic one, the pit with insulated pit walls is nevertheless a valuable simplification for understanding and demonstrating the concepts.

VII.2. Future Direction

This research raises some new questions and possibilities for future work:

- How do the operating conditions such as temperature, condensation rate, and solution conductivity affect the corrosion characteristics and the pit growth?

- Is there any contribution of $FeCO_3$ precipitation inside the pit to its stabilization?

- How can the pit geometry, particularly depth to width ratio, affect the pit growth?

- Does the steel microstructure, e.g. cementite structure orientation with respect to rolling direction, influence the pit growth (see **Figure VII.2**)?
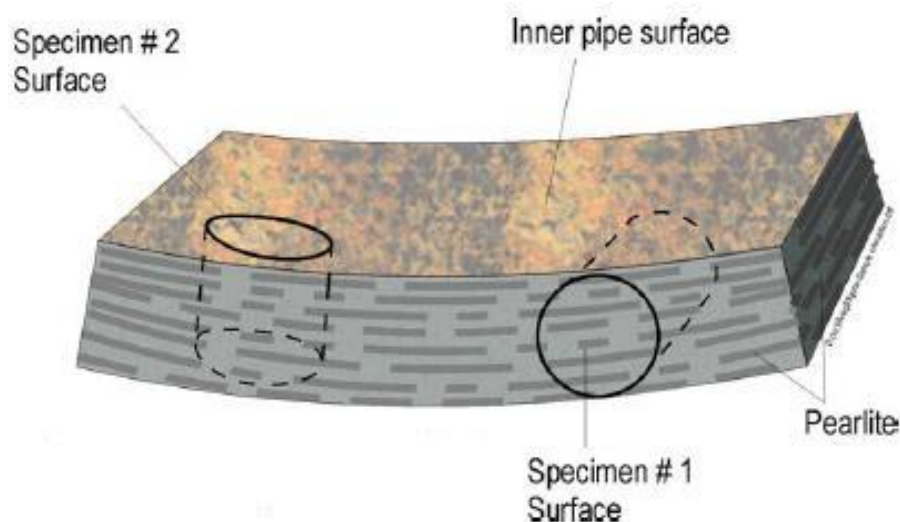
Figure VII.2. *Orientation of pearlite bands in ferrite-pearlite steel pipeline.*

We also saw that the predicted coupling current was overestimated particularly for deep pits, notwithstanding the fact that for shallow pits, simulations and experiments were in very good agreement. This underscores the need for further extension of the model, including:

- Further input data for pH > 5.5 and P_{CO2} < 1 bar

- CO_2 reaction part: polarization curves versus P_{CO2} and reaction limiting current for H_2CO_3

- Diffusion limiting current for HAc

- Corroding sidewalls

Journal Articles

.

Corrosion Science

Numerical simulation of a single corrosion pit in CO_2 and acetic acid environments

J. Amri [a,b], E. Gulbrandsen [a], R.P. Nogueira [b,*]

[a] *Institute for Energy Technology, P.O. Box 40, N-2027 Kjeller, Norway*
[b] *UMR5266 and 5631 INP Grenoble-CNRS-UJF, SIMAP and LEPMI, BP 75, 38402 St Martin d'Hères, France*

ARTICLE INFO

ABSTRACT

The present paper bears on a numerical model of steady-state behaviour of a single corrosion pit in CO_2-containing media in the presence of acetic acid. The kinetics of electrochemical reactions occurring on the electrode surface is described by Tafel equations fitted to experimental data obtained on API 5L X65 pipeline steel. Simulation results provide an interesting insight into both the chemistry and electrochemistry inside the active pit. Particular attention is paid to the effect of HAc on the coupling behaviour between the attack base and the outer surrounding surface and to the comparison with experimental data obtained in similar conditions.

© 2010 Elsevier Ltd. All rights reserved.

1. Introduction

Modern theories of localized corrosion ensue from the active dissolution theory developed in the 1960s [1,2]. According to this theory, the local conditions become substantially aggressive so that the metal dissolving inside the cavity is in the active state. This implies that the potential drops inside the cavity and often lies in the active region of the polarization curves [3]. The active dissolution theory was further challenged by the later observations of large potential drops as high as 1 V [4–7]. A competing theory based on *IR* drop concept was therefore formulated. The *IR* theory assigns major importance to potential (instead of compositional change) as the factor controlling both the rate and location of attack.

It is generally accepted that in all cases the activation of established pits or crevices stems from the driving force induced by the environmental difference between the localized corrosion site and its surrounding [1,8,9]. The compositional change theory stipulates that the basic role of the occluded geometry is to act as a barrier to chemical fluxes by restricting mixing of the cavity solution with the bulk. The change in electrolyte composition includes metal ion concentration cell [10], differential aeration cell [11,12], inhibitor concentration cell [13], pH [14,15], and chloride ion concentration cell [16,17]. Each of all these chemical gradients may drive the active dissolution of the metal inside the occluded region at a much higher rate than on the boldly exposed surface. This also supposes that the cavity solution must reach a critical degree of aggressiveness to trigger the active dissolution. The concept was

originally proposed by Mears and Evans [12], and it has become known as the critical crevice solution criterion (CCS). Oldfield and Sutton [18–20] were the first to develop a mathematical model based upon the CCS concept explicitly formulated by Fontana and Greene [1]. Even though it was developed specifically for crevice corrosion of stainless steel in neutral halide solutions, the Fontana and Greene concept has nevertheless been adapted with minor modifications for most alloys and can also be extended to other phenomena as those intervening in CO_2 corrosion. Basically, the concept identifies four stages. In the first stage, the metal dissolves over the entire surface. The cathodic reaction occurs both inside the cavity and on the boldly exposed surface. However, owing to the restricted mass transport to the occluded site, the oxidant is progressively depleted inside the cavity until the spatial separation of the anode and cathode becomes effective. The cavity then corrodes as being galvanically coupled to the outer surface. This marks the onset of the second stage. The accumulation of metallic cations, enhanced by the mass transport restrictions inherent in the geometry, is concomitantly balanced by the electromigration of aggressive anions into the cavity from the bulk solution. Upon reaction with metallic cations, some of aggressive anions are tied up in instable complexes, which are then quickly hydrolyzed. This hydrolysis lowers the local pH through the production of hydrogen ions, thereby increasing the dissolution current inside the cavity. In a later stage, the large cathode-to-anode area ratio and the self-sustaining nature of the process stabilize the active dissolution by exceeding the rate at which Fickian driving force can upset the established balance. All the mechanisms based on the compositional change theory were however questioned by Vetter and Strehblow [21]. The authors stipulated that the deterministic factors of pitting should be influential during all the stages of pit

* Corresponding author. Tel.: +33 4 76 82 65 93.
 E-mail address: ricardo.nogueira@grenoble-inp.fr (R.P. Nogueira).

growth even for the detectable pits as small as one micron in diameter, and that such compositional changes would be initially meaningless to be considered at the origin of pitting phenomena.

The inability of the compositional change theory to rationalize some observed cases of active dissolution in the absence of local acidification or large influx of aggressive anions (anions build-up), which are the two pre-requisites for the Fontana and Greene model, has prompted Pickering et al. to propose the *IR* drop theory [6,7,22,23]. Unlike the former theory, the *IR*-drop mechanism ascribes primacy to the electrical changes inside the occluded site. Once the oxidant is totally depleted inside the cavity, the spatial separation of the anode and cathode occurs. This results in a net current flowing through the resistive electrolyte path towards the boldly exposed surface. The basic feature of the theory is that the ohmic drop in the cavity electrolyte causes the local electrode potential to become less oxidizing than the electrode potential at the outer surface until it lies in the active region of the polarization curve. In this way, the metal inside the cavity dissolves actively at a much higher rate than the outer surface. However, the effect of the resulting potential drop strongly depends on the electrochemical kinetics of the metal. For a metal exhibiting anodic Tafel behaviour, a potential drop is always protective as it lowers the driving force for active dissolution. The *IR*-drop mechanism does therefore operate only for passive metals exhibiting an active peak on the anodic branch. By analogy with the CCS theory, Pickering et al. conceptualized the critical potential drop IR^* as a pre-requisite for the onset of active dissolution inside the cavity. One of the aspects that Pickering and co-authors have emphasized is the ability of the *IR* drop theory to anticipate and rationalize the morphological trend of corrosion attacks [23,24]. Since the local potential is being continuously shifted towards the less noble direction, the expected morphology would be related to the polarization curve as a function of the position inside the cavity. The concept thus anticipates the existence of a critical depth around which the active dissolution is confined. The maximum dissolution rate at the critical depth corresponds to the active peak on the anodic branch of the polarization curve.

These two major lines of interpretation, compositional changes and *IR* drop, can be considered when dealing with some particular corrosion cases in CO_2-containing media (sweet systems). Internal CO_2 corrosion of carbon steel pipelines for transportation of crude or semi-processed oil and gas is still a major concern in the petroleum industry. In the absence of preventive and corrective measures like injection of inhibitors, the engineering structure can suffer high corrosion rates up to 10 mm per year (mm/y). Besides CO_2 and water, other acidic gases such as hydrogen sulphide (H_2S) or volatile short chain carboxylic acids are usually co-produced with hydrocarbons. Acetic acid, commonly denoted as HAc, is one of the most prevalent organic compounds found in oilfield brines with concentrations ranging from a few hundreds up to thousands of ppm. Results reported from either field observations or laboratory investigations have shown that the presence of HAc may induce a detrimental effect on the overall corrosion rate and the pitting morphology in sweet systems [25]. For this reason, the role of organic acids in general and HAc in particular has increasingly caught up the attention of the major actors in oil and gas fields over the last few years. The HAc issue has been addressed in a large number of independent studies over a wide range of operating conditions as discussed and summarized in recent literature reviews [26,27]. Even though considerable progress has been achieved on the understanding of the effect of HAc on the uniform corrosion of carbon steel in CO_2 environments, little information however exists regarding the basic role of this organic acid in the growth mecanism of localized attacks [28–32]. This is particularly relevant in the case of the so-called top of line corrosion (TLC), which is recognized as the most severe forms of internal corrosion encountered in wet gas transportation. In which is referred to as TLC, the fast pit initiation stage (that can be assimilated to the Fontana and Greene model) is often followed by the stifling of the pit growth which could be related to ohmic drops along the pit depth. In some previous works [30–32] we have been dealing with this issue by means of specific experimental assemblies, where it was possible to reproduce this growth-stifling behaviour. Such behaviour was ascribed to the competing effects of the concomitant depletion of both CO_2 and HAc inside the pit. In the present paper we tried to validate these results thanks to a numerical model that could better control or emulate some of the key parameters involved in the evolution of single pit in CO_2–HAc containing media as discussed hereafter. Before going deeper in the subject, it is important to mention that what is here called pit is not to be straightforwardly associated with the ubiquitous passive film – corroding pit systems in chloride rich environments. Indeed, the reaction mechanisms in that case are certainly different from the one discussed hereafter. Nevertheless, in which concerns the current distribution behaviour and the simulation inputs, our central pit did behave as a purely anodic region fully surrounded by a passive large surface. More precisely, even if the localized attack mechanism is not related to an active–passive transition as in the case of chloride attack of passive films, the macroscopic features of the pit evolution in the present case does approach the behaviour of a corroding pit separated from the surrounding surface. References to the chloride pitting literature are hence proposed as a bridge between the two phenomena that also help the non expert reader to have a more clear insight in what we do believe take place in terms of current distribution between the inner and the outer electrodes as a consequence of the presence of both CO_2 and HAc inside the pit.

2. Modelling localized corrosion

Despite the technical challenges posed by the geometric constraints, considerable advances have been achieved in the experimental characterization and modelling of localized corrosion of passive metals. Particularly, recent studies have made strides toward advancing of the fundamental understanding of the role of some key factors [33] in localized corrosion such as temperature [34,35], metal microstructure [36–39] and electrolyte composition [40,41]. Difficulty in studying pitting corrosion also arises due to the fact that the current measured from a corroding electrode may flow from several indiscriminate sites with unknown active pit surface area. In order to alleviate this ambiguity, an alternative technique consists of studying a single attack in naturally simulated pit environments. Multiple pits are therefore avoided, and only the dissolution kinetics of the active pit is probed. This has been made technically feasible by means of artificial pit assembly. Such technique has been successfully used in our recent works [30–32] and in a number of previous studies [42–44]. Because of these geometric constraints, however, experimental measurements can only be performed at discrete points in time and space, and can therefore only provide limited information about the key factors controlling the pit behaviour. There are many difficulties associated with the experimental characterization of the local conditions inside corrosion pits. Pit dimensions are exceedingly tight and the insertion of probes can influence the corrosion process, thereby rendering the measured values unrealistic. Also, there is a small solution inside a pit available for analysis. As a result, a number of mathematical models have been developed in literature over the last years. Mathematical modelling can bridge the gaps between experimental values and allows prediction of the impact of a large range of variables, thus helping to provide a more complete framework of the pit behaviour. One of the major advantages

of modelling is also its ability to uncouple factors that in practice cannot be separated. Indeed, the implementation of virtual experiments with only a subset of gathered data can sometimes be used to gain a valuable insight into the interrelations between experimentally inseparable factors.

To date, most of modelling (and simulation) approaches of localized corrosion attacks have been fundamentally based on Newman's mass transport theory for dilute electrolyte [45,46]. From a broad point of view, modelling localized corrosion must involve consideration of the environmental conditions and the interfacial processes that occur between the metal and its environment. These considerations include; chemical equilibria, mass transport modes, and metal kinetics. In most cases, however, governing processes are described by a large set of equations of tightly coupled and non-linear nature. A number of models in literature have therefore had recourse to simplifying assumptions to make the problem easier to solve. Also, the scarce of either theoretical or experimental data does not permit use of the complete solution and making assumptions may prove to be essential in certain cases and this will not be different here.

Most of pit and crevice corrosion models have been developed on the basis of infinite dilution theory. A few illustrative examples of steady-state models are presented here In a series of papers, Galvele [47,48], and Galvele and Gravano [49] developed three CCS pitting corrosion models. Unlike the two first models, where mass transport was assumed to occur exclusively via diffusion mode, the final model included the electromigration term and the electroneutrality condition was applied. The results were drawn in terms of concentration profile as a function of the product "*current × depth*" for a unidirectional pit. The authors attributed the pit activation to the local acidification arising from the metal ions hydrolysis with the major change occurring near the pit opening. Sharland and Tasker [50] simulated the propagation stage of a pit on carbon steel. The pit was modelled as a parallel-sided slot in a dilute sodium chloride solution. Mass transport process was described in terms of diffusion and electromigration and convection was neglected. This assumption deserves an important comment. At these dimensions, convection should probably not be formally disregarded. Nevertheless, we preferred to proceed to this simplifying assumption held to approach experiments results obtained with the 2 mm artificial pit assembly. This has been also the case in several other papers from different authors [51–53] that also worked with pits or crevices larger than 1 mm radius without finding major drawbacks from this assumption. A physical justification for this to be held is related to the fact that natural convection is driven by density gradients caused by concentration or temperature differences. In the present case, the solution density is expected to increase continuously downwards into the pit as a consequence of the increasing Fe^{2+} and Cl^-, i.e. the heaviest liquid in the bottom of the pit. If this holds true the density gradient would not contribute to convection (this would be different for an actual top-of-line pit, but holds for our experimental setup which we intend to model and compare to). The lower part of the pit would have the lowest solution resistance, hence more heating and lower liquid density towards the top of the pit. This could cause some natural convection at the pit mouth, but at deeper depths the temperature/density gradient would again oppose convection.

The model predicts the steady-state chemistry and kinetics inside the active cavity as a function of many parameters such as external electrode potential and cavity dimensions. A comparison was made between pits with reactive and non-reactive sidewalls. The one-dimensional pit model developed by Walton [54] accounted for mass transport in both acetic and sulphuric solutions by diffusion and electromigration. The condition for local charge neutrality was also applied and the concentrations were assumed to be constant at the pit mouth. Upon a dimensional analysis of the governing equation, Walton concluded that the condition inside the corrosion cell is no more than a consequence of the counteracting effects of transport process and species generation. By analogy with the "*severity factor*" of Bernhardsson [55], Walton determined the "*geometry factor*", *depth²/width*, as a key indicator of the solution aggressiveness inside the cavity. A transient version of this model was also presented later by Walton et al. [56]. In recent years, modelling studies of corrosion phenomena, including stochastic modelling [57] and neural network modelling [58], have been paid increasing attention and valuable advances have been made in this area.

In spite of the large amount of information brought by these precursor works, it is worth noticing that much is still to be done, mainly in which concerns the combined effects of reactants as in the case of CO_2–HAc corroding systems. The presence of HAc and other weak organic acids, indeed, makes the water chemistry much more complex, thereby making this sound like a difficult proposal for modelling. Based on mostly field reports, the presence of organic acids was associated with the onset of localized attacks, little is however understood about the role of these compounds in the growth mechanism. In a recent review devoted to the key issues related to modelling internal corrosion of oil and gas pipelines [27], Nešić identified one of the main drawbacks of this subject as being the scarce information concerning the role of HAc in localized attacks. This was precisely the aim of the present paper as well as that of our previous recent articles [30–32].

3. The pit model – conceptual description

3.1. Theoretical background

In aqueous environments, mass transfer of species from one location to another is driven either by differences in electrical or chemical potential between the two locations or by motion of a volume element of the electrolyte. The modes of mass transfer are thus migration, diffusion and convection. This underscores the need for the concept of the electrochemical potential ($\tilde{\mu}_j$) that obeys the same criteria at equilibrium as the chemical potential. In a stagnant electrolyte subjected to diffusion and migration, where mass transfer phenomena due to the convective forces are relatively small so that they can be ignored, the net molar flux of a species j is written in a functional form of the electrochemical potential:

$$N_j = -u_j C_j \nabla(\tilde{\mu}_j) \tag{1}$$

where u_j is the mobility and C_j is the concentration. The electrochemical potential is formally the sum of the chemical potential (μ_j) and the contribution from charged species described by the electrostatic potential (V) in the electrolyte:

$$\tilde{\mu}_j = \mu_j + z_j F V \tag{2}$$

with z_j being the charge number and F being the Faraday's constant. From rigorous thermodynamic considerations, Eq. (2) must be regarded as a simplifying postulate since chemical interactions of given species with its environment are also electrical in nature. Since

$$\mu_j = \mu_{j0} + RT \ln(\gamma_j C_j) \tag{3}$$

Then,

$$N_j = -D_j \nabla C_j - u_j z_j C_j F \nabla V \tag{4}$$

Here, γ_j and μ_{j0} denote the activity coefficient and the standard chemical potential, respectively. The other parameters have their usual meanings. The diffusion coefficient varies with the mobility according to the following correlation:

$$D_j = u_j RT \left(1 + \frac{\partial \ln \gamma_j}{\partial \ln C_j}\right) \tag{5}$$

The above equation still holds even under the influence of long-range and short-range electrostatic interactions between cations and anions. For electrolytes that are sufficiently diluted so that the infinite dilution theory may apply, the expression in the brackets is close to 1. That is

$$\lim_{C_j \to 0} \frac{\partial \ln \gamma_j}{\partial \ln C_j} = 0 \tag{6}$$

In Eq. (4), the first term on the right hand side represents the diffusion contribution arising from a concentration gradient while the second term represents the migration contribution induced by the electric field in the electrolyte. Assuming a mass-conservation condition, the full transport-reactive phenomena may be fundamentally described by:

$$\frac{\partial C_j}{\partial t} + \nabla(N_j) = R_j \tag{7}$$

R_j stands for the reaction rate including both production and consumption parts. Substituting N_j in Eq. (7) yields the following general form:

$$\frac{\partial C_j}{\partial t} = D_j \nabla^2 (C_j) + z_j u_j F \nabla[C_j \nabla(V)] + R_j \tag{8}$$

The second order gradient of the electrostatic potential is related to the space charge density (ρ) in the electrolyte via Poisson's equation that operates on a much faster time scale than electromigration and diffusion:

$$\nabla^2 (V) = -\frac{\rho}{\varepsilon_0 \varepsilon_r} = -\frac{F}{\varepsilon_0 \varepsilon_r} \sum_j z_j C_j \tag{9}$$

where ε_0 and ε_r denote the vacuum permittivity and the relative permittivity of the electrolyte, respectively. The solution conductivity (σ) is given by:

$$\sigma = \frac{F^2}{RT} \sum_j z_j^2 D_j C_j \tag{10}$$

3.2. Assumptions

The model consisted of a single pit in a dilute electrolyte. All the diffusion coefficients were assumed isotropic and constant. A major geometrical simplification was made by assuming conveniently the pit as a perfect cylindrical hole with a base diameter of 2 mm and a finite depth within the range 0–20 mm. Note that the pit dimensions were selected so that a comparison between simulation results and experimental findings recently published by the authors [30,31] was feasible. Thanks to the cylindrical symmetry, the model was reduced to a two-dimensional pattern. The axial symmetry also allowed the consideration of only the one-half of the model, thus reducing substantially the resolution time. On the other hand, it was assumed that natural convective forces were sufficiently large so that the homogeneity and equilibrium conditions were ascertained in the bulk. The calculation domain for the outer electrode was then set within the Nernst diffusion layer of a thickness δ estimated to 300 μm for natural convection conditions [59]. Inside the cavity, however, this mode of mass transport was neglected due to the geometrical restrictions. According to Poisson's Eq. (9), the term $(\varepsilon_0 \varepsilon_r)^{-1}$ is sufficiently large ($\sim 10^9$) so that any slight deviation from the charge neutrality would induce very large electrical restoring forces [60,61]. These forces tend to remove charge gradients on a much faster time scale than those associated with pure electromigration or diffusion processes [50]. The issue was actually circumvented by considering the motion of charged species so fast so that the condition for the local charge neutrality of volume elements is met at any time and any point. That is

$$\sum_j z_j C_j = 0 \tag{11}$$

3.3. Boundary settings

The boundary settings are particularly important since they describe both the chemical and electrochemical processes occurring at the metal-electrolyte interface. In this condition, the molar fluxes are proportional to the overall current density generated by the cathodic (i_a) and anodic (i_c) reactions at the metal surface through Faraday's law:

$$i = i_a + i_c = F \sum_j z_j N_j \tag{12}$$

A dimensional description of the model and the corresponding boundary settings are schematically represented in Fig. 1. To allow the comparison between predictions and experimental results, simulations were exclusively carried out on a single attack with non-reactive and electrically insulating sidewalls. The kinetics of electrochemical reactions occurring on the electrode surface is essential for determining the corrosion rate of a metal exposed to a corrosive medium. These reactions strongly depend on the electrode potential E:

$$E = \varphi_{WE} - \varphi_{RE} \tag{13}$$

where ϕ_{WE} and ϕ_{RE} are the Galvani potentials of the working electrode and the reference electrodes, respectively. For a freely corroding electrode (i.e. at zero net current) at its open circuit potential, E_{corr}, as well as for IR-compensated data in polarized conditions, the interfacial electrochemical processes can be described in terms of current–potential relationships, for instance Tafel equations if appropriate. To simulate the galvanic coupling effect, the sum of the partial currents integrated over the area of the pit base must balance the total current integrated over the area of the boldly exposed surface. In the finite-element calculations, both the potential and the current distributions are rather calculated in the electrolyte domain. In that case, the electrode is just represented as a boundary condition describing the current–potential relationship at the metal–electrolyte interface. This therefore underscores the need for a new formalism that relates to the electrolyte domain. One simple definition, which directly relates to experimental measurements, is the potential $V(r, \theta, z)$ of a reference electrode versus the corroding electrode. That is,

$$V(r, \theta, z) = \varphi_{RE}(r, \theta, z) - \varphi_{WE} \tag{14}$$

with r, θ and z being the cylindrical coordinates. Hence, the electrolyte potential $V(r, \theta, 0)$ at a given point of the boundary representing the working electrode surface as well the new open circuit potential V_{corr} are given by:

$$V(r, \theta, 0) = -E \tag{15}$$
$$V_{corr} = -E_{corr} \tag{16}$$

Here E denotes the potential of the working electrode versus the reference electrode located at a given point of the surface (i.e. IR-compensated data). Note that the new electrode polarization ΔV remains unchanged as if it would have been obtained in a more conventional manner:

$$\Delta V = V_{corr} - V(r, \theta, 0) = (-E_{corr}) - (-E) = E - E_{corr} \tag{17}$$

3.4. Model application

The electrochemical kinetics was described by Tafel equations fitted to experimental data obtained on API 5L X65 pipeline steel (see Ref. [32] for steel composition) in CO_2-containing media in the presence of HAc. According to experimental results, the corro-
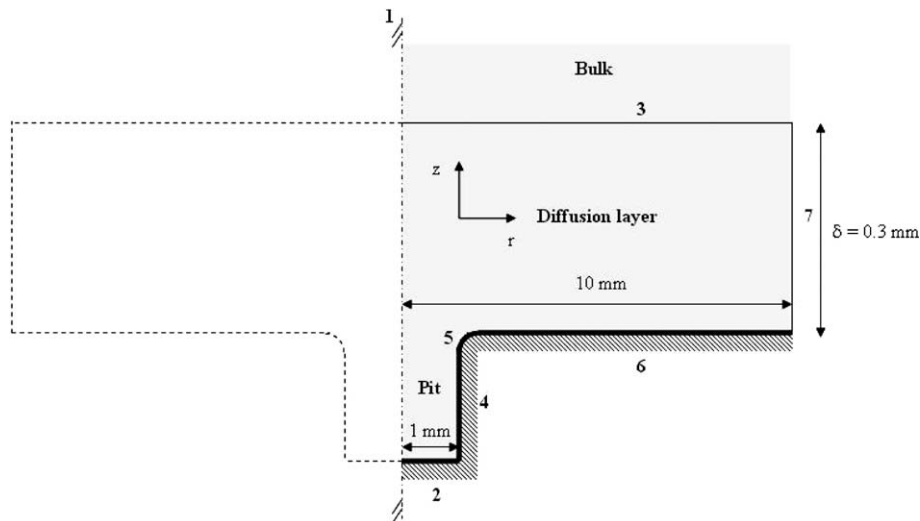
Fig. 1. Dimensional description of the 2D-axisymmetric pit and the corresponding boundary settings. 1- Axial symmetry; 2- Pit bottom: $i = i_a + i_c$; 3- $C_j = C_j^{eq}$; 4- Pit sidewall: Electric insulation; 5- Chamfer: Electric insulation; 6- Outer surface: $i = i_a + i_c$; 7- Electric insulation. The chamfer (boundary 5) was used to smooth the straight corner, thereby simplifying the numerical grid pattern.

sion potential has been shown to increase monotonically with HAc concentration [30–32]. In the present model, we implemented the E_{corr} data reported in Fig. 3 of Ref. [31]. A similar fitting of i_{corr} – HAc data was also used. The anodic and cathodic Tafel slopes were experimentally found to be fairly independent of HAc concentration for a pH within the range 3.5–5.5 and were hence assumed constant with b_a and b_c being 50 mV/decade and −120 mV/decade, respectively. Since proton reduction and iron dissolution were the only electrochemical reactions considered in this model, the net fluxes of H^+ and Fe^{2+} at the metal boundaries were given by Eq. (12); the fluxes for all other species were hence assumed zero. The simulated supporting electrolyte consisted of 17 mM aqueous NaCl solutions containing different amounts of HAc and saturated with 1 bar CO_2. The chemical reactions as well as their respective equilibrium (K_{eq}) and reaction rate (k_j) constants at 25 °C are listed in Table 1. In addition to water, these reactions involved eleven aqueous species. They are reported in Table 2 along with their diffusion coefficients and initial concentrations [26,62–67]. The sodium and chloride ions do not take part in the chemical reactions, but help preserving the local charge neutrality. Further simplification of the model was made by omitting the formation of iron carbonate layers. This simplification sounds reasonable since $FeCO_3$ precipitation is very slow at room temperature [26,68], and the formation of protective layers takes weeks at such temperatures even under conditions of artificially elevated pH [67].

4. Simulation results

4.1. Pit chemistry

Since no moving boundaries were involved in the model, each calculation was therefore carried out independently in a static geometry (i.e. at a given depth) using Comsol Multiphysics© with a convergence criterion of 10^{-4}. The predicted steady-state composition of the pit electrolyte is shown in Fig. 2. Large quantities of ferrous ions are generated by the metal dissolution with concentrations exceeding 100 mM deeper into the cavity. At such concentrations, the dilution theory still nevertheless applies. The major impact of high ionic concentrations is through the *IR* drop in electrolyte. Within this range, the maximum error in the calculation of the electrostatic potential is less than 1%. Also, most of the ionic flux within the pit is carried by diffusion. The effect that this error would have on the rate of ionic transport via electromigration mode is hence negligible. The increasing positive charges of metallic cations are balanced by a large migration of chloride ions from the bulk electrolyte and the formation of bicarbonate and acetate anions. The relatively high concentration observed for bicarbonate anions results from a high dissociation rate of carbonic acid.

4.2. CO₂ depletion

According to the Law of Mass Action, a high dissociation rate of carbonic acid should boost the hydration reaction of carbon dioxide (cf. reactions 3 and 4 in Table 1). Moreover, the geometric constraints would limit the ability of aqueous carbon dioxide to move into the pit so that CO_2 depletion occurs faster than diffusion can follow. This is what was actually observed as shown in Fig. 3. The predicted depletion of CO_2 is of major importance regarding the steep decrease of the coupling current beyond a certain depth that has been observed in recent work [32]. Indeed, beyond a critical depth the depletion of CO_2 should in principle lead to a decrease of the corrosiveness and thereby an increase of the polarization resistance. To validate the hypothesis of CO_2 depletion as the key parameter behind the process of stifling observed in Fig. 4 of Ref. [32], some specific measurements were performed with a split-cell in which two identical electrodes were placed in two identical compartments separated by a salt bridge, so that

Table 1
List of the chemical reactions considered in this model and their respective thermodynamic and kinetic constants at 25 °C. The subscripts "b" and "f" stand for backward and forward (reactions), respectively. All the reaction rate constants are in s^{-1} units, except for k_b expressed in $m^{-1} s^{-1}$.

	Chemical reactions	pK_{eq}	k_j (reaction rate constant)	Refs.
1.	$H_2O \rightleftharpoons H^+ + OH^-$	14	$k_b = 7.85 \times 10^{10}$	[62]
2.	$CO_2(g) \rightleftharpoons CO_2(aq)$	1.468	–	[63,64]
3.	$CO_2(aq) + H_2O \rightleftharpoons H_2CO_3$	2.588	$k_f = 3 \times 10^{-2}$	[63,64]
4.	$H_2CO_3 \rightleftharpoons HCO_3^- + H^+$	3.5	$k_f = 7.80 \times 10^6$	[26,63,64]
5.	$HCO_3^- \rightleftharpoons CO_3^{2-} + H^+$	10.33	$k_f = 6.07$	[26,65,66]
6.	$HAc \rightleftharpoons H^+ + Ac^-$	4.80	$k_f = 3.20 \times 10^5$	[26,67]

Table 2

List of aqueous species considered in the model along with their diffusion coefficients and initial concentrations. (*) pH; (**) calculated from K_j; (***) calculated using the condition of mass conservation of total acetic species. The concentration of undissociated HAc is expressed in ppm units and corresponds to 600 ppm of total acetic species (HAc + Ac⁻) at pH 3.38.

| Species | | | | | | | | | | |
Na^+	Cl^-	H^+	OH^-	Fe^{2+}	CO_2	H_2CO_3	HCO_3^-	CO_3^{2-}	HAc	Ac^-
Diffusion coefficients at 25 °C in units of $10^{-9}\ m^2\ s^{-1}$										
1.3	2	9.3	5.3	0.7	1.96	2	1.1	0.92	1.2	1.1
Initial conditions										
17 mM	17 mM	3.38*	**	0	1 bar	**	**	**	578	***

Fig. 2. Simulated steady-state composition of the electrolyte along the pit depth in the base solution (17 mM NaCl, 600 ppm HAc, 1 bar CO_2).
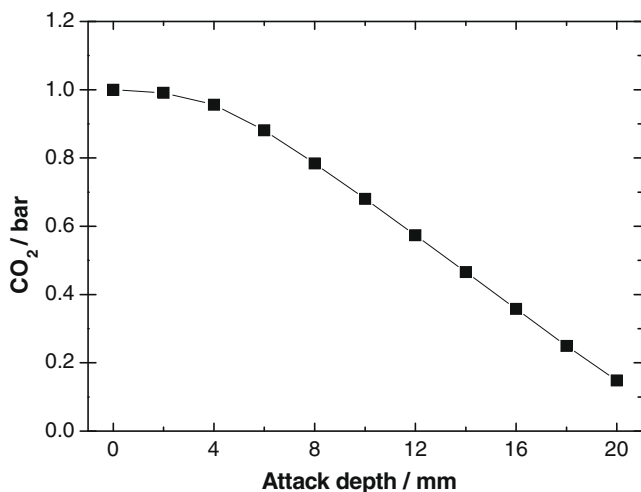

Fig. 3. Simulated steady-state profile of CO_2 concentration, reported as equilibrium partial pressure, along the pit depth in the base solution (17 mM NaCl, 600 ppm HAc, 1 bar CO_2).
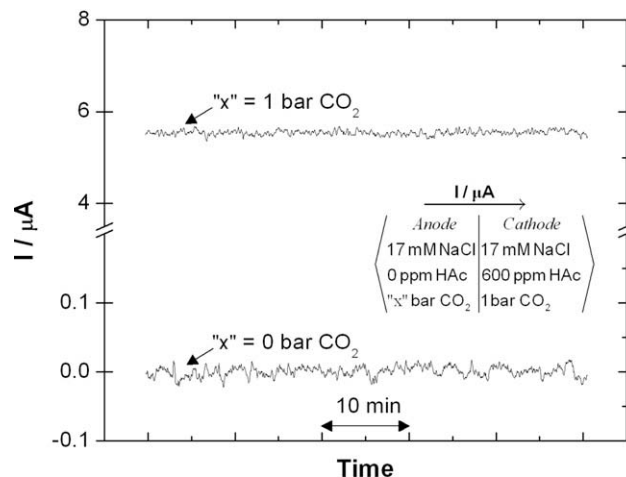

Fig. 4. Current flow between two identical electrodes in a split-cell composed of two identical compartments separated by a high conductivity salt bridge. One of the compartments (cathode) contained the base 17 mM NaCl aqueous solution containing 600 ppm HAc and saturated with 1 bar CO_2. The other compartment (anode) was filled with HAc-free solution of 17 mM NaCl saturated with "x" bar CO_2, thus simulating distinct conditions of no depletion ("x" = 1) and total depletion ("x" = 0) of CO_2.

no geometric differences were present. The salt bridge was connected to both compartments through porous glass frits that allow ion migration but restrict bulk mixing of the two solutions. One of the compartments was filled with the simulated supporting electrolyte, that is, 17 mM NaCl aqueous solution containing 600 ppm HAc and saturated with 1 bar CO_2, the second being filled with HAc-free solutions of 17 mM NaCl saturated with "x" bar CO_2. Fig. 4 depicts the current flow between the two electrodes in distinct conditions simulating no depletion ("x" = 1) and total deple-

tion ("x" = 0) of CO_2. For the latter case, the solution was de-aerated by purging nitrogen for 2 h prior to each experiment, and the nitrogen gas flow was maintained over the solution throughout the measurement to prevent oxygen ingress. To make the comparison feasible, the pH of the HAc depleted compartment (i.e. anode) was adjusted to 3.80 in the case "x" = 0. This value refers to the pH measured in the anodic compartment in the condition "x" = 1. Results clearly point out a net anodic polarization induced by the HAc depletion – resulting in a net anodic current – of the electrode exposed to the electrolyte simulating no CO_2 depletion ("x" = 1) as seen in the figure. This anodic polarization of the HAc depleted compartment was always and reproducibly observed throughout the test duration. In comparison, a significant shrinkage of the coupling current was found between the two electrodes in CO_2 depleted conditions that would make the solution less aggressive. This is consistent with the idea of CO_2 depletion causing the stifling of pit growth [32]. In this case, pits would thus propagate and stifle mainly according to the counteracting depletions of acetic acid and CO_2. A SEM cross-section of a pre-initiated pit after immersion during 3 months in 17 mM NaCl and 600 ppm HAc showed that propagation did not occur in CO_2 free-solutions regardless of the presence of HAc as illustrated by Fig. 5, which also agrees well with the results of Fig. 4. This suggests that the potential difference induced by HAc differential concentration cell, only, is not enough to trigger the active dissolution inside the pit in the absence of CO_2. In such case, pit activation would be a matter of interfacial interactions of carbonic species with the metal, with HAc being a driving factor.
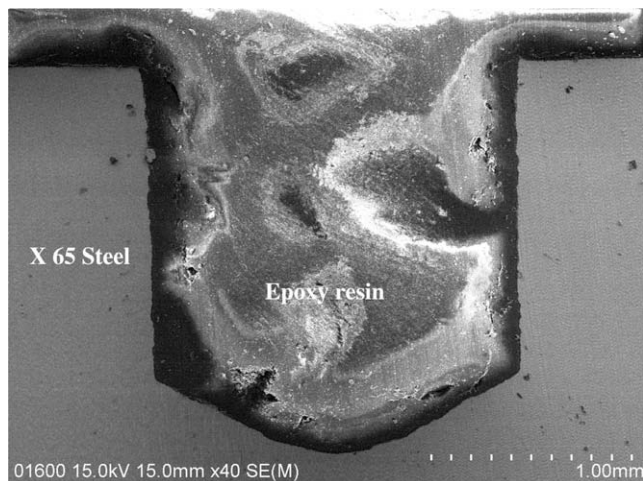
Fig. 5. SEM cross-section of 2 mm-depth attack on API 5L X65 sample after immersion during 3 months in 17 mM NaCl and 600 ppm HAc (0 bar CO₂). The solution was continuously purged with nitrogen to prevent oxygen ingress.

4.3. HAc depletion

The other important feature of the steady-state behaviour of the pit is related to the variation of undissociated HAc concentration between the bulk electrolyte and the cavity as depicted in Fig. 6. The predicted profile clearly shows a depletion of HAc inside the pit. This depletion is not only due to the consumption of protons by the cathodic reaction at the pit base but also to mass transport limitations induced by the geometric constraints. Shallow pits are indeed more easily fed by mass transport of HAc than deep ones. The acid depletion inside the pit induces a concentration gradient in respect with the bulk, that is, a HAc differential concentration cell is formed. The depletion of HAc is also an important fact since the corrosion potential decreases with decreasing HAc concentration as reported in our previous studies [30–32]. The differential cell thus establishes a potential difference so that the pit is anodically polarized by the outer large surface. This result is in good agreement with the experimental findings, where HAc was clearly found to trigger and sustain pit growth via galvanic coupling mechanism in CO₂-containing environments [30]. SEM cross-sections of two pre-initiated pits immersed during 3 months in HAc-containing and HAc-free solutions indeed showed that propagation
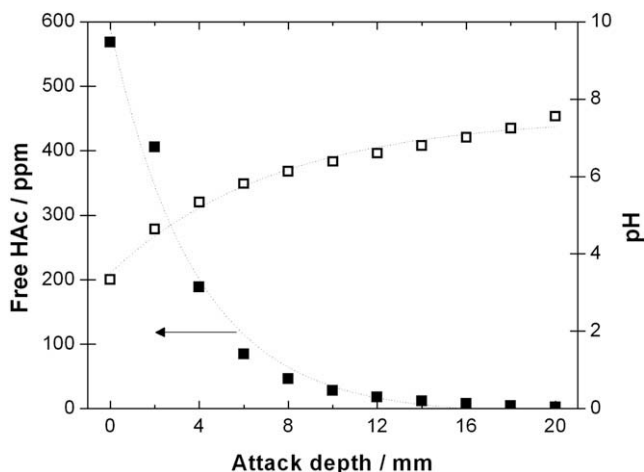
is appreciably enhanced in the presence of HAc (Figs. 7 and 8). For instance, a rough estimation of the corrosion rate from the depth of attack inside the pit in both cases indicated that propagation was three times larger in CO₂–HAc corroding systems. As the HAc depletion goes on deeper into the attack, CO₂ corrosion is expected to become prevailing, thus resulting in a local alkalinization as evidenced by the predicted steady-state pH profile of Fig. 6. In a similar way to the aforementioned study, a complementary investigation was performed by means of the split-cell technique to assess the effect of HAc on the coupling behaviour. One of the compartments was filled with 17 mM NaCl aqueous solutions containing "x" ppm HAc and saturated with 1 bar CO₂, the second contained 17 mM NaCl aqueous solution saturated with 1 bar CO₂ and simulated a total depletion of HAc. The variation of the current flow between the two electrodes as a function of HAc concentration is featured in Fig. 9. Considering the E_{corr}–HAc relation [31], increasing HAc concentration was unsurprisingly shown to enhance the net anodic polarization – resulting in an increase of the net anodic current – of the electrode exposed to the electrolyte simulating depleted conditions. Results also show that the current levels off towards high concentrations of the organic compound, thereby suggesting a saturation of the electrode surface with HAc adsorbates.

4.4. Comparison of model predictions with experimental data

The simulated values of the *IR*-uncompensated potential difference between the outer surface and the pit base at distinct positions inside the cavity were likened to the previous experimental data [31]. As indicated by Fig. 10, the agreement between the model predictions and the experimental measurements is very good. In both cases, the potential difference was shown to increase monotonically with pit depth until it levels off for deeper pits. This is unsurprising considering the monotonic depletion of HAc depicted in Fig. 6, on the one hand, and the close relationship between the organic compound and the corrosion potential, on the other hand. Also shown in Fig. 10 is an inset featuring a comparison between simulated and measured values of the pure ohmic resistance (R_s) of the narrow electrolyte path inside the pit. The predicted R_s values were calculated via Eq. (10). Recently [31], it was demonstrated that the *IR*-drop mechanism is unlikely to operate for localized corrosion of carbon steel in CO₂/HAc brine. This was actually corroborated by the low values of R_s, which also suggest that the local depletion of CO₂ is the main cause of stifling. The simu-

Fig. 6. Simulated steady-state profiles of HAc concentration and pH in the base solution (17 mM NaCl, 600 ppm HAc, 1 bar CO₂).
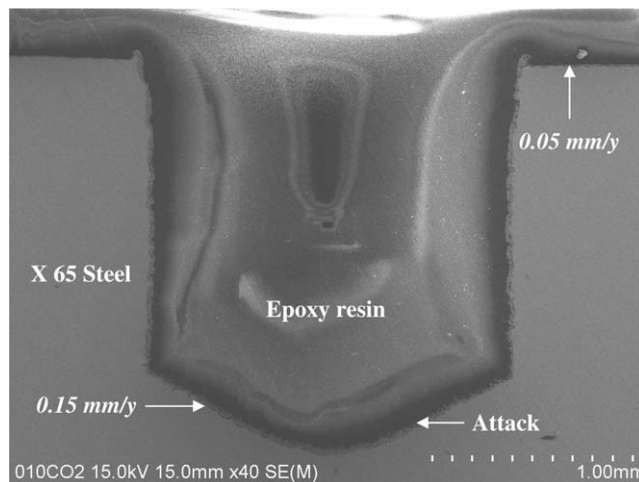

Fig. 7. SEM cross-section of 2 mm-depth attack on API 5L X65 sample after immersion during 3 months in 17 mM NaCl and 0 ppm HAc saturated with 1 bar CO₂.
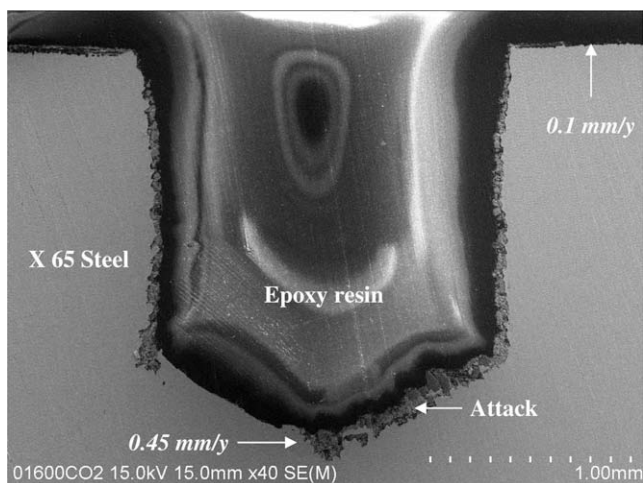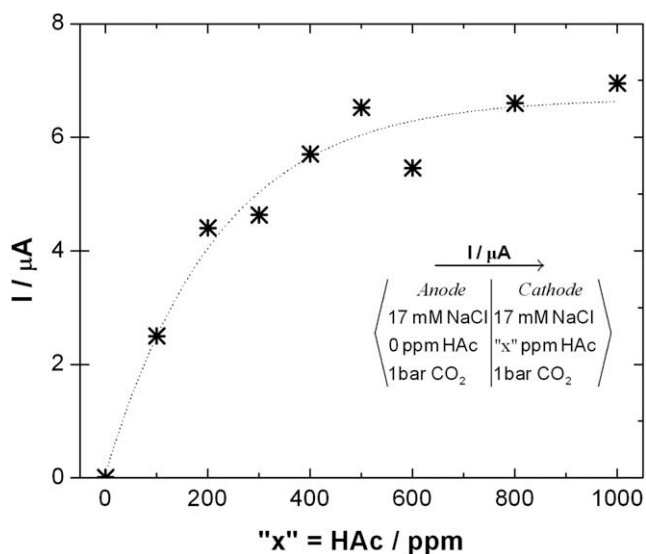
Fig. 8. SEM cross-section of 2 mm-depth attack on API 5L X65 sample after immersion during 3 months in 17 mM NaCl and 600 ppm HAc saturated with 1 bar CO_2.
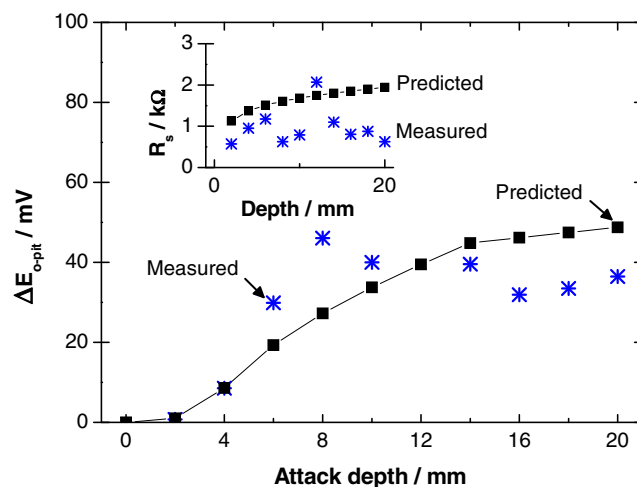

Fig. 10. Simulated and measured IR-uncompensated distributions of the potential difference between the outer large surface and the pit bottom in the base solution (17 mM NaCl, 600 ppm HAc, 1 bar CO_2). Also shown in the inset is a comparison between simulated and measured values of the ohmic resistance of the narrow electrolyte path inside the pit.
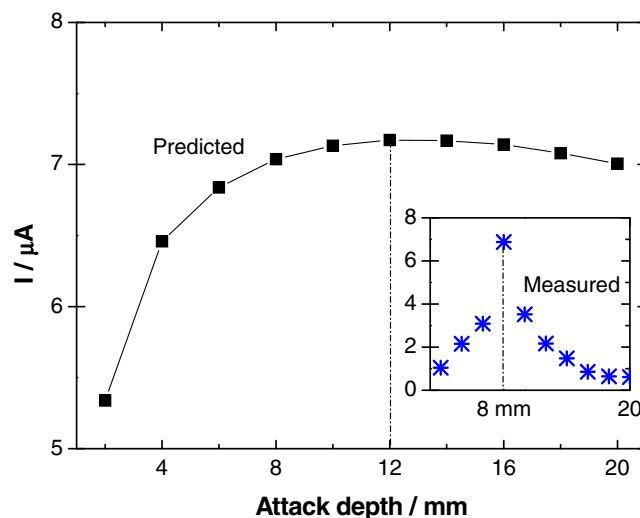

Fig. 9. Current flow between two identical electrodes in a split-cell composed of two identical compartments separated by a high conductivity salt bridge. One of the compartments (cathode) contained the base 17 mM NaCl aqueous solution containing "*x*" ppm HAc and saturated with 1 bar CO_2. The other compartment (anode) was filled with HAc-free solution of 17 mM NaCl saturated with 1 bar CO_2.

Fig. 11. Simulated and measured distributions of the coupling current in the base solution (17 mM NaCl, 600 ppm HAc, 1 bar CO_2).

lated distribution of the coupling current between the pit bottom and the outer large surface is depicted in Fig. 11. Recall that the coupling current is the sum of the individual current densities integrated over the area of the exposed surface. The model reveals that the current reaches a maximum at 12 mm. The simulated distribution corroborates the experimental result obtained with the help of zero resistance ammeter and artificial pit electrodes [30]. In fact, typical distributions of the coupling current flowing between the actively corroding attack bottom and the outer large surface clearly showed the existence of a transition depth at 8 mm below which the current increases and beyond which it sharply drops off. It is also worth noticing that the magnitude of the calculated current is in fair agreement with the experimental data. The predicted current-depth peak however seems not as sharp as that found experimentally. This may be ascribed to the fact that measured electrochemical data implemented in the present model were limited to pH ⩽ 5.5 and P_{CO_2} = 1 bar. Implementation of data for high

pH and lower P_{CO_2} would probably give a sharper current-depth peak. This issue is discussed further in the section hereafter. At 2 mm depth, however, the partial pressure of CO_2 is practically 1 bar (see Fig. 3) and the pH is almost 4.5 (see Fig. 6). This gave very good agreement between predicted and experimental results as illustrated by Fig. 12.

4.5. Model limitations and proposal for future improvements

The steady-state model described in this paper gives some reasonable qualitative predictions, which are globally and quantitatively in fair agreement with experimental results. However, the comparisons also reveal some weakness of the model primarily related to the limited range of the key input parameters. For instance, the overestimation of the coupling current particularly towards deeper pits underscores the need for reliable empirical input data required for modelling the system at higher pH and lower CO_2 partial pressures. Indeed, the electrochemical kinetic correlations implemented in the present model are strictly valid for 1 bar CO_2 and for a pH within the range 3.5–5.5. In contrast, the actual results
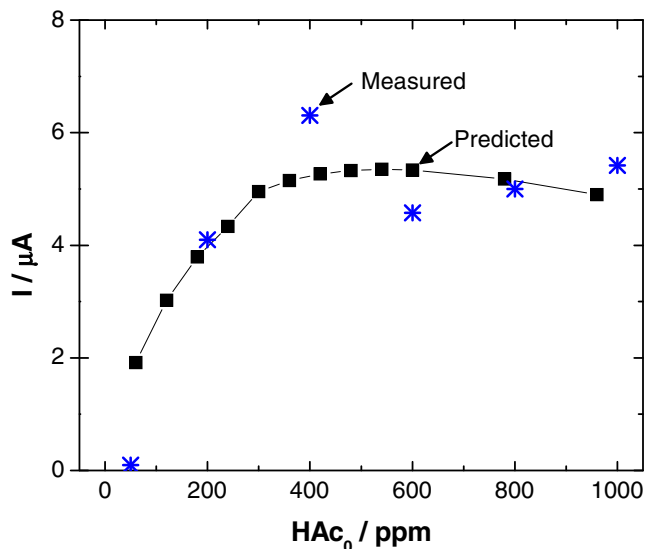
Fig. 12. Simulated and measured coupling currents versus the initial concentration of HAc for a pit of 2 mm diameter and 2 mm depth in 17 mM NaCl solution saturated with 1 bar CO_2.

cover the CO_2 partial pressure range from 1 to 0.15 bar and the pH range from 3.5 to 7.5 down the pit as illustrated in Figs. 3 and 6, respectively. The sensitivity of the model results to the key input parameters must therefore be analyzed with an extreme caution regarding the reaction orders of the anodic and cathodic reaction kinetics with respect to H^+ (i.e. pH) and CO_2. The pH dependency of the overall anodic dissolution of iron in CO_2 corroding systems has been controversial until the detailed mechanistic studies of Nešić et al. [69]. The authors have experimentally showed that a direct extrapolation of the mechanism developed by Bockris et al. [70] to CO_2 corrosion at pH > 4 is unreliable. An alternative reaction scheme accounting for the effects of pH and CO_2 partial pressure has therefore been proposed. In comparison to strong acids, the new scheme emphasizes that the elementary dissolution kinetics of iron in CO_2 solutions is catalyzed by carbonic species acting as adsorbed chemical ligands, $Fe–CO_2$ [27,69]. On the other hand, it has been demonstrated that the anodic dissolution of iron does not depend significantly on OH^- concentration above pH 4, but is affected by the presence of CO_2 [69]. This also corroborates the previous studies of Davies and Burstein [71] who suggested that the active dissolution of iron in bicarbonate solutions is triggered by the formation of the complex $Fe(CO_3)_2^{2-}$. Likewise, Videm [72] reported that the presence of CO_2 increased the anodic part reaction rate, being otherwise independent of pH at values higher than 4.2. This effect was tentatively ascribed to bicarbonate anions. Considering the pH range of interest in the present study and the weak dependency of the anodic process on OH^- above pH 4, it is unlikely that the local alkalinization observed in Fig. 6 would at once accelerate corrosion and hinder the precipitation of iron carbonate within the pit. A more rigorous consideration of the effect of CO_2 partial pressure on the anodic reaction inside the pit would nevertheless have been made in the present model over the whole range of pH studied. In their work, Nordsveen et al. [73,74] reported a reaction order with respect to P_{CO_2} changing from 2 at pH < 4 to 1 within an intermediate pH range 4 < pH < 5 and completely vanishing for higher values. At 1 bar CO_2, the anodic reaction is independent of pH [73,74]. The profile of Fig. 3, however, indicates that CO_2 is progressively depleted inside the cavity. To allow for this local CO_2 fluctuation, a reaction order of 1 with respect to H^+ [73,74] could have been used for the anodic reaction inside the pit beyond 4 mm depth. In addition, a better representation of

the pH dependency of the overall cathodic reaction for pH > 5.5, for instance a reaction order of 0.5 [73,74], is also required and should be a subject for future improvements of the model. The anodic Tafel slope was also shown to be pH-dependent [69,73,74]. In comparison, b_a and b_c were experimentally found to be fairly independent of HAc concentration for a pH within the range 3.5–5.5 in this study, and were hence assumed constant. According to Bockris et al. [70] an apparent transfer coefficient of 1.5 for the anodic reaction and 0.5 for the cathodic reaction gives an anodic Tafel slope of 40 mV/decade and cathodic Tafel slope of 118 mV/decade at 25 °C, which agreed well with the input data and other experimental findings [75].

5. Conclusions

A flexible and predictive model of steady-state behaviour of a single pit was developed and applied to API 5L X65 pipeline steel in CO_2/HAc media. The model is general in form, thus allowing extension and application to a variety of systems. A promising agreement was obtained between the model predictions and experimental data acquired with the help of artificial pit measurements. This agreement gave complementary evidence about the major role played by HAc in the growth mechanism of actively corroding pits through galvanic coupling effect. The predicted results clearly showed a local depletion of HAc, which is due not only to the consumption of protons by the cathodic reaction inside the pit but also to mass transport restrictions that are inherent to the occluded geometry. The model also predicted a progressive depletion of CO_2 with depth. The depletion of CO_2 should in principle lead to a decrease of the corrosiveness and thereby an increase of the polarization resistance. This finding is of a major importance in the sense that it rationalizes the steep decrease observed for the current-depth distribution towards deeper pits. In view of all these elements, established pits are likely to propagate according to the counteracting depletions of HAc and CO_2. As indicated by the predicted pH-depth profile, a local alkalinization is therefore expected rather than an acidification, which would also contribute to hinder the active dissolution inside the pit as a result of $FeCO_3$ precipitation for a wide time scale. In agreement with experimental observations, the predicted distribution for the coupling current versus depth relation showed the existence of a transition depth beyond which the pit is no more self-sustained. The magnitude of the predicted coupling current was in fair agreement with experimental data. The predicted current-depth peak was however not as sharp as that found experimentally, notwithstanding the fact that for shallow pits, simulations and experiments were in very good agreement. The overestimation of the coupling current particularly for deep pits was ascribed to the restricted range of experimental data implemented in the model. Overall, even though a certain similarity with the compositional change theory can be inferred from the described pit growth mechanism, the latter nevertheless deviates in several ways from that of stainless steels and other passive metals. The *IR*-drop formalism is hence unlikely to operate in such conditions.

References

[1] M.G. Fontana, N.D. Greene, Corrosion Engineering, McGraw-Hill, New York, 1967. 41.
[2] J. Tousek, Theoretical Aspects of the Localized Corrosion of Metals, Trans. Tech. Publications, Switzerland, 1985.
[3] H.J. Engell, Electrochim. Acta 22 (1977) 987.
[4] H.W. Pickering, Mater. Sci. Eng. A198 (1995) 213.
[5] C.M. Chen, F.H. Beck, M.G. Fontana, Corrosion 27 (1971) 234.
[6] H.W. Pickering, Corros. Sci. 29 (1989) 325.
[7] A. Valdes, H.W. Pickering, Advances in Localized Corrosion, in: H. Isaacs, U. Bertocci, J. Kruger, Z. Szklarska-Smialowska (Eds.), NACE-9, NACE, Houston, TX, 1990.
[8] L.L. Shreir, Corrosion, vol. 1, Newnes, Butterworths, 1976.
[9] F. Dabosi, G. Beranger, B. Baroux, Corrosion Localisée, Les Editions de Physique, les Ulis, 1994.
[10] R.J. McKay, Trans. Electrochem. Soc. TESOA 41 (1972) 201.
[11] U.R. Evans, J. Inst. Metals 30 (1923) 239.
[12] R.B. Mears, U.R. Evans, Trans. Faraday Soc. 30 (1934) 417.
[13] U.R. Evans, L.C. Bannister, S.C. Britton, Proc. Roy. Soc. A131 (4131) (1931) 355.
[14] I.L. Rosenfeld, I.K. Marshakov, Corrosion 20 (1964) 115t.
[15] W.D. France, N.D. Greene, Corrosion 24 (1968) 247.
[16] I.B. Ulanovskii, J. Appl. Chem. 39 (1966) 768.
[17] J. Mankowski, Z. Szklarska-Smialowska, Corros. Sci. 15 (1975) 493.
[18] J.-L. Crolet, J.M. Defranoux, L. Seraphin, R. Tricot, Mem. Sci. Rev. Metall. 71 (1974) 797.
[19] J.W. Oldfield, W.H. Sutton, Brit. Corros. J. 13 (1978) 13.
[20] J.W. Oldfield, W.H. Sutton, Brit. Corros. J. 13 (1978) 104.
[21] K.J. Vetter, H.H. Strehblow, Localized Corrosion, in: B.F. Brown, J. Kruger, R.W. Staehle, A. Agarwal (Eds.), NACE-3, NACE, Houston, TX, 1974.
[22] H.W. Pickering, Corrosion 42 (1986) 125.
[23] H.W. Pickering, Advances in Localized Corrosion, in: H. Isaacs, U. Bertocci, J. Kruger, Z. Szklarska-Smialowska (Eds.), NACE-9, NACE, Houston, TX, 1990.
[24] Y. Xu, M. Wang, H.W. Pickering, J. Electrochem. Soc. 140 (1993) 3448.
[25] A. Dugstad, CORROSION/06, Paper no. 06111, NACE, 2006.
[26] E. Gulbrandsen, K. Bilkova, CORROSION/06, Paper no. 06364, NACE, 2006.
[27] S. Nešić, Corros. Sci. 49 (2007) 4308.
[28] Y. Sun, K. George, S. Nešić, CORROSION/03, Paper no. 03327, NACE, 2003.
[29] M. Singer, D. Hinkson, Z. Zhang, H. Wang, S. Nešić, CORROSION/09, Paper no. 09292, NACE, 2009.
[30] J. Amri, E. Gulbrandsen, R.P. Nogueira, Electrochem. Commun. 10 (2008) 200.
[31] J. Amri, E. Gulbrandsen, R.P. Nogueira, Electrochim. Acta 54 (2009) 7338.
[32] J. Amri, E. Gulbrandsen, R.P. Nogueira, Corrosion, in press.
[33] G.S. Frankel, J. Electrochem. Soc. 145 (1998) 2186.
[34] M.H. Moayed, N.J. Laycock, R.C. Newman, Corros. Sci. 45 (2003) 1203.
[35] M.H. Moayed, R.C. Newman, Corros. Sci. 48 (2006) 1004.
[36] M. Kaneko, H.S. Isaacs, Corros. Sci. 44 (2002) 1825.
[37] G.O. Ilevbare, G.T. Burstein, Corros. Sci. 45 (2003) 1545.
[38] L. Peguet, B. Malki, B. Baroux, Corros. Sci. 51 (2009) 493.
[39] T.-S. Huang, G.S. Frankel, Corros. Sci. 49 (2007) 858.
[40] M. Kaneko, H.S. Isaacs, Corros. Sci. 42 (2000) 67.
[41] M.H. Moayed, R.C. Newman, Corros. Sci. 48 (2006) 3513.
[42] J. Marsh, J.W. Palmer, R.C. Newman, CORROSION/2002, Paper no. 02288.
[43] D. Deforge, F. Huet, R.P. Nogueira, P. Ponthiaux, F. Wenger, Corrosion 62 (2006) 514.
[44] C. Gabrielli, S. Joiret, M. Keddam, N. Portail, P. Rousseau, V. Vivier, Electrochim. Acta 53 (2008) 7539.
[45] J.S. Newman, Localized Corrosion, in: B.F. Brown, J. Kruger, R.W. Staehle, A. Agarwal (Eds.), NACE-3, NACE, Houston, TX, 1974.
[46] J.S. Newman, Advances in Localized Corrosion, in: H. Isaacs, U. Bertocci, J. Kruger, Z. Szklarska-Smialowska (Eds.), NACE-9, NACE, Houston, TX, 1990.
[47] J.R. Galvele, J. Electrochem. Soc. 124 (1976) 464.
[48] J.R. Galvele, Corros. Sci. 21 (1981) 551.
[49] J.R. Galvele, J.R. Gravano, Corros. Sci. 24 (1984) 517.
[50] S.M. Sharland, P.W. Tasker, Corros. Sci. 28 (1988) 603.
[51] F.M. Song, N. Sridhar, Corros. Sci. 50 (2008) 70.
[52] G. Engelhardt, M. Urquidi-Macdonald, D.D. Macdonald, Corros. Sci. 38 (1996) 1613.
[53] S.M. Sharland, C.P. Jackson, A.J. Diver, Corros. Sci. 29 (1989) 1149.
[54] J.C. Walton, Corros. Sci. 30 (1990) 915.
[55] S. Bernhardsson, L. Eriksson, J. Oppelstrup, I. Puigdomenech, T. Wallin, in: 9th Scandinavian Corrosion Congress (1984).
[56] J.C. Walton, G. Cragnolino, S.K. Kalandros, Corros. Sci. 38 (1996) 1.
[57] J.L. Alamilla, E. Sosa, Corros. Sci. 50 (2008) 1811.
[58] S. Nešić, M. Nordsveen, N. Maxwell, M. Vrhovac, Corros. Sci. 43 (2001) 1373.
[59] S. Nešić, B.F.M. Pots, J. Postlethwaite, N. Thevenot, J. Corros. Sci. Eng. 1 (1995) (Paper 3).
[60] S.M. Sharland, Corros. Sci. 27 (1987) 289.
[61] A. Turnbull, Modelling Aqueous Corrosion: From Individual Pits to System Management, NATO Science Series, vol. 266 (1993).
[62] P. Delahay, J. Am. Chem. Soc. 74 (1952) 3497.
[63] S. Nešić, M. Nordsveen, R. Nyborg, A. Stangeland, CORROSION/01, Paper no. 40, NACE, 2001.
[64] D.A. Palmer, R.V. Eldik, Chem. Rev. 83 (1983) 651.
[65] M. Eigen, Angew. Chem. 75 (1963) 489.
[66] W. Knoche, Biophysics and Physiology of Carbon Dioxide, Springer-Verlag, Germany, 1980. 3.
[67] K.J. Vetter, Electrochemische Kinetics, Springer-Verlag, 1960. 406.
[68] A. Dugstad, R. Nyborg, M. Seiersten, CORROSION/03, Paper no. 03314, NACE, 2003.
[69] S. Nešić, N. Thevenot, J.-L. Crolet, D.M. Drazic, CORROSION/96, Paper no. 1100, NACE, 1996.
[70] J.O.M. Bockris, D. Drazic, A.R. Despic, Electrochim. Acta 4 (1961) 325.
[71] H. Davies, G.T. Burstein, Corrosion 36 (1980) 385.
[72] K. Videm, Progress in the Understanding and Prevention of Corrosion, in: Proceedings from 10th European Corrosion Congress, vol. 1, Institute of Metals, London, 1993, p. 513.
[73] S. Nešić, M. Nordsveen, R. Nyborg, A. Stangeland, CORROSION/01, Paper no. 01040, NACE, 2001.
[74] M. Nordsveen, S. Nešić, R. Nyborg, A. Stangeland, Corrosion 59 (2003) 443.
[75] S. Nešić, J. Postlethwaite, S. Olsen, Corrosion 52 (1996) 280.

Propagation and Arrest of Localized Attacks in Carbon Dioxide Corrosion of Carbon Steel in the Presence of Acetic Acid

J. Amri,[‡], E. Gulbrandsen,** and R.P. Nogueira****

ABSTRACT

The presence of acetic acid (HAc) has been identified as one factor that may contribute to enhance localized top-of-the-line corrosion attacks in gas condensate pipelines. The role of free HAc on the growth of localized attacks in carbon dioxide (CO_2) corrosion of carbon steel pipelines therefore was studied by means of a preinitiated localized attack electrode assembly ("artificial pit electrode"). The current flowing between the localized attack and the outer surface was measured with a zero-resistance ammeter. It is shown that the corrosion potential increases with increasing free HAc concentration. Depletion of free HAc inside the attack imposed a potential difference that triggered the propagation of the attack at room temperature. The pit growth was self-sustained in CO_2 and HAc environments only to a certain depth, beyond which the dissolution current at the bottom of the attack vanished. This is in good agreement with field observations in the case of top-of-the-line corrosion phenomena.

KEY WORDS: acetic acid, carbon dioxide corrosion, localized attack, pipeline steel

INTRODUCTION

Internal carbon dioxide (CO_2) corrosion of pipelines for transportation of unprocessed oil and gas constitutes a major problem to the petroleum industry,

where carbon steel is still the principal material of choice.[1] In the absence of preventive mitigation efforts like injection of inhibitors, the corrosion rates may be several mm per year, thus leading to premature failure of installations.[2] Top-of-the-line corrosion (TLC) is the most serious concern encountered in the transportation stage of hydrocarbons.[3] TLC occurs in wet gas transportation when the coproduced water vapor condenses on the internal upper part of the pipe due to external cooling. TLC rates significantly increase with water condensation rate, which can be too high if the pipe is not properly thermally insulated. TLC is also difficult to mitigate by corrosion inhibition in wet gas lines operated in stratified flow regime, since the inhibitors cannot easily reach and protect the upper part of the pipe. The TLC rate can even be increased dramatically in the presence of short chain carboxylic acids. Acetic acid (CH_3COOH), denoted as HAc, is frequently the most abundant organic acid found with high concentrations up to thousands ppm in the coproduced aqueous phase.

Increasing attention has been paid to the effect of HAc on the corrosion of carbon steel over the last years. On the basis of results issued from field observations and laboratory investigations, HAc is recognized to contribute considerably to the overall corrosion rate.[3-5] Recent results showed that the type of corrosion in the presence of HAc is influenced by the operating temperature.[4] According to these results, HAc was found to inhibit general corrosion while promoting the propagation of few, but deep, localized attacks at room temperature. At elevated temperatures, however, the corrosion was high but

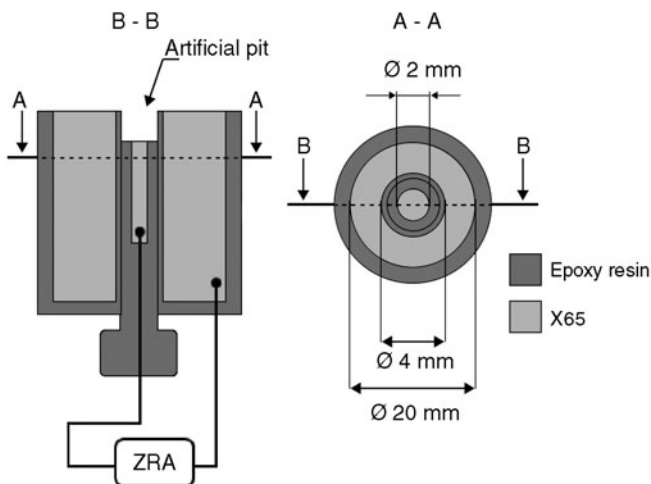| C	Si	Mn	S	P	Cr	Ni	V	Mo	Cu	Al	Sn	Nb
0.08	0.25	1.54	0.001	0.019	0.04	0.05	0.095	0.01	0.02	0.038	0.001	0.043

FIGURE 1. *Schematic illustration of the artificial pit assembly.*

uniform with rates exceeding several tens of mm per year.[4] In a previous laboratory study on CO_2 corrosion of carbon steel, results obtained with artificial pit electrodes at room temperature also identified free HAc as a driving factor that triggers and sustains the growth of localized attacks through a coupling effect.[6]

Inspection of gas lines from different fields indicates that the TLC attacks have stabilized in many cases (i.e., stopped growing) after an initial period of high rates.[7] Despite comprehensive studies that have been devoted to the effect of HAc on the uniform corrosion in CO_2-containing media, rudimentary understanding however exists regarding the basic role of this organic compound in localized corrosion. This is of particular interest in the case of TLC, which is the most severe form of internal corrosion encountered in wet gas transportation. The underlying mechanisms controlling TLC attacks are still not well understood, and this makes TLC phenomenon even more difficult to predict. The goal of the present chapter is therefore to go deeper in the analysis of the qualitative behavior often found in actual situations of TLC phenomenon, that is, increasing localized corrosion rates and steep shrinkage after certain—not predictable—time delay. The focus is on how free HAc influences the mechanism of the growth of localized corrosion attacks.

EXPERIMENTAL PROCEDURES

Potentiodynamic polarization measurements were performed in a conventional three-electrode cell on coupons machined from API 5L X65 pipeline steel.

The elemental composition of the steel is given by Table 1. The working electrodes were wet-polished with silicon carbide (SiC) papers down to 1200 grit size, rinsed with distilled water, and cleaned with acetone (CH_3COCH_3). The test solutions were 0.1 wt% aqueous sodium chloride (NaCl) saturated with 1 bar CO_2 during 2 h prior to each experiment. The CO_2 gas flow was maintained over the solution throughout the measurement. Different amounts of HAc, within the range from 0 to 600 ppm, were also added initially to the test solution. The potential was scanned at a rate of 1 mV/s in the cathodic-to-anodic direction. Slower sweep rates also would certainly be appropriate, but this could entail compositional changes in the electrolyte inside the artificial pit assembly described below. In this sense, in order to perform polarization curves in equivalent experimental conditions all over the study, we preferred to keep the 1 mV/s, which is nonetheless very frequently used in the literature. A coiled titanium wire was used as the counter electrode and all potentials were measured against a saturated calomel electrode (SCE) connected to the cell via a Luggin capillary. For all the sections hereafter, the term "base solution" is referred to as 0.1 wt% NaCl, 600 ppm of total acetic species (575.40 ppm free HAc and 24.60 ppm Ac⁻ at free pH 3.38) saturated with 1 bar CO_2.

Artificial pit measurements were acquired thanks to the asymmetric assembly successfully used in previous studies[8-9] and schematically illustrated in Figure 1. The working electrode surfaces were the cross sections of two concentric rods of 2 mm and 20 mm diameters, respectively, embedded in epoxy resin. Preinitiated attacks were simulated by adjusting the central electrode to a given depth within the range from 0 to 20 mm. The specimen was positioned vertically into the cell with the electrode surfaces facing upward. Real-time record of the current flowing between the two coupled electrodes was monitored with a zero-resistance ammeter (ZRA). Considering the large ratio between the two exposed surfaces (1:96), the measured couple potential was governed practically by the electrochemical reactions occurring on the outer large electrode. The ZRA setup was connected in such a way that any positive current flow is indicative of an anodic behavior of the central electrode (i.e., the pit bottom). Such technique was used successfully to investigate the propagation of localized CO_2 corrosion attacks on mild steel induced by the galvanic effect between scale-covered and scale-free surfaces, respectively.[10] This technique was also

shown to be useful in the evaluation of the corrosion inhibitor's ability to slow down the propagation rate of localized attacks.[11]

Unless stated otherwise, all measurements were performed on preinitiated pits with inert, insulating sidewalls (insulating epoxy resin).

RESULTS AND DISCUSSION

The effect of free HAc on the polarization curves of carbon steel at three pH values was investigated at room temperature. The choice of room temperature was intended to overcome some difficulties that may rise while investigating the pit behavior at elevated temperatures such as the high risk of crevice corrosion and the presence of hydrogen bubbles trapped inside the pit, which could act as a gas-cavity. This work constitutes, nevertheless, a first understanding and a basis for future studies at high temperatures. For all measurements at a given pH value, the total concentrations of acetic species (free HAc + acetate) added to the test solution were 60, 180, and 600 ppm. Figure 2 shows the variation of free HAc concentration with pH at different total acetic species concentrations. The bulk pH was held constant to assess the contribution of free HAc to the cathodic and anodic reactions, respectively. This was achieved by measuring regularly the pH and, if needed, adjusting with the addition of droplets of hydrochloric acid (HCl) or sodium hydroxide (NaOH). Also, measurements were carried out in a large 2-L cell to prevent any significant depletion of free HAc in the bulk. The concentration of free HAc at equilibrium was determined by considering the partial dissociation of the weak acid and the condition for mass conservation of total acetic species. It clearly appeared from Figures 3 through
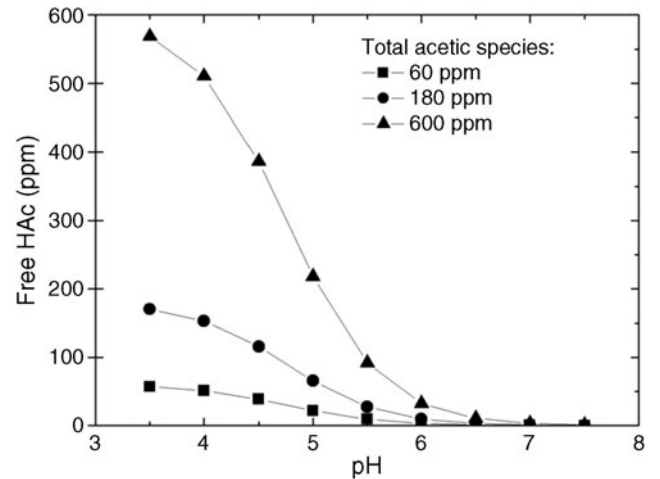

FIGURE 2. *Variation of the free HAc concentration with pH at different amounts of total acetic species. 0.1 wt% NaCl, 1 bar CO_2, room temperature.*

5 that free HAc entails a significant enhancement of the cathodic part reaction rate (hydrogen evolution). A slight shift of the anodic polarization branch toward higher potentials was also observed. Further increase of the pH, however, resulted in a less positive shift of the anodic branches. The cathodic reaction acceleration in the presence of free HAc results in a subsequent monotonic evolution of the corrosion potential (E_{corr}), as depicted in Figure 6. Systematic measurements at constant pH indeed showed a positive shift of E_{corr} with increasing free HAc concentration. Previous results issued from a laboratory study on CO_2 corrosion of carbon steel pipeline showed that free HAc acts as a driving factor in the propagation stage of localized corrosion attacks.[6] It is worth stress-
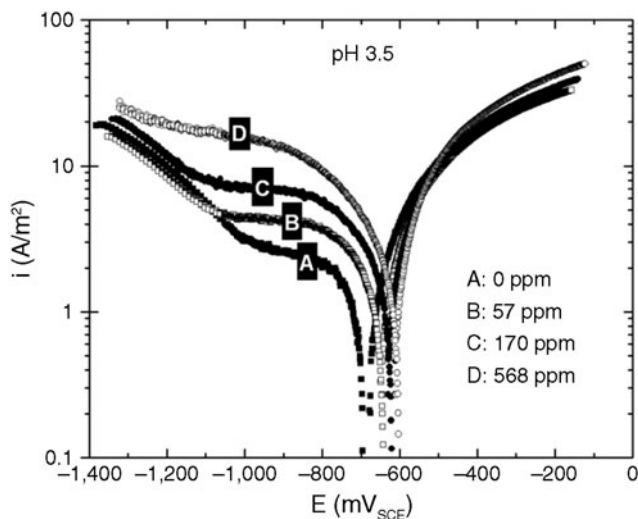

FIGURE 3. *Polarization curves of X65 steel at different concentrations (A, B, C, D) of free HAc at pH 3.5. 0.1 wt% NaCl, 1 bar CO_2, room temperature.*

FIGURE 4. *Polarization curves of X65 steel at different concentrations (A, B, C, D) of free HAc at pH 4.5. 0.1 wt% NaCl, 1 bar CO_2, room temperature.*
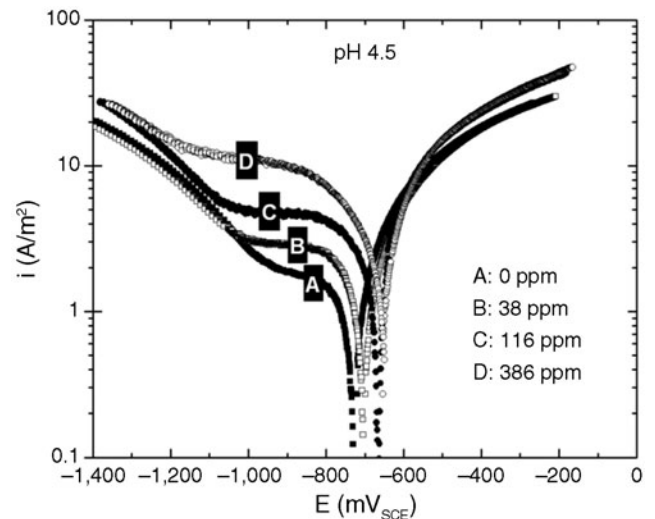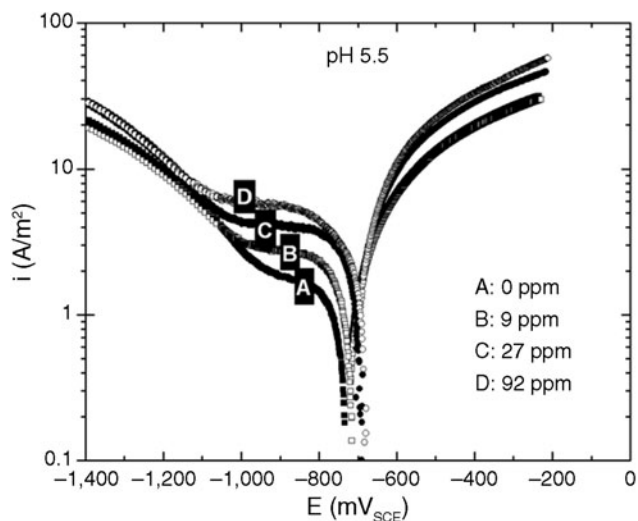
FIGURE 5. *Polarization curves of X65 steel at different concentrations (A, B, C, D) of free HAc at pH 5.5. 0.1 wt% NaCl, 1 bar CO₂, room temperature.*
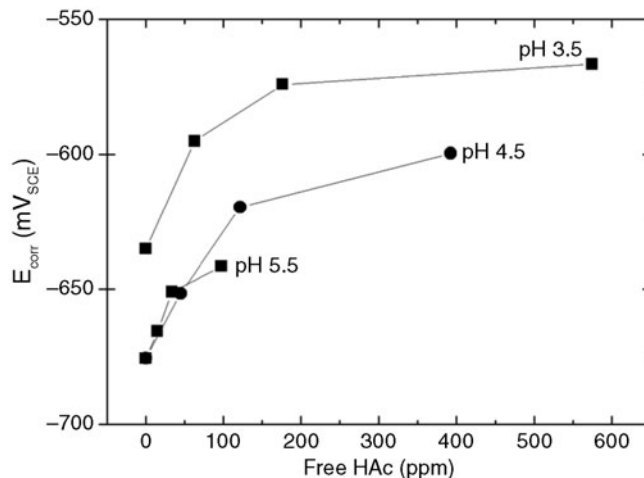

FIGURE 6. *Variation of the corrosion potential of X65 steel with free HAc concentration at different pH values. 0.1 wt% NaCl, 1 bar CO₂, room temperature.*
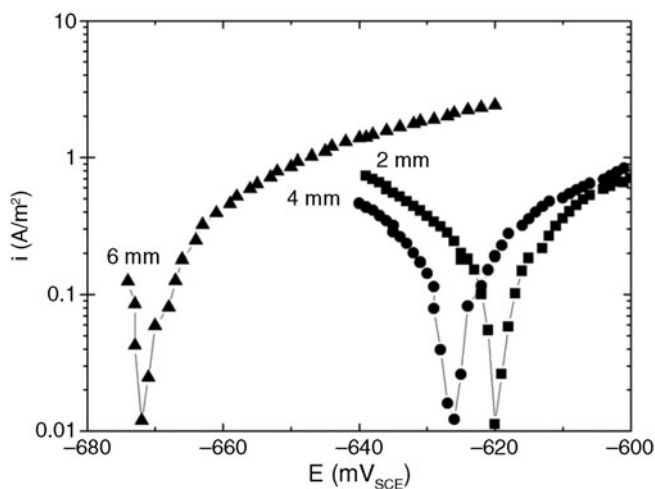

FIGURE 7. *Polarization curves of the attack bottom at different depths in the base solution at room temperature.*

ing, however, that the corrosion potential reported in Figure 6 is actually referring to the uncoupled potential of the outer large electrode of Figure 1. Based on those results and the monotonic evolution of the E_{corr} with free HAc concentration, a scenario was therefore proposed for the propagation mechanism. Results obtained, thanks to the asymmetric assembly described above, also showed that shallow attacks do not propagate in the absence of free HAc.[6] This behavior indicates that mass-transfer limitations induced by geometric constraints and the solution resistance (IR drop) only are not enough to trigger the propagation in CO_2 environment, at least for shallow attacks.

To assess the role of free HAc in the pit propagation stage independently from the IR effect, poten-

tiodynamic measurements were performed at room temperature on the uncoupled inner electrode for shallow attacks. Figure 7 shows the IR-compensated polarization curves obtained at three depths in the base solution. It can be seen, as expected, that increasing the depth leads to a horizontal displacement of the polarization curves toward lower potential values. This indicates that the deeper the attack, the more anodically polarized it will be when coupled to the external electrode. The effect of depth on the local kinetics behavior inside the attack goes together with the general trend observed for E_{corr} while varying the concentration of free HAc. The fact that E_{corr} significantly dropped even for shallow attacks constitutes strong evidence that this behavior is not mainly due to the presence of acetic acid, but to the lack of undissociated HAc in the system. This also has been supported by recent computed results as shown by Figure 8.[12] It is worth noticing, however, that the results shown in Figure 7 represent the behavior of the uncoupled inner electrode, which may be biased by starting the scan at high cathodic polarization. An alternative way is to study the steady-state behavior of the attack coupled to the outer surface by taking advantage of the ZRA setup described in the previous section with a zero bias voltage applied between the two electrodes.

The ZRA circuit was broken periodically for short time intervals (few seconds) as illustrated by Figure 9, and the corrosion potential of the central electrode was measured against the reference electrode in a Luggin capillary located at the mouth of the artificial pit. The potential difference (ΔE) between the coupled state (dominated by the corrosion potential of the outer surface) and the corrosion potential of the central electrode in the cavity was therefore evaluated.
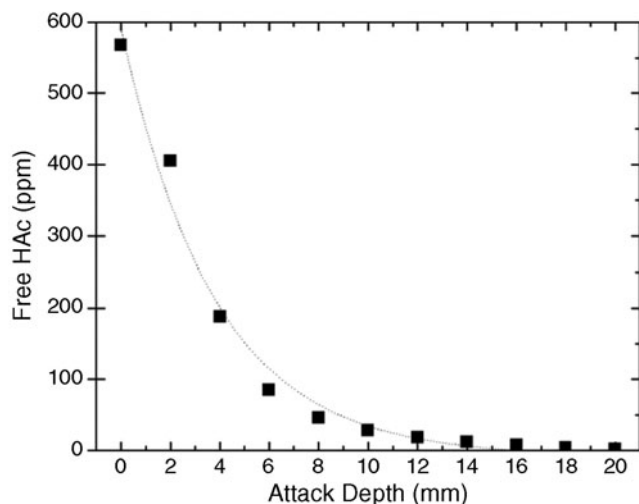
FIGURE 8. *Simulated concentration profile of free HAc at the bottom of the attack for each given depth in the base solution at room temperature.*
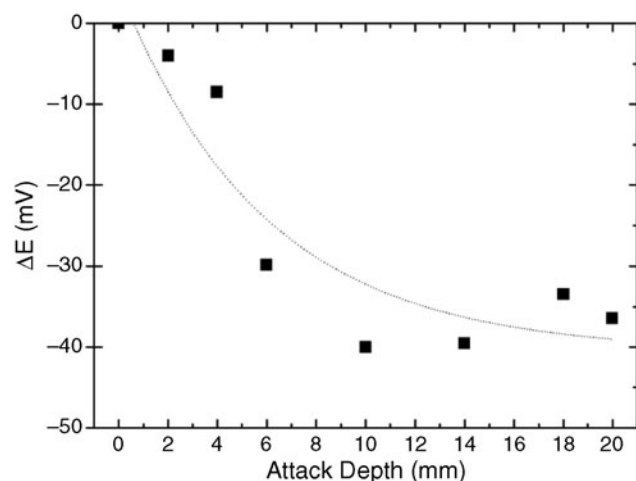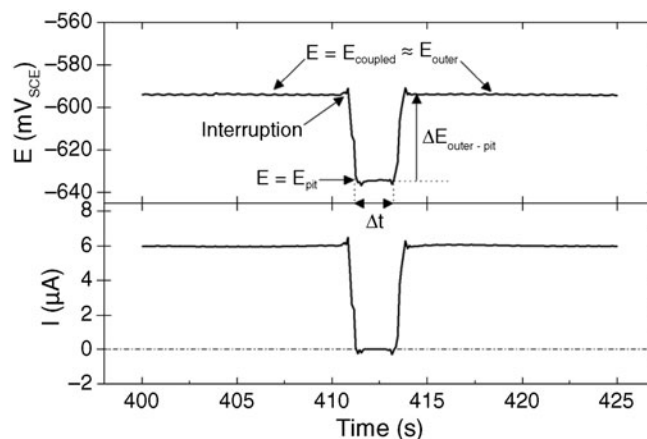

FIGURE 9. *Interruption procedure of the ZRA circuit for the estimation of the corrosion potential difference between the outer surface and the electrode at the bottom of the pit.*
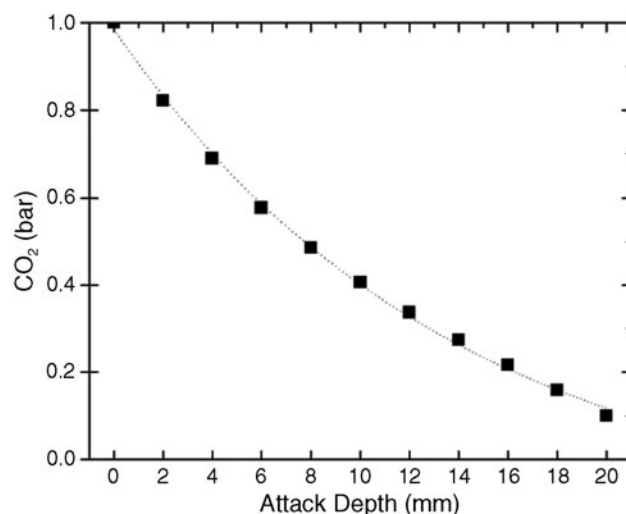

FIGURE 10. *Variation of the potential difference ΔE with attack depth with insulating sidewalls in the base solution at room temperature. At a given depth, ΔE is reported as the average of many interrupt measurements during 2 h of exposure time.*

FIGURE 11. *Simulated concentration profile of CO_2, reported as equilibrium partial pressure, at the bottom of the attack for each given depth in the base solution at room temperature.*

Since the interruption is short, the local conditions approximate those of the coupled state. The potential difference is therefore a measure of the polarization of the central electrode plus the IR drop. As HAc is progressively depleted deeper into the attack, the E_{corr}-free HAc evolution implies the establishment of an increasing ΔE as shown by Figure 10. The attack hence propagates as anodically polarized by the outer surface. It also can be seen from Figure 10 that ΔE does not increase indefinitely and reaches a limiting value. This is consistent with the results of Figure 8, which indicate a total depletion of free HAc toward much deeper attacks. On the other hand, numerical simulation results also revealed a similar depletion of CO_2 as depicted in Figure 11.[12] Once free HAc is

totally depleted, it should be expected that a decrease of the dissolution current at the lower part of the attack (Figure 12) will occur. Although the ohmic drop may contribute to slow down the growth of the attack, the overall dissolution current evolves, mainly according to the counteracting effects of free HAc and CO_2 as it has already been discussed in a recent work.[13] This also corroborates the general trend observed for the coupling current versus depth relation as depicted in Figure 13, which revealed the existence of a critical depth beyond which the attack is no longer self-sustained.

It is however worth stressing that the previous results related to the behavior of preinitiated attacks were obtained in the case of inert, electrically insulating sidewalls thus far. Artificial pit electrode measurements acquired thanks to the same experimental
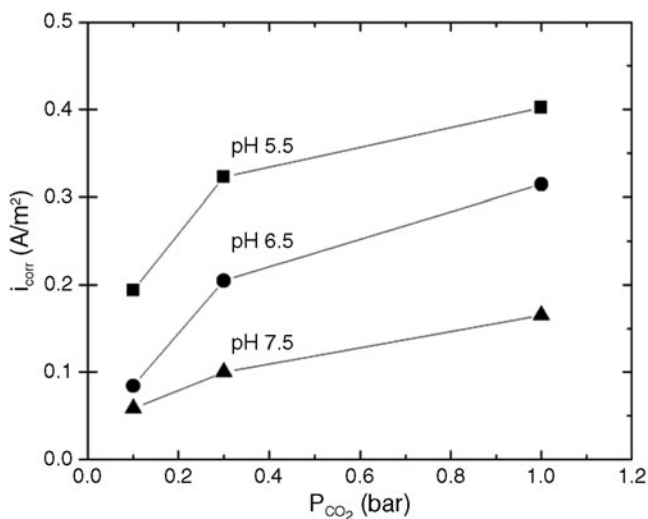
FIGURE 12. *The effect of CO_2 partial pressure on the corrosion current density at different pH values. Data were estimated from polarization curves measured on X65 steel under different CO_2 partial pressures and pH. 0.1 wt% NaCl, 600 ppm of total acetic species, room temperature.*

FIGURE 13. *Average coupling current for artificial pits with (□) reactive and (■) inert insulating sidewalls in 0.1% NaCl, 600 ppm of total acetic species, 1 bar CO_2, room temperature.*

setup with corroding carbon steel sidewalls nonetheless yielded a similar trend for the current versus depth as illustrated in Figure 13. The critical depth was shown, however, to shift toward smaller values, thus minimizing the polarization of the deeper portions.[14] In view of the elements argued above, a schematic scenario is therefore proposed in Figure 14 and can be described as follows: once the critical depth is reached, the attack stops growing downward and the highest dissolution rate is confined to the sidewalls. The attack thereafter opens upward and completely loses its cover. Mass transfer, therefore, is restricted no longer. As a consequence, the driving force for the growth vanishes and the attack undergoes the final process of stifling. This morphological trend is in good agreement with the hemispherical shape observed for developing localized attacks (Figure 15) and the further development into mesa attacks, which is commonly reported from laboratory studies and field observations, particularly in the case of TLC phenomena.[3-4]
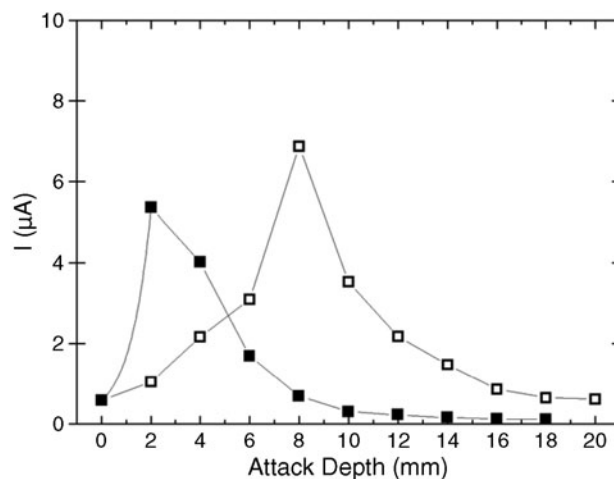
CONCLUSIONS

❖ The monotonic evolution of the corrosion potential with free HAc concentration was identified as a driving force in the propagation stage of localized attacks. The results acquired with the help of artificial pit electrode measurements indeed showed that the depletion of free HAc induces a local potential difference. Attack growth was also shown to be self-sustained only to a critical depth, beyond which the coupling current sharply drops off as it effectively occurs in actual TLC cases.

❖ Artificial pit measurements performed on the same experimental arrangement but with corroding sidewalls nonetheless yielded a similar qualitative dependence for the coupling current versus the attack depth with the current peak occurring closer to the attack mouth. For a preformed attack, but with corroding sidewalls, the vanishing coupling current beyond a critical depth would confine the high dissolution region to the sidewalls around this critical depth. This would then trigger the lateral growth of the attack, which leads to an important issue related to the morphological trend of actual growing attacks.
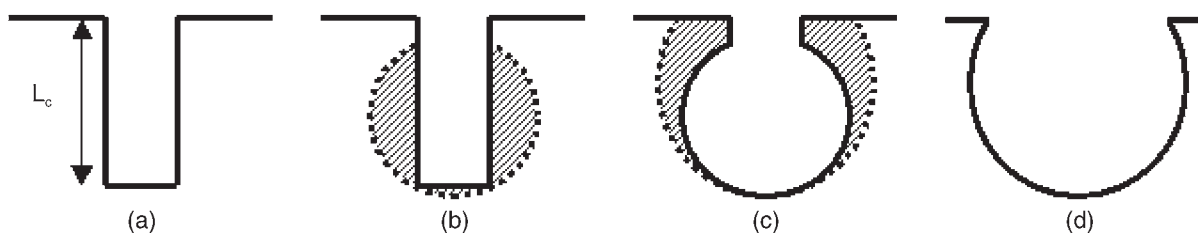

FIGURE 14. *Descriptive scenario for propagation and stabilization of localized attacks. (a) The attack stops propagating downward when reaching the critical depth L_c. (b) The attack undergoes a lateral growth. (c) The attack propagates upward. (d) The attack is stabilized.*
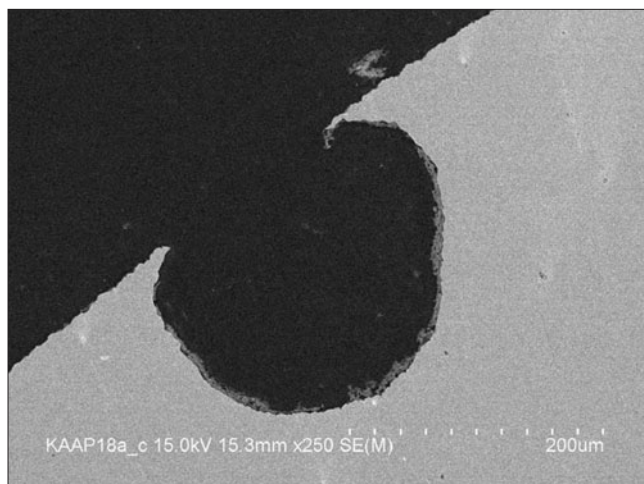
FIGURE 15. *SEM image of a typical hemispherical morphology of localized corrosion attacks observed for carbon steel exposed to CO₂/HAc environment. 0.3 wt% NaCl, 1 bar CO₂, 600 ppm of total acetic species, room temperature.*

ACKNOWLEDGMENTS

REFERENCES

1. R. Nyborg, "Overview of CO₂ Corrosion Models for Wells and Pipelines," CORROSION/2002, paper no. 02233 (Houston, TX: NACE International, 2002).
2. A. Dugstad, L. Lunde, K. Videm, "Parametric Study of CO₂ Corrosion of Carbon Steel," CORROSION/1994, paper no. 14 (Houston, TX: NACE, 1994).
3. Y.M. Gunaltun, D. Larrey, "Correlation of Cases of Top-of-Line Corrosion with Calculated Water Condensation Rates," CORROSION/2000, paper no. 71 (Houston, TX: NACE, 2000).
4. E. Gulbrandsen, K. Bilkova, "Solution Chemistry Effects on Corrosion of Carbon Steels in Presence of CO₂ and Acetic Acid," CORROSION/2006, paper no. 06364 (Houston, TX: NACE, 2006).
5. M.W. Joosten, J. Kolts, J.W. Hembree, M. Achour, "Organic Acid Corrosion in Oil and Gas Production," CORROSION/2002, paper no. 02294 (Houston, TX: NACE, 2002).
6. J. Amri, E. Gulbrandsen, R.P. Nogueira, *Electrochem. Commun.* 10 (2008): p. 200.
7. M. Thammachart, Y. Gunaltun, S. Punpruk, "The Use of Inspection Results for the Evaluation of Batch Treatment Efficiency and the Remaining Life of the Pipelines Subjected to Top of Line Corrosion," CORROSION/2008, paper no. 08471 (Houston, TX: NACE, 2008).
8. A. Aballe, F. Huet, *J. Electrochem. Soc.* 149, 3 (2002): p. B89.
9. D. Deforge, F. Huet, R.P. Nogueira, P. Ponthiaux, F. Wenger, *Corrosion* 62 (2006): p. 514.
10. J. Han, Y. Yang, B. Brown, S. Nešić, "Electrochemical Investigation of Localized CO₂ Corrosion on Mild Steel," CORROSION/2007, paper no. 07323 (Houston, TX: NACE, 2007).
11. J. Marsh, J.W. Palmer, R.C. Newman, "Evaluation of Inhibitor Performance for Protection Against Localized Corrosion," CORROSION 2002, paper no. 02288 (Houston, TX: NACE, 2002).
12. J. Amri, E. Gulbrandsen, R.P. Nogueira, "Computational Model of a Localized Attack in CO₂ Corrosion in the Presence of Acetic Acid," EUROCORR 2008 (Edinburgh, U.K.: European Federation of Corrosion [EFC], 2008).
13. J. Amri, E. Gulbrandsen, R.P. Nogueira, *Electrochim. Acta* (2009): doi:10.1016/j.electacta.2009.07.061.
14. J.A. Beavers, N.G. Thompson, *Corrosion* 43 (1987): p. 185.

Pit growth and stifling on carbon steel in CO_2-containing media in the presence of HAc

J. Amri [a,b], E. Gulbrandsen [a], R.P. Nogueira [b,*,1]

[a] Institute for Energy Technology Instituttveien 18, NO-1254 Kjeller, Norway
[b] Grenoble INP, SIMAP and LEPMI BP, 75, 38402 St. Martin d'Hères, France

ABSTRACT

CO_2 corrosion of carbon steel pipelines in the presence of acetic acid was studied using artificial pit electrode assembly. The potential difference and the coupling current between the small attack and the outer large surface were monitored by means of a zero resistance ammeter (ZRA). The results give strong and complementary evidence about the major role of acetic acid in the growth mechanism of localized attacks in CO_2 corrosion. Pits seem to propagate and stifle mainly according to counteracting depletion effects of respectively acetic acid and CO_2. It is also shown that the purely ohmic drop is not the only factor contributing to the stifling of localized corrosion attacks in systems like those of top of line corrosion. On the basis of the obtained results, a complete scenario was therefore proposed for the morphological trend of localized attacks, which is in good agreement with field observations.

© 2009 Elsevier Ltd. All rights reserved.

1. Introduction

CO_2 corrosion of carbon steel is still a major concern particularly encountered in oil and gas production and transportation industry [1,2]. Carbon steel is widely used in the field for being presently the only economically feasible material. Being however highly vulnerable to CO_2 corrosion, carbon steel can experience severe damages leading to premature failure of installations in the absence of preventive mitigation efforts like injection of corrosion inhibitors [3–5]. CO_2 corrosion is often associated to the presence of some other acidic gases such as hydrogen sulphide (H_2S) or volatile short chain carboxylic acids usually co-produced with unprocessed hydrocarbons. Acetic acid (CH_3COOH, commonly denoted HAc) is one of the most prevalent organic acids found in oil and gas reservoirs with high concentrations up to thousands of ppm in the produced aqueous phase.

The effect of HAc on the corrosion rate of carbon steel in CO_2-containing media has been extensively investigated over a wide range of conditions during the last few years, as summarized in recent literature reviews [6,7]. Results issued from field observations and laboratory studies have shown that HAc has an additional contribution to the overall CO_2 corrosion rate [6,8,9]. There seems a consensus that HAc entails a significant enhancement of the

cathodic reaction due to proton reduction either after acid dissociation or directly from the undissociated acid or the combination of both [10,11]. The presence of HAc has also been observed to cause a shift of the anodic polarization branch towards higher potentials, i.e. an inhibition of the anodic branch [6,12–15]. The latter effect is however not well understood yet.

Furthermore, even though comprehensive studies have been devoted to the effect of HAc on the uniform corrosion in CO_2-containing media, little information however exists regarding its basic role in the initiation and growth of localized attacks [14]. This is of particular interest in the case of the so-called top of line corrosion (TLC) which is recognized as one of the most severe forms of internal corrosion encountered in wet gas transportation [3]. It is typically associated with partially or completely failed thermal insulation of the pipeline. Due to the external cooling that induces large temperature gradients, the co-produced water vapour contained in the gas phase condenses on the whole circumference of the internal walls of the line. As most of the condensing water drains under the effect of gravity to the lower part, corrosion is first expected to occur at the bottom of the line. Under sustained dewing conditions, a continuous thin film of liquid nevertheless forms on the upper parts, which is saturated with the acidic gases present in the gas phase. In this case, the top of the line is also subject to corrosion. Although corrosion prevention is usually achieved by injection of inhibitors, TLC is still difficult to mitigate. Indeed, as TLC occurs in wet gas lines operated in stratified flow regime, corrosion inhibitors remain at the bottom and are not prone to reach and protect the top of the line. Although significant efforts have

---

* Corresponding author. Tel.: +33 4 76 82 65 93.
  E-mail address: ricardo.nogueira@phelma.grenoble-inp.fr (R.P. Nogueira).
  [1] ISE Member.

been undertaken to understand TLC, the underlying mechanisms controlling the propagation and stifling of localized TLC attacks is still not well understood. This makes TLC difficult to both predict and control.

The main goal of the present paper is to go deeper in the analysis of previous results that seemed to succeed to reproduce this qualitative behaviour often found in the case of TLC, that is, increasing corrosion rates and steep shrinkage after a certain – not predictable – time delay. In that previous work [16], the corrosion potential, E_{cor}, was found to increase monotonically with HAc concentration in CO_2 saturated electrolytes. A similar result was also reported for low carbon steel in acetic acid ethanolic solutions [17]. Zero resistance ammeter (ZRA) measurements on an artificial pit electrode assembly to be described below showed that HAc triggers and sustains the pit growth through a galvanic coupling between the pit bottom and the surrounding outer surface. Consumption of HAc inside the pit, in combination with restricted convection and the extended diffusion path give rise to a HAc concentration gradient between the pit bottom and the bulk of the solution. That is, a HAc differential concentration cell is formed. Since the corrosion potential increases with HAc concentration as shown in Ref. [16], this differential cell establishes a corrosion potential difference so that the pit bottom is anodically polarized by the outer surface. This scenario would predict a monotonic increase of the corrosion rate as long as the acetic acid is depleted. Nevertheless, measurements of the coupling current flowing between the pit base and the outer surface at different depths within the range 0–20 mm showed the existence of a critical depth below which the coupling current increases and beyond which it sharply drops off as it effectively occurs in TLC cases. The peak value of the coupling current reached at this critical depth suggested a total depletion of HAc for which the potential difference between the pit base and the outer surface is maximum. These results are in line with field observations. Indeed, inspections of gas lines operated by different companies in the field indicate that the propagation rate of TLC attacks in many cases slows down with time and stabilizes at low rates. The present paper goes further in the analysis of this issue, mainly in which concerns the mechanisms of growth and stifling of localized corrosion attacks. In particular, it is shown that ohmic drops across the pit only cannot explain this corrosion current decrease.

2. Experimental

All electrodes were made from API 5L X65 pipeline steel. Samples were wet-ground with SiC papers up to 1200 grit finish, rinsed with distilled water and degreased with acetone. The corrosive medium consisted of CO_2 saturated (1 bar CO_2) 0.01 M NaCl aqueous solutions containing different amounts of HAc at room temperature.

The solution pH, depending on the HAc concentration, was measured before and after the experiments. For long range experiments, the bulk pH was regularly measured and, if needed, adjusted with the addition of droplets of HCl or NaOH. It is worth stressing, however, that for 1 bar CO_2 saturated solution of 0.01 M NaCl and 600 ppm of total acetic species, the pH is 3.38. In this case, most of acetic acid is still in its undissociated form. Some complementary experiments have been carried out at pH 4.5 and 5.5 to evaluate the corrosion potential behaviour with increasing HAc concentrations at different fixed pH values. Measurements were carried out in a large 2L cell to prevent any significant depletion of either free proton (by H^+ reduction) or undissociated HAc (by the increase of pH and/or direct reduction of HAc) in the bulk.

Unless specifically mentioned, the ensemble of measurements consisted in pit propagation experiments performed thanks to the asymmetric assembly schematically illustrated by Fig. 1. The working surfaces were the cross sections of concentric, mutually insulated rods of 2 mm and 20 mm diameter for the inner and the outer electrodes, respectively. The specimen was positioned vertically in the test cell with the electrode surfaces facing upwards. Pre-initiated attacks were simulated by adjusting the central electrode to a given depth within the range 0–20 mm. It must be emphasized that, as appears in Fig. 1, the lateral walls inside the pit consisted of insulating epoxy resin: only the pit bottom was then made of steel.

The electrochemical measurements were carried out on the large outer surface and the inner artificial pit electrodes connected through the ZRA by applying a zero-voltage difference between them. Real-time records of the current flowing between the coupled electrodes as well as their coupled potential measured against a saturated calomel reference electrode with the help of a Luggin capillary probe located at the pit mouth were then simultaneously
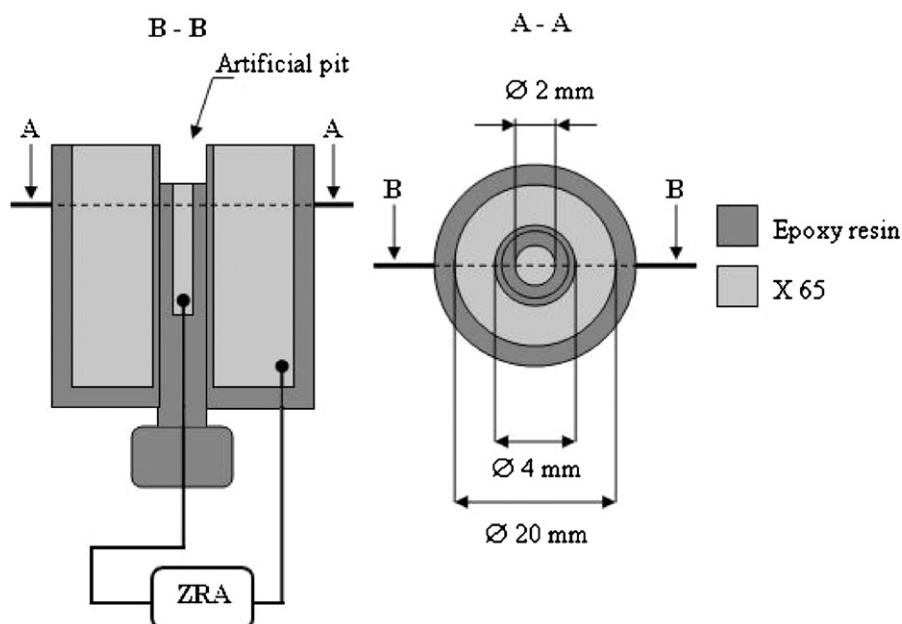

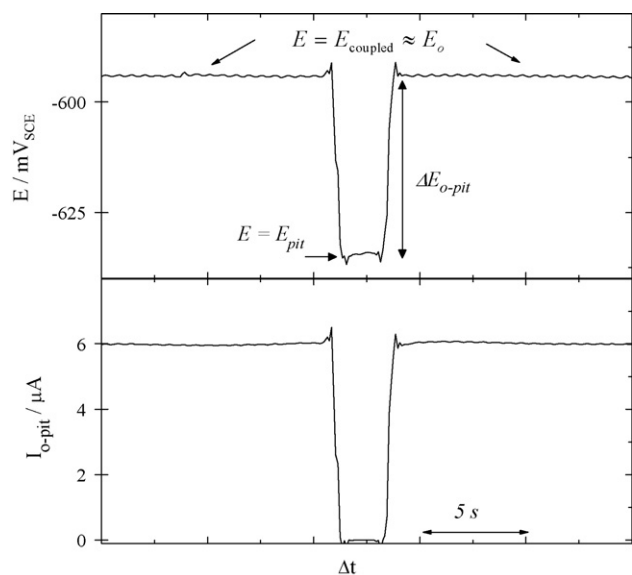**Fig. 1.** Artificial pit assembly and ZRA connection.

Fig. 2. Interrupting the ZRA connection for the determination of the potential difference between the outer large electrode (o) and the inner artificial pit electrode for the case of a 8 mm depth pit after 2 h of immersion in 0.01 M NaCl, 600 ppm HAc and 1 bar CO_2. Arbitrary time origin.

Fig. 3. Corrosion potential as a function of the undissociated HAc concentration at different pH values in 0.01 M NaCl saturated with 1 bar CO_2. The total concentrations of acetic species were 0, 60, 180 and 600 ppm.

measured. The electrical connections of the ZRA setup were kept in such a way that a net anodic current to the inner electrode is reported as positive. Due to the 100-fold surface ratio, the potential of the couple was approximately equal to that of the outer big one, which means that whenever the electrodes were coupled by the ZRA, the potential value sensed was assimilated to the corrosion potential of the outer big electrode, E_o. To estimate the potential at the pit base, E_{pit}, the ZRA circuit was periodically broken as illustrated in Fig. 2. During disconnection, the big outer electrode was kept out of the circuit and the system directly measured the potential difference between the reference electrode and the small inner one. This overall procedure allowed hence the potential difference between the pit bottom (as mentioned before, lateral walls were insulated) and the outer surface to be monitored as well as the current flowing between them.

Electrochemical impedance measurements were also performed on the small inner electrode in both flat and mechanically drilled conditions in a conventional three electrodes cell with a large titanium plate as the counter-electrode. The excitation was a 10 mV$_{rms}$ sinusoidal signal in the 50 kHz to 10 mHz frequency range.

3. Results and discussion

The two electrodes depicted in Fig. 1 being of the same material and exposed to the same electrolyte, the corrosion potential is a priori expected to be the same for the outer and the inner electrodes so that a mean current value close to zero is supposed to be sensed by the ZRA setup. This is what effectively happens for zero pit depths or even shallow pits. Nevertheless, for deeper pits (typically > 1 mm), a net current different from zero was always and reproducibly sensed. Furthermore, this current being always positive indicated that the small inner electrode was anodically polarized by the outer one. This potential difference between the outer and the inner electrodes is not straightforwardly accessible since the ZRA imposes a zero-voltage difference between the two electrodes. It can nevertheless be evaluated by intermittently disconnecting the ZRA, as illustrated in Fig. 2 taking as an example the case of an 8 mm depth artificial pit. Since the interruption is short (few seconds), the concentration profiles approximate those of the
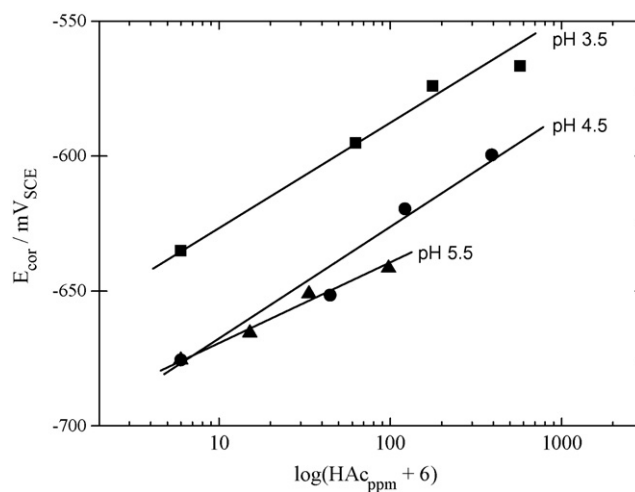
coupled condition. As expected, immediately after uncoupling the electrodes, the current fell to zero and the potential of the artificial pit dropped about 45 mV with respect to the coupled condition in the case illustrated by Fig. 2.

The interpretation of this potential difference can be related to the fact that the corrosion potential of X65 steel monotonically decreases with decreasing HAc concentration as reported in the literature [6,10,11,18,19]. This dependence of the corrosion potential on the HAc concentration is confirmed in Fig. 3 which depicts the monotonic increase of the corrosion potential of a single electrode exposed to a CO_2 saturated electrolyte containing increasing amounts of undissociated HAc at distinct fixed pH values. Once acetic acid was added to the test solution, the pH was adjusted using HCl and NaOH droplets as mentioned before. Assuming an equilibrium state, the concentration of undissociated HAc is straightforwardly estimated according to the postulate of mass conservation of acetic species (acetates + HAc).

As proposed in Ref. [16], in the case of the artificial pit assembly, geometrical constraints would restrain solution renewal inside the pit. Thus, the consumption of HAc inside deep artificial pits would entail a difference in HAc concentration and hence different potential values between the outer and the inner electrodes. In other words, the depletion of HAc inside the pit would trigger its anodic polarization and hence the preferential dissolution at the bottom of the pit. This means that the anodic polarization inside the pit is actually changed in the sense of easier dissolution, this change being caused by the change of the environment inside pit. It is interesting to see that applying the 45 mV found in Fig. 2 to the pH 3.5 curve in Fig. 3 would effectively correspond to a strong ca 15-fold depletion of HAc inside the pit. This is consistent with results from other works, where the concentration of the undissociated form of the weak acid, rather than pH, was shown to be a critical factor in CO_2 corrosion of X65 steel in the presence of HAc. Indeed, the undissociated HAc would act as the main reactant in the cathodic process rather than the reduction of proton or carbonic acid [10,11].

To validate this hypothesis of HAc depletion as the key parameter behind the electrochemical asymmetry between the inner and the outer electrodes, some specific measurements were carried out with a split-cell in which two identical electrodes were placed in two identical compartments separated by a salt bridge, so that no geometric differences were present. The salt bridge is connected to both compartments through porous glass frits that allow ion migration but restrict bulk mixing of the two solutions. One of the compartments was filled with the same base solution of that in
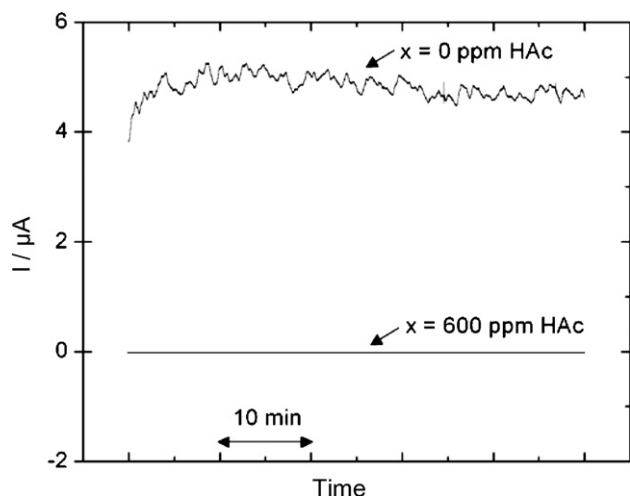
Fig. 4. Current flow between two identical electrodes in a split-cell composed of two identical compartments separated by a high conductivity salt bridge. One of the compartments contained the base CO_2 saturated (1 bar CO_2) 0.01 M NaCl aqueous solution containing 600 ppm. The other compartment simulated distinct conditions of no depletion ($x = 600$ ppm) and total depletion ($x = 0$ ppm) of HAc.

Fig. 5. Potential difference between the outer large electrode and the artificial pit electrode as a function of the pit depth in 0.01 M NaCl, 600 ppm HAc and 1 bar CO_2.

previous measurements, that is, CO_2 saturated (1 bar CO_2) 0.01 M NaCl aqueous solution containing 600 ppm of HAc, the second being filled with different electrolytes depending on the experiment. Fig. 4 depicts the current flow between the two electrodes in distinct condition simulating no depletion (solutions are strictly the same in both compartments) and total depletions (no HAc is added in the second compartment). Results clearly point out a net anodic polarization – resulting in a net anodic current – of the electrode exposed to the electrolyte simulating depleted conditions as seen in the figure. It is worth noticing that an expected ca zero current was also found between the two electrodes when the HAc concentration was made zero at both sides, which is also consistent with the idea of HAc concentration gradient triggering the current flow.

These results seem to be a sound although indirect corroboration of the basic idea that the potential drop illustrated in Fig. 2 can be ascribed to the HAc depletion inside the artificial pit due to hindered hydrodynamic conditions. This scenario is expected to be dependent on the pit depth due to the increasing difficulty of supplying the reactant the deeper the pit is. One should hence expect an in principle monotonic increase of the potential difference till a given limit depth beyond which the acid would be totally depleted and the potential difference should reach a maximum. This issue is illustrated in Fig. 5 where it can be seen that the potential difference (measured in each case after 2 h of exposure to the corrosive solution) does not increase indefinitely. It goes through a maximum for 8 mm depth before slightly decreasing again. This seems consistent with our previous results [16], where the dissolution rate has been shown to reach its maximum value at about 8 mm beyond which it sharply drops off. Similar behaviours have also been reported for iron [20] and steel [21] in NaAc–HAc buffer solution.

Before analysing the dependence between the potential difference and the current flow between the outer surface and the artificial pit, Fig. 6 shows their time evolution for two cases, 8 mm and 20 mm depth artificial pits. As well as in Fig. 5, potentials were measured after 2 h of exposition. Unlike the coupled potential, which was stable over the whole period of the experiment, the potential at the pit bottom slightly but gradually increased with time. As a consequence, the potential difference monotonically decreased during several hours before reaching a steady behaviour as seen in Fig. 6A, which is consistently followed by a decreasing tendency of the current flowing between the outer surface and the pit, as shown in Fig. 6B. This slow evolution may be ascribed to con-
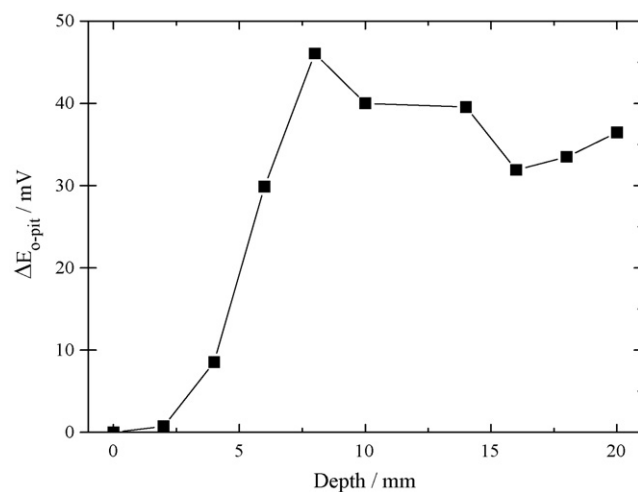
centration changes due to consumption of reactants and production of reaction products coupled to restricted mass transfer.

It is worth noticing that the coupling current and the potential difference behaved in a very reproducible way reflecting the intrin-
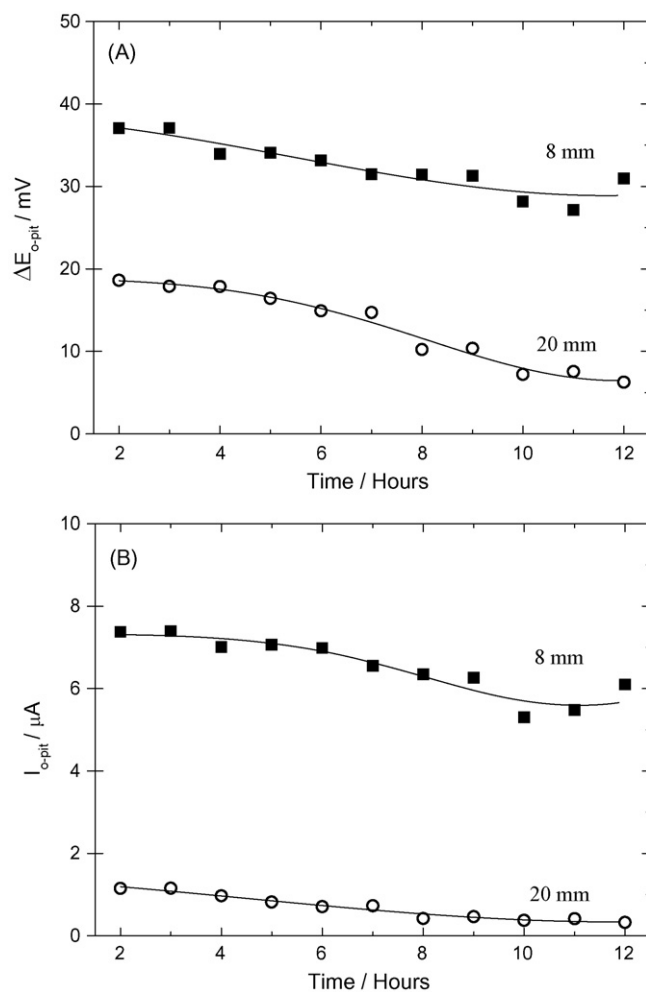

Fig. 6. Typical time evolution of the potential difference (A) and the coupling current flow (B) between the outer large electrode and the artificial pit electrode for 8 mm and 20 mm depths in 0.01 M NaCl, 600 ppm HAc and 1 bar CO_2.
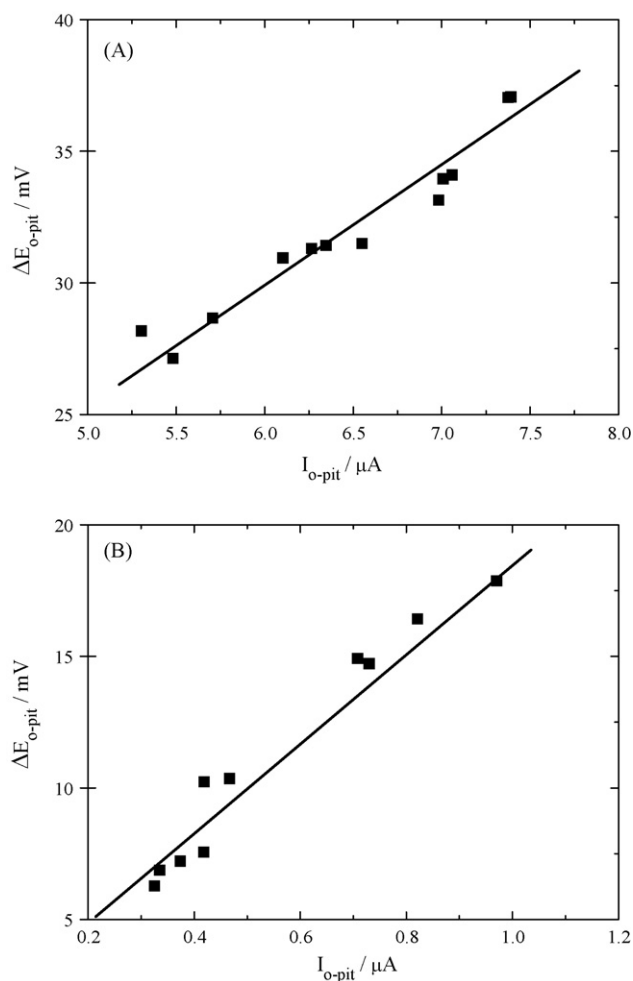
Fig. 7. Potential–current relationship for 8 mm (A) and 20 mm (B) pit depth during the time evolution of the potential difference and the coupling current between the outer large surface and the artificial pit as depicted in Fig. 5. 0.01 M NaCl, 600 ppm HAc and 1 bar CO_2.

sic kinetic behaviour of the coupled interface. Indeed, rearranging the results depicted in Fig. 6 A and B, it appeared that the joint evolution of the potential difference and the current coupling between the two electrodes behaves linearly as seen in Fig. 7A and B for the 8 mm and 20 mm depth artificial pits, respectively. This linear correspondence appeared for all pit depths not only when following their time evolution, as done in the case of Fig. 6, but also when computing values issued from different experiments performed in similar conditions.

The persistence of this current–potential linearity brings to the forefront of the problem the idea of a macroscopic overall resistance value that controls this behaviour, at least in steady state conditions as discussed in this paper. Fig. 8 shows the evolution with the pit depth of the slope R, directly obtained from the E–I plots like those in Fig. 7. It is interesting to see that the curve goes through a minimum value at the same 8 mm depth for which the maximum current flowing between the two electrodes is reached as shown in Fig. 4 of Ref. [16]. This indicates that this current behaviour is not merely a coincidence but is clearly related to the intrinsic kinetic behaviour of the interface illustrated by Fig. 7. In that previous work, the steep decrease of the current for deeper pits was tentatively ascribed to the increase of the electrolyte resistivity ρ inside the pit. The validity of such hypothesis can be verified by incorporating in Fig. 8 the linear evolution of the theoretically estimated electrolyte resistance, R_e, obtained by applying the measured elec-
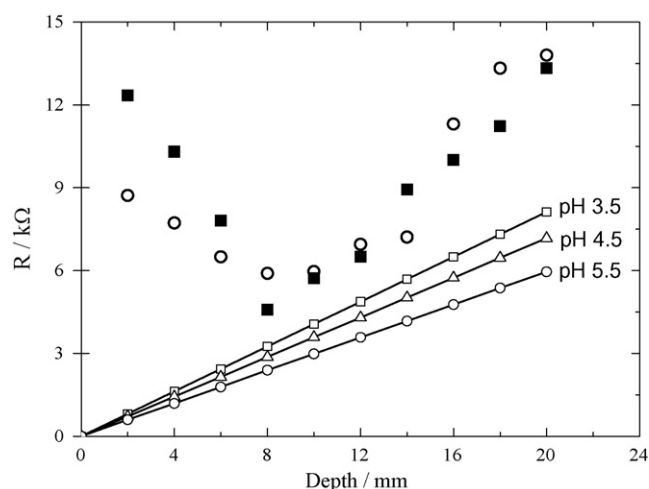

Fig. 8. Experimental values of the slope R of the potential–current linear relationship as shown in Fig. 6 as a function of the pit depth (■); theoretical electrolyte resistance R_e at different pH values for a perfect cylindrical geometry (solid lines) and R values computed from Eq. (3) with R_s and $R_{p, \text{pit}}$ obtained from electrochemical impedance measurements (○), see Fig. 9.

trolyte conductivity at different pH values to a perfect cylindrical geometry of a length L and a cross-sectional area S simulating the artificial pit, $R_e \approx \rho(L/S)$. It appears hence that the pure electrolyte resistance, being always smaller than the slope R, cannot account for the overall ohmic behaviour of the pit electrode.

The general behaviour of the slope R in Fig. 8 must thus be addressed by considering that the small potential differences involved in the coupled measurements (typically less than 50 mV as seen in Figs. 5 and 6) allow the current–potential curves to be investigated with the help of a simple linear equivalent circuit analysis in the frequency domain [22,23] according to Fig. 9 that yields

$$I_{\text{o-pit}} = \frac{\Delta E_{\text{o-pit}}}{\left(Z_o + R_s + Z_{\text{pit}}\right)} \tag{1}$$

where Z_o and Z_{pit} account for the electrochemical impedances of the outer large surface and the artificial pit, respectively, and R_s the actual solution resistance. Since we were interested only in the steady values of both the potential difference and the current flow obtained under stationary conditions, the electrochemical impedance of each electrode can be assimilated to its polarization resistance ($R_p \lim_{\omega \to 0} Z(\omega) = R_p$). Besides, taking into account the 100-fold surface ratio, one can estimate the polarization resistance of the inner electrode, $R_{p,\text{pit}}$, to be 100 times greater than that of the outer one and write

$$I_{\text{o-pit}} \approx \frac{\Delta E_{\text{o-pit}}}{R_s + R_{p,\text{pit}}} \tag{2}$$

According to Eq. (2), the slope R of the current–potential curves as those in Fig. 7A and B is hence given by
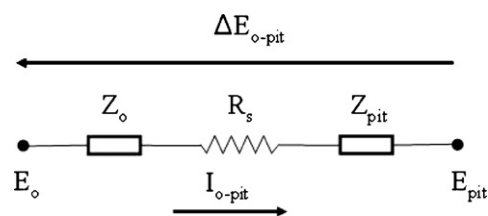
$$R = R_s + R_{p,\text{pit}} \tag{3}$$

Fig. 9. Equivalent circuit for the asymmetric artificial pit electrode assembly of Fig. 1.
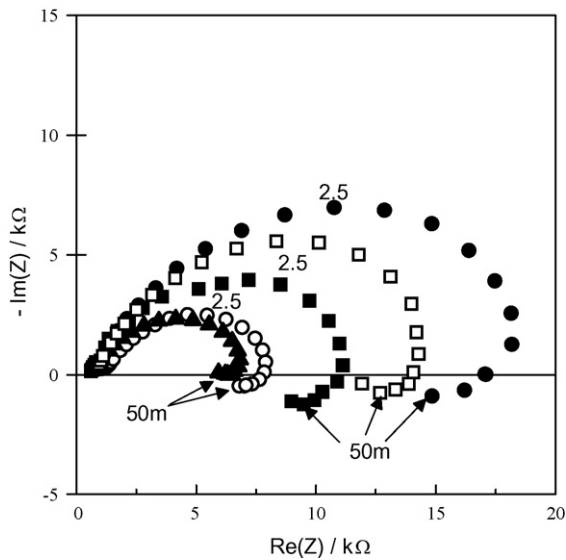
Fig. 10. Nyquist plots of the electrochemical impedance of artificial pits of different depths in 0.01 M NaCl, 600 ppm HAc and 1 bar CO_2: (■) 2 mm; (○) 6 mm; (▲) 10 mm; (□) 16 mm; (♦) 18 mm. Frequency values in Hz.

Fig. 11. Average coupling current versus pit depth with corroding steel sidewalls in 0.01 M NaCl, 600 ppm HAc and 1 bar CO_2.

This hypothesis was evaluated with the help of electrochemical impedance measurements, shown in Fig. 10, performed on the smallest electrode at different depths in the range 2–20 mm. The electrode was DC polarized to the coupled potential prior to and during the EIS measurements in order to establish the actual concentration profiles inside the pit. It must be noticed that we were interested in the goodness of Eq. (3) to describe the overall macroscopic behaviour and not in the deep analysis of the impedance behaviour that is beyond the aims of the present paper and is not discussed here. The general behaviour of Nyquist diagrams is, however, in good agreement with previous results from the recent literature [24]. The impedance modulus decreased for increasing depths till the critical 8 mm value beyond which it increased again, which reflects very well the qualitative behaviour of the coupling current. For the sake of comparison, the values of R according to Eq. (3) and obtained from the Nyquist diagrams were also plotted in Fig. 8. A good general agreement between these values and those issued from the overall kinetic behaviour appearing from the ZRA measurements and illustrated in Fig. 7 indicates that Eq. (3) represents a good approximation for the description of the macroscopic behaviour of the artificial pit at different depths. It must be noticed that the R_s values obtained from the Nyquist diagrams are smaller than those predicted by the theoretical curves for deeper pits, probably because of changes in the composition of the confined electrolyte. This confirms that purely ohmic effects related to R_s are not the only factor contributing to the inversion of the curve tendency beyond 8 mm.

In view of the elements argued above, the role of HAc is likely to be related to the pit growth. The complete scenario can then be described as follows: the coupling current is related to the potential difference induced by the HAc depletion inside the pit. The inner electrode is hence anodically polarized and corrodes according to its polarization resistance for shallow pits, for which the depletion and hence the potential difference between the electrodes is not too high and the electrolyte resistance can be neglected. As the pits go deeper towards the critical depth, the depletion and hence the anodic polarization increase yielding a strong decrease of the polarization resistance. Beyond the critical depth the decreasing current may tentatively be explained by a further depletion of HAc and CO_2, which leads to a decrease of the corrosiveness and thus an increase of the polarization resistance. This hypothesis is
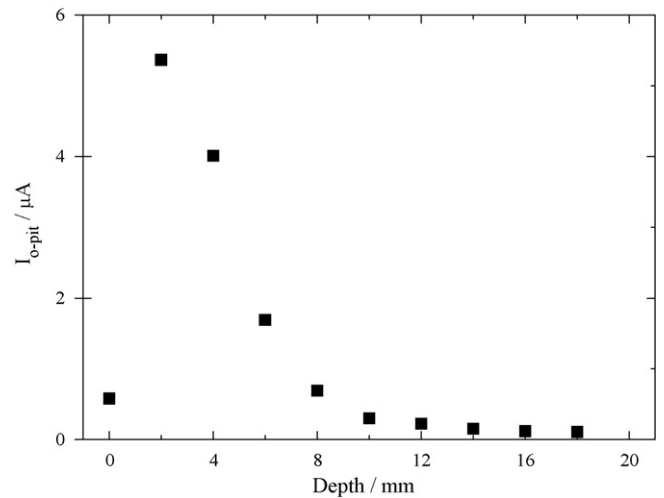
supported by preliminary results of numerical simulations, which indicate a significant depletion of CO_2 beyond the critical depth [25]. The solution resistance does not seem to contribute substantially to the overall resistance in this stage. It must be emphasized however, that these results were obtained with inert, electrically insulating lateral walls of the artificial pit, which is obviously not a realistic configuration. In this sense, experiments were also performed on artificial pits with corroding steel walls, and with the same geometrical proportions as that in Fig. 1. The corroding lateral walls were part of the external electrode, while the inner electrode was located in the bottom of the pit as before. The results showed that the peak in the coupling current now occurred closer to the pit mouth (two instead of 8 mm critical depth as seen Fig. 11). This suggests that the concentration gradients were steeper due to the increased area of corroding steel inside the pit. The results have nonetheless given a similar qualitative dependence for the coupling current versus the pit depth. This justifies to some extent the extrapolation of the results obtained with non-reactive wall pits to undertake our following reasoning on the morphological trend of the growing pit.

For a pre-formed artificial pit, but with corroding lateral walls, the vanishing coupling current beyond a critical depth as shown in Fig. 11 would confine the high dissolution region to the sidewalls around this critical depth with a concomitant rapid slowdown of the growth rate at the pit bottom as the pit grows deeper. This would then trigger the lateral growth of the pit, which leads to an important issue related to the hemispherical morphology trend of actual growing pits particularly reported in the case of Top-of-line corrosion phenomena according to field observations and laboratory studies [6,8]. In that case, a possible scenario, schematically represented in Fig. 12, would be that at the first stages, the pit bottom would dissolve faster and faster as the HAc is depleted and not sufficiently fed because of diffusion constraints. As the critical
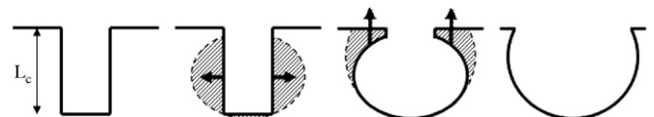

Fig. 12. Schematic illustration of the hemispherical morphology trend of the propagating attack after an initial growing down period till the critical depth L_c. From the left to the right the scheme illustrates the pre-initiated attack, the lateral growth, the mouth opening and the final shape. Once the attack undergoes a sufficient mouth widening (step 3), the growth process may stifle due to increased convection and inward mass transfer. Clustering of attacks may also be envisaged.

depth is approached, the faster dissolving region is shifted to the lateral walls and gradually moves towards the pit mouth. The pit should therefore progressively become hemispherical and the pit mouth would widen to the extent where mass transport is no more seriously limited, the concentration gradient and consequently the potential difference between the pit mouth and bottom vanishes as well as the driving force for the pit growth: the pit is then stifled as found in actual situations of TLC.

4. Conclusions

Results acquired thanks to artificial pit electrodes showed that HAc has a substantial effect on the propagation stage of localized attacks in CO_2 corrosion of carbon steel pipelines. As a consequence of the E_{corr}–HAc relation observed in our previous work, the depletion of HAc induces a potential difference so as the attack is anodically polarized by the outer surrounding surface. The present study also demonstrated that the IR drop mechanism of localized corrosion does not operate for this system and the process of stifling seems to be rather induced by CO_2 depletion inside the attack.

Acknowledgement

References

[1] R. Nyborg, CORROSION/2002, Paper no. 02233.
[2] B.M. Kermani, A. Morshed, Corrosion 59 (2004) 659.
[3] C. De Waard, D.E. Milliams, Corrosion 31 (1975) 177.
[4] A. Dugstad, L. Lunde, K. Videm, CORROSION/1994, Paper no. 14.
[5] S. Nešić, J. Postlethwaite, S. Olsen, Corrosion 52 (1996) 280.
[6] E. Gulbrandsen, K. Bilkova, CORROSION/2006, Paper no. 06364.
[7] S. Nešić, Corros. Sci. 49 (2007) 4308.
[8] Y.M. Gunaltun, D. Larrey, CORROSION/2000, Paper no. 71.
[9] M.W. Joosten, J. Kolts, J.W. Hembree, M. Achour, CORROSION/2002, Paper no. 02294.
[10] Y. Garsany, D. Pletcher, B. Hedges, J. Electroanal. Chem. 538–539 (2002) 285.
[11] Y. Garsany, D. Pletcher, D. Sidorin, W.M. Hedges, Corrosion 60 (2004) 1155.
[12] G. Bech-Nielsen, Electrochim. Acta 19 (1974) 821.
[13] J.-L.-Crolet, N. Thevenot, A. Dugstad, CORROSION/1999, Paper no. 24.
[14] Y. Sun, K. George, S. Nešić, CORROSION/2003, Paper no. 03327.
[15] R. De Marco, Z.T. Jiang, D. John, M. Sercombe, B. Kinsella, Electrochim. Acta 52 (2007) 3746.
[16] J. Amri, E. Gulbrandsen, R.P. Nogueira, Electrochem. Commun. 10 (2008) 200.
[17] R.S. Gonçalves, N.M. Coradini, W.X. Olivera, Corros. Sci. 33 (1992) 1667.
[18] W.M. Hedges and L. McVeigh, CORROSION/1999, Paper no. 21.
[19] Y. Garsany, D. Pletcher, B. Hedges, CORROSION/2003, Paper no. 03324.
[20] M. Vankeerberghen, M. Abdulsalam, H. Pickering, J. Deconinck, J. Electrochem. Soc. 150 (2003) B445.
[21] E.A. Nystrom, J.B. Lee, A.A. Sagüés, H.W. Pickering, J. Electrochem. Soc. 141 (1994) 358.
[22] A. Bautista, U. Bertocci, F. Huet, J. Electrochem. Soc. 148 (10) (2001) pB412.
[23] A. Aballe, F. Huet, J. Electrochem. Soc. 149 (3) (2002) pB89.
[24] G.A. Zhang, Y.F. Cheng, Corros. Sci. 51 (2009) 87.
[25] J. Amri, E. Gulbrandsen, R.P. Nogueira, EUROCORR 2008, Edinburgh, UK.

ELSEVIER

The effect of acetic acid on the pit propagation in CO$_2$ corrosion of carbon steel

J. Amri [a,b], E. Gulbrandsen [a], R.P. Nogueira [b,*]

[a] *Institute for Energy Technology, NO-1254 Kjeller, Norway*
[b] *Grenoble INP, SIMAP and LEPMI; CNRS, UMR5266 and 5631, BP 75, 38402 St. Martin d'Hères, France*

Abstract

The role of acetic acid (HAc) on the pit growth in CO$_2$ corrosion of carbon steel pipelines is studied by means of an artificial pit electrode. The current flowing between the artificial pit and the outer surface was measured with a zero resistance ammeter. It is shown that the corrosion potential increases with increasing HAc concentration. Depletion of HAc inside the pit imposed a potential difference that triggered the pit growth. The pit did not grow in absence of HAc. The pit growth was self-sustained only to a certain pit depth, beyond which the dissolution current at the bottom of the pit vanished. This is in good agreement with field observations mainly in the case of top-of-line corrosion phenomena.
© 2007 Elsevier B.V. All rights reserved.

Keywords: CO$_2$ corrosion; Carbon steel; Top-of-line corrosion; Acetic acid; ZRA

1. Introduction

Internal corrosion of pipelines constitutes a significant problem to the petroleum industry [1]. Water and acidic gases (carbon dioxide (CO$_2$), hydrogen sulphide (H$_2$S), and volatile organic acids) co-produced with the hydrocarbons constitute the corrosive environment. Carbon steel is presently the only economically feasible material for such pipelines. The corrosion rates may reach 10 mm per year (mm/y) or more [2–4] in absence of mitigation efforts, like injection of corrosion inhibitors.

Acetic acid (HAc) is one of the most abundant volatile organic acids, and can be present in concentrations up to several thousand ppm in the aqueous phase. The effect of HAc on the internal corrosion has been investigated in several studies during the last few years; see Ref. [5] for a recent review. Field experience shows that HAc is a key

factor in the localized top-of-line corrosion attacks in gas-condensate pipelines [6].

In a recent laboratory study on CO$_2$ corrosion it was shown that presence of HAc caused pitting at room temperature [5]. Few, but deep pits were formed, i.e. the pit growth dominated over the pit nucleation. At 80 °C, the corrosion rate was uniform. Being a weak acid, the HAc accelerated the cathodic part reaction. It was furthermore observed that the HAc inhibited the anodic part reaction. The average corrosion rate at room temperature, decreased slightly with increasing HAc concentration, despite the significant increase of the cathodic reaction. The pit penetration rate increased with increasing concentration, however. The anodic inhibition effect was also observed in other studies on iron and steel corrosion in HAc containing media [7–10]. The mechanism of the pit initiation and growth in HAc/CO$_2$ environments is however not studied. The present paper reports the overall mechanism of the pit growth in terms of galvanic effects caused by the presence of HAc.

---

* Corresponding author. Tel.: +33 4 76 82 66 37; fax: +33 4 76 82 67 09.
E-mail address: ricardo.nogueira@enseeg.inpg.fr (R.P. Nogueira).

2. Experimental

All electrodes were made from API 5L X65 steel. Samples were wet-ground with SiC papers up to 1200 grit finish, rinsed with distilled water and degreased with acetone. The corrosive medium consisted of 0.01 M NaCl solutions containing different amounts of HAC (0–1000 ppm) saturated with 1 bar CO_2 at room temperature. Unless otherwise noted, the electrolyte was permanently stirred with a rotating magnet at 100 or 200 rpm speed, placed at the bottom of the cell.

Potentiodynamic measurements ($5 \, mV \, s^{-1}$) were performed in a three-electrode cell, with a coiled titanium wire as the counter-electrode and a saturated calomel (SCE) as the reference one.

The pit growth was studied using an artificial pit electrode assembly successfully employed in previous studies [13,14]. The working surfaces were the cross sections of concentric, mutually insulated rods of 2 and 20 mm diameter for the artificial pit and the outer big surface, respectively. Pre-initiated pits were simulated by machining the inner electrode down to different depths (0–20 mm). The current (I) flowing between the inner and the outer electrodes was measured by a zero resistance ammeter. The inner small electrode was connected as the working electrode, which means that positive current values indicate anodic behaviour of the pit. See Fig. 1 of Ref [13] for a schematic representation of the electrode assembly.

3. Results and discussion

Fig. 1 shows the polarization curves with 0 and 600 ppm of acetic acid under natural convection conditions. HAc entails an important enhancement of the cathodic branch, probably due to both proton reduction after acid dissociation and to the direct reduction of the undissociated acid

[11,12]. For the aims of the present work, however, the important effect of the presence of HAc is the shift of the corrosion potential to less negative values.

The corrosion potential (E_{corr}) increased monotonically with HAc concentration, as illustrated in Fig. 2 for forced convection conditions. The constant supply of fresh solution yielded a larger range of potential shift when compared to Fig. 1. On the other hand, the corrosion current, which can be roughly estimated as $\cong 0.5 \, A \, m^{-2}$ from the curves in Fig. 1, remained practically unchanged. The kinetic behaviour depicted in Figs. 1 and 2 thus indicates that the overall effect of the HAc is a balance between a boosted cathodic branch and a depressed anodic one, with no uniform corrosion current increase related to the presence of HAc. This scenario seems then to be consistent with field and laboratory observations of localized attack of carbon steel in the presence of both CO_2 and HAc [5,6].

Figs. 1 and 2 are obtained from measurements performed with a single electrode so that they deliver only macroscopic global information. On the other hand, the role of HAc on the pit growth has been evaluated taking advantage of the specific experimental arrangement described in the previous section. If no preferential attack of the artificial pit takes place, the current is expected to remain close to zero, because of the 0 V applied by the ZRA. This is what was actually observed in the absence of HAc even in the case of pre-initiated pits as shown in Fig. 3. On the contrary, the introduction of HAc even at small concentrations induced an always positive I, monotonically increasing with the acid concentration.

The fact that the pre-initiated pit did not start growing in the absence of HAc is a strong evidence that geometric constraints only are not enough to trigger pitting in CO_2 environment, at least in the experimental conditions of the present study. On the other hand, even small quantities of HAc seem to be sufficient to trigger and sustain pit
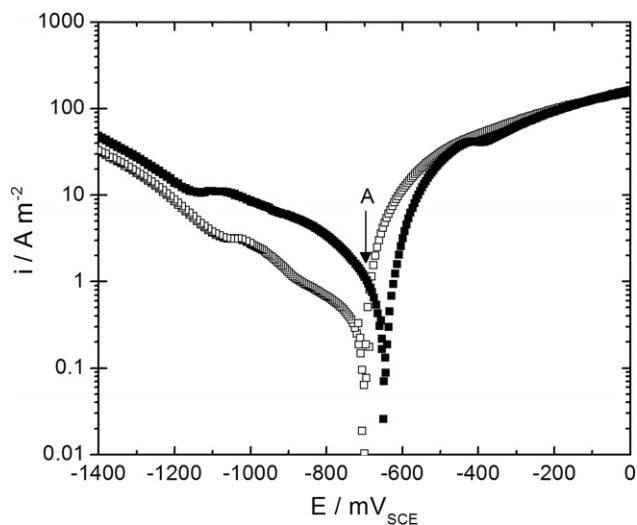

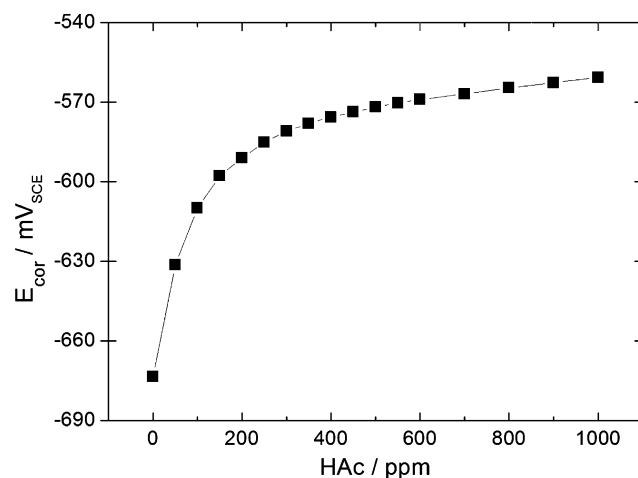Fig. 1. Polarization curves of X65 steel in 0.01 M NaCl and 1 bar CO_2 at 0 (□) and (■) 600 ppm of HAc. Natural convection.

Fig. 2. Corrosion potential of X65 steel in 0.01 M NaCl and 1 bar CO_2 as a function of HAc concentration. In this case, E_{corr} (mV) $= -740 + 27 \ln([HAc] + 6)$. Magnet stirrer rotation $\omega = 100$ rpm.
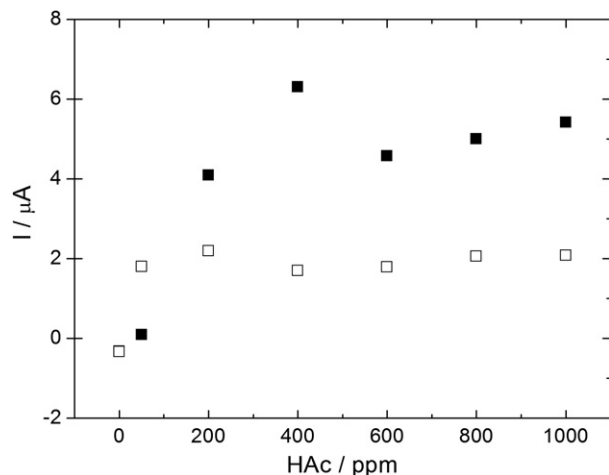
Fig. 3. Average values after 12 h of exposure, of the current I flowing to a pre-initiated 2-mm depth artificial pit as a function of HAc concentration. 0.01 M NaCl and 1 bar CO_2 .(■) $\omega = 100$ rpm. (□) $\omega = 200$ rpm.

Fig. 4. Average coupling current versus pit depth in 0.01 M NaCl, 600 ppm HAc and 1 bar CO_2.

growth. This can be ascribed to the combined effect of geometric constraints and the presence of HAc. As shown in Fig. 1, the presence of HAc strongly enhanced the cathodic activity. Inside the pre-initiated pit, the acid is more rapidly depleted because of mass transport limitations that establish a HAc concentration gradient between the artificial pit surface and the outer one. This is confirmed from Fig. 3, since the current I is lower for higher magnet rotation speeds that increased HAc supply to the artificial pit, hence reducing the potential difference between the pit and the outer surface. It is worth noticing that the coupled current density at point A in Fig. 1 for the fully depleted 0 ppm and the 600 ppm HAc solutions, is of about 1.0 A m^{-2} ($I \cong 3.0$ μA for a 0.03 cm^2 surface as that of the artificial pit). This is about the order of magnitude of the values given in Fig. 3, which indicates that the artificial pit assembly gives reliable results.

The idea that the HAc depletion inside the pit is at the origin of the pit growth leads to an important issue related to the monotonic evolution of the corrosion potential observed in Fig. 2. Shallow pits must be more easily fed by mass transport of HAc than deep ones. This entails that the potential difference, and hence the current I should increase with the pit depth till a certain critical value for which the surface HAc depletion is total inside the pit. Results shown in Fig. 4 indicates that the pit growth is self-sustained only to a certain critical depth, beyond which the dissolution current vanishes. One of the possible reasons of this behaviour is the ohmic potential drop between the electrodes. For very deep pits, where the supply of HAc is strongly restrained, the ohmic drop may be a major component and I would then be expected to decrease, which is in agreement with experimental results. After reaching a maximum at about 8 mm, however, I drops too sharply to be only ascribed to ohmic drop. This has been the matter of repeated experiments that always gave the typical profile of Fig. 4. Another possible explanation would be the accu-
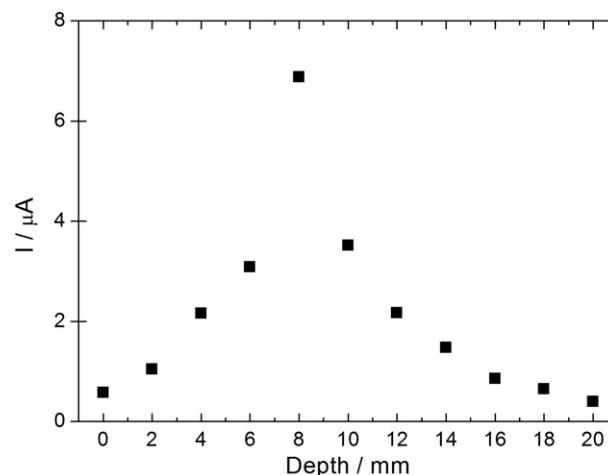
mulation of corrosion products, or the presence of small hydrogen bubbles trapped inside the pit [15,16], which could act as a gas-cavity [17]. The described pit growth mechanism hence deviates in several ways from that of stainless steels and other passive metals. The pit growth is self-sustained only to a certain depth, and it occurs under anaerobic, acid corrosion conditions, with no acidic cations present. The pK_a of the first hydrolysis step of Fe^{2+} is 9.6, compared to 2.2 for Fe^{3+} [18]. Since acid is consumed inside the pit, alkalinization is expected rather than an acidification, which would also contribute to hinder the dissolution at the bottom of the pit as a result of $FeCO_3$ precipitation.

These results suggest that a real pit may grow spherically until a certain radius is reached, followed by opening of the pit mouth and lateral growth, which is the morphology observed in previous laboratory tests [5] and top-of-line corrosion attacks in the field [6]. This issue, as well as the inferred alkalinization inside the pit will be matter of numerical simulation that can help elucidating the origin of this abrupt current – pit depth profile.

Acknowledgement

References

[1] B.M. Kermani, A. Morshed, Corrosion 59 (2004) 659–683.
[2] C. De Waard, D.E. Milliams, Corrosion 31 (1975) 177–181.
[3] A. Dugstad, L. Lunde, K. Videm, CORROSION/94, Paper No. 14, NACE International, Houston, TX, 1994.
[4] S. Nesic, J. Postlethwaite, S. Olsen, Corrosion 52 (1996) 280–294.
[5] E. Gulbrandsen, K. Bilkova, Solution Chemistry Effects on Corrosion of Carbon Steel in Presence of CO_2 and Acetic Acid, CORROSION/2006, Paper no. 06364, NACE International, Houston, TX.

[6] Y.M. Gunaltun, D. Larrey, Correlation of Cases of Top of Line Corrosion With Calculated Water Condensation Rates, CORROSION/2000, Paper no. 71, NACE International, Houston, TX, 2000).

[7] G. Bech-Nielsen, The anodic dissolution of iron – V, Electrochim. Acta 19 (1974) 821.

[8] J.-L. Crolet, N. Thevenot, A. Dugstad, Role of Free Acetic Acid on the CO2 Corrosion of Steels, CORROSION/99, Paper no. 24, NACE International, Houston, TX, 1999.

[9] Y. Sun, K. George, S. Nesic, The Effect of Acetic Acid on Localized CO_2 Corrosion in Wet Gas Flow, CORROSION/2003, Paper no. 03327, NACE International, Houston, TX.

[10] R. De Marco, Z.T. Jiang, D. John, M. Sercombe, B. Kinsella, Electrochim. Acta 52 (2007) 3746.

[11] Y. Garsany, D. Pletcher, B. Hedges, J. Electroanal. Chem. 538–539 (2002) 285.

[12] Y. Garsany, D. Pletcher, D. Sidorin, W.M. Hedges, Corrosion 60 (2004) 1155.

[13] D. Déforge, F. Huet, R.P. Nogueira, P. Ponthiaux, F. Wenger, Corrosion 62 (2006) 514.

[14] A. Aballe, F. Huet, J. Electrochem. Soc. 149 (3) (2002) B89.

[15] H.W. Pickering, Mater. Sci. Eng. A198 (1995) 213–223.

[16] B.G. Ateya, H.W. Pickering, J. Electrochem. Soc. 122 (1975) 1018.

[17] C. Gabrielli, F. Huet, R.P. Nogueira, Electrochim. Acta 50 (2005) 3726.

[18] R.M. Smith, A.E. MartellCritical Stability Constants, vol. 6, Plenum Press, New York, 1989, Second Suppl.